DESIGN, SYNTHESIS, AND BIOLOGICAL STUDY OF HISTONE DEACETYLASE2 INHIBITORS TO ENHANCE MEMORY FORMATION

by

A. F. M. Towheedur Rahman

A Dissertation Submitted in

Partial Fulfillment of the

Requirements for the Degree of

Doctor of Philosophy

in Chemistry

at

The University of Wisconsin-Milwaukee

December 2024

ABSTRACT

DESIGN, SYNTHESIS, AND BIOLOGICAL STUDY OF HISTONE DEACETYLASE2 INHIBITORS TO ENHANCE MEMORY FORMATION

by

A. F. M. Towheedur Rahman

The University of Wisconsin-Milwaukee, 2024
Under the Supervision of Professor M. Mahmun Hossain

Histone deacetylase 2 (HDAC2) is a critical regulator of neurocognitive functions. Its suppression is linked to improved memory and mitigation of Alzheimer's disease (AD) pathologies by enhancing neuronal plasticity. However, the structural similarity among class-I HDACs has posed challenges in developing selective HDAC2 inhibitors.

In this study, we report on the synthesis and characterization of a novel small-molecule HDAC2 inhibitor, JRM-28, to achieve selectivity and neuronal plasticity. JRM-28, initially synthesized as a prodrug with disulfide-linked monomers, demonstrated selective inhibition of HDAC2 with an IC50 of 0.107 μM. Comparative binding assays with other HDACs and in-silico docking studies further validated its specificity for HDAC2 over other HDACs.

Functional evaluations revealed that JRM-28 induces morphological plasticity in neurons, evidenced by dendritic morphogenesis, spine maturation, and enhanced post-synaptic neurotransmission in both SHSY5Y and primary hippocampal neurons. Mechanistically, JRM-28 inactivated HDAC2, triggering the transcriptional activation of CREB (cAMP

response element-binding protein), a central regulator of neuronal plasticity. This effect was selective for CREB, with no activation of related transcription factors CREM or ATF-1. When applied to AD neurons derived from iPSC-derived neural stem cells, JRM-28 upregulated CREB-dependent proteins, such as NR2A and GluR1, and stimulated NMDA- and AMPA-driven calcium influx, thereby enhancing neuronal plasticity and synaptic function. CREB silencing confirmed its essential role in mediating these effects.

Our findings highlight JRM-28 as a promising small molecule for selective HDAC2 inhibition, offering a potential therapeutic approach to restore neuronal plasticity and cognitive functions in neurodegenerative diseases like AD.

© Copyright by A.F.M. Towheedur Rahman, 2024
All Rights Reserved

TABLE OF CONTENTS

LIST OF FIGURES viii

LIST OF TABLES x

LIST OF ABBREVIATIONS xi

ACKNOWLEDGEMENTS xii

1. Introduction 1

1.1. An Overview of Epigenetics **1**
1.1.1. DNA Methylation 2
1.1.2. histone modifications 3
1.1.2.1. Histone Acetylation 3
1.1.2.2. Histone Deacetylation 4
1.2. Histone Deacetylases (HDACs) 5
1.2.1.Classification of HDACs 5
1.2.2. Catalytic Mechanism of Class I HDACs 6
1.2.3. Biological Roles of HDACs 7
1.2.4. HDACs and Cancer 8
1.2.5. HDAC and Neural Development 9
1.2.6. HDAC2 and Alzheimer's Disease 12
1.2.7. Cellular Mechanism of Neuroplasticity: Implication to Alzheimer's Disease 13
1.2.7.1. NMDA Receptor in Neuroplasticity 14
1.2.7.2. AMPA Receptor in Neuroplasticity 15
1.3. HDAC Inhibitors (HDACi) 16
1.3.1. Structural Features of HDACi 17
1.3.2. HDACis in Cancer Treatment 19
1.3.3. HDACi as Cognitive Enhancer 21
1.3.4. Selective HDAC2 Inhibitors to Improve Synaptic Plasticity 22
1.3.5. Prospect of HDAC2 Inhibitors in Fighting Alzheimer's Disease 24
1.4. Earlier Discovery of HDACi in Hossain Lab 26

2. Materials and Methods 29
2.1. Reagents and cell lines 29
2.2. Reagents for chemical synthesis 30
2.3. In silico docking of JRM-28a in HDAC2 and HDAC4 31
2.3.1. Preparation of structures for docking 31
2.3.2. Docking of JRM-28. 31
2.4. HDAC2 inhibition assay 32
2.4.1. Luminometric method 32
2.4.2. Fluorimetric method 33

2.5. Cell culture strategies of primary hippocampal neurons, SHSY5Y, and AD neurons 34
2.6. Lactate dehydrogenase assay 35
2.7. TUNEL Assay 35
2.8. Measurement of spine density and size 36
2.9. Calcium Influx Assay in Neuronal Stem Cells 36
2.10. Semi-quantitative RT-PCR 37
2.11. Immunofluorescence analysis 38
2.14. Immunoblot assay 40
2.13. Creb siRNA transfection 41
2.14. CRE luciferase assay 41
2.15. Statistical analyses 41

3. Results 43
3.1. Synthesis of JRM Series Compounds 43
3.1.1. Ester Analogs 43
3.1.2. Ketone Analogs 44
3.1.3. Amide Analogs 45
3.1.4. Sulfoxide Analogs 46
3.2.HDAC2 Inhibition Study 49
3.2.1. HDAC2 Inhibition of Ester Analogs 51
3.2.2. HDAC2 Inhibition by Ketone Analogs 52
3.2.3. HDAC2 Inhibition by Amide Analog 52
3.2.4. HDAC2 Inhibition by Sulfoxide Analogs 53
3.3. HDAC2 Selectivity Study of JRM-28 53
3.4. Possible Fate of JRM-28 After Reduction by DTT 55
3.5. In-Silico Study of JRM-28 for HDAC2 Specificity 58
3.6. Effect of JRM-28 on HDAC2 Expression 59
3.7. Intracellular HDAC2 Inhibition by JRM-28 60
3.8.Cytotoxicity Study of JRM-28 61
3.9. Investigation for the Enhancement of Neuroplasticity by JRM-28 62
3.9.1. Effect of JRM-28 on the SHSY5Y Cells 63
3.9.2. Effect of JRM-28 on E18 Mouse Primary Hippocampal Neurons 65
3.10. Investigation for the Involvement of CREB in JRM-28-mediated Enhancement of Morphological Plasticity 67
3.11. Relationship Study Between HDAC2 Inhibition by JRM-28 and CREB Expression 68
3.12. Assessment of the Connectivity Between Ca2+ Influx and JRM-28 Treatment .. 70
3.13...Investigation on the JRM-28-Mediated Augmentation of Neuroplasticity in iPSC-derived AD neurons via activation of CREB 74

4.0. Discussion 78
4.1. Synthesis 78
4.2. JRM-28 is a selective HDAC2 inhibitor 80

4.3. JRM-28 displays a strong neuroprotective response by inducing morphological plasticity in neurons 81
4.4. The JRM-28-mediated inactivation of HDAC2 triggers the transcriptional activation of CREB 82
4.4.5. JRM-28 upregulates neuronal plasticity in AD neurons 82
References 83
Appendix A: General Methods and Experimental 97
Appendix B: Supporting Information 146

LIST OF FIGURES

Figure #	Figure title	Page #
Figure 1	Composition of Nucleosome	1
Figure 2	DNA methylation pathways	2
Figure 3	and repression by histone acetylase (HAT) and histone deacetylase (HDAC)	4
Figure 4	Schematic depiction of the different isoforms of HDAC.	5
Figure 5	Simplified illustration of the catalytic mechanism of deacetylation by HDACs	6
Figure 6	Represents the signaling pathways from NMDA and AMPA receptors.	14
Figure 7	FDA-approved HDAC inhibitors with their CAP group (red), ZBG (green) and Linker (blue)	18
Figure 8	Effects of combined histone deacetylases inhibitors (pan- or selective HDACis) with different antitumor therapies on tumor cells.	20
Figure 9	Development of MJM-1 series HDACi based on Romidepsin	27
Figure 10	Binding of JRM-20 (green) and JRM-20 sulfoxide (blue) to HDAC-2 with SAHA (red)	47
Figure 11	Characterization of JRM-28. (A) Mass spectrum of JRM-28, (B) 1H NMR of JRM-28	49
Figure 12	HDAC-Glo™ I/II Assay Chemistry	50
Figure 13	Inhibition of HDAC2 by ester analogs of MJM-1	51
Figure 14	Inhibition of HDAC2 by ketone analogs	52
Figure 15	HDAC Inhibition by Amide and Sulfoxide Analogs	53
Figure 16	JRM-28 is an HDAC2 inhibitor.	54
Figure 17	Mass spectrum of the DTT-treated JRM-20 and JRM-28.	56
Figure 18	Possible fate of JRM-28 after DTT treatment	57
Figure 19	HDAC2 inhibitory role of JRM-28 and its monomers JRM-28a and b.	57
Figure 20	In-silico binding comparison of JRM-28 with HDAC2 and HDAC4.	59
Figure 21	Immunoblot (IB) analysis of HDAC2 in the total cell lysate of SHSY5Y cells treated with increasing doses of JRM-28 for 24 hrs.	60
Figure 22	Intracellular HDAC2 Inhibition by JRM-28	61
Figure 23	In-vitro Cytotoxicity Study of JRM-28	62
Figure 24	JRM-28 induces structural plasticity in SHSY5Y neurons.	64
Figure 25:	Effect of JRM-28 on E18 Mouse Primary Hippocampal Neurons	65
Figure 26	JRM-28 stimulates transcriptional activity of CREB via inhibition of HDAC2.	66
Figure 27	JRM-28 upregulates CREB expression	69
Figure 28	JRM-28 enhances post-synaptic calcium influx in E18 mouse primary hippocampal neurons.	71

Figure 29	Effect of JRM-28 on Ca2+ influx on SHSy5Y cells	72
Figure 30	Pre-synaptic protein synaptotagmin was dual labelled with NR2A	73
Figure 31	The effect of JRM-28-mediated suppression of HDAC2 on the upregulation of CREB and MAP2 in AD neurons with A246E psen1 mutation.	75
Figure 32	The effect of JRM-28-mediated activation of CREB on the upregulation of NR2A, and GluR1 and in-duction of metabotropic ionotropic calcium entry in AD neurons.	76
Figure 33	The effect of JRM-28-mediated activation of CREB on in-duction of metabotropic ionotropic calcium entry in AD neurons.	77

LIST OF TABLES

Table #	Table title	Page #
Table 1	List of Primers	37
Table 2	List of antibodies used for Western Blot and Immunostaining	39
Table 3	Docking Study	47

LIST OF ABBREVIATIONS

ABC	Explanation
Et_3N	triethyl amine
CH_2Cl_2	dichloromethane
C_6H_6	benzene
LDA	lithium di-isopropylamide
THF	tetrahydrofuran
I_2	iodine
NaOAc	sodium acetate
MeOH	methanol
mCPBA	meta-chloroperoxybenzoic acid
HDAC	Histone deacetylase
HAT	Histone acyl transferase
NMDARs	N-methyl-d-aspartate receptors
AMPARs	α-amino-3-hydroxy-5-methyl-4-isoxazole propionic acid receptors
PSDs	postsynaptic densities
LTP	long-term potentiation
LTD	long-term depression
MOE	Molecular operating environment
GluR1	Glutamate receptor subtype 1

ACKNOWLEDGEMENTS

First and foremost, I express my deepest gratitude to my supervisor, Dr. M. Mahmun Hossain, whose unwavering guidance, encouragement, and insightful discussions were instrumental in the conception, design, and execution of my Ph.D. research. Your mentorship has been a cornerstone of my academic journey, and I am forever indebted to your support.

I extend my sincere thanks to my dissertation committee members, Dr. Alexander L. Arnold, Director of the Milwaukee Institute of Drug Discovery, for his invaluable expertise and guidance; Dr. Xiaohua Peng, for her insightful feedback and encouragement; Dr. David N. Frick, whose collaborative efforts significantly enhanced the quality of my research; Dr. Arsenio Pacheco, for his thoughtful advice and support; and Dr. Douglas Steeber, Professor Emeritus, for his expertise and guidance. Your collective contributions have been crucial to the successful completion of this work.

A special note of gratitude goes to Dr. Avik Roy, Chief Scientific Officer at Simmaron Research Institute, for his wholehearted support and strategic planning for the mechanistic studies with the lead compound. I am deeply grateful to Dr. Anna Benko, Manager of SAILARC at the University of Wisconsin-Milwaukee, for her technical assistance, and to Dr. F. Holger Foersterling, Supervisor of the Nuclear Magnetic Resonance Laboratory, for his invaluable support in the characterization of small molecules.

Last but not least, I would like to acknowledge the many colleagues, collaborators, and mentors who have played a vital role in my journey. To all who contributed their time, knowledge, and encouragement, thank you for helping me achieve this milestone.

Finally, I wish to express my deepest appreciation and heartfelt gratitude to my wife, Sifat E. Sharmeen, for her unwavering mental support and countless sacrifices throughout this arduous journey toward my Doctoral degree. I am equally thankful to my two-year-old son for his remarkable understanding and patience during this demanding period. Furthermore, I extend my sincere gratitude to my parents, whose constant encouragement and motivation have inspired me to strive for the pinnacle of academic achievement.

1. Introduction

1.1. An Overview of Epigenetics

"Epigenetics" refers to the complicated interactions between the genome and its environment that influence differentiation and development in higher organisms.[1] Epigenetic changes refer to stable, heritable changes in chromatin specifically DNA and the associated histone proteins independent of the underlying DNA sequence. A nucleosome is a unit of DNA that is packaged around histone proteins in chromatin. The nucleosome consists of 147 bp of DNA folded around histone octamers containing two copies of each of the histone proteins H2A, H2B, H3, and H4. At only a few sites in the histones, H2A and H3 exist in multiple forms with distinct amino acid sequences.[2] N-terminal histone tails protrude from nucleosomes into the nuclear lumen. A linker DNA is located between the nucleosomes and the H1 histone binds to it (Figure 1). Depending on the spacing of nucleosomes, chromatin can be broadly divided into heterochromatin and euchromatin. Changing chromatin structure allows or prevents specific multiprotein transcriptional regulator complexes from accessing DNA. Several factors are involved in the modification of chromatin structure, including DNA methylation, histone modifications, and ATP-dependent remodeling.[3]

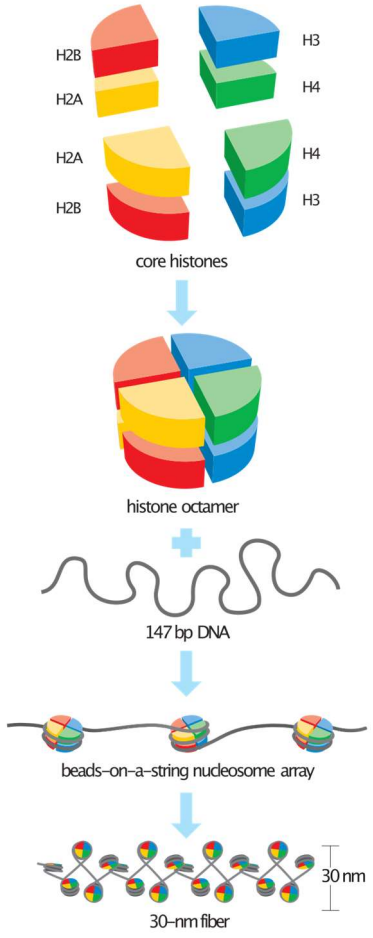


Figure 1: Composition of Nucleosome

1.1.1. DNA Methylation

The discovery of DNA methylation in animals coincided with the identification of DNA as genetic material.[4] 1948 In 1948, Rollin Hotchkiss used paper chromatography to find a change in cytosine in the calf thymus.[5] Hotchkiss (1948) proposed that this modified cytosine was naturally present in DNA and identified this fraction as 5-methylcytosine (5mC) since it separated from cytosine similarly to how thymine (also known as methyl uracil) does. In the 1980s, numerous studies showed that DNA methylation controls gene expression and cell differentiation, although many researchers had suggested that DNA methylation might. These days, it is commonly acknowledged that DNA methylation is an epigenetic factor that works in tandem with other regulators to affect gene activity.[6]

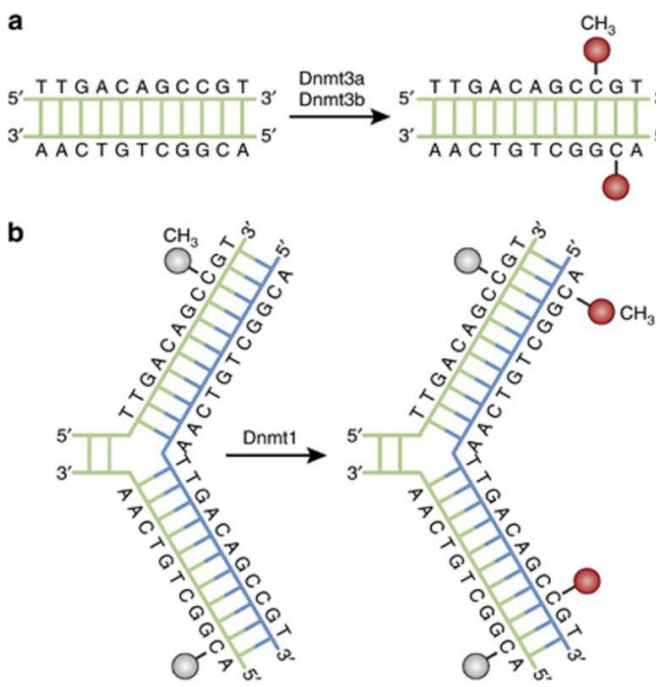


Figure 2. DNA methylation pathways. A family of DNA methyltransferases (Dnmts) catalyzes the transfer of a methyl group from S-adenyl methionine (SAM) to the fifth carbon of cytosine residue to form 5-methylcytosine (5mC). (a) Dnmt3a and Dnmt3b are the de novo Dnmts and transfer methyl groups (red) onto naked DNA. (b) Dnmt1 is the maintenance Dnmt and maintains DNA methylation pattern during replication. [8,11]

DNA methyltransferases (Dnmts) are enzymes that move a methyl group from S-adenyl methionine (SAM) to the fifth carbon of a cytosine residue, starting the DNA methylation process (Figure 1). De novo Dnmts are so named because the Dnmt3a and Dnmt3b enzymes can produce novel methylation patterns from unmodified DNA (Figure 2a).

Additionally, Dnmt1 replicates the DNA methylation pattern of the parental DNA strand onto the freshly produced daughter DNA strand during DNA replication. (Figure 1b). All three DNMs play a significant role in the development of the embryo. When cells reach terminal differentiation, their expression of Dnmt significantly decreased. This implies that postmitotic cells have a persistent DNA methylation pattern. It seems that DNA methylation and Dnmts play greater functions than previously thought, even though postmitotic neurons in mature mammalian brains express significant levels of Dnmts.[7]

DNA methylation is essential for the inactivation of X chromosomes, the creation of genomic imprints, the regulation of tissue-specific gene expression, and the silencing of retroviral elements. Crucially, liable on their genetic sequence, distinct forms of DNA methylation can impact gene activity in different ways.[8]

1.1.2. histone modifications

Histones can undergo post-translational modifications that alter chromatin in a variety of ways, including phosphorylation, ubiquitination, acetylation, and methylation.[9] A 'Histone Code Hypothesis' postulates that distinct combinations of histone modifications may impact chromatin shape and transcriptional state.[9] The location of nucleosomes in relation to gene transcriptional start sites, as well as the kinds, degrees, and combinations of histone modifications, are some of the elements that contribute to the complexity of the histone code.[10]

1.1.2.2. Histone Acetylation

Nearly 60 years have passed since research on histone lysine acetylation revealed how important this acylation is for boosting DNA accessibility, which permits genes to express themselves.[11] A

positively charged lysine residue in the tail of histone H4 may interact with negatively charged DNA or neighboring nucleosomes. Acetylation of the ε-amino group of lysin (Kac) in histone tails and globular domains is catalyzed by histone acetyltransferases (HAT). Acetylation contributes to an open state of chromatin by counteracting the positive charge of lysine, which prevents histones from interacting with DNA. Higher DNA accessibility makes it possible for transcription factors to attach and can stimulate transcription.[12] Additionally, Kac can directly interact with some proteases (sometimes referred to as "reader proteins"), such as transcription factors that include bromodomains and enhance gene expression.[13] Several genome-wide distribution studies have demonstrated a positive relationship between gene expression and the enrichment of histone acetylation at transcriptional start sites (TSS).[14] There is growing evidence that Kac controls transcriptional regulation for cells to operate since abnormal acetylation has been connected to metabolic, neurological, and cancer conditions.[15]

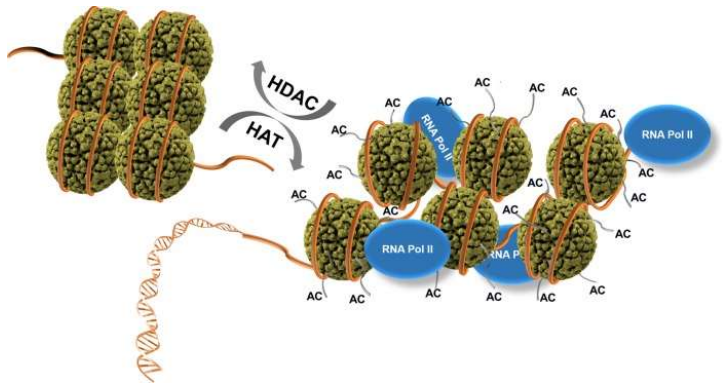


Figure 3. Regulation of gene expression and repression by histone acetylase (HAT) and histone deacetylase (HDAC).[16]

1.1.2.1. Histone Deacetylation

The reverse epigenetic process of histone acetylation is called histone deacetylation, in which the enzyme histone deacetylase enzymatically removes an acetyl group from the lysine tail, transforming the neutral lysine tail into a strongly positively charged species. Because of their compact structure, which results from interactions between their positively charged histones and positively

charged DNA backbones, transcription machinery is unable to access the nucleosomes. (Figure 3).[16]

1.2. Histone Deacetylases (HDACs)

In eukaryotes, a class of proteins known as HDACs is highly conserved.[17] They primarily remove acetyl groups from DNA-binding histone proteins, which decreases chromatin accessibility for transcription factors (TFs) and inhibits gene expression. The complexity of gene regulation networks is thereby enhanced by HDACs, which accurately regulate transcript levels in all eukaryotic cells.[18] HDACs are necessary for physiological processes such as cellular growth and balance,[19] in addition to illnesses like neurodegenerative disorders,[20] genetic conditions,[21] and cancers.[22] Therefore, it is essential to comprehend the intricate role that HDAC plays in cells to develop pharmacological interventions that block or modify their action.

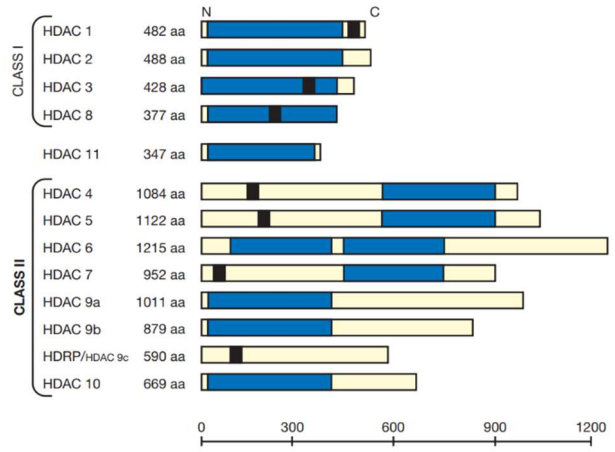


Figure 4. Schematic depiction of the different isoforms of HDAC. Bars depict the length of the protein. The catalytic domain is shown in blue. Black depicts NLS (nuclear localization signal).[25]

1.2.1. Classification of HDACs

There are two families of HDAC proteins: the standard HDAC family and the NAD+-dependent SIR2 HDAC family, which is not the subject of this review. There are two evolutionary classes in the classical HDAC family: class I and class II. (Fig. 4).[23] The yeast transcriptional regulator RPD3 (Saccharomyces cerevisiae) is closely linked to HDACs of class I (HDAC1, 2, 3, and 8). HDA1, another yeast deacetylase, shares domains with

class II deacetylases, including HDAC4, 5, 6, 7, 9, and 10.[23] Recently, HDAC11, a novel member of the HDAC family, was discovered.[24] The minimal sequence similarity prevented us from classifying HDAC11 into class I/II or the SIR2 family, despite Figures 4 suggesting that it is most closely linked to class I HDACs because it has all the traits required to be classified as an HDAC.[24] While class II HDACs have a more limited pattern of expression (Fig. 4), indicating their involvement in cellular differentiation and development, class I HDACs are currently thought to be expressed in the majority of cell types.[25]

1.2.2. Catalytic Mechanism of Class I HDACs

Analysis of the structure and comparative analysis of the catalytic pocket of HDLP and Class I

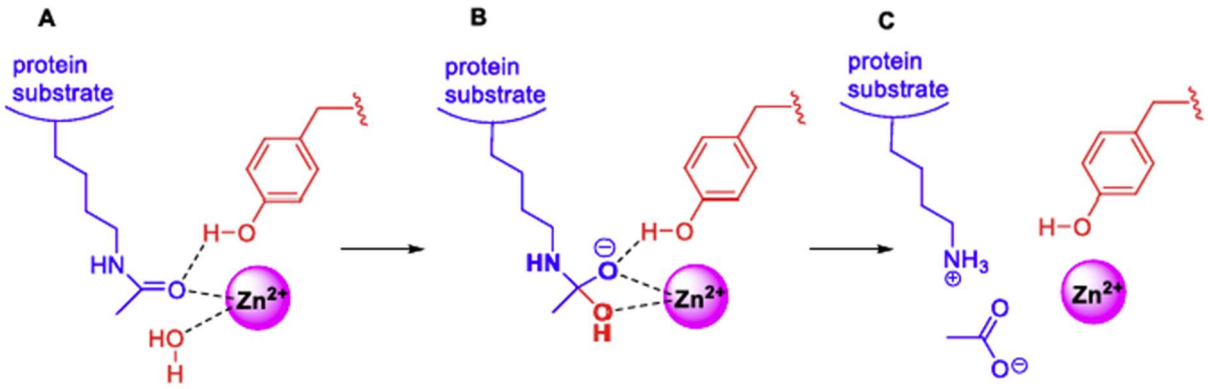


Figure 5. A simplified representation of how HDACs catalyze deacetylation: The acetyllysine-bearing protein substrate, a tyrosine residue, and the zinc cation in the HDAC active site form the binding interactions of the enzyme-substrate complex (A); the tetrahedral oxyanion enzyme intermediate, which results from water's nucleophilic attack; and the enzyme-product complex, which includes the lysine residue and acetate before it is released from the active site (B)..[26, 161]

HDAC8 enabled speculation as to their catalytic mechanisms (Figure 5).[26] In order to stabilize the acetyl-lysine inside the catalytic pocket, zinc ions (Zn2+), which are needed as cofactors in this reaction, are coordinated by three amino acid residues (DDH). Because the Zn2+ cation activates the histidine (H) residue, the acetyl group's C-O bond is more electrophilic, which makes the

carbonyl carbon a more vulnerable target for water molecules' nucleophilic attack. With a tyrosine (Y) residue supporting the transition state, histidine facilitates the final removal of the acetyl group from the substrate.

1.2.3. Biological Roles of HDACs

Class I HDACs can control cell cycle progression, differentiation, and proliferation epigenetically.[27] Interestingly, HDACs are mostly found in the nucleus since they comprise a nuclear localization signal (NLS) and no nuclear export signal (NES).[28] Among class I HDACs, HDAC3 is an anomaly since it has both NES and NLS.[29] It is interesting to note that class I HDACs perform a variety of tasks in multiprotein complexes. Co-repressors of RE1 silencing transcription factors and neuronal restrictive silencing factors (CoREST), nucleosome remodeling and deacetylases (NuRD), co-repressors of retinoid and thyroid receptors, and switch-independent 3A (Sin3A) complexes are among the many large complexes whose catalytic core is comprised of conjugated HDAC1-HDAC2 proteins.[27] HDAC3 is conjugated with HDAC4, 5, 7, and other molecules of class I, whereas HDAC8 is the only exception that can work by itself. Class II HDACs differ from class I HDACs in that they have a non-regulatory domain, a NLS, and a NES. They can also travel inside or outside of the cytoplasm and nucleus, depending on the status of photophosphorylation.[28] Apart from histones, Class II HDACs are also capable of deacetylating non-histone proteins.[27,29] Additionally, only a small number of natural substrates can be bound by Class IIa HDACs by enlisting the help of co-repressors or co-activators.[28] Class IIa HDACs typically have low deacetylation capacity unless they are linked to class I HDACs. It is crucial to remember that HDAC4's catalytic activity depends on both its connection with HDAC3 within the broader NCoR-SMRT complex and the complex's transcriptional control of target genes.[30] On the

other hand, class IIb HDACs eventually play non-classical epigenetic activities.[31] In contrast to the other traditional HDACs, HDAC6 is mainly cytoplasmic and regulates the cytoskeleton by deacetylating α-tubulin.[30,31] Class III HDACs, which include SIRT1-7, are members of the NAD+-dependent deacetylase family and structurally resemble the yeast Sir2 protein.[32] Many intracellular proteins undergo post-translational changes due to SIRTs, either by acetylation or adenosine diphosphate (ADP) ribosylation.[28] However, using the energy obtained from the hydrolysis of NAD+, SIRTs help to deacetylate proteins.[28] SIRT1 can control the expression of many different genes either directly by enlisting other SIRTs and targeting a number of transcription factors and co-activator/repressor proteins, or indirectly by altering the structure of the chromatin. Through several levels of transcriptional control, SIRTs have been closely linked to the emergence of cancer, metabolic imbalance, and medication resistance.[33] The cytoplasm of resting CD4+ T cells and the perinuclear compartment of lymphoblastoid cells are the primary locations of HDAC11, a single member of class IV.[34] HDAC11 mainly regulates diverse immune functions, sensitivity in CD4+ T cells and inflammation.[27, 28, 34] In addition, the N-terminal portion of HDAC11 has a catalytic domain.[34] Class IV HDACs function via the Zn2+-dependent mechanism, just as the other two classes.[28] HDAC11 interacts with HDAC6 but not with NCoR or SMRT, in contrast to class I and II HDACS.[34]

1.2.4. HDACs and Cancer

Tumor suppressor genes and oncogenes are thought to express abnormally as a result of genetic alterations, such as gene mutations, deletions, rearrangements, and chromosomal abnormalities, which result in cancer.[35] However, there is growing evidence that epigenetic alteration plays a crucial role in the initiation and progression of cancer.36 In contrast to genetic defects, epigenetic

alterations can be reversed, making them a viable new type of mechanistic anti-cancer therapy. It has been shown that a global loss of histone H4 monoacetylation is one feature shared by human tumor cells.[37] Histone H4 acetylation changes early in the carcinogenic process.[37] When chromosomes move or repressive transcription factors that interact physically with HDACs are overexpressed, the result is an abnormal recruitment of HDACs to promoters through their physical connection with oncogenic DNA-binding fusion proteins. Abnormal recruitment of HDACs to promoters is caused by chromosomal translocations or overexpression of repressive transcription factors that physically interact with oncogenic DNA-binding fusion proteins.[38] The oncogenic transcription factors PML-RARα (promyelocytic leukemia-retinoic acid receptor α), PLZF-RARα (promyelocytic leukemia zinc fingerretinoic acid receptor α), and AML-1 (acute myeloid leukemia-1), as well as the AML1-ETO (eight-twenty-one) corepressor fusion proteins, for instance, cause leukaemogenesis by enlisting HDAC-containing repressor complexes to constitutively suppress the expression of particular target genes.[39] By enhancing its DNA binding activity in Ewing sarcoma (EWS), inhibition of HDAC activity increased the transcriptional activity of the oncogenic fusion protein and transcription factor EWS-FLI1. In many cancers, specific HDACs, such as HDAC1, HDAC2, HDAC3, and HDAC6, are overexpressed.[40] Certain tumor cell lines exhibit reduced tumor cell growth and survival when individual HDACs are knocked down by siRNA (small interfering RNA)[41], proving that HDACs are important targets for anticancer treatments and in the initiation and spread of malignancies.

1.2.5. HDAC and Neural Development

Various post-translational modifications have been observed during nervous system development, among which deacetylation has been intensively investigated regarding the dominance of HDACs.

One important post-translational modification in eukaryotes is protein acetylation, which involves the addition of acetyl groups to lysine residues.[42] An essential enzyme for the development of the neurological system is HDAC.

For oligodendrocytes to develop into adult oligodendrocytes, a post-translational change called histone deacetylation is required.[43] Additionally, following administration of the HDAC inhibitor trichostatin A (TSA), an in vitro study in a chick fertilized egg model by Murko et al. revealed neural tube closure defects and premature expression of neural crest markers, such as neural plate boundaries (PAX3) and pre-migratory neural crest markers (cadherin 6B).[44] This study showed that the formation of the neural tube depends on the HDAC protein family.

Class I HDAC proteins play a crucial role in supporting the development of the nervous system at different stages through a variety of processes. HDAC1 can play an activation-regulatory role during cell proliferation,[45] and HDAC1 deficiency causes developmental abnormalities, including glial cell and neuronal impairments in the hindbrain.[46] The P56 component of nuclear factor κB (NF-κB) is deacetylated by HDAC1/2, which activates the Sox10 and Mpz promoter activity and promotes myelin synthesis in Schwann cells in a mouse model, according to Chen et al.'s work.[47] In an early zebrafish model, HDAC1 increased motor neurogenesis and decreased the expression of Notch target genes.[48] Furthermore, in order to support the development of the zebrafish nervous system, HDAC1 can control gene transcription factors (anterior membrane bHLH protein Ascl1, as well as Neurod and Neurod4). Although it is not expressed in fully differentiated glial cells, CNSHDAC2 is first expressed in neural progenitors and is increased during mitosis.[45] Neuronal progenitors and glial cells both express HDAC1. HDAC2 mostly functions before brain progenitor differentiation, while HDAC1 functions during both differentiation and proliferation.[49]

The Class II HDAC protein family has a variety of functions in the development of the nervous system. The mRNA levels of Class II HDAC members (HDAC5/6/7/9) are raised during the early development of rat embryonic hippocampus cells, according to Ajamian et al. This could be related to chromatin rearrangements during neural differentiation.[50] The expression of HDAC6 is directly linked to dendritic growth, promoting dendritic formation through its interaction with CDC20-APC.[51] HDAC6 contributes to dendritic elongation by deacetylating tubulin, and Aurora kinase is necessary to control microtubule remodeling during dendritic elongation.[51] Only post-mitotic and mature neurons express HDAC9, which is intimately linked to neurological function.HDAC9 is closely linked to neurological function and is only expressed in adult, post-mitotic neurons.[52] HDAC5 promotes neuronal differentiation after nuclear export. In order to enhance neuronal development, Schneider et al. demonstrated that isoxazole-induced Ca(2+) upregulation triggers CaMK phosphorylation and mediates the nuclear export of the MEF2 regulator HDAC5.[53] This implies that the development of the nervous system involves HDAC5. Although Ajamian's earlier work found no discernible changes in HDAC4 mRNA levels, it has been proposed that HDAC4 has a negative regulatory function in neural development.[50] HDAC4 is implicated in the suppression of MEF2- and cAMP-responsive element (CRE)-binding protein (CREB)-dependent transcription, and its increased nuclear translocation activates downstream cysteine asparaginase, which worsens cerebellar granule cell death.[54] According to Xu et al., short-chain fatty acids that stimulate HDAC4 expression via the gut-brain axis caused mouse hippocampus neurons to undergo more apoptosis.[55] HDAC4 may therefore have a detrimental effect on the development of the nervous system. Additionally, class IV HDACs—like HDAC11—have a role in neurogenesis. HDAC11 expression in the mouse brain (cerebral cortex and brainstem) rose gradually with

development, according to Liu et al.'s immunohistochemical and protein immunoblot investigations in an in vivo animal model.[56]

In conclusion, distinct HDAC proteins are essential for the maturation, differentiation, and creation of neural tubes of neurons and play significant roles in the normal development of the nervous system. Nevertheless, the precise chemical mechanisms by which the HDAC isoforms function in the growing nervous system remain unclear. All things considered, HDAC3, HDAC8, and HDAC10 require more research.

1.2.6. HDAC2 and Alzheimer's Disease

The development of long-term memory has long been known to need de novo protein synthesis.[57] Following training, it has also been shown that there are critical periods for the synthesis of proteins[58] indicating that gene expression events for memory consolidation have a finite lifetime. There is mounting evidence that histone acetylation has an equally significant role in long-term memory persistence. At different lysine locations inside the core histone, histone acetylation takes place.[59] As a result, it's plausible that various learning styles cause distinct acetylation patterns at particular gene promoters. Based on how closely their sequences resemble those of yeast proteins, HDAC can be divided into three major classes.[60] Memory and synaptic plasticity are adversely regulated by HDAC2, which is extensively expressed in the central nervous system.[61] The study of synaptic plasticity in neuroscience assesses how post-synaptic neurotransmission, dendritic arborization, spine density, spine maturation, and other structural elements of neurons affect how neurons operate.[62] Research has demonstrated that the neurodevelopment of cognition is supported by the elevation of dendritic spine density, [63] augmentation of spine maturation, and enhancement of dendritic strength. These factors also play a crucial role in the experience-based remodeling of

neurons in early adulthood. Morphological plasticity provides cognitive resilience against Alzheimer's disease (AD) in addition to these physiological effects.[64] Numerous neuroprotective compounds, such as brain-derived neurotrophic factor (BDNF) and cellular homolog of v-FOS (c-FOS) proteins, have been shown to have their expression suppressed by HDAC2.[65] Furthermore, by destabilizing the cytoskeletal protein α-tubulin by removing an acetate from lysine 40, HDAC2 activation was also demonstrated to reduce morphological plasticity, much like HDAC6.[61] HDAC2-overexpressing mice's hippocampi displayed hypoacetylation of histone H4 on lysines 12 and 5 (H4K12, H4K5) but not H3K14. This was accompanied by a decrease in the number of synapses and synaptic plasticity, which led to a worse ability to acquire memories. The mechanism is thought to involve HDAC2 binding to the promoters of genes linked to synaptic plasticity and adversely regulating their transcription.[61] AD patients' post-mortem brain samples exhibit elevated HDAC2 expression. Because HDAC2 reverse-regulates H4K12 acetylation of the memory-related gene promoters, short-hairpin RNA knockdown of HDAC2 rescues structural synaptic plasticity and memory impairments in CK-p25 mice.[66] These results highlight the critical role that HDAC2-regulated chromatin remodeling plays in controlling synaptic plasticity and memory formation in the context of AD-related cognitive impairment.

1.2.7. Cellular Mechanism of Neuroplasticity: Implication to Alzheimer’s Disease

In Alzheimer's disease (AD), synapse breakdown and cognitive dysfunction are hallmarks of a progressive neurodegenerative illness. Neurodegeneration is known to have a negative correlation with synaptic plasticity. Due to this negative connection, glutamatergic neurotransmission through α-amino-3-hydroxy-5-methyl-4-isoxazole propionic acid (AMPA) and N-methyl-D-aspartate (NMDA) receptors is highlighted as a crucial mediator of synaptic plasticity.[67] Glutamatergic

neurons are typically engaged in a variety of central nervous system processes, including memory, learning, and synaptic plasticity.[68] It appears that the brain needs a certain amount of glutamate to function normally, and that an excess of glutamate causes synaptic dysregulation and memory loss.[69]

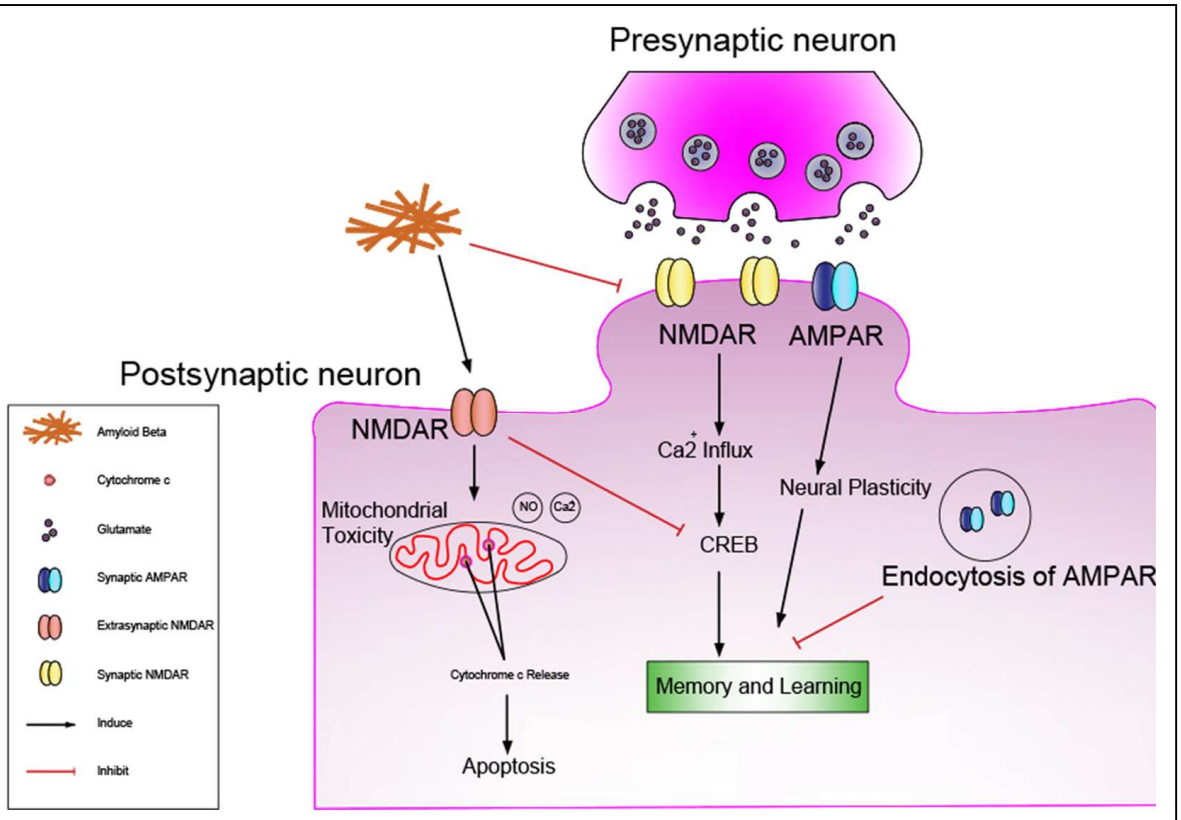


Figure 6: NMDA and AMPA receptor signaling pathways are represented. Endocytosis of AMPA receptors affects memory and learning. By blocking CREB, amyloid-beta binding to extrasynaptic NR2B NMDA receptors impairs memory. On the other hand, synaptic NR2A NMDA receptors activate CREB, which promotes LTP and improves memory. Amino-amino-3-hydroxy-5-methyl-4-isoxazolepropionic acids, or AMPAs. Long-term potentiation (LTP) and cAMP-response element-binding protein (CREB).[67]

1.2.7.1. NMDA Receptor in Neuroplasticity

The ligand-gated ion channels known as NMDA receptors are essential for the development of memory.[70] The postsynaptic density proteins (PSD) and postsynaptic locations in dendritic spines are often home to NMDA receptors, which are implicated in a number of synaptic plasticity

processes, including long-term hippocampus potentiation (LTP).[71] AMPA receptors are activated by the presynaptic release of glutamate during LTP, and the NMDA channel's Mg^{2+} blockage is removed by the ensuing depolarization, allowing Ca^{2+} to enter. Strong NMDA receptor activation sets off a cascade of Ca^{2+}/calmodulin-dependent protein kinases II (CaMKII) signaling that results in synaptic amplification, LTP, and the release of brain-derived neurotrophic factor (BDNF).[72] In addition to their location, NMDA receptors' subunit makeup also affects how glutamate affects them.[73] For example, NMDA receptors that contain NR2A and NR2B are mostly present extrasynaptically and synaptically, respectively, and have different effects on neurons.[74] In order to participate in the neuroprotective activity, calcium entry via synaptic GluN2A-containing receptors raises cAMP response element binding protein (CREB) and BDNF. On the other hand, the CREB pathway is inhibited by Ca^{2+} input via extra-synaptic GluN2B-containing NMDA receptors.[75]

1.2.7.2. AMPA Receptor in Neuroplasticity

Ionotropic glutamate receptors of the AMPA receptor class mediate rapid excitatory neurotransmission. A variety of GluA1-GluA4 combinations make up AMPA receptors. The AMPA In brain slices, when LTP is induced, GluA1 receptors are introduced into synapses,[76] and play an important role in memory formation.[77] Neural plasticity depends on synaptic AMPA receptors, which are made up of the GluA1 and GluA2 combination.[78] GluA2/3 receptors are continually released into synapses regardless of synaptic activity, whereas AMPA GluA1 receptors are given to the synapses in an activity-dependent way. Since AMPA receptor recruitment to the postsynaptic membrane is favorably connected with LTP and their endocytosis is negatively correlated with LTP, trafficking has been recognized as a crucial mechanism driving synaptic

plasticity.[79] The AMPA GluA1 receptors are phosphorylated and their conductance is increased by activated CaMKII, which is triggered by Ca^{2+} influx through NMDA receptors during LTP.[80]

Since CREB is crucial for synaptic plasticity and overexpression of HDAC2 can result in its diminution, pharmacological inhibition of HDAC2 may have a significant impact on enhancing morphological plasticity and maintaining cognitive function in the AD brain.

1.3. HDAC Inhibitors (HDACi)

The significance of HDAC enzymes in numerous processes makes them an attractive class of therapeutic targets, including cell cycle regulation, proliferation, survival, differentiation, metabolism, protein trafficking, DNA repair, and angiogenesis. A family of drugs that inhibit HDAC activity has recently been identified. Through the hyperacetylation of histones, these inhibitors can prevent gene silence, impact cell development and differentiation, control gene expression, and trigger apoptosis in neoplasms.[81] Although there is growing interest in the class III Sirtuin family, several synthetic or natural compounds targeting classes I, II, and IV enzymes have been created and characterized. Deacetylase activity in classes I, II, and IV is dependent on $Zn2^{+}$. The deacetylase activity of these proteins is changed and their enzymatic function is harmed when HDACi attach to this ion, which is present in the active site of HDACs.[82] As the expression of HDACs is not organized in several types of cancer, the disrupted balance between HATs and HDACs in neoplastic cells can contribute to carcinogenesis and the reversible modulation function of HDACs makes these proteins interesting targets for cancer treatment.[83] HDACi can stimulate the expression of tumor suppressors and negate the aberrant acetylation state of proteins present in cancer cells. Additionally, cancer cells might be more susceptible than healthy cells to HDACi-induced apoptosis, which would increase HDACi's therapeutic potential.

1.3.1. Structural Features of HDACi

In the last twenty years, the chemical library of Zn^{2+}-dependent HDAC inhibitors (HDACis) has grown significantly. Despite the different structures of these substances, whether they are naturally occurring or manufactured, the majority of Zn^{2+} HDACis share a common pharmacophore model. (Figure 7). There are three key components to this model: (1) the Zn2+ binding group (ZBG), which can be a saturated or unsaturated linear chain or a hydrophobic long chain with a ring structure, and (2) the cap structure (Surface Recognition Domain), which usually consists of a hydrophobic aromatic moiety that interfaces with the enzyme surface; (3) a Zn2+ binding group (ZBG), such as isohydroxamic acid, carboxylic acid, or benzamide, which coordinates the Zn2+ ion at the enzyme catalytic center.[84]

Research on isohydroxamic acid HDACis and HDACs co-crystallized complexes has clarified the relationship between the amino acids close to the catalytic site of the enzyme and the cap structure. To create the complex, the ZBG structure attaches itself to the metal ion at the base of the active site. The ZBG group's location inside the active region of HDACs is greatly influenced by the linker, an essential component. In order for the ZBG group to bind with Zn2+ and form hydrogen bonds with amino acids such as tyrosine and histidylic acid, the linker's ideal length is crucial. By using forces like van der Waals interactions, the lengthy linker chain interacts with the amino acid residues that occupy the active site. Conversely, the cap structure serves as a cover for the enzyme's active site entrance.[85] By competitively preventing the substrate's acetyl-lysine residues from attaching to the enzyme's active site, HDACis function. However, changes to any one of the three HDACis pharmacophore constituents may impact their selectivity or activity, which may impact

their safety and therapeutic efficacy. ZBG is commonly found in isohydroxamic acid, benzamide, carboxylic acid, sulfhydryl groups, ketones, and epoxides. Using isohydroxamic acid, benzamide, and carboxylic acid as chelating groups, respectively, a comparison of therapeutic HDACis SAHA, entinostat (MS275), and valproic acid reveals notable variations in their inhibitory effectiveness against HDACs. Interestingly, the most effective zinc ion chelation capacity is shown by isohydroxamic acid.[86] The structural properties of linker structures, including lengths, linearity, cyclicality, saturation, unsaturation, and alterations, might vary. Researchers have discovered that altering the linker can have a substantial impact on an HDACi's activity, hence altering its effectiveness. Among the most widely utilized linker types are vinyl-aromatic rings, aromatic rings, and aliphatic chains.[87]

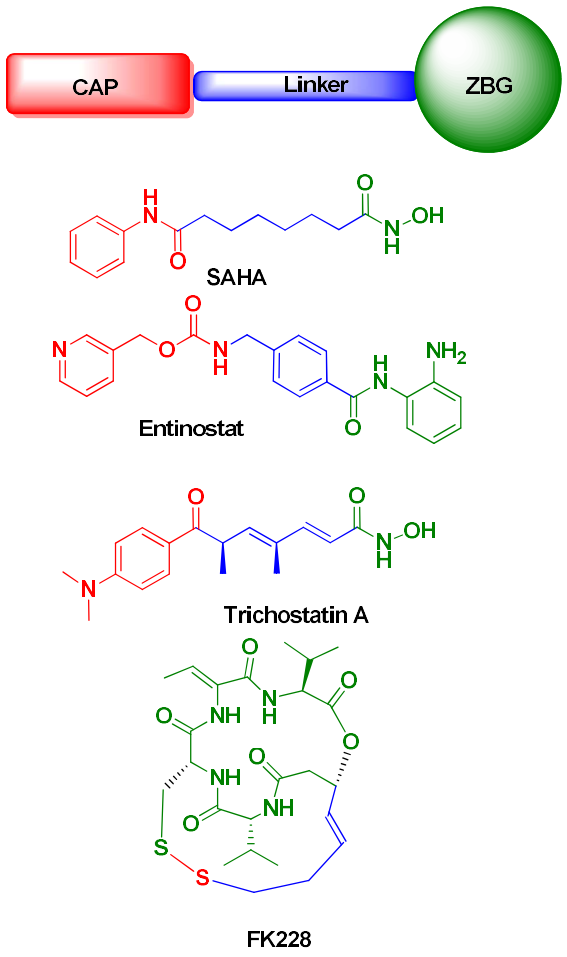


Figure 7: FDA-approved HDAC inhibitors with their CAP group (red), ZBG (green) and Linker (blue)

Studies using docking and energy-optimized pharmacophore localization have shown that inhibitors with at least one aromatic ring in their linker region can have a greater affinity for the target. Furthermore, the linker region's carbon number (n) of six was found to have the strongest enzyme inhibitory action. The cap groups' phenyl, naphthyl, and thiophene groups boost the hydrophobicity and high capacity of the compounds, which improves HDAC inhibition. The

presence of more lipophilic substituents, like trifluoromethyl, also tends to produce stronger HDAC inhibition. Substitutions of methoxy and trifluoromethyl in the cap group at the adjacent, ortho-, and para-positions intensify the effect. Lipophilicity clearly increases the hydrophobic interaction between the inhibitor and the HDAC active site, which raises the inhibitor activity significantly.[88] To more efficiently design therapeutic molecules, it is critical that we have a better knowledge of the mechanism of HDACi inhibition. Using structural information about the enzyme active site in conjunction with the pharmacophore model of HDAC inhibitors is one method to accomplish this. With this generally recognized method, HDAC inhibitors can be logically designed and optimized by altering their structure according to the three pharmacophore components. The FDA-approved pharmacophore of various HDACi is shown in Figure 8.

1.3.2. HDACis in Cancer Treatment

HDACis's anticancer action includes a variety of molecular and physiological processes, including the suppression of TGFβ1, endothelial nitric oxide synthase (eNOS), and vascular endothelial growth factor (VEGF)..[89–91] The ability of HDACis to selectively control proapoptotic pathways, which does not occur in normal cells, is linked to the apoptosis of tumor cells.[90] There are several kinds of HDACis that can be used to treat malignancies.

First, there are medications that have a hydroxamic acid group, such vorinostat, whose structure is shown in Figure 8 together with that of other HDACis. Chelation with zinc, which is found in the enzymes' active region, is the role of the hydroxamic acid group. The extremely dangerous substance trichostatin A is another HDACi that has the hydroxamic acid group.[92] All kinds of HDACs are inhibited by these substances. Benzamide derivatives are a second family of medications that interact with zinc. One example of this is entinostat, which inhibits class I

HDACs. A third category of HDACs consists of short-chain fatty acids, such valproic acid, which has been used extensively to treat epilepsy. HDACs of classes I and IIa are inhibited. Butyric acid and phenylbutyric acid also inhibit HDACS in classes I and II.[93] Romidepsin, a class I inhibitor and cyclic tetrapeptide, is another HDACi.[94]

For the treatment of different neoplasms and several in vitro[95–97] and in vivo[98] studies, pan- and selective HDACis have demonstrated extremely encouraging outcomes have sought to understand the methods of action and the pathways involved in the anticancer process of these molecules. Only five medications have received approval for clinical trials in the US thus far: romidepsin (FK228), panobinostat (LBH589), belinostat (PXD101), vorinostat (SAHA), and chidamide (CS055/HBI-8000). Several hematological malignancies can be treated with these chemicals because they exhibit antineoplastic action.[99–102]

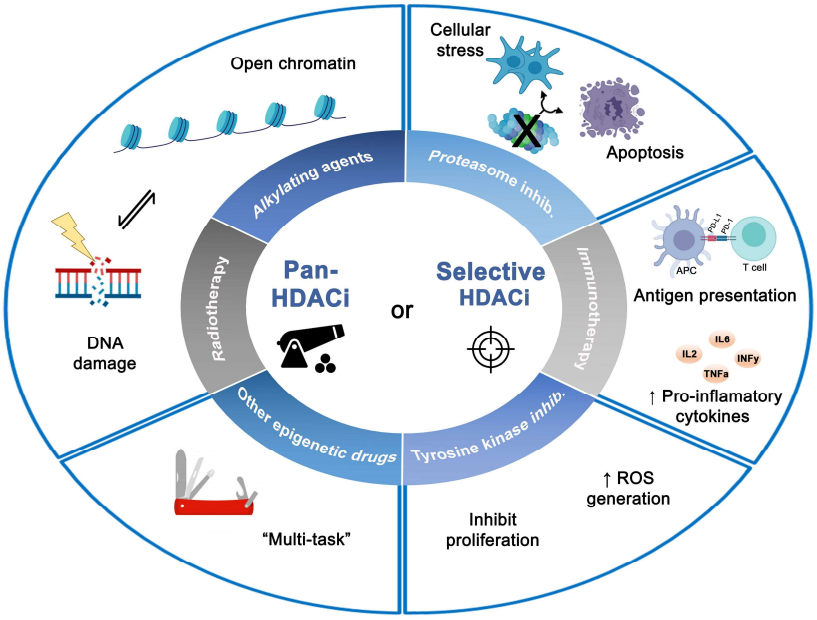


Figure 8: effects on tumor cells of combining various anticancer treatments with inhibitors of histone deacetylases (either pan- or selective HDACis). The various combinations with HDACis shown synergistic anticancer effects that resulted in a broad range of physiological effects, including cellular stress, DNA damage, apoptosis induction, and proliferation inhibition.[162]

Even while HDACis are exhibiting significant activity, mostly in the oncological domain, their cytotoxicity and side effects remain severe, and they do not exhibit selective inhibition among HDAC isoforms.[103] Since HDACi alone do not exhibit therapeutic advantages in almost all solid tumor types, designing a successful HDACi requires the molecule to work in concert with other anticancer treatments.[104] The reason that HDACis are so active in changing normal phenotypes into malignant ones is due to their engagement in the levels of epigenetic change for which they are accountable. Four HDACis' structures are shown in Figure 7, but others are still being developed.

1.3.3. HDACi as Cognitive Enhancer

The modulation of neural plasticity, memory formation, and memory improvement are strongly linked to epigenetic mechanisms, according to recent studies. Long-term memory development has been thought to need de novo gene transcription within hours of learning.[105] Long-term memory impairment results from site-directed mutations of the CREB Binding Protein (CBP).[106] HDAC inhibition improves long-term memory. HDAC inhibition has been demonstrated to circumvent CREB binding interactions in object recognition[107] whereas CBP-mediated interactions are necessary for object location memory to work.[108]

Crebinostat is a recently approved HDAC inhibitor that has been demonstrated to increase the expression of multiple CREB target genes and to facilitate the formation, organization, and stability of synapses. Mice given Crebinostat systemically for 10 days demonstrated improved memory in a hippocampus-dependent contextual fear conditioning paradigm.[109]

Small molecule inhibitor-induced neural activity modifies the profiles of over 20 acetylation events and controls the epigenomic landscape in the hippocampus region. It has been demonstrated that whole genome profiling of HDAC inhibition with Trichostatin-A causes notable changes in H4K12 acetylation levels. In active loci pre-marked with H3K4 trimethylation, H3K9 acetylation, and H3K14 acetylation, trichostatin-A was also observed to induce histone hyperacetylation. Because trichostatin-A causes changes in the DNA, it may help us understand how abnormal acetylation profiles contribute to mental and cognitive diseases. In vivo studies have demonstrated that trichostatin-A increases hippocampal acetylation. For AcH3K9, Ac H314, AcH4K12, and AcH2B, TSA increased the number of acetylation islands at transcription start sites, intragenic regions, and putative enhancers by 51, 128 and 18%, respectively, in female C57/DBA F1 hybrid mice aged 3–5 months.[110]

When sodium butyrate is injected into the rat's insular cortex, it improves object identification memory while having no effect on object location memory. In mice, NR4A gene blockage significantly reduces long-term memory. Through transcriptional programs, trichotin-A has been demonstrated to increase the expression of NR4A genes and, consequently, long-term memory events.[111] It has been demonstrated that class I selective HDAC inhibitors, such as MS-275, are more effective at improving memory and changing behavior mediated by depression.[112]

Recent research on animal models of Alzheimer's disease has demonstrated that by promoting the breakdown of the amyloid beta peptide, a new mercapto acetamide-based Class II HDAC inhibitor coded W2 and a Class I and Class II-based inhibitor coded I-2 enhance memory and learning. While W2 reduced Tau phosphorylation at Thr181, an unidentified effect of HDAC inhibitors, I-2 decreased the expression of β- and γ-secretase components and raised the mRNA levels of Aβ

breakdown enzymes.[113] In the APPswe/PS1dE9 Alzheimer's disease mouse model, which has severe memory impairment, treatment with sodium valproate, sodium butyrate, and vorinostat was found to fully restore contextual memory. Because all three inhibitors exhibited a similar inhibitory impact on Class I HDACs, specific inhibition of Class I HDAC isoforms was required in order to treat Alzheimer's disease.[114]

1.3.4. Selective HDAC2 Inhibitors to Improve Synaptic Plasticity

It is commonly known that upregulation of the Fos gene is linked to neuronal plasticity. Mice with distant fear memories have hypoacetylation at the Fos gene promoter in comparison to mice with recent fear memories, according to recent investigations employing hippocampus slices. In contrast to remote memory recall, the recollection of recent memories was associated with the inactivation of hippocampus HDAC2 via S-nitrosylation. This implies that, in contrast to distant traumatic experiences, the recall of current memories is linked to an environment that is conducive to gene transcription, which may promote neural plasticity. In order to eliminate remote fear memories, this supports the use of HDAC inhibitors in conjunction with behavioral therapies and shows how important HDACs are in fostering neuronal plasticity in the hippocampus during consolidation, which makes remote memory attenuation easier.[115]

It has recently been discovered that two kinetically specific inhibitors of HDAC2 (BRD4884 and BRD6688) can restore memory deficits in a mouse model of neurodegeneration (CK-p25) that exhibits severe deficiencies in associative and spatial memory. In comparison to their vehicle-treated controls, these inhibitors significantly increased the levels of H3K9 and H4K12 acetylation when applied to primary mouse forebrain neuronal cells at a concentration of 10μM for a 24-hour period. In contextual fear training, these inhibitors were found to restore the memory impairments

linked to p25-induced neurotoxicity. Quantitative Structure Activity Relationship (QSAR) investigations, IC50 values, and simulation target engagement experiments on these compounds demonstrated improved selectivity to HDAC2 over HDAC1 and HDAC3. In models of cognitively impaired mice, these HDAC2 selective inhibitors improve site-specific acetylation, which improves learning behavior.[116]

Overexpression of HDAC2 in particular neurons has been demonstrated to reduce dendritic spine density, synapse number, synaptic plasticity, and memory formation in gain-of-function and loss-of-function mice models. While mice lacking HDAC2 were unable to change these, chronic SAHA treatment was demonstrated to alleviate learning impairment and reduce the number of synapses brought on by HDAC2 overexpression.[117] While HDAC1 knockout animals did not produce such neural responses, HDAC2 knockout mice have been demonstrated to improve associative learning and the extinction of conditioned fear response without affecting non-associative learning or episodic memory.[118] Therefore, using HDAC2's memory-suppressive properties to target HDAC2-mediated neuroplasticity may be one way to treat cognitive problems.

1.3.5. Prospect of HDAC2 Inhibitors in Fighting Alzheimer’s Disease

According to the Alzheimer's Association's most recent annual report, Alzheimer's Disease Facts and Figures, an estimated 6.9 million Americans 65 and older currently have Alzheimer's dementia. By 2060, this figure might rise to 13.8 million if no new treatments are developed to prevent or treat AD. In 2021, 119,399 deaths from AD were reported on official death certificates. Alzheimer's was the seventh most common cause of death in the US in 2020 and 2021, when COVID-19 was included in the top ten causes of death. More recent years' official counts are still being compiled. The fifth most common cause of mortality for Americans 65 and older is still Alzheimer's disease.

While recorded deaths from AD climbed by more than 140% between 2000 and 2021, mortality from heart disease, stroke, and HIV decreased during the same period. In 2023, it was predicted that around 11 million family members and other unpaid caregivers gave 18.4 billion hours of care to individuals suffering from dementias like Alzheimer's. When compared to ten years ago, these numbers show a decrease in the number of caregivers and an increase in the amount of care that each caregiver who remains provides. In 2023, unpaid dementia caring was estimated to be worth $346.6 billion. The expected total 2024 payments for health care, hospice, and long-term care services for individuals with dementia who are 65 years of age or older is $360 billion.[119] Scholars have made significant strides in comprehending Alzheimer's disease and creating novel therapies, such as a number of drugs presently undergoing late-stage clinical studies.[120] The US Food and Drug Administration (FDA) has authorized a number of prescription medications to treat Alzheimer's disease symptoms.[121] Lecanemab, the newest Alzheimer's drug approved by the FDA earlier this year, slows the progression of the illness by lowering amyloid deposits in the brain. [122] There is no clinical proof, though, that it has an impact on clinical symptoms or outcomes like dementia or cognitive decline. Those with Alzheimer's disease who are in the early or middle stages of the illness also benefit from the majority of medications.[123]

Conventionally, anti-amyloid medication (like Aducanumab) or choline esterase inhibitors (like Donepizil) are the main treatments for memory impairment associated with neurodegenerative diseases. However, these approaches overlook the role of epigenetics in memory formation.[124] Although FDA-approved HDACi, including trichostatin A (TSA), have been shown in recent years to enhance memory in rodents, their therapeutic potential in humans is still restricted due to their inability to selectively target particular isoforms of HDAC enzymes.[125] For example, HDAC1 suppression can affect cell differentiation and embryonic development.[126] HDAC3 inhibition may

have an impact on bone remodeling, neural activity, and energy consumption.[127] Moreover, it has been discovered that HDAC8 suppression compromises energy balance, muscular contraction, and microtubule integrity.[128] This represents a significant challenge in treating neurological disorders by nonselective HDAC inhibitors. Moreover, FDA-approved HDACis, such as romidepsin and SAHA, which have traditionally been used for the treatment of cancer, have limited ability to cross the blood-brain barrier (BBB).[129] To combat the effects of Alzheimer's disease and other neurodegenerative disorders by specifically inhibiting HDAC2, it is crucial to investigate a new and different strategy for creating medications that improve memory formation.

1.4. Earlier Discovery of HDACi in Hossain Lab

Inspired by romidepsin (also known as FK-228), which comprises naturally occurring depsipeptide type inhibitors, the Hossain group created the MJM class of HDACi to investigate alternative treatment approaches to treat Alzheimer's disease and age-related dementia. When glutathione reduces the disulfide link inside the cell, Romidepsin forms its active monocyclic dithiol form (Figure 9B). By entering the catalytic pocket and chelating with zinc, the released thiol group with the longer aliphatic linker stops the enzyme's activity.[130]

Despite its strong potency against some cancers, romidepsin's severe cytotoxicity and extremely poor BBB permeability emphasize its limitations in therapeutic settings for neurodegenerative condition.[30] Increasing the lipophilicity of HDAC inhibitors has been the main focus of efforts to increase their BBB permeability.[130,131] In this effort, we speculate that some designer small compounds that are modeled after the romidepsin scaffold might have more "drug-able" qualities, like improved solubility and bioavailability, decreased toxicity, high brain uptake when administered intraperitoneally, and sufficient potency on memory formation. Therefore, using the

standard pharmacophore model, we set out to construct tiny HDACi that are structurally derived from romidepsin.

Accordingly, we made HDACi bearing the C6 linker with a smaller cap group while still containing a disulfide bond as in romidepsin, which should act by the same prodrug mechanism.33 which retained a critical ZBG (the thiol group from romidepsin), a C5 linker, and different cap groups. Our findings indicate that our novel compound MJM-1 increases the overall level of histone 3 (H3) acetylation in a prostate cancer cell line. In mice, MJM-1 injcted intraperitoneally (i.p.) crossed the BBB and could be detected in the hippocampus, a brain region that mediates memory. Consistent with this finding, we found that the post-training i.p. administration of MJM-1 enhanced hippocampus-dependent spatial memory consolidation in male mice. Therefore, MJM-1 represents a potential lead for synthesizing

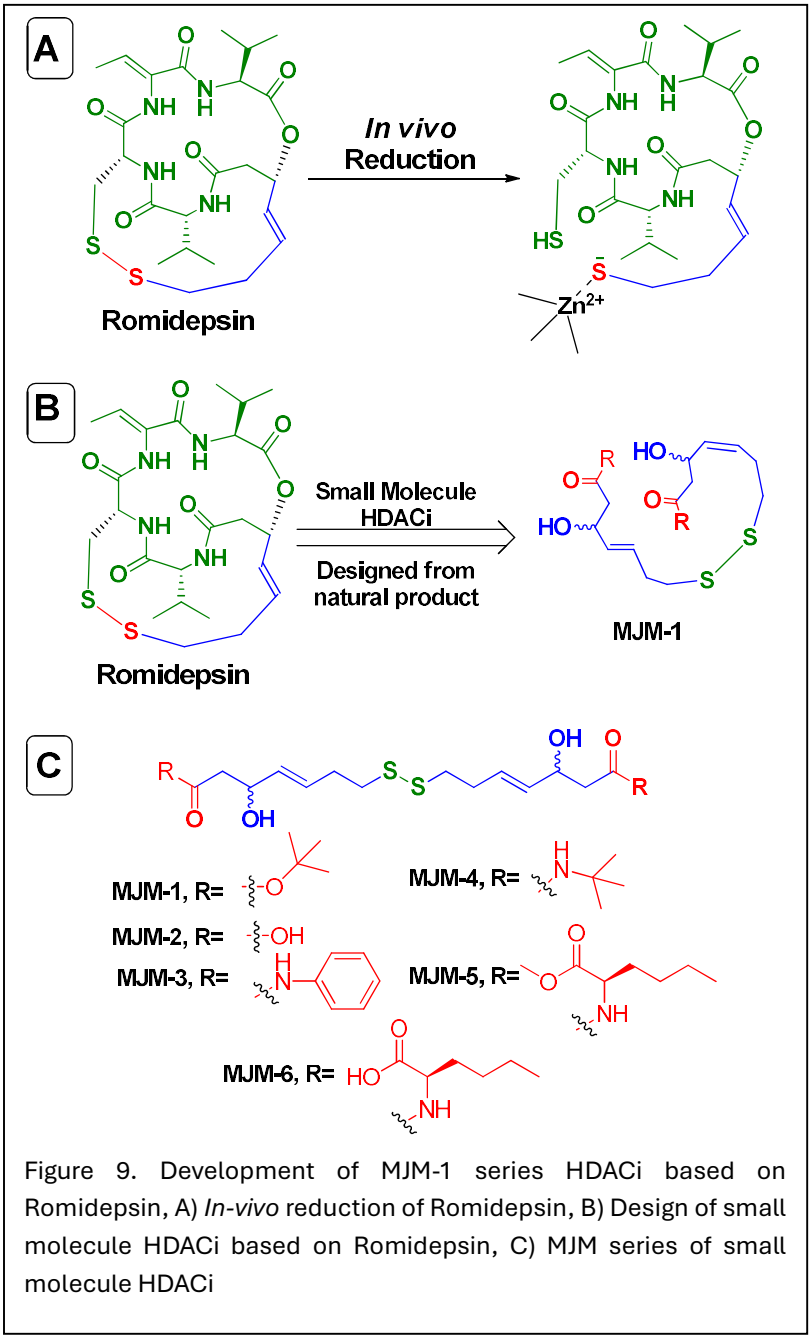


Figure 9. Development of MJM-1 series HDACi based on Romidepsin, A) *In-vivo* reduction of Romidepsin, B) Design of small molecule HDACi based on Romidepsin, C) MJM series of small molecule HDACi

more selective and efficacious HDACi to ameliorate cognitive deficits in aging and neurodegenerative diseases.[132]

MJM-1 inhibits HDAC2 at an IC50 value of around 10 μM, which is not significant in comparison to FDA-approved HDACi and is also not selective. In addition, the biological half-life in the brain may not be enough for lasting memory formation.[132] Considering these limitations of MJM-1, in this project we attempted to design and synthesize some new series of analogs to study structure-activity relationships to explore more potent and less toxic, stable, and HDAC-2 enzyme selective HDACi.

2. Materials and Methods

2.1. Reagents and cell lines

SHSY5Y, an immortalized neuronal cell line, was purchased from ATCC (Cat# CRL-2266). A 31-year-old female AD patient (A246E mutation at psen1 gene)-derived neural stem cells (NSCs) were purchased from AXOL Bioscience Ltd. (Cat#ax0114, Midlothian, UK. Regular cell culture supplies including neurobasal medium (Cat# 21103049; GibcoTM), B-27™ Plus Supplement (Cat#A3582801; GibcoTM), serum-free B-27™ supplement (Cat#17504001; GibcoTM), 0.05% trypsin-EDTA (Cat# 25300062), Dulbecco's Modified Eagle Medium (DMEM)/F-12 (Cat#11320033; GibcoTM), heat-inactivate fetal bovine serum (FBS) (Cat#16140071; GibcoTM), L-glutamine (Cat#21051024), antibiotic-antimycotic solutions (Cat#15240096), and Nalgene™ gen-eral long-term storage cryogenic tubes (Cat#5000-0020) were purchased from Ther-mofisher Scientific. Specialized cell culture reagents for iPSC-derived neural stem cell culture including KnockOutTM DMEM/F12 media (Cat#12660012), StemProTM Neural Supplement (Cat# A10508-01), recombinant human FGF-basic (AA10-155) protein (Cat#PHG0024), recombinant human EGF (Cat# PHG0314), GlutMAXTM Supplement 200 mM (Cat# 35050061), StemProTM Accutase (Cat# A1105), and GeltrexTM basement membrane matrix (Cat#A14133) were purchased from ThermoFisher Scientific. West-ern blot supplies including 0.45 μm nitrocellulose membrane (Cat#LC2001; Ther-mofisher Scientific), Novex™ Value™ 4 to 12% tris-glycine, 1.0 mm, mini protein gel (Cat# XV04120PK20; ThermoFisher Scientific), TBS blocking buffer (Cat#; Licor Bio-sciences, Lincoln, NE), IRDye 680-conjugated secondary antibody (Cat#; Licor Biosci-ences), IRDye800-conjugated secondary antibody (Cat#; Licor Biosciences), and Cha-meleon® duo pre-stained protein ladder (Cat# 928-60000; Licor Biosciences) were purchased from various

vendors. For calcium entry assay, Fluo-4 Direct™ Calcium Assay Kit (Cat# F10471), 96-well fluorescence microplates (Cat# M33089), N-methyl-D-aspartic acid (Cat#J61361.MF), (+/-)-alpha-amino-3-hydroxy-5-methyl-4-isoxazolepropionic acid (Cat# J64884.MA) were purchased from ThermoFisher Scientific. For transfection assay, Lipofec-tamine™ 3000 transfection reagent (Cat# L3000015) and pre-designed/validated creb siRNA (Cat#AM16708) were purchased from ThermoFisher Scientific, whereas CRE dual luciferase (Firefly/Renilla) was purchased from BPS Biosciences (Cat# 60611). For the immunofluorescence (IF) assay, FITC-conjugate goat anti-mouse (Cat# A16085) 2º antibody, TRITC-conjugated anti-rabbit (Cat# A16101) 2º antibody, CY5-conjugated Phalloidin (Cat# A30107), and DAPI (Cat# D3571) were purchased from ThermoFisher Scientific. Cy5-conjugated anti-mouse (Cat# A10524) 2º antibody was purchased from Jackson Laboratories. Information, application, and dilution of all primary and sec-ondary antibodies were summarized in a separate table. For cytotoxicity assay, CyQUANT™ LDH cytotoxicity assay kit (Cat# C20301) was purchased from Ther-moFisher Scientific, and DeadEnd™ Colorimetric TUNEL kit (Cat# G7360) was pur-chased from Promega.

2.2. Reagents for chemical synthesis

For the overall synthesis, triethylamine (Cat# T0886) n-butyllithium solution,2.5 M in hexanes (Cat# 230707), diisopropylamine (Cat# 471224), sodium acetate (Cat# S8750-250G), 3-Chloroperbenzoic acid (Cat# 273031-25G), dichloromethane (Cat# 270997-18L-P1) and sodium thiosulfate (Cat# 217263-1KG) were purchased from Mil-lipore Sigma. Triphenylphosphoranylidene acetaldehyde (Cat# AC307491000) and triphenylmethyl mercaptan (Cat# AC140411000) were acquired from Acros. Acrolein (Cat# 103755-5g), ammonium chloride

(Cat# S8750-250G), reagent grade hexane (Cat# 102187-200L) and ethyl acetate (Cat# 18-602-510) was purchased from Oakwood Chemicals. Iodine (Cat# AC38705-1000) and acetone (Cat# BDH1101-19L) were pur-chased from VWR Chemicals.

2.3. In silico docking of JRM-28a in HDAC2 and HDAC4

2.3.1. Preparation of structures for docking. Structures were built in ChemDraw Professional-16 (PerkinElmer, CT, USA) and saved as .mol format. To eliminate internal strains, originating from the unfavorable, bond length, bond angle, and torsion, energy minimization was performed using MOE2022.02 (Molecular Operating Environment, Chemical Computing Group, 910-1010 Sherbrooke W., Montreal QC H3A 2R7). First, the .mol file of the desired structure was imported to the MOE interface. Then from the "Compute" option, the "Energy Minimize" interface was opened. The "MMFF94x" forcefield was selected for molecular mechanics calculation for energy minimization. The gradient parameter was changed from 0.1 to 0.0001 to control the level of minimization accuracy. Finally, the energy minimization algorithm was run to achieve a more realistic 3D structure for docking.

2.3.2. Docking of JRM-28. Crystal structures of recombinant human HDAC2 (PDB ID: 4lxz) and HDAC4 (PDB ID: 4cbt) enzymes were obtained from the RCSB Protein Data Bank (https://www.rcsb.org/). Energy minimization of these structures was performed by the conjugate gradient and steepest descent algorithm to exclude inappropriate contacts of protein atoms. GROMOS 96 43B1 parameters set was used to execute the computations in vacuo. The overall protein preparation for docking was implemented using the Swiss-PDB Viewer Version 4.1.0

(http://spdbv.vital-it.ch/). The SDF (structure-data format) structure of compound JRM-28 for docking was generated by ChemDraw Professional (Version 16.0, PerkinElmer Informatics, Inc., 710 Bridgeport Avenue Shelton, CT, USA). The docking at the active site of enzymes was performed by the Molecular Operating Environment (MOE, Version: 2020.0901, Chemical Compu-ting Group Inc., Canada) under the MMFF94x force field. The active sites of 4lxz and 4cbt were identified by the Alpha SiteFinder function in MOE software and the coor-dinates of the ligands at the crystal structure. The active sites were protonated and solvated before the rigid docking simulation was executed. The best five docking poses were generated based on the lowest binding energy, designated by the S-score of the MOE software.

2.4. HDAC2 inhibition assay

HDAC2 inhibition assay was performed either by luminometric or fluorimetric method applying the following procedures.

2.4.1. Luminometric method

HDAC2 inhibition assay was performed by HDAC-Glo™ I/II Assays and Screen-ing System (Catalog# G6420, Promega Corporation, Madison, WI) by Luminometric method according to the manufacturer protocol. Human recombinant HDAC-2 (Cat#50002) was purchased from BPS Bioscience (San Diego, CA 92121, United States). The HDAC-2 inhibition assay was performed as previously described to determine IC values. In brief, the purified HDAC2 was diluted in HDAC assay buffer (provided with the HDAC-Glo™ I/II Assays and Screening System) to the same concentration based on their calculated molar mass. JRM-28 were first activated by reducing

dithiothreitol (DTT) and then serially diluted in HDAC-Glo buffer. Next, 10 µL of JRM-28 after serial dilution was added to 10 µL of diluted HDAC2 in such a way that the final HDAC2 concentration was 0.5 nM in each well of a 384-well microplate (Greiner). After 30 minutes of incubation, 20 µL of the HDAC-Glo substrate/developing reagent was added to each well according to the manufacturer's instructions. The 384-well plate was then agitated on an orbital shaker for the mixing of components in each well for another 30 minutes at room temperature. Finally, luminescence was measured using a POLARstar Omega plate reader (BMG Labtech). Luminescence values for each well were fitted, using GraphPad Prism (v6) to estimate the concentration of each HDACi needed to inhibit the reaction by 50% (IC50) as described earlier.[132]

2.4.2. Fluorimetric method

The inhibition of HDAC1, 2, 3, and 6 by JRM-28 was fluorometrically measured using the HDAC Fluorogenic Assay Kit (Catalog# 50034) by BPS bioscience. Purified recombinant human HDAC1 (Cat# 50051), HDAC3 (Cat# 50051), and HDAC6 (Cat# 50046) were also obtained from BPS Bioscience. The enzyme inhibition assay was performed according to the manufacturer's protocol. Briefly, the test inhibitor solution in DMSO was made in such a way that the final DMSO concentration did not exceed 1%. Purified recombinant HDAC2 (supplied with the fluorogenic kit) was diluted to 6 ng/µL (5 µL/well with the supplied HDAC assay buffer. HDAC 1,3 and 6 were also diluted to the optimized concentration (5µL/well) with the HDAC assay buffer. The activity of JRM-28 was measured along with DTT control and DMSO as blank. After adding 5 µL of the diluted HDAC enzymes in designated wells, the 96-well plate (supplied with the kit) was incubated at 37°C. Then the reaction was initiated by adding 5 µL of diluted HDAC substrate to each well followed by another incubation at 37°C for 30 minutes. Next, 50 µL of the developer

reagent was added to each well and incubated at room temperature for another 15 minutes. Finally, fluorescence was measured by a microplate absorbance spectrophotometer (PerkinElmer Enspire 2300 Multilabel Multimode Microplate Reader) with an excitation at λ=485 and detection at λ=528 nm.

2.5. Cell culture strategies of primary hippocampal neurons, SHSY5Y, and AD neurons

Primary neuronal cell culture was performed based on a protocol approved by the Institutional Animal Care and Use Committee of the University of Wisconsin Milwaukee, Milwaukee, WI-53211, and by the guidelines set by the National Institute of Health. Embryonic day 18 (E18) fetuses were harvested, hippocampal tissue was dissected from brains and then processed for single cell culture in poly-D-lysine coated plates as discussed elsewhere.[133] Neuronal cells were maintained with B-27TM plus-supplemented complete neurobasal media for 7 -10 days until fully differentiated. After that, the treatment with JRM 28 was performed. SHSY5Y cells were grown, maintained, and passaged with complete DMEM media (A bottle of DMEM supplemented with 10% FBS, 2 mM L-glutamine, and 100 units/mL antibiotics), otherwise, for neuronal differentiation study, SHSY5Y was seeded with complete neurobasal medium. For making AD neurons, commercially purchased (Axol Bioscience Ltd.) A246E psen1 neural stem cells (NSCs) were maintained with KnockOutTM DMEM/F12 media supplemented with StemProTM Neural Supplement, bFGF, EGF, 2mM GlutMAXTM supplement, and 10 mL/L antibiotic-antimycotic solution. These pluripotent NSCs were grown in a 25 mm cell culture flask coated with GeltrexTM matrix until fully confluent and then detached by Accutase, centrifuged, washed, and plated in a poly-d-lysine coated plate supplemented with complete neurobasal media for neuronal

differentiation. After one week, when neurons were differentiated JRM-28 treatment was conducted.

2.6. Lactate dehydrogenase assay

Lactate dehydrogenase (LDH) cell cytotoxicity assay was performed as per the manufacturer's protocol. Briefly, SHSY5Y cells were grown in a 96-well plate with up to 70% confluency followed by the treatment with increasing doses of JRM-28 under serum-free conditions. Serially diluted JRM-28 was used in a concentration range from 75 nM to 50 μM. As a control, serially diluted DMSO controls were added. After 24 hrs, supernatants were harvested by a multi-channel pipette and then assessed for LDH release by CyQUANT™ LDH Cytotoxicity Assay Kit. Briefly, 50 μL of supernatant was incubated with an equal volume of the working reaction mixture (generated after combining the 600 μl of assay buffer Stock Solution with the 11.4 mL of Substrate Stock substrate mix), incubated at room temperature for 30 minutes protected from light, terminated by 50 μL of stop solution, and then measured at 490 nm using a microplate absorbance spectrophotometer (Perkin Elmer Enspire 2300 Multilabel Multimode Mi-croplate Reader). The percentage of cytotoxicity was determined following the formula provided with the LDH assay kit and then converted to relative cell cytotoxicity.

2.7. TUNEL Assay

To assess the effect of JRM-28 on the apoptosis in SHS5Y cells, a total of 3×105 cells suspended in 3.5 mL of complete neurobasal medium was distributed in each well of a poly-D-lysine coated 8-well Chamber Slide. After 48 hrs, cells were treated with 2, 5, 10, 20, 30, and 50 μM of JRM-28 under serum-free conditions, and then incubated for an additional 24 h. The TUNEL activity was

measured by colorimetric microscopy as directed in the protocol described in DeadEnd™ Colorimetric TUNEL System (Promega, Madison, WI, USA). Hematoxylin staining was adopted to counterstain the slide.

2.8. Measurement of spine density and size

For counting spine density, E18 hippocampal neurons were stained with Alexa-647 conjugated phalloidin (Cat #A22287) and MAP2. Only densely stained neurons were counted. The total length of each dendrite was measured at 400X magnification using an Accu-Scope EXC-500 microscope. The number of spines on the dendrites was counted under oil immersion. As some of the spines were hidden under the dendrite, only spines that protruded laterally from the shafts of the dendrites into the surrounding area of clear neuropil were counted. The spine density of a pyramidal neuron was calculated by dividing the total number of spines on a neuron by the total length of its dendrites and was expressed as the number of spines/10 mm dendrite. The size of the dendritic spines was measured by calculating the ratio of mean fluorescent intensity (MFI) of the spine head and MFI of the dendritic shaft as described elsewhere.[133]

2.9. Calcium Influx Assay in Neuronal Stem Cells

Mouse primary hippocampal neurons and AD neurons were loaded with Fluo4-fluorescence conjugated calcium dye (Invitrogen Molecular Probes, Cat #F10471) and incubated at 37ºC for 60 min as described before.[133] Briefly, fluorescence excitation and emission spectra were recorded in a Perkin–Elmer Victor X2 Fluorimetric Spectrometer (Versiti Blood Center, Wauwatosa, WI) in the presence of 50 μM NMDA and AMPA solutions. The recording was performed with 100 repeats at 0.1 ms intervals. The oscillogram was generated with the help of Parkin Elmer 2030 software

that was connected to the Victor X2 calcium recorder unit. The real-time calcium noise graph was generated as a kinetic chart plotted on a linear scale.

2.10. Semi-quantitative RT-PCR

Total RNA was isolated from SHSY5Y neurons using Gene JET RNA Purification Kit (Thermofisher Scientific; Cat #K0731) following the manufacturer's protocol. RNA was converted to cDNA using the GoScript™ Reverse Transcriptase kit (Promega, Cat # A5001). Semi-quantitative RT-PCR was carried out as described earlier[133] using an RT-PCR kit from Promega (Cat#M7502). Briefly, 1 µg of total RNA was re-verse-transcribed using oligo(dT)12–18 as a primer and MMLV reverse transcriptase in a 20-µl reaction mixture. The resulting cDNA was diluted by nuclease-free H_2O in a ratio of 1:2, and diluted cDNA was amplified using the primers shown in Table 1.

Table 1: List of Primers

Gene	Forward Primer	Reverse Primer	Product Length
Creb	ATTGCCACATTAGCCCAGGT	GTGTAGGAAGTGCTGAAGTCTC	400
Atf-1	GCCCCCAAATAAAAAGACGAGG	TGCTGGGCACAAGTATCTGC	355
Crem	GTGAGCTGAGATCAGGCACCAG	TTCAAGCACAGCCACACGAT	806

Cebpa	TCGGTGGACAAGAACAGCAA	AGGCACCGGAATCTCCTAGT	372
Cebpb	TTTGTCCAAACCAACCGCAC	CCCCCAAAAGGCTTTGTAACC	437
c-fos	CCTAACCGCCACGATGATGT	AGCACAAGGTTGGTCGCATT	190
p65	GATTGGGCCATGAACTCCCA	TTCATTCAGCCGATCCCACC	209

2.11. Immunofluorescence analysis

An Immunofluorescence analysis was performed as described earlier.[134] Briefly, cells cultured on coverslip contained in 6-well plates (Lab-Tek II) were fixed with 4% paraformaldehyde for 20 min followed by 2 rinses in TBST. Samples were incubated in a 1:1 solution of TBST and blocking buffer containing rabbit anti-NR2A (1:250), an-ti-GluR1 (1:250), ant-HDAC2 (1:250), anti-CREB (1:250) and anti-MAP2 (1:250) for 2 hrs at 37ºC. After three washes in PBST (15 min each), slides were further incubated with FIT-C and TRIT-C-conjugated secondary antibodies. For negative controls, a set of culture slides was incubated under similar conditions without the primary antibodies. The samples were mounted and observed under an Accuscope fluorescent microscope. The images were captured and merged in CaptaVisionTM imaging software.

Table 2: List of antibodies used for Western Blot and Immunostaining

Antibody	Vendor	Catalog#	Host	Application	Dilution
NR2A/GRIN2A Polyclonal antibody	Proteintech	28525-1-AP	Rabbit		1:1000(WB) 1:250 (IF)
GluR1 Recombinant Rabbit Monoclonal Antibody	Invitrogen	MA5-32344	Rabbit	WB, IF	1:500 (WB) 1:250 (IF)
MAP2 Monoclonal Antibody	Invitrogen	13-1500	Mouse	WB, IF	1:500 (WB) 1:250 (IF)
CREB Monoclonal Antibody	Invitrogen	MA1-083	Mouse	WB, IF	1:500 (WB) 1:250 (IF)
beta Actin Loading Control Monoclonal Antibody	Invitrogen	MA5-15739	Mouse	WB	1:1000 (WB)
IRDye® 680RD Donkey anti-Mouse IgG Secondary Antibody	Li-Cor	926-68072	Donkey	WB	1:500 (WB)
IRDye® 680RD Donkey anti-Rabbit IgG Secondary Antibody	Li-Cor	926-68073	Donkey	WB	1:500 (WB)

IRDye® 800CW Donkey anti-Rabbit IgG Secondary Antibody	Li-Cor	926-32213	Donkey	WB	1:500 (WB)
IRDye® 800CW Donkey anti-Mouse IgG Secondary Antibody	Li-Cor	926-32212	Donkey	WB	1:5,000 (WB)
Goat anti-Rabbit IgG (H+L) Cross-Adsorbed Secondary Antibody, TRITC	Invitrogen	T-2769	Goat	IF	1:200
Goat anti-Mouse IgG1 Cross-Adsorbed Secondary Antibody, Alexa Fluor™ 488	Invitrogen	A-21121	Goat	IF	1:200

2.14. Immunoblot assay

Immunoblot analysis was carried out as described earlier.[135] Briefly, SHSY5Y neuronal cell homogenates were electrophoresed by 4-12% Tris-Glycine gradient gel, proteins were transferred onto a 0.45 μm nitrocellulose membrane, and protein band was visualized with Odyssey Sa infrared scanner after immunolabeling with primary antibodies followed by infra-red fluorophore-tagged secondary antibody (Licor Bio-sciences, Lincoln, NE).

2.13. Creb siRNA transfection

SHSY5Y neurons were transfected with Lipofectamine PLUS® (Invitrogen) and Nupherin-neuron (Biomol) as described earlier (27). Briefly, SHSY5Y cells were main-tained with transfection media followed by the addition of 0.25 μg (each well in a 6-well plate) or 0.1 μg (each well in a 96-well plate) of creb siRNA complexed with Neupherin peptide and Lipofectamine PLUS®. After 5 hrs. the cells were supplemented with 20% FBS-containing media and after another 18 hrs, cells were treated with JRM-28.

2.14. CRE luciferase assay

CRE luciferase assay was performed using a dual luciferase kit (Cat# 60611; BPS Bioscience). The CRE reporter is premixed with a constitutively expressing Renilla (sea pansy) luciferase vector that serves as an internal control for transfection efficiency. The reporter construct is transfected in SHSY5Y cells with Lipofectamine3000TM transfection reagent mixed with serum-free Opti-MEMTM Transfection media followed by the supplementation with 20% FBS-containing media. After 24 hours, cells will be treated with JRM-28 for 5 hrs and then measured dual luciferase activity by cell lysis. The re-action was set in a 96-well plate and the assay endpoint was recorded in a PerkinElmer Enspire multimodal platereader.

2.15. Statistical analyses

All statistical analyses were performed in GraphPad Prism 9. An unpaired t-test was performed when comparing means between the two groups. One-way ANOVA was performed when analyzing the significance of the mean in multiple groups with a single effector of treatment. The null hypothesis is rejected at $p<0.05$, analysis with treatment as an effector. For correlation

analyses, the first D'Agostino-Pearson normality test was performed. If the dataset passed the normality test, then a parametric Pearson correlation analysis was performed, otherwise, a non-parametric Spearman correlation statistic was performed. Results are plotted as mean ± SD of three different experiments.

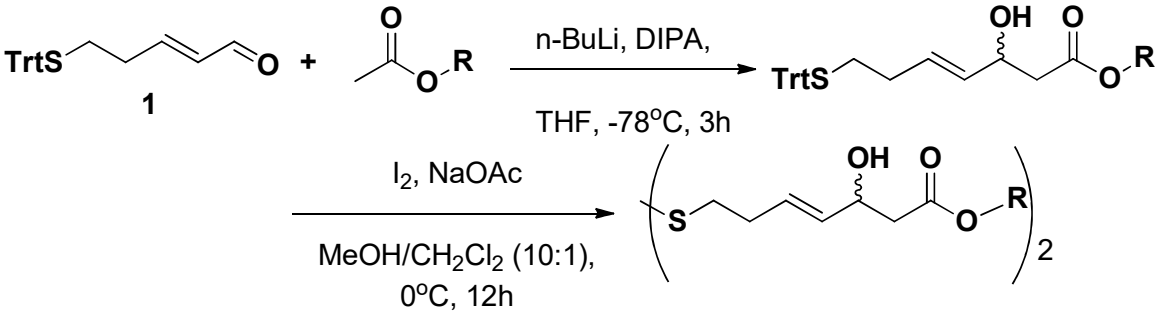
3. Results

3.1. Synthesis of JRM Series Compounds

To develop a selective HDAC2 inhibitor, initially, a library of compounds was synthesized based on MJM-1, keeping the sulfur as ZBG, and the C-5 linker intact, altering the cap groups. This resulted in three different series of derivatives of MJM-1: esters, ketones, and amides.

3.1.1. Ester Analogs

Series-1: Ester Analogs



Compounds	Yield (%)	Compounds	Yield (%)
JRM-1, R=	82	JRM-5, R=	70
JRM-2, R=	80	JRM-7, R=	78
JRM-3, R=	76	JRM-8, R=	70
JRM-4, R=	67	JRM-9, R=	65
JRM-5, R=	55		

Scheme 1: Synthetic scheme of ester analogs with corresponding yields

Compounds JRM-1 to JRM-9 (Series-1) are synthesized in different ester derivatives similar to MJM-1. Initially, all the disulfide products were synthesized from αβ-unsaturated aldehyde (1)[132] and the corresponding ester as an enolate source, followed by the dimerization in the presence of iodine and sodium acetate (Scheme 1). This set of compounds is designed to understand the influence of different aliphatic and aromatic ester cap groups on bioactivity since our previous lead compound was an ester. The yield was lowest for JRM-5, and comparatively lower for JRM-9, possibly due to having a bulky terbutylcyclohexyl moiety. A bulky carbonyl group generally hinders the aldol condensation reaction by creating steric hindrance, making it more difficult for the nucleophilic enolate ion to approach and attack the carbonyl carbon, thus reducing the reaction rate and potentially lowering the yield of the desired product.[136]

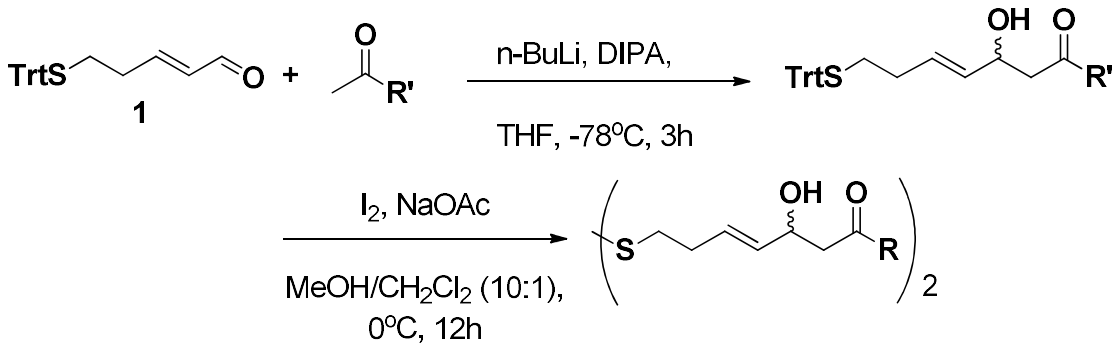
3.1.2. Ketone Analogs

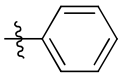
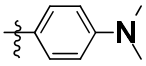
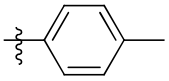
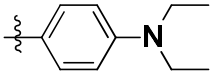
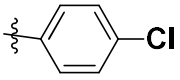
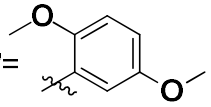
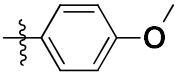
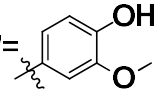
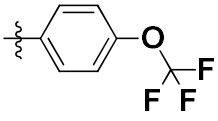
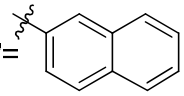
The idea behind synthesizing MJM-1 analogs with ketone cap group derived from the potent pan HDACi, Trichostatin A (Figure 8). Ketone-based functionalities capable of forming reversible covalent adducts, while displaying high metabolic stability, and imparting improved water solubility. Thus, introducing a reactive carbonyl to a scaffold is a potentially useful strategy for enhancing compound potency. JRM-10 to JRM-19 (Series-2) were synthesized from the same αβ-unsaturated aldehyde 1 and corresponding ketones as an enolate source. Since ketone is more stable than the ester group, it could increase its half-life in the brain and would enhance memory formation even better. In addition, we have synthesized ketones with electron donating and electron withdrawing aromatic moiety to evaluate the electronic effect on HDAC inhibition.[137]

The yield of the ketone analogs with electron withdrawing moiety showed better yield than that of the electron donating moieties. It is scientifically proven that, an electron-withdrawing group on

an enolate aromatic carbonyl moiety will increase the rate of an aldol condensation reaction by stabilizing the enolate anion, making it a more potent nucleophile and facilitating its attack on the electrophilic carbonyl carbon of the other reactant.[138]

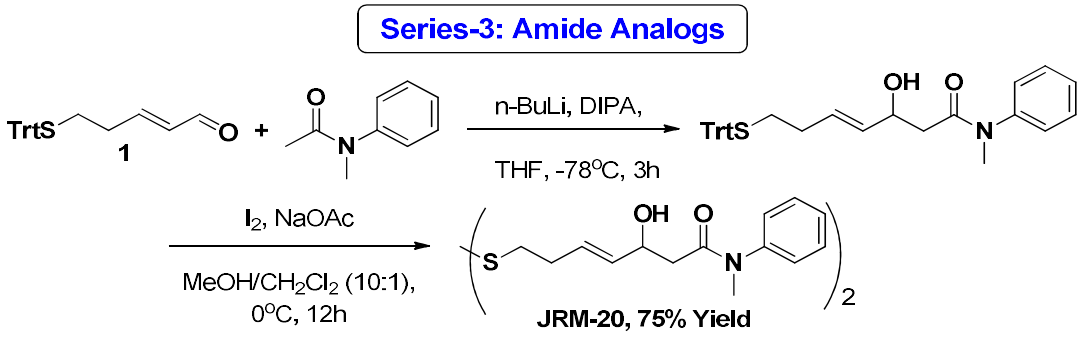
Series-2: Ketone Analogs



Compounds	Yield (%)	Compounds	Yield (%)
JRM-10, R'= 	72	JRM-15, R'= 	80
JRM-11, R'= 	70	JRM-16, R'= 	79
JRM-12, R'= 	75	JRM-17, R'= 	70
JRM-13, R'= 	70	JRM-18, R'= 	73
JRM-14, R'= 	79	JRM-19, R'= 	75

Scheme 2: Synthetic scheme of ketone analogs with corresponding yields

3.1.3. Amide Analogs



Scheme 3: Amide analog of MJM-1

Inspired by the cap group of Entinostat, an FDA-approved HDACi (Figure 8), a series of amide analogs were synthesized earlier (MJM-3 to MJM-6). However, these compounds did not display significant HDAC inhibition as compared with MJM-1.[132] Later, JRM-20 was synthesized in this series where the enolate source was N-methyl acetanilide. It is scientifically established that incorporating a methyl group replacing the amide hydrogen can enhance chemical and metabolic stability as well as can improve permeability.[139]

3.1.4. Sulfoxide Analogs

In order to identify a better HDAC-2 inhibitor, we also focused our attention on modifying the ZBG. As sulfoxide has the potential to have better binding affinity than thiol31, we decided to convert the thiol ZBG to sulfoxide. To prove this fact, we also docked monomers of thiol analogs (ester MJM-1, ketone JRM-11, and N-methyl amide JRM-20) and corresponding sulfoxide analogs using Molecular Operating Environment (MOE) (Table 3).

In all three cases, we found that sulfoxide analogs showed stronger binding at the active site (Table 2). For example, the binding of JRM-20 (green) is due to interactions of the sulfur of the ZBG with

Asp 269 (3.95 Å, -0.8 kcal/mol), Asp 181(3.45 Å, -2.3 kcal/mol) and the Zinc (2.31 Å, -2.9 kcal/mol) at the active site (Figure 10).

However, docking with the sulfoxide monomer of JRM-28 (blue) displayed better interaction at the active site than JRM-20: oxygen of the sulfoxide moiety interacted with His 145 (3.40 Å, -3.9 kcal/mol), His 146 (3.11 Å, -5.3 kcal/mol) and Zinc (1.99 Å, -4.8 kcal/mol) (Figure 10). The better interactions of JRM-23 are attributed to greater affinity towards the active site of HDAC-2 than JRM-20. We, therefore, hypothesize that sulfoxide could have better HDAC inhibition and a higher degree of histone acetylation than that of their parent analogs. To verify the correlation of the docking score with HDAC-2 inhibition, we synthesized sulfoxides; JRM-21, JRM-22, JRM-23, and JRM-24 from the corresponding thiols; MJM-1, JRM-11, JRM-19, and JRM-20, respectively (Scheme 4). The oxidation from sulfur to sulfoxide was carried out with 1.1 equivalent of m-chloroperbenzoic acid (mCPBA) in DCM at 40°C. All the sulfoxides displayed better HDAC2 inhibition than their parent compound and the lowest inhibition was observed for JRM-24. Further

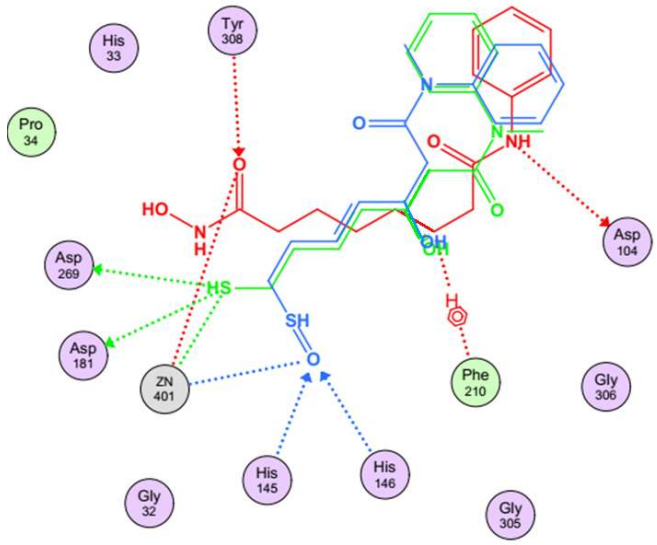
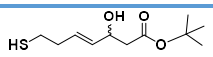
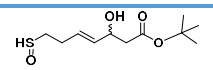
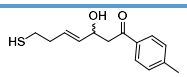
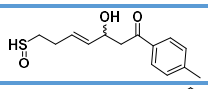
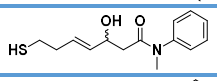
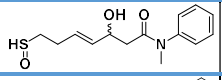
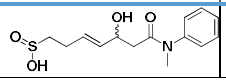
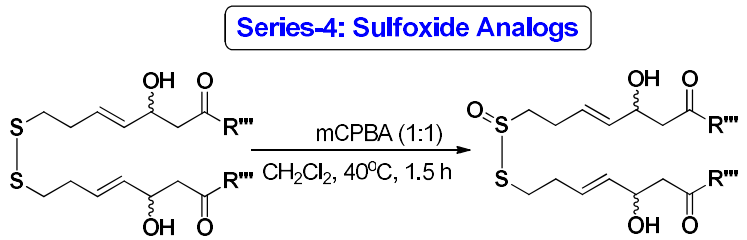


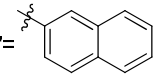
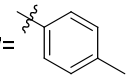
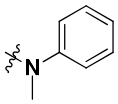
Figure 10. Binding of JRM-20 (green) and JRM-20 sulfoxide (blue) to HDAC-2 with SAHA (red)

Table 3: Docking Study

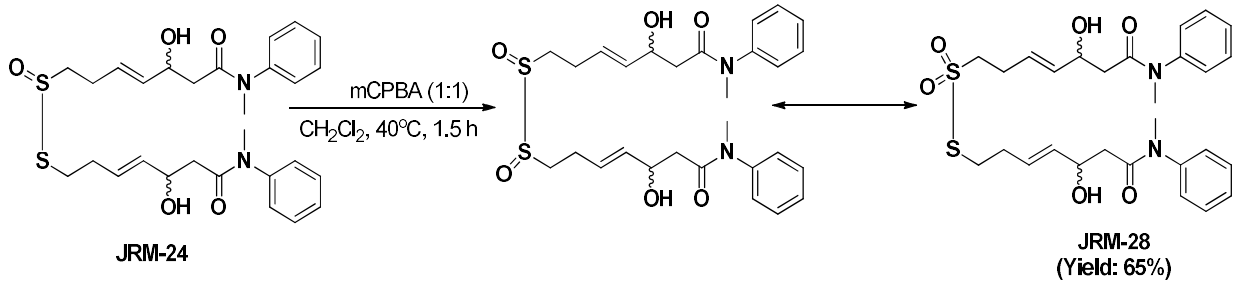
Analogs	Structure (Monomers)	Docking Score (kcal.mol^{-1})
MJM-1		-6.30
JRM-21		-7.55
JRM-11		-6.36
JRM-22		-7.62
JRM-20		-6.42
JRM-24		-7.80
JRM-28		-8.31

oxidation of JRM-24 using 1.1 equivalent of m-chloroperbenzoic acid (mCPBA) in DCM at 40°C generated the corresponding disulfoxide with readily transformed to the monosulfone, JRM-28 (Scheme 5).[140] The mass of JRM-28 was confirmed by mass spectrometry showing 561 m/z for the M+1 product and 583 m/z for the M+Na+ species (Figure 11A). The structure of JRM-28 was confirmed by ^{1}H NMR (Figure 11B).



Compounds	Yield (%)
JRM-21, R'''= 	80
JRM-23, R'''= 	78
JRM-22, R'''= 	75
JRM-24, R'''= 	75

Scheme 4: Sulfoxide Analogs



Scheme 5: Synthesis of JRM-28

The JRM-28 showed the highest docking score and lowest IC50 value against HDAC2 enzyme and is considered as the lead compound for further mechanistic studies.

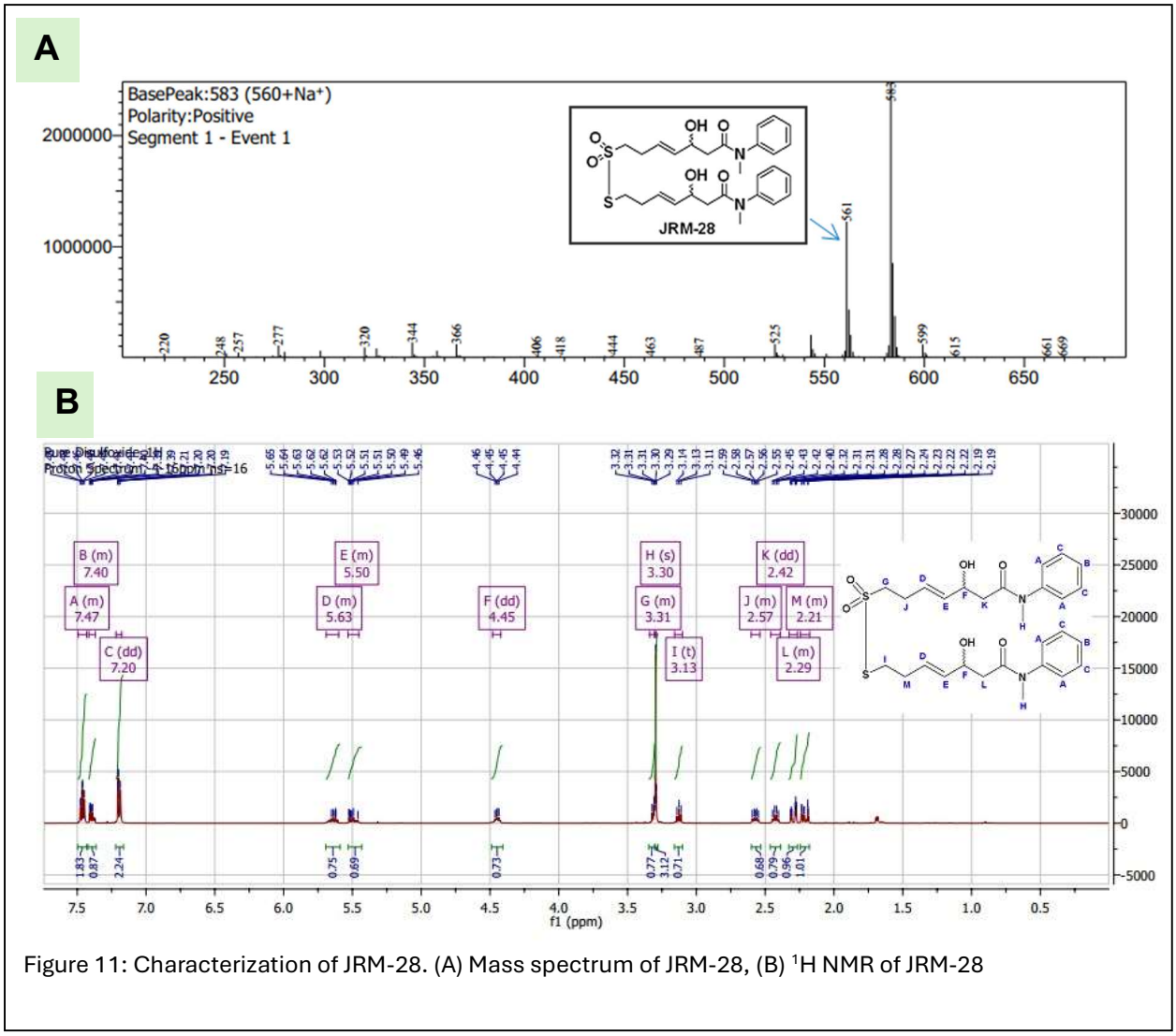


Figure 11: Characterization of JRM-28. (A) Mass spectrum of JRM-28, (B) ^{1}H NMR of JRM-28

3.2. HDAC2 Inhibition Study

Compounds that inhibit the HDAC-2 enzyme could increase the acetylation of histone, which is important for the expression of the gene responsible for neuroplasticity and, thus, memory formation.[61]

To screen the HDAC2 inhibitory activity of the synthesized compounds, at first luminometric assay were performed using HDAC Glo Assays and Screening Systems (Promega Corporation, Madison, WI, USA). The HDAC-Glo™ I/II Assays and Screening Systems are single-reagent-addition, homogeneous, luminescent assays that measure the relative activity of histone deacetylase (HDAC) class I and II enzymes using purified enzymes, extracts or cells directly in culture plates. The add-mix-measure protocol allows for simple measurements of deacetylating activities and

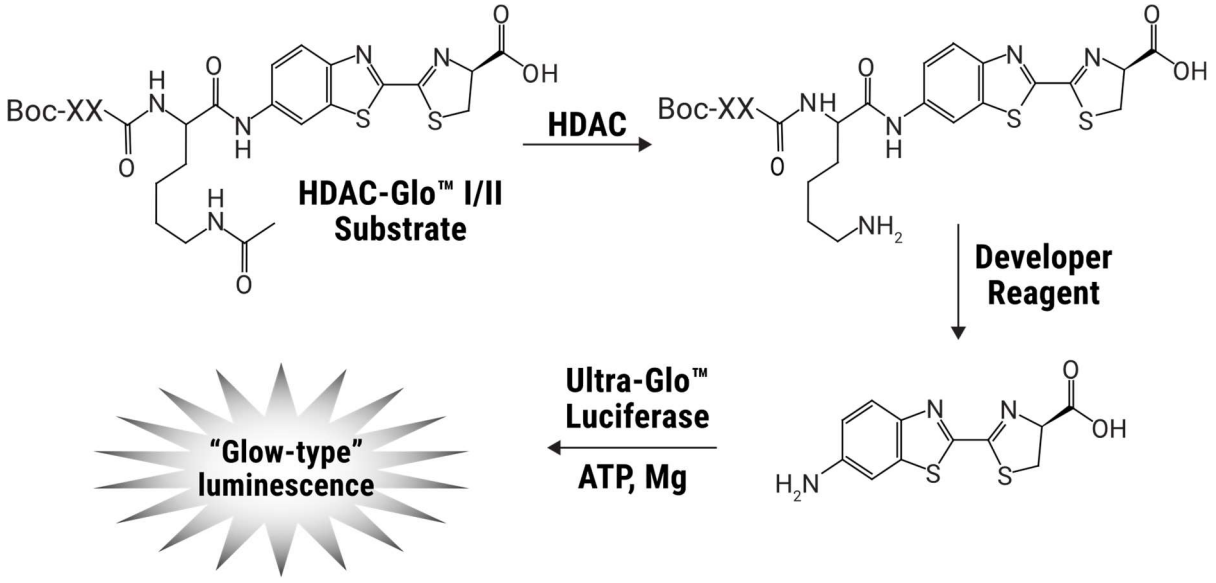


Figure 12: HDAC-Glo™ I/II Assay Chemistry

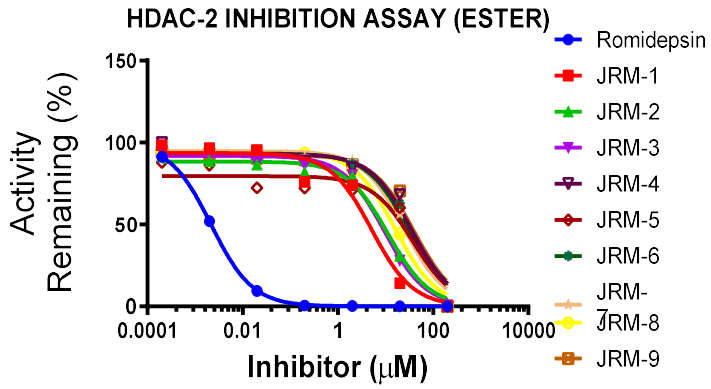
easy implementation from benchtop to screening. The HDAC-Glo™ I/II Assays and Screening Systems can be used to determine HDAC inhibitor potency, selectively profile HDAC inhibitors, correlate HDAC inhibitor potency with cellular fate in same-well multiplexed viability assays or determine off-target HDAC effects of compounds.

The assays use an acetylated, live-cell-permeant, luminogenic peptide substrate that can be deacetylated by HDAC activities. Deacetylation of the peptide aminoluciferin substrate is measured using a coupled enzymatic system in which a protease in the Developer Reagent cleaves

the deacetylated peptide from the aminoluciferin substrate, releasing aminoluciferin, which is quantified in a reaction using Ultra-Glo™ recombinant firefly luciferase (Figure 12).

Before performing the assay, optimum HDAC2 concentration was determined by plotting HDAC2 activity Vs. concentration plot according to the manufacturer's protocol. The assay was performed in the presence and absence of dithiothreitol (DTT), a thiol-containing reducing agent. As depicted previously, MJM-1 displayed a strong HDAC inhibitory effect once its disulfide bond was reduced with DTT.[132]

3.2.1. HDAC2 Inhibition of Ester Analogs



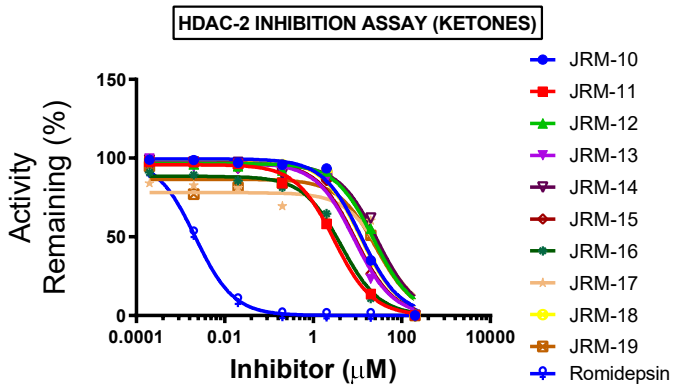
	IC50	IC50
Romidepsin	0.002162	0.002071 to 0.002256
JRM-1	5.113	2.103 to 12.43
JRM-2	11.31	7.067 to 18.08
JRM-3	9.471	5.970 to 15.03
JRM-4	35.36	13.99 to 89.43
JRM-5	37.37	10.80 to 129.3
JRM-6	30.80	14.31 to 66.31
JRM-7	24.76	13.28 to 46.19
JRM-8	16.00	11.11 to 23.05
JRM-9	38.82	15.63 to 96.43

Figure 13: Inhibition of HDAC2 by ester analogs of MJM-1

The smaller cap group showed better HDAC2 inhibition. Least HDAC2 inhibition was observed for JRM-9 which contains tert-butylbenzyl cap group. Second lowest inhibition was observed for the tert-butylcyclohexyl cap group (Figure 13). One possible explanation supporting the lower HDAC2 inhibition is the steric hindrance posed by bulky cap group. In addition, big hydrophobic cap group can reduce the solubility of the molecule and thus reduce the extent of HDAC2 inhibition.

3.2.2. HDAC2 Inhibition by Ketone Analogs

Usually, ketone-based small molecules possess better solubility and are metabolically more resistant than ester compounds.[137,138] Among the ketone analogs, the lowest HDAC2 inhibition was observed for JRM-11 which contained a 4-methyl acetophenone cap group. No significant differences in HDAC-2 inhibition were observed for incorporating electron donating or electron withdrawing groups in the aromatic ring. But, just like ester analogs, increased hydrophobicity decreased the HDAC2 inhibitory activity of these compounds (Figure 14).



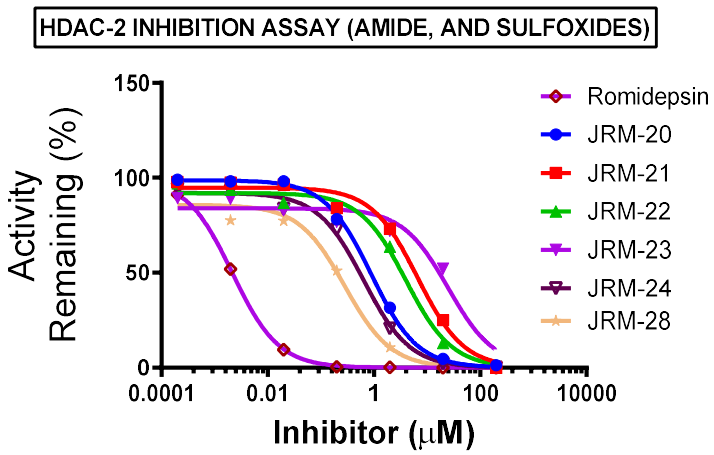
	IC50	IC50
Romidepsin	0.002162	0.002071 to 0.002256
JRM-10	12.19	7.480 to 19.86
JRM-11	2.972	2.150 to 4.109
JRM-12	23.37	13.47 to 40.53
JRM-13	8.459	4.626 to 15.47
JRM-14	27.78	13.87 to 55.64
JRM-15	8.932	5.701 to 13.99
JRM-16	4.329	2.790 to 6.717
JRM-17	37.30	10.27 to 135.4
JRM-18	11.79	7.378 to 18.85
JRM-19	26.17	9.675 to 70.78

Figure 14: Inhibition of HDAC2 by ketone analogs

3.2.3. HDAC2 Inhibition by Amide Analog

In our previous work, amide analogs (MJM-3 to MJM-8) displayed poor HDAC-2 inhibition. So, in the current research, we slightly modified the amide cap group by replacing amide hydrogen with a methyl group and this is how we generated JRM-20. It is scientifically proven that incorporating a methyl group in amide functionality works as a metabolic blocker and enhances the bioavailability of the compound.[139] Among all the compounds, the JRM-20 displayed the lowest HDAC2 inhibition (IC50= 0.88 μM) (Figure 15).

3.2.4. HDAC2 Inhibition by Sulfoxide Analogs



	IC50	IC50
Romidepsin	0.002162	0.002071 to 0.002256
JRM-20	0.8811	0.7492 to 1.036
JRM-21	6.639	4.071 to 10.83
JRM-22	3.990	2.552 to 6.237
JRM-23	24.96	10.83 to 57.53
JRM-24	0.6383	0.4405 to 0.9248
JRM-28	0.2828	0.1415 to 0.5655

Figure 15: HDAC Inhibition by Amide and Sulfoxide Analogs

To develop promising HDAC2 inhibitors, we also changed the ZBG from disulfide to corresponding monosulfoxide for compounds from each series with significant HDAC2 inhibition and screened them against HDAC2. Among them, JRM-24, the monosulfoxide of JRM-20 displayed the highest HDAC2 inhibition (IC50= 0.63 μM). This finding inspired us to make monosulfone from JRM-24 and lead to the development of JRM-28. Interestingly, JRM-28 showed the best HDAC2 inhibition (IC50= 0.2828 μM) among all the analogs so far, we have synthesized (Figure 15).

3.3. HDAC2 Selectivity Study of JRM-28

HDAC Glo Luminescence assay utilizes Ultra-Glo luciferase enzyme in the developer to emit luminescence. There is a possibility that our HDAC inhibitors can interfere with the luciferase activity and can give false positive results. To eliminate this possibility, a fluorescence-based HDAC2 inhibition assay was carried out. In addition, HDAC isoform selectivity of JRM-28 was

investigated with class I (HDAC1, 2, and 3) and class II (HDAC6) HDACs using fluorescence-based enzyme assay.

The fluorescence was normalized with DMSO control and adjusted in the presence of DTT. JRM-

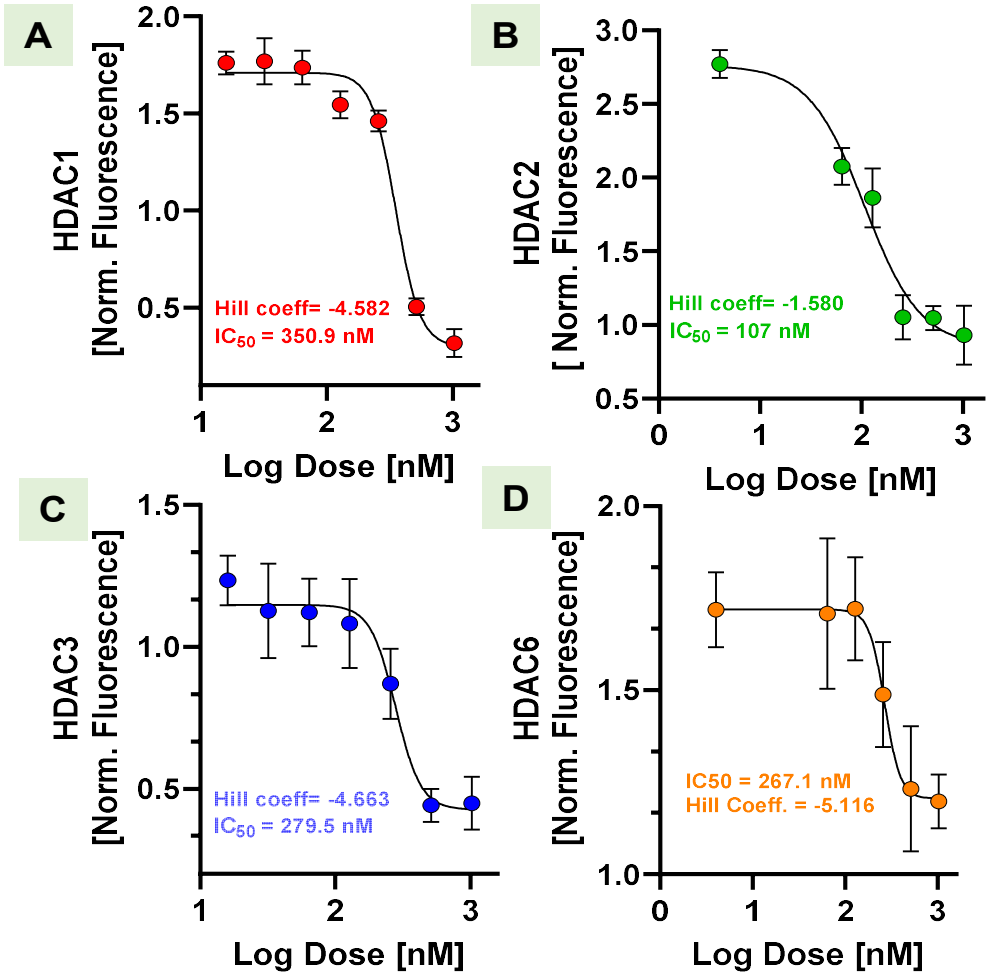


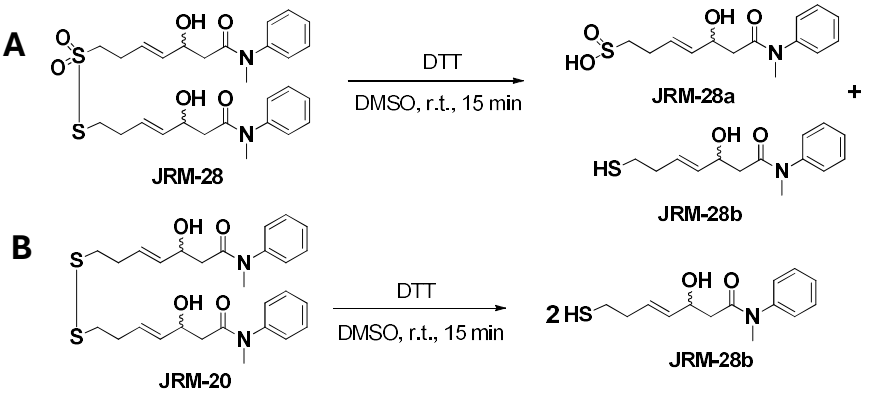
Figure 16: JRM-28 is an HDAC2 inhibitor. Fluorimetric inhibition analyses (Ex/Em = 480/528 nm) with purified (A) HDAC1, (B) HDAC2, and (C) HDAC3, and (D)HDAC6 were performed in the presence of increasing doses of JRM-28 (reduced with DTT).

28 dose-dependently inhibited the activity of HDAC2 (Figure 16B) only, but not other class-I HDACs, including HDAC1 (Figure 16A) and HDAC3 (Figure 16C). In fact, reduced JRM-28 displayed the characteristic sigmoidal binding curve (IC50 ~ 107 nM and Hill slope = -1.580) only

with HDAC2, but not with HDAC1 (IC50 =350.9 nM; Hill coefficient = -4.582) and 3 (IC50 =279.5 nM; Hill coefficient = -4.663). Next, the interaction between JRM-28 and class-II HDAC HDAC6 was assessed resulting in no appreciable inhibition (IC50 =267.1 nM; Hill coefficient = -5.116) (Figure 16D).

3.4. Possible Fate of JRM-28 After Reduction by DTT

Since JRM-28 is a dimer with a similar disulfide linkage, we proposed the reduction of JRM-28 by DTT forming two different monomers. The monomer with the sulfinic acid (SO2H) moiety was termed JRM-28a, and the monomer with the sulfhydryl (SH) group was termed JRM-28b. Accordingly, upon treatment with 350 mM DTT, JRM-28 was reduced to JRM-28a (Scheme 6A) and JRM-28b, whereas, the precursor molecule, JRM-20 generated only JRM-28b under the same condition as confirmed by mass spectrometry (Scheme 6B).



Scheme 6: Schematic presentations for the reduction of JRM-28 to JRM-28a and JRM-28b (A), and the reduction of JRM-20 to JRM-28b (B) by DTT.

The mass spectrum of the DTT-treated JRM-28 identified the predominant existence of JRM-28 (base peak 561 m/z) with traces of JRM-28b (266 m/z) and JRM-20 (529 m/z) in positive ion mode (Figure 17A). In the negative ion mode, we observed JRM-28a (296 m/z) as major product (Figure 17B). On the other hand, DTT-treated JRM-20 displayed base peak of 266 m/z in mass spectrum which represents the predominant existence of JRM-28b (Figure 17C).

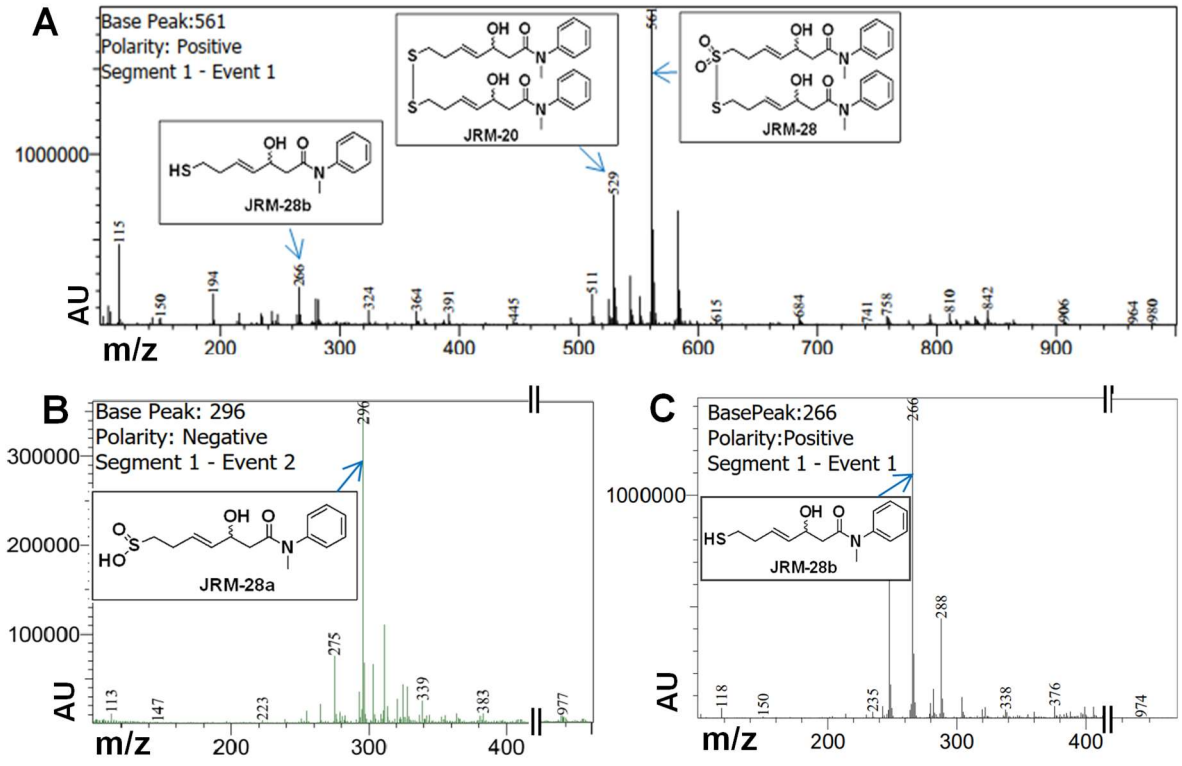


Figure 17: Mass spectrum of the DTT-treated JRM-20 and JRM-28. The mass spectrum of the sample containing JRM-28 and DTT confirms the existence of JRM-28a (trace), JRM-20 (trace), and JRM-28 (predominant, base peak at 561) in positive ion mode (A). Whereas the negative ion mode predominantly confirmed the generation of JRM-28a (B). The mass spectrum for JRM-20 with DDT displayed the base peak at 266 for JRM-28b (C).

JRM-28 generates two heterogeneous species (JRM-28a and JRM-28b) when a 19.3 µL solution of JRM-28 (10 mM) in DMSO was treated with 0.7 µL aqueous solution of DTT (350 mM) for 15 minutes at room temperature. DTT breaks the thiosulfonate bond in JRM-28 by nucleophilic attack (red curved arrows in Figure 18) and generates one thiol species (JRM-28a) and another sulfinic acid (JRM28b) by a previously reported route shown in scheme 6A.[141] The sulfinic acid species is more thermodynamically stable than the thiol species.[142] As a result, the reactive thiol species further undergoes a similar type of disulfide exchange reaction as DTT with JRM-28 to generate JRM-20 and JRM-28a (green curved arrows as shown in Figure 18).[143] Due to the symmetrical structure of precursor molecule JRM-20, DTT treatment generates only JRM-20b.The mass

spectrum of the sample containing JRM-28 and DTT confirms the existence of JRM28a (trace), JRM-20 (trace), and JRM-28 (predominant, base peak at 561) in positive ion mode (Figure 17A), whereas the negative ion mode predominantly confirmed the generation of JRM-28a (Figure 17B).

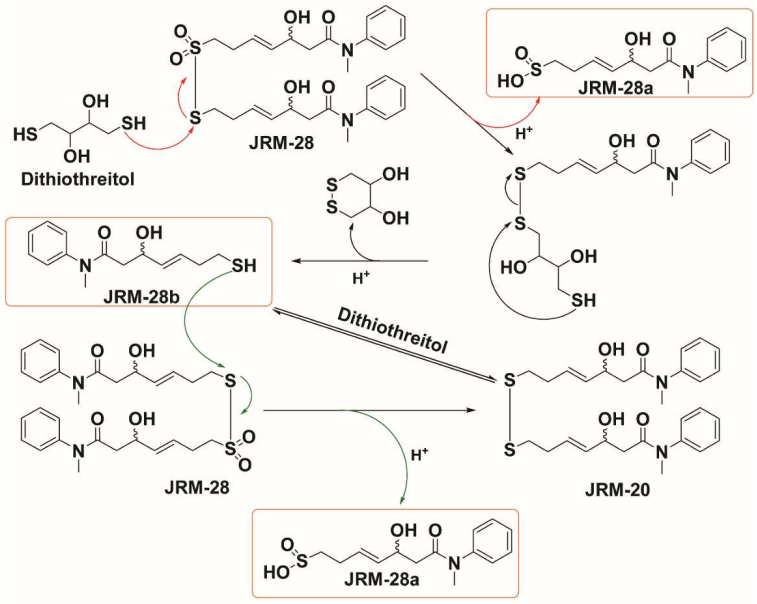


Figure 18: Possible fate of JRM-28 after DTT treatment

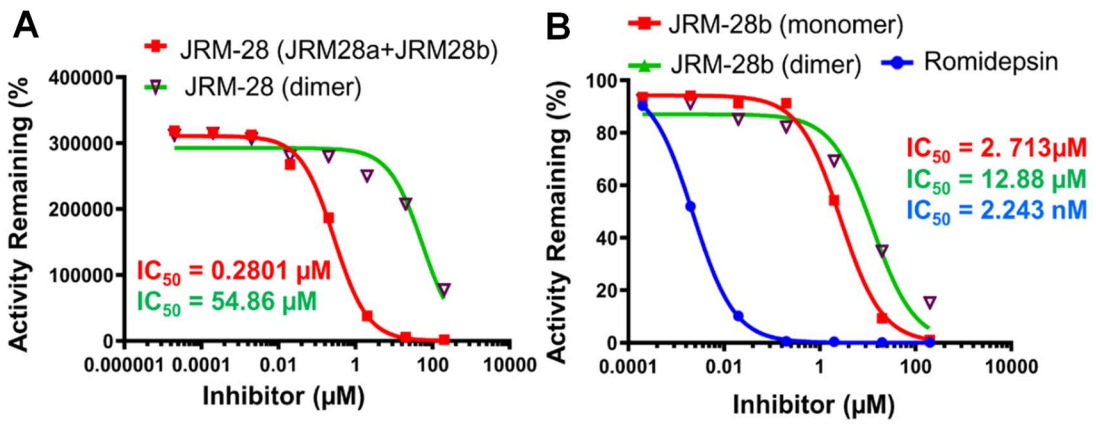


Figure 19: HDAC2 inhibitory role of JRM-28 and its monomers JRM-28a and b. Luminescence assay for purified recombinant HDAC2 inhibition by JRM-28 (A) and JRM-20 (B) with and without DTT. HDAC2 assays were done in triplicate, and the averages were plotted on the non-linear regression graph of the concentration-response equation using GraphPad Prism 8 software. In this assay, aminoluciferin and luciferase were coupled to deacetylase activity such that luminescence (arbitrary units, au) linearly reflected the rate of deacetylation. HDAC2 concentration (0.5 nM) and the dose of inhibitors were consistent in each reaction.

The mass spectrum for JRM-20 with DDT displayed the base peak at 266 for JRM-28b (Figure 17C). While analyzing the effect of JRM-28 on the HDAC2 inhibition, we observed that the

addition of DTT markedly increased the inhibitory effect of JRM-28 by almost 200-fold (Figure 19A). The inhibition curve of JRM-28 in the presence of DTT resulted in an IC50 of 0.28 μM, whereas without DTT, the IC50 was 54.86 μM. Since upon reduction, JRM-28 breaks down to JRM-28a and 28b, the HDAC2-inhibitory effect of each monomer is warranted. We monitored the dose dependent inhibitory effect effects of JRM-28b by reducing JRM-20 (Figure 19B). The observed IC50 was 2.7 μM for JRM-28b whereas JRM-20 in the non-reduced form display an IC50 value of 12.9 μM. Thus, it can be concluded that JRM-28a, but not 28b, is the most potent isoform that displays a strong HDAC2 inhibitory effect. We were not able to directly measure the HDAC activity of JRM-28a because the molecule spontaneously dimerized to form JRM-28.

3.5. In-Silico Study of JRM-28 for HDAC2 Specificity

Our in-silico docking analysis of JRM-28a with HDAC2 (Figure 20) predicted the complex formation of JR28a with HDAC2. The most stable pose was predicted based on the full-fitness score (-8.524 kcal/mol). According to that docking pose, the N-phenyl acetanilide group of JRM-28a was found at the surface of the HDAC2 enzyme, the linker connected the ZBG of JRM-28a at the catalytic side of HDAC2. The high-resolution wire representation of the docking image further identified surrounding amino acid residues such as Gly 154, Phe 155, His 183, and Tyr 208 at 10 Å resolution in the catalytic site. Electrostatic potential surface representation displayed the hydrophobic and hydrophilic nature of the catalytic pocket (Figure 20B). The in-silico analysis of JRM-28a with another class-II HDAC, HDAC4 demonstrated (Figure 20C) that the ZBG of JRM-

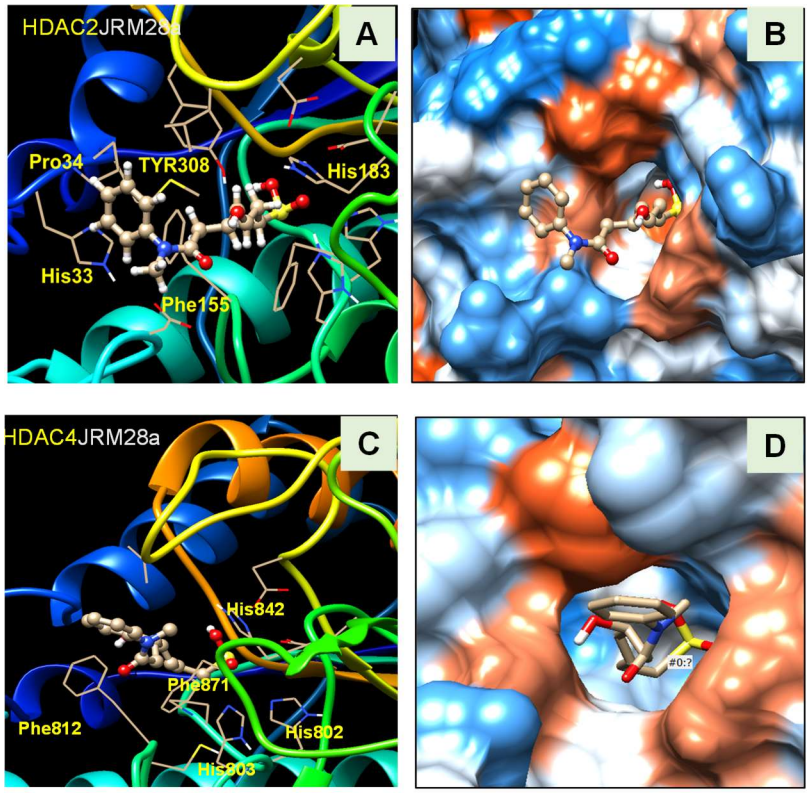


Figure 20: In-silico binding comparison of JRM-28 with HDAC2 and HDAC4. The high-resolution image showed amino acid residues within an 11 Å distance of JRM-28a in a catalytic binding pocket of HDAC2 (A) and HDAC4 (C). The electrostatic potential surface displayed the charge distribution of HDAC2 (B) and HDAC4 (D) protein around JRM-28a. Blue = positive charge, white = neutral, and red = negative charge.

28a posed far from the catalytic pocket of HDAC4 comprised of His802, His803, and His842, even though, an electrostatic potential surface representation predicted the docking of JRM-28 in the catalytic pocket of HDAC4 (Figure 20D). Collectively, our results suggest that JRM-28a, the active component of JRM-28, serves as a strong inhibitor of HDAC2, but not other HDACs.

3.6. Effect of JRM-28 on HDAC2 Expression

We wanted to study the effect of lower concentrations of HDAC2 on the regulation of HDAC2 activity. An immunoblot (IB) analysis of HDAC2 (Figure 21A) followed by densitometric assessment (Figure 21B) revealed that lower concentrations such as 2, 5, and 10 µM of JRM-28 did not upregulate the expression of HDAC2 in SHSY5Y cells compared to the control. Interestingly, subsequent immune cytochemical analyses (Figure 21Ci & iii) together with

quantitative estimation (Figure 21C ii & iv) indicated that 5 µM of JRM-28 significantly arrested

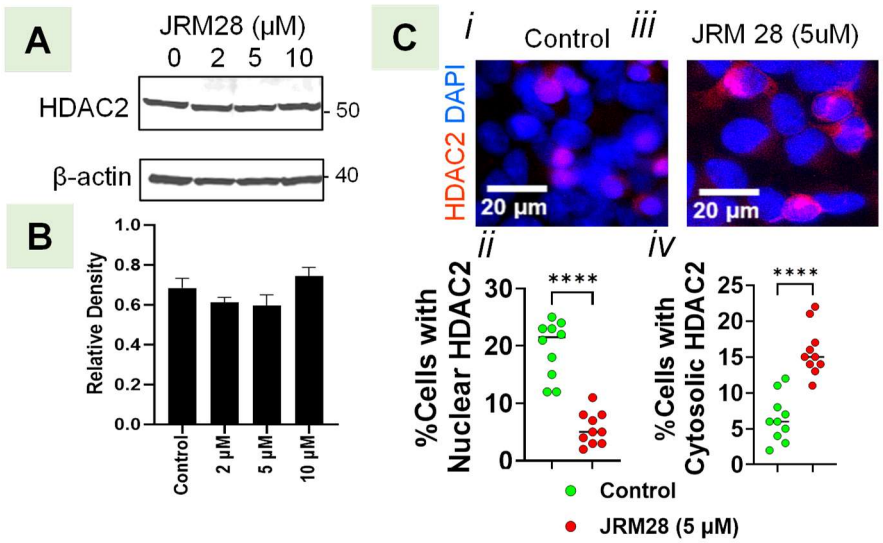


Figure 21: Immunoblot (IB) analysis of HDAC2 in the total cell lysate of SHSY5Y cells treated with increasing doses of JRM-28 for 24 hrs. IB assay of β-actin was performed as a housekeeping protein (A). The band density of individual HDAC2 bands was assessed in ImageJ software followed by the normalization with respective β-actin band density. The relative densitometry was plotted by a bar diagram (B). Immunofluorescence (C) analysis of HDAC2 in SHSY5Y cells treated with DMSO (i) 5 µM JRM-28 (iii). Nuclei were stained with DAPI. (ii) Cells with nuclear and (iv) cytosolic HDAC2 were counted in 10 independent images for both control and JRM-treated groups followed by scatter histogram analyses in percent scale. Unpaired t-test (****p<0.0001) was done to measure the significance of mean between groups.

the nuclear translocation of HDAC2 suggesting that low concentrations of JRM-28 inhibited the activation, but not the expression of HDAC2.

3.7. Intracellular HDAC2 Inhibition by JRM-28

We performed a luminescence-based HDAC2 activity assay in SHSY5Y cells with increasing doses of JRM-28. JRM-28 was not reduced by DTT during the treatment as the cellular reductase and oxidoreductase enzymes are expected to reduce JRM-28 in its "active 28a/b" components. Shorter time points up to 45 min of treatment were selected, because the HDAC2 activation occurs rapidly after the treatment.[144]

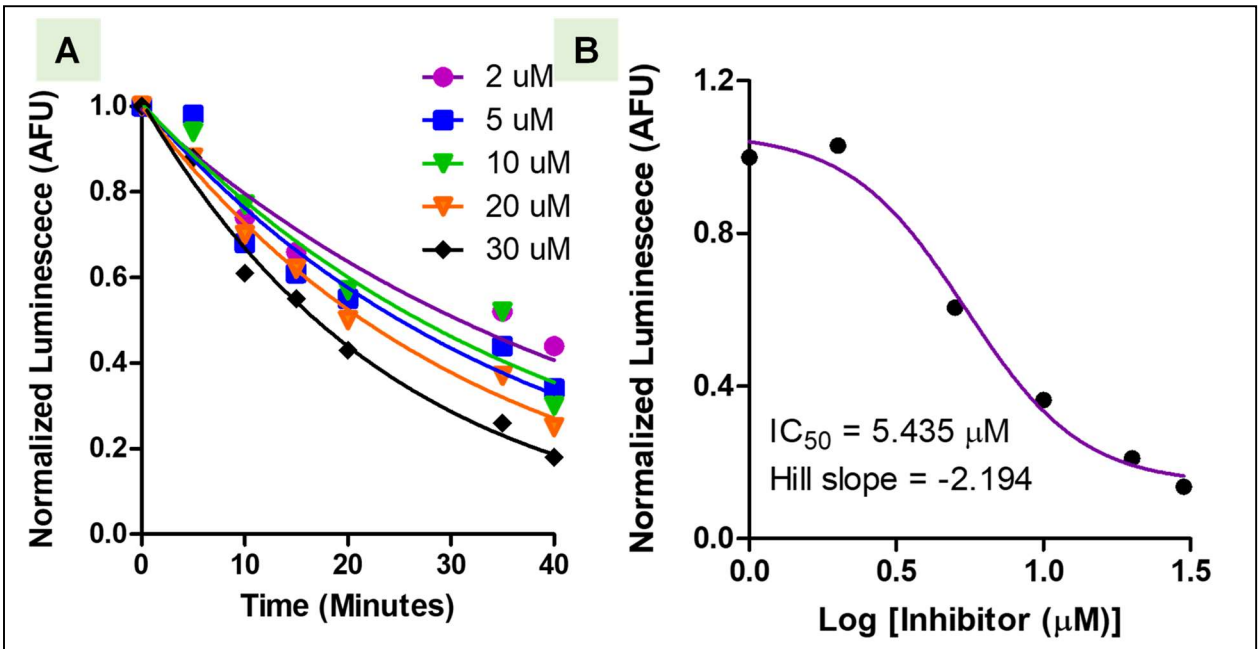


Figure 22: Intracellular HDAC2 Inhibition by JRM-28, (A) Endogenous HDCA2 inhibition assay in the cell lysate of SHSY5Y cells treated with increasing doses of JRM-28. The assay was performed at a different time after the treatment with JRM-28. (H) Dose-dependent endogenous HDAC2 inhibition assay in SHSY5Y cells with increasing doses of JRM-28. A characteristic sigmoidal non-linear inhibitor binding curve was drawn in GraphPad Prism 9 software followed by measuring IC50 and Hill slope. Results are confirmed after three different experiments.

3.8. Cytotoxicity Study of JRM-28

JRM 28 in the presence of DTT was evaluated by cytotoxicity assays. A TUNEL assay was performed with SHSY5Y neuronal cells using increasing concentrations JRM-28 in the presence of DTT. According to the assay (Figure 23A), higher doses of JRM-28 were found to be toxic as 20 µM JRM-28 caused nuclear condensation (Figure 23A; row 6 duplicates), whereas 30 µM (Figure 23A; row 7 duplicates) and 50 µM (Figure 23A; row 8 duplicates) concentrations of JRM-28 induced significant cell death as shown by increased TUNEL-positive inclusion bodies (brown spots) in the nuclei (blue) of SHSY5Y cells. Lower doses of JRM-28 up to 10 µM (Figure 23A; top 5 rows in duplicate) did not induce any cell death. The results were further confirmed by

quantitative analysis (Figure 23B). Next, an LDH release assay (Figure 23C) demonstrated that 30 µM and 50 µM, but not lower concentrations of JRM-28 significantly induced LDH release by SHSY5Y cells.

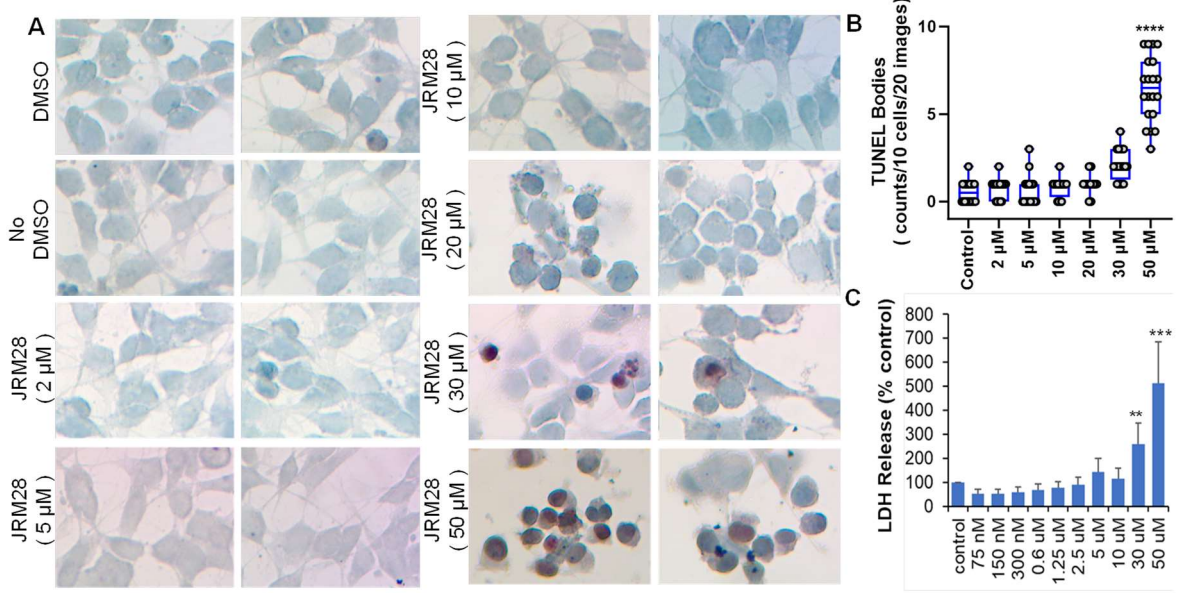


Figure 23: In-vitro Cytotoxicity Study of JRM-28, (A) Representative images are duplicate analyses of TUNEL staining in SHSY5Y neurons with increasing doses of JRM-28. TUNEL+ve cells were detected as condensed brown bodies, whereas nuclei were stained with hematoxylin (blue). (B) TUNEL bodies were counted per 10 randomly selected cells in 20 different images. Results were plotted as a dotted boxplot and the significance of the mean was analyzed by one-way ANOVA (single effector = treatment). **p<0.01 and ****p<0.00001 versus DMSO control. (C) LDH (Lactate dehydrogenase) release assay was performed in the supernatants after 24 hrs of treatment with increasing doses of JRM-28. One-way ANOVA resulted in **p<0.01 and ***p<0.001 versus control.

Collectively, these results identified that a 5 µM concentration of JRM-28 is optimum to achieve the maximum HDAC2 inhibition without causing a cytotoxic response.

3.9. Investigation for the Enhancement of Neuroplasticity by JRM-28

Neuroplasticity refers to the morphological plasticity of neurons that is attributed to the ability of the brain to reorganize and modify its neural connections in response to environmental stimuli,

experience, learning, injury, and disease processes. It encompasses a range of mechanisms, including changes in synaptic strength and connectivity, the formation of new synapses, alterations in the structure and function of neurons, and the generation of new neurons. Neuroplasticity plays a crucial role in developing and maintaining brain function, including learning and memory, as well as in recovery from brain injury and adaptation to environmental changes.[145] To establish the memory formation potential of JRM-28, it is crucial to investigate whether JRM-28 treatment can enhance the morphological plasticity of neuronal cells. To carry out this study, we have employed three different types of neuronal cells; neuroblastoma cells (SHSY5Y), mouse primary neuronal cells, and IPC-derived neuronal stem cells from Alzheimer's patients and estimated the level of marker proteins that are linked with neuroplasticity upon treating with JRM-28.

3.9.1. Effect of JRM-28 on the SHSY5Y Cells

We studied lower doses of JRM-28 in respect to morphological plasticity in neurons. SHSY5Y neurons were grown in complete neuro-basal media and then treated with different doses of JRM-28 for 24 hrs, and then analyzed for dendritic morphogenesis by different immunoassay. Dendritic morphogenesis, which directly correlates to the morphological plasticity of neurons, can be best evaluated by measuring the increase in length and branches of basal dendrites in neurons.[144] Therefore, the effect of JRM-28 was monitored to explore the numbers of MAP2-ir dendrites in SHSY5Y human neuronal cultures. Briefly, SHSY5Y human neuronal cells were treated with 2, 5, and 10 μM concentrations of JRM-28 for 48 h followed by immunofluorescence and immunoblot (IB) analyses of MAP2. Interestingly, 5 μM JRM-28 significantly stimulated dendritic pruning (Figure 24A) as indicated by increased numbers of MAP2-ir small appendages on neuronal cell bodies compared to the control. Moreover, a scatter histogram comparison (Figure

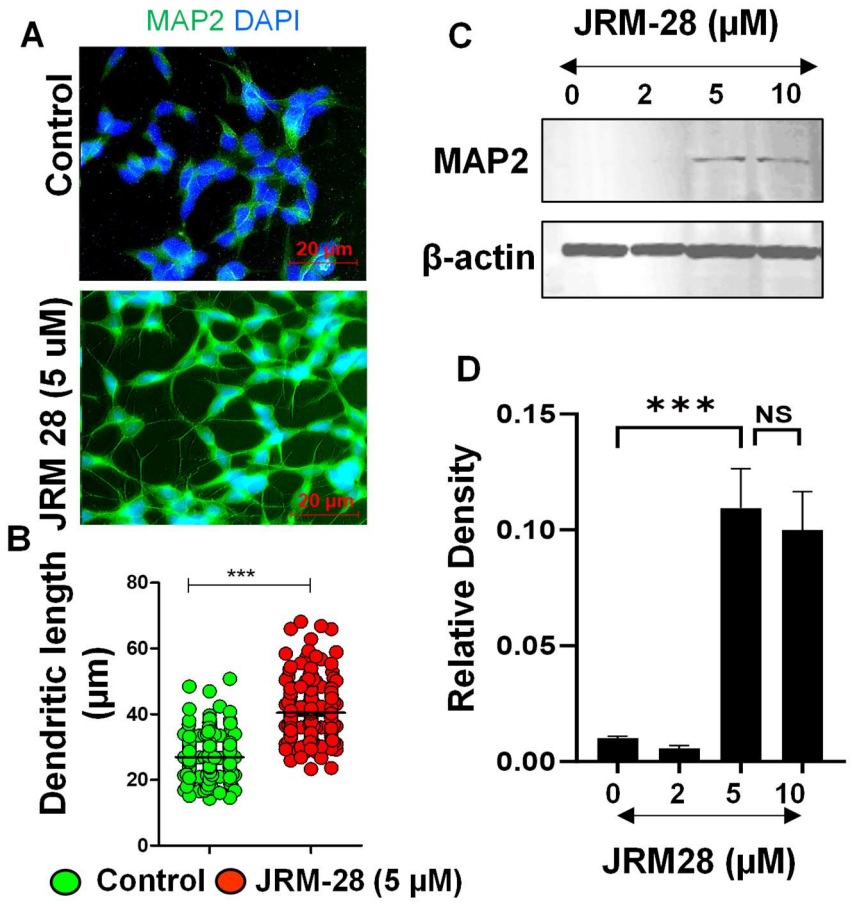


Figure 24: JRM-28 induces structural plasticity in SHSY5Y neurons. (A) After 24 hrs of seeding, JRM-28 was treated for an additional 24 hrs. After that, the immunofluorescence (IF) assay of dendritic marker MAP2 (green) was performed as described in the method section. Nuclei were stained with DAPI (blue). (B) The dendritic length was measured in 200 randomly selected neurons per group in ImageJ software. Briefly, scalebar calibration was performed after converting pixel to micrometer scale followed by measuring dendritic length by line tool. Two-tailed unpaired t-test was per-formed to test the significance of the mean between groups resulting in ***p<0.0001 (t= 18.26; df =398) (C) Immunoblot analysis of MAP2 (top) and beta-actin (bottom) in SHSY5Y cells treated with 2, 5, and 10 µM doses of JRM-28. (D) The band intensity was measured in ImageJ software and then normalized with the respective band density of beta-actin. Unpaired t-test resulted ***p<0.0001 vs. control and ns = no significance.

24B) of dendritic length between control and 5 µM JRM-28 (n=200 per group) followed by an unpaired t-test analysis ($t_{1,398} = 18.26$; ***p<0.001) confirmed that JRM-28 treatment indeed augmented the dendritic morphogenesis in neuronal cells. Moreover, an immunoblot analysis

(Figure 24C) followed by densitometric analysis (Figure 24D) also indicated that 5 and 10 µM of JRM-28 upregulated the expressions of MAP2 in SHSY5Y cells.

3.9.2. Effect of JRM-28 on E18 Mouse Primary Hippocampal Neurons

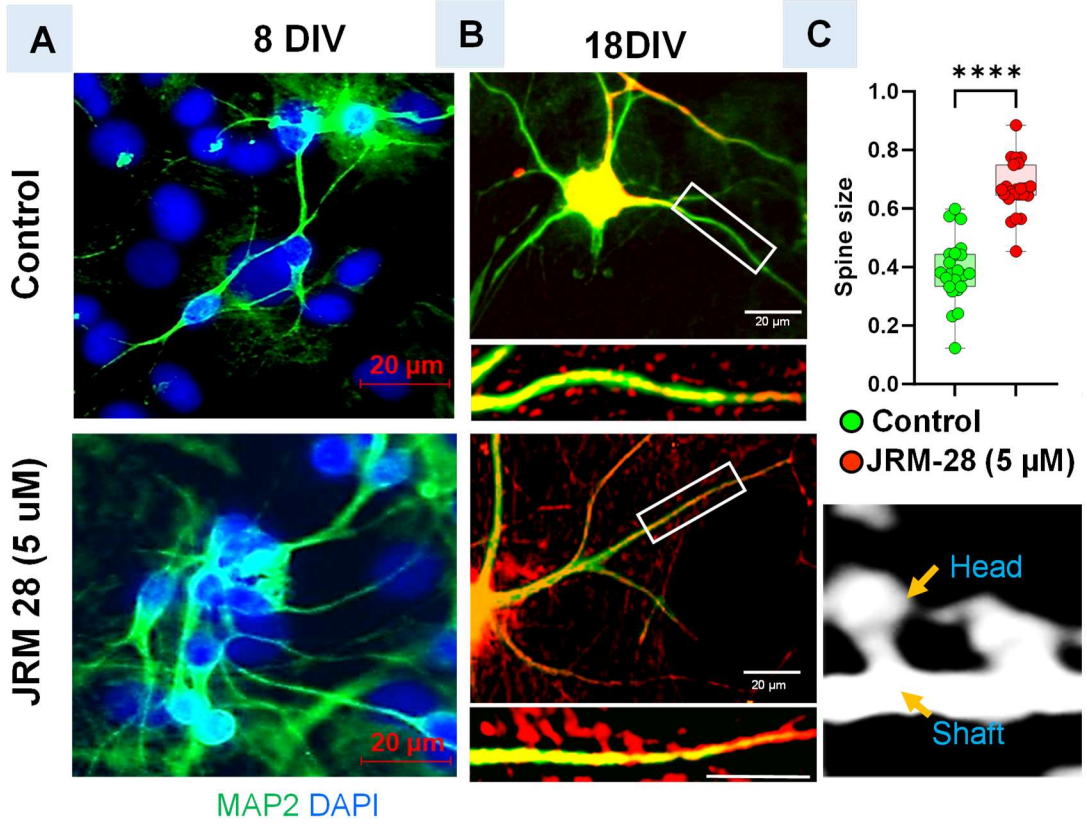
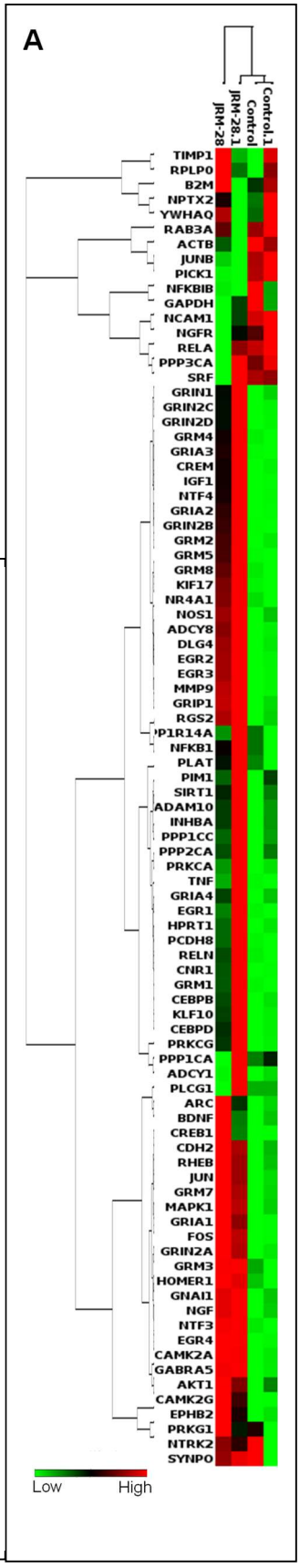
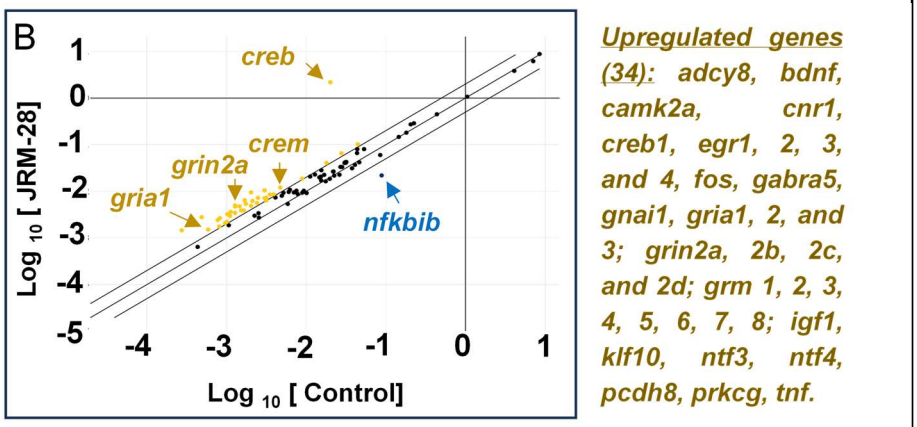


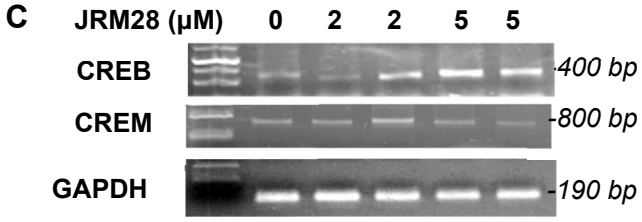
Figure 25: Effect of JRM-28 on E18 Mouse Primary Hippocampal Neurons, (A) E18 mouse primary neurons were grown in complete neurobasal media for 7 days in vitro (DIV). After that, 5 µM JRM-28 was treated for 24 hrs followed by IF analysis of MAP2 (Green). Nuclei were stained with DAPI. For spine analysis, E18 neurons were grown in 18 DIV. Alexa 640-tagged Phalloidin staining (Red) was performed together with MAP2 (green) to visualize dendritic spines on the dendrites in control and 5 µM JRM-28-treated neurons (B). The image was captured in 100X objective after oil immersion followed by visualizing in LSM Zeiss image browsing software at 400X magnification. (C) Spine size was measured following the measurement of the ratio between the MFI of the spine head and the MFI of the spine shaft as described in the adjacent image and method. Spines were considered to be mature if the ratio was≥ 0.6 µm. Unpaired t-test generated ****p< 0.00001 versus control. Results are confirmed with mean ± SD of three different experiments.

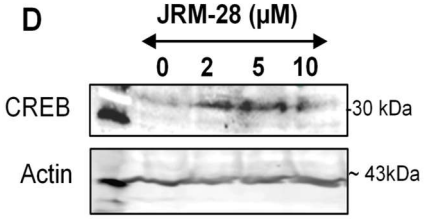
Next, the effect of JRM-28 on the upregulation of MAP2 was investigated in embryonic (E18) mouse primary hippocampal neurons (18 days in vitro). Accordingly, our immunocytochemical analysis (Figure 25A) demonstrated that 48 h of incubation with 5 µM JRM-28 significantly upregulated the synthesis of MAP2-ir basal dendrites in hippocampal neurons. Synthesis and maturation of dendritic spines on the surface of dendrites also regulated the morphological plasticity of hippocampal neurons. However, the





Upregulated genes (34): adcy8, bdnf, camk2a, cnr1, creb1, egr1, 2, 3, and 4, fos, gabra5, gnai1, gria1, 2, and 3; grin2a, 2b, 2c, and 2d; grm 1, 2, 3, 4, 5, 6, 7, 8; igf1, klf10, ntf3, ntf4, pcdh8, prkcg, tnf.





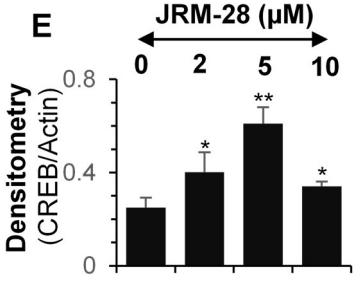


Figure 26: JRM-28 stimulates transcriptional activity of CREB via inhibition of HDAC2. SHSY5Y neurons were cultured, differentiated, treated with different doses of JRM-28 for 24 hrs, and then analyzed for PCR, immunoblot, dual IF, and firefly/renilla dual luciferase reporter assay. (A) A cDNA-based array for 88 CREB and CREB-dependent genes were performed in a commercially available array kit (RT2 Profiler PCR Array for human synaptic plasticity; Qiagen: Cat # PAHS-126-EZ). The Ct data were uploaded in Qiagen's web analysis server. The result was summarized by (A) Heatmap and (B) Scatter plot analyses. Thirty-eight genes including CREB were found to be upregulated. (C)Semi-quantitative RT-PCR analyses for CREB family of genes including creb and crem. The 100 bp DNA ladder was run to identify the amplified products of these genes. The gapdh gene was included as the housekeeping gene. (Supplementary Fig. 18 for raw PCR gel) (BD) Immunoblot analysis of CREB (top) and beta-actin (bottom) in SHSY5Y cells treated with increasing doses of JRM-28. (Supplementary Fig. 18 for raw blot). (E) The band intensity was measured in ImageJ software and then normalized with the respective band density of beta-actin. *p<0.05 (=0.0324), **p<0.01 (=0.0031), *p<0.05 (=0.0477) vs. control.

spine maturation can be best assessed in hippocampal neurons after 18 DIV growth condition Therefore, E18 mouse hippocampal neurons were first dissected from E18 fetal brain, grown in complete neurobasal media for 18 days, and treated with either DMSO control (Figure 25B top) and 5 μM of JRM-28 (Figure 25B bottom) for 48 h followed by the evaluation of dendritic spines by MAP2 and phalloidin dual-labeling. Dual immunostaining followed by a quantitative estimation of spine size by a scatter boxplot analysis (Figure 25C) indicated that JRM-28, but not the control, significantly induced the maturation of spines with increased head-to-shaft ratio (>0.6 μm). Our results suggest that JRM-28 augments structural plasticity by enhancing dendritic morphogenesis and spine maturation in hippocampal neurons.

3.10. Investigation for the Involvement of CREB in JRM-28-mediated Enhancement of Morphological Plasticity

Previous reports suggest that the cAMP response element binding protein CREB plays a pivotal role in the induction of morphological plasticity. A cDNA-based array for 88 CREB and CREB-dependent genes were performed in a commercially available array kit (RT2 Profiler PCR Array

for human synaptic plasticity; Qiagen: Cat # PAHS-126-EZ). The Ct data were uploaded in Qiagen's web analysis server. The result was summarized by (A) Heatmap Accordingly, RT2profiler PCR array™ analysis of CREB family genes and CREB-dependent plasticity-associated genes (Figure 26A & 26B) indicated that 5 μM JRM-28 strongly upregulated the expressions of creb gene and 37 other CREB-dependent genes. To further confirm the effect of JRM-28 on the expressions of plasticity-associated neuronal genes CREB-family genes, we performed by gene expression analyses (Figure 26A) of creb and its other family member crem (cAMP responsive element modulator) in SHSY5Y neuronal cells.

Accordingly, semi-quantitative RT-PCR analyses revealed that increasing concentrations of JRM-28 upregulated the mRNA expression of creb 5 μM, whereas 2 and 5 μM of JRM-28 failed to upregulate the expression of crem. Interestingly, crem gene was found to be marginally but significantly(for significance, the cut-off>2 fold compared to control) upregulated according to cDNA array analysis. However, according to scatter plot analysis (Figure 26B) followed by PCR study (Figure 26C), the expression of CREB was observed to be the most significant. Therefore, combining cDNA array and PCR data, we confirmed that the upregulation of CREB could be the direct target after HDAC2 inhibition by JRM-28. Moreover, immunoblotting (Figure 26D) followed by densitometric (Figure 26E) analysis further confirmed that increasing concentrations of JRM-28 upregulated the expression of CREB protein. These results suggest that suppression of HDAC2 activity could specifically upregulate the transcription of creb but not its other gene family members.

3.11. Relationship Study Between HDAC2 Inhibition by JRM-28 and CREB Expression

To explore the effect of JRM-28-mediated inhibition of HDAC2 in respect to transcriptional upregulation of CREB, a series of experiments followed by quantitative analyses were carried out that indicated that the downregulation of HDAC2 by JRM-28 plays a critical role in the upregulation of CREB. First, a dual immunofluorescence analysis (Figure 27A) of HDAC2 and CREB demonstrated that the treatment with 5 µM JRM-28 significantly attenuated the expression

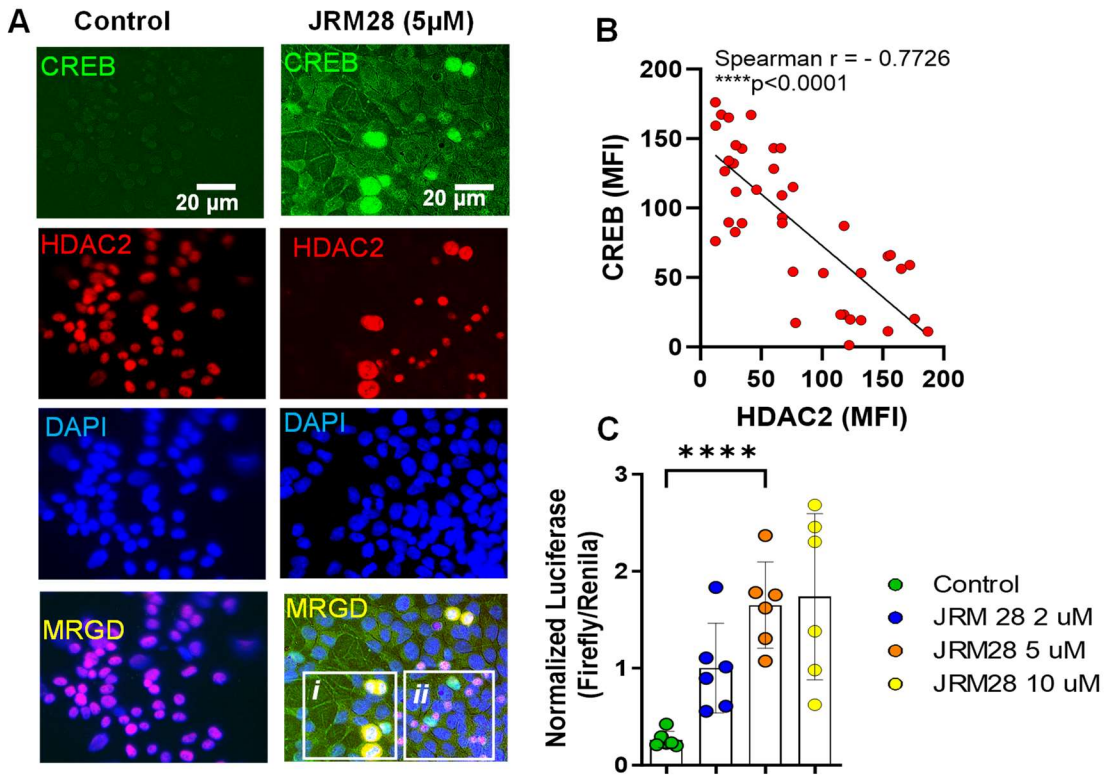


Figure 27: JRM-28 upregulates CREB expression (A) Dual IF analysis of CREB (Green) and HDAC2 (Red) in control and 5 µM JRM-28-treated SHSY5Y cells. Nuclei were stained with DAPI. (Inset) Enclosed boxes magnified to estimate the relative distribution of CREB and HDAC2 for (i) cytosolic HDAC2 (CytHDAC2) and CREB as well as (ii) nuclear HDAC2 (NucHDAC2) and CREB. (B) A non-parametric Spearman correlation analyses in 40 randomly selected dual-stained cells with CREB and HDAC2 were considered for MFI calculations followed by correlation statistics. The non-parametric correlation was considered once the dataset failed to pass the normality test. (C) The firefly cre luciferase assay was per-formed in 2,5,10 µM JKRM28 treated SHSY5Y cells, normalized with renilla luciferase, and then offset with negative control. The normalized luciferase was plotted as a dotted histogram. One-way ANOVA demonstrated F3,20 =9.731;****p<0.0005 (= 0.0004). Results are confirmed with mean ± SD of three different

of HDAC2 in the nuclei of SHSY5Y cells. Interestingly, analyzing the subcellular distribution of

HDAC2 further indicated that the expression of CREB was only observed in cells with no HDAC2 or cells with inactive cytosolic HDAC2 (Figure 27Ai). On the contrary, cells with active and nuclear HDAC2 displayed a very marginal to no CREB immunoreactivity (Fig. 27Aii) suggesting that the JRM-28-mediated inactivation of HDAC2 was associated with the upregulation of CREB expression. A non-parametric Spearman correlation analysis (Figure 27B) between the mean fluorescence intensity (MFI) of CREB and that of HDAC2 further demonstrated a strong negative correlation suggesting that the suppression of HDAC2 expression by JRM-28 upregulated the expression of CREB protein. Finally, a dual (renilla/firefly) CRE-luciferase reporter assay (Figure 27C) clearly indicated that increasing doses of JRM-28 upregulated the CREB-driven reporter activity, suggesting that the HDAC2 inhibition by JRM-28 not only upregulated the expression but also stimulated the transcriptional activity of CREB.

3.12. Assessment of the Connectivity Between Ca2+ Influx and JRM-28 Treatment

The cDNA analyses demonstrated that JRM-28 treatment significantly upregulated genes those are essential for calcium ion transmission in neurons such as genes for ionotropic NMDA receptors (grin2a, 2b, 2c, and 2d) and ionotropic AMPA receptors (gria 1, 2, and 3). NMDA- and AMPA-driven calcium influx through metabotropic these ionotropic calcium channels directly control the morphological plasticity in post-synaptic hippocampal neurons.[146] Recent studies indicated that upon activa-tion,[147] CREB upregulates expressions of critical subunits of NMDA and AMPA receptors, such as Grin2a or NR2A, a critical subunit of NMDA receptor and Gria1 or GluR1, a functional subunit of AMPA receptor. Accordingly, our IF studies followed by MFI analyses

indicate that 5 µM JRM-28 upregulated expressions of both NR2A (Figure 28A & 28C) and GluR1 (Fig. 28B & 28D) in E18 mouse hippocampal neurons.

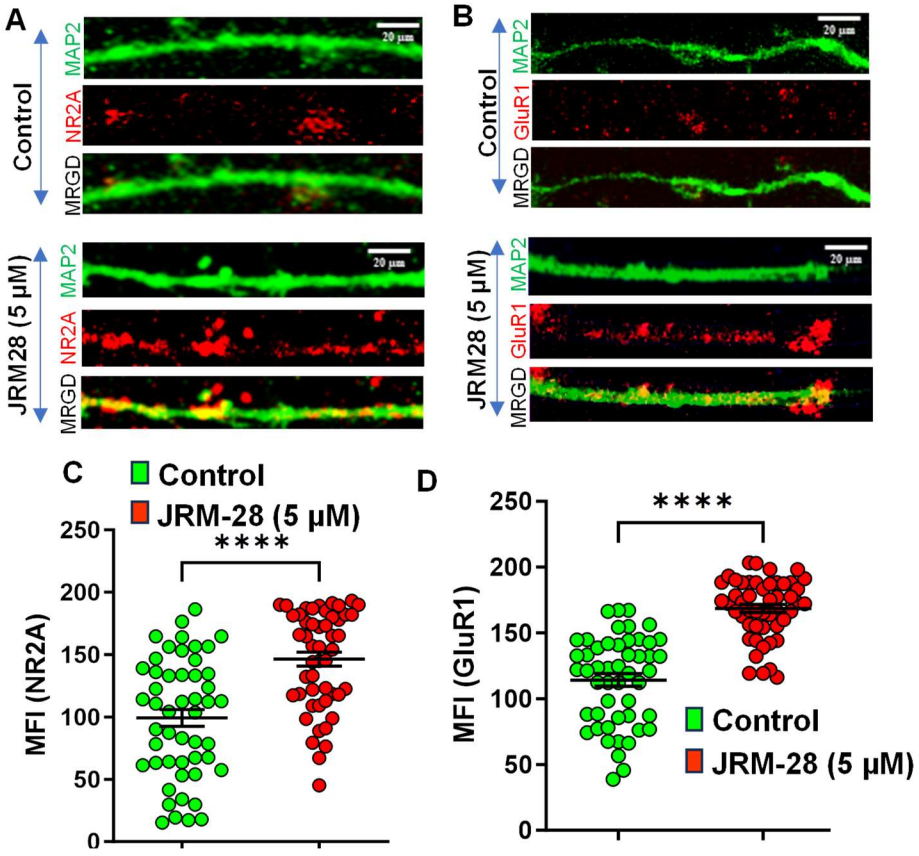


Figure 28: **JRM-28 enhances post-synaptic calcium influx in E18 mouse primary hippocampal neurons.** Mouse primary hippocampal neurons were generated from E18 fetal brains as described in the method section. After 18 days of differentiation, these neurons were treated with 5 µM of JRM-28 for 48 hrs and then analyzed for IF and calcium influx assay. The representative images demonstrate dual IF analyses of (**A**)MAP2 (green) plus NMDA receptor subunit NR2A(red); and (**B**) MAP2 (green) plus AMPA receptor subunit GluR1 (red). Nuclei were stained with DAPI (blue). (**C**) MFIs (Mean fluorescence intensities) of NR2A and (**D**) GluR1 were calculated in ImageJ software in 50 different NR2A-ir and GluR1-ir receptors (as shown in red-colored dense bodies) per group and then plotted as dotted histograms. An unpaired t-test was adopted to test the significance of the mean between groups resulting in $^{****}p<0.0001$ versus control (t=5.334; df =98) in NR2A analysis and $^{****}p<0.0001$ versus control(t=9.608; df =98) for GluR1.

Since upregulations of proteins do not necessarily correlate with the function of the receptor, next we were interested in studying if JRM-28 stimulated the NMDA- and AMPA-sensitive calcium influx in primary hippocampal neurons. A dose-dependent calcium influx study was performed in E18 hippocampal neurons at 100 repeats of 0.1 s intervals after 24 hrs of treatment with 2,5, and

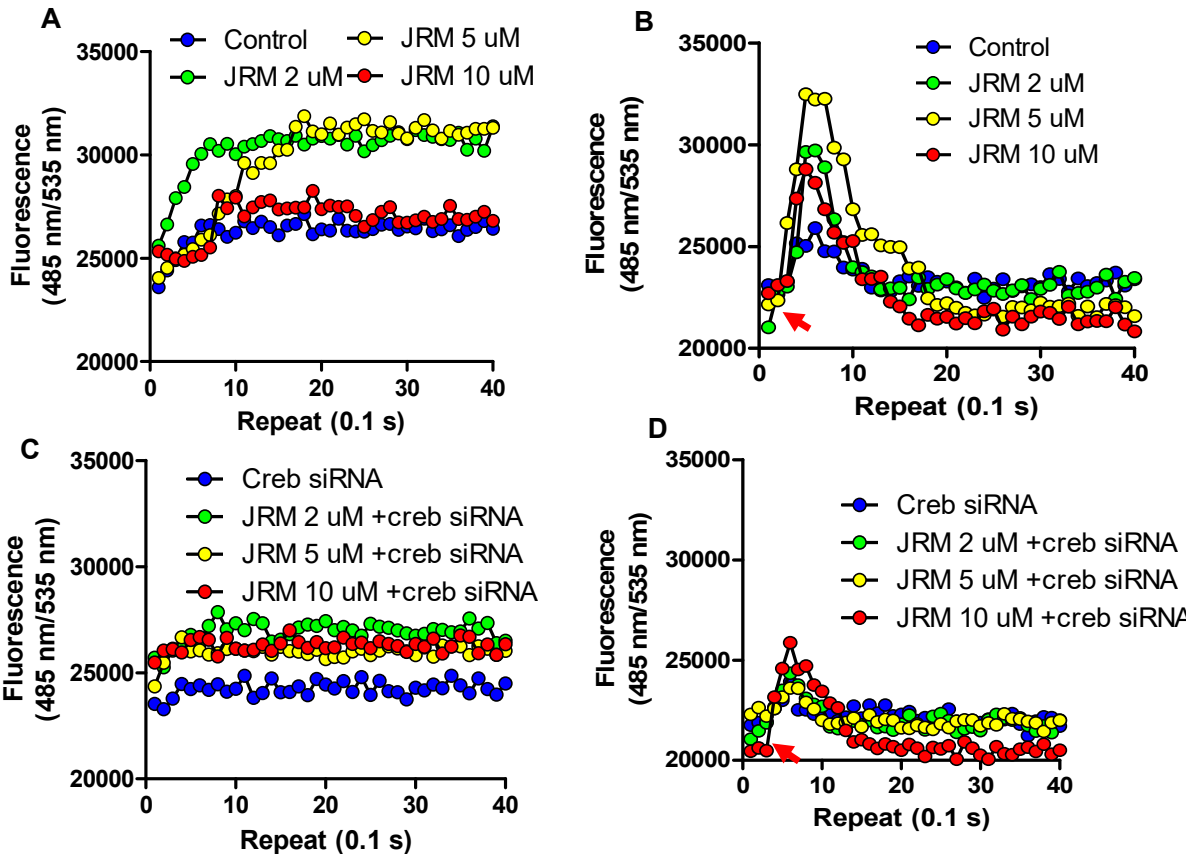


Figure 29: Effect of JRM-28 on Ca2+ influx on SHSy5Y cells (A) Ionotropic calcium assay was performed in hippocampal neurons with increasing doses of JRM-28. Recording started 0.1 s after the addition of 20 µM NMDA via a dual pump autoinjector and the kinetic plot was recorded at Ex: Em 485:535 nm filter set at 0.1s interval for 100 readings. The result was normalized with the baseline and plotted as a linear scale. (B) AMPA-driven calcium influx assay in hippocampal neurons treated with 2, 5, and 10 µM of JRM-28. The recording was performed at a 0.1 sec time interval for 100 repeats following the addition of 20 µM AMPA. (C) Hippocampal neurons were transfected with creb siRNA for 24 hrs followed by the treatment with different doses of JRM-28 for another 24 hrs. After that, an NMDA-sensitive calcium influx assay was performed. (D) AMPA-sensitive calcium entry assay was measured in creb siRNA-transfected hippocampal neurons after the treatment with increasing doses of JRM-28.

10 µM of JRM-28 treatment. Interestingly, a real-time calcium influx study indicated that

increasing doses of 5µM JRM-28 strongly upregulated the NMDA-(Figure 29A) and AMPA-(Figure 29B) sensitive calcium influx in mouse primary hippocampal neurons at 5 µM. The optimum dose of JRM-28 for the calcium influx was found to be 5 µM as the higher concentration may desensitize the receptor to prevent uncontrolled calcium entry. According to previous reports,[146]

CREB plays a vital role in the augmentation of NMDA- and AMPA-driven metabotropic ionotropic calcium influx through the dendritic spines of hippocampal neurons. Hence, the direct role of CREB was next evaluated in JRM-28-stimulated calcium influx through NMDA and AMPA receptors. Accordingly, the knocking down of creb gene expression by creb siRNA was found to significantly abrogate the NMDA- (Figure 29C) and AMPA- (Figure 29D) driven calcium influx in JRM-28-stimulated hippocampal neurons suggesting the essential role of CREB in JRM-28-mediated metabotropic ionotropic calcium influx in hippocampal neurons. The role of NMDA receptor-driven calcium influx in the augmentation of synaptic plasticity is often debated for its cytotoxic response. To

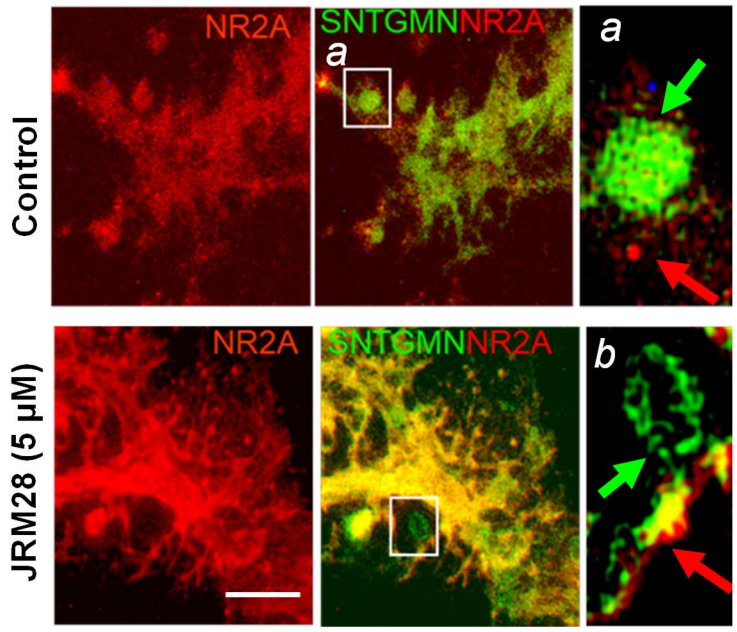


Figure 30: Pre-synaptic protein synaptotagmin was dual labelled with NR2A. The enhanced interaction between these two proteins may represent augmented synaptic transmission. (a) In control cell, synaptotagmin-ir endocytic membrane fold (circular) is found to be present near the post-synaptic NMDA receptor (red dot; NR2A). (b) Synaptotagmin-ir Endocytic membrane complex was found to be latched on NR2A-ir 9(red) NMDA receptor in JRM-28 (5 µM) -treated neuron. Scale bar = 5 µm. Results are confirmed after three independent experiments.

nullify that possibility, we performed a dual immunolabeling analysis of pre-synaptic protein synaptotagmin and post-synaptic NMDA receptor protein NR2A (Figure 30) in 18 DIV hippocampal neurons. During calcium transmission through vesicle, the synaptotagmin-ir pre-synaptic membrane fold is expected to interact with NR2A-ir post-synaptic NMDA receptor. Interestingly, we observed that JRM-28 treatment, but not control, facilitates the interaction of endocytic membrane with the post-synaptic NMDA receptor suggesting that 5 μM JRM28 treatment augments dendritic strength via induction of NMDA-dependent calcium current.

3.13. Investigation on the JRM-28-Mediated Augmentation of Neuroplasticity in iPSC-derived AD neurons via activation of CREB

Alzheimer's disease (AD) is a progressive neurodegenerative disease in the mid-brain that severely impairs the hippocampal function of learning and memory.[148]

During the progression of AD, neuronal cells of the cortex and hippocampus suffer loss in synaptic function and dendritic morphologies[148,149] resulting in neurocognitive impairments. Next, we examined the effect of JRM-28 on improving the morpho-logical plasticity in AD neurons. These neurons were derived from neural stem cells (NSCs) of a 31-year-old female AD patient having A246E pathogenic mutation at the psen1 gene. These NSCs were derived from induced pluripotent stem cells (iPSCs) after reprogramming of skin fibroblast cells and obtained commercially from AXOL Bio-science (Edinburgh, UK). NSCs were maintained and differentiated into neurons as described in the method section. Next, we were interested in studying if JRM-28-mediated suppression of HDAC2 upregulated the expression of CREB in these AD neurons. Interestingly, a dual IF assay of CREB and HDAC2 (Figure 31A) supported by a negative Pearson correlation analysis (Figure 31B) indicated that upon treatment with 5 μM JRM-28 for 24 hrs, iPSC-derived

AD neurons exhibited a strong upregulation of CREB coupled with a significant downregulation of HDAC2. Interestingly, a similar dual IF analysis (Figure 31C) of HDAC2 and MAP2 indicated

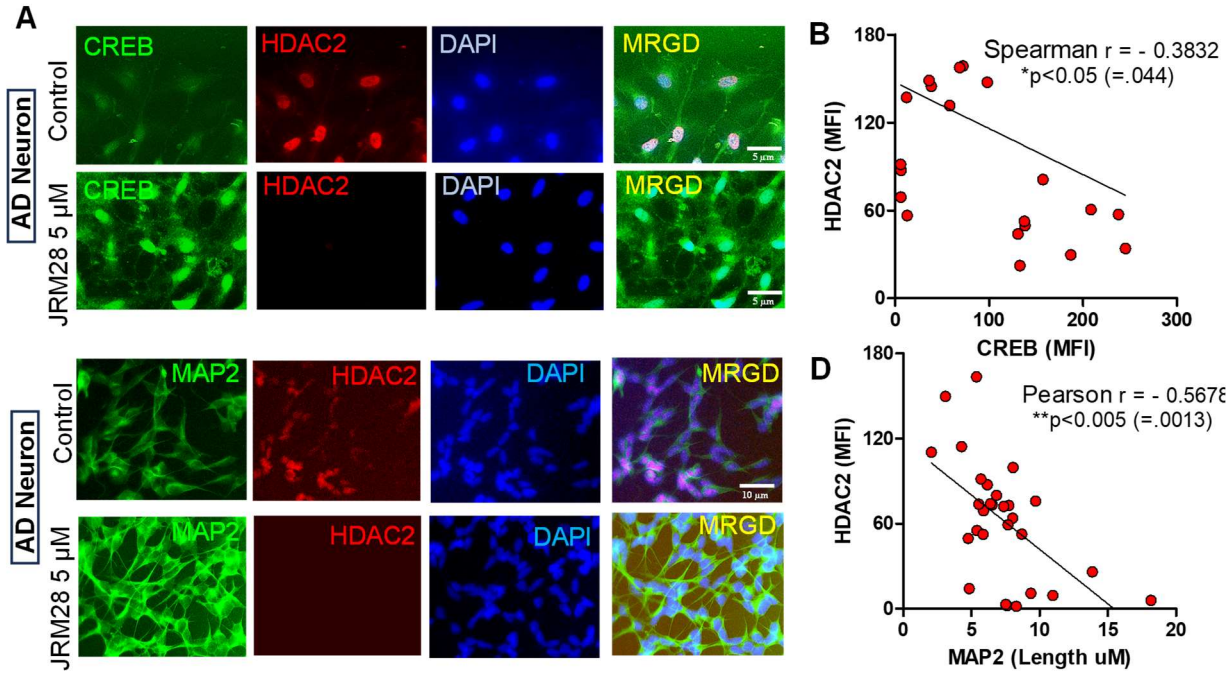


Figure 31: The effect of JRM-28-mediated suppression of HDAC2 on the upregulation of CREB and MAP2 in AD neurons with A246E psen1 mutation. AD neurons were differentiated from iPSC-derived neural stem cells (NSCs) in a conditional neurobasal media as described in the method section. AD neurons were stimulated with 5 µM of JRM-28 for 48 hrs and then immunolabeled. (A) The rep-resentative image exhibits a dual IF analysis of CREB (green) and HDAC2(red). Nuclei were stained with DAPI (blue). (B) A non-parametric Spearman correlation analysis of mean fluores-cence intensities (MFIs) was performed between CREB and HDAC2. The resultant scatter plot displays a moderate negative correlation (*p<0.05). A total of 30 random neurons were selected from 6 different images (3 images per group) in this analysis. MFI was calculated in ImageJ soft-ware, the raw values were recorded, and the derived dataset was analyzed for the normality test in GraphPad Prism 8 software. Spearman correlation analysis was decided once the dataset failed to pass the D'Agostino & Pearson normality test. (C) A representative dual IF image of MAP2 (green) and HDAC2 (red). Nuclei were labeled with DAPI (blue). (D) A parametric Pearson cor-relation statistic of MFIs between HDAC2 and MAP2 was performed after the normality test was successfully executed in GraphPad Prism 8 software. A total of 30 neurons from 6 independent images (3 images /group) were selected in this analysis. Results are confirmed after three different experiments.

that JRM-28-mediated downregulation of HDAC2 was found to increase the length of MAP2-ir

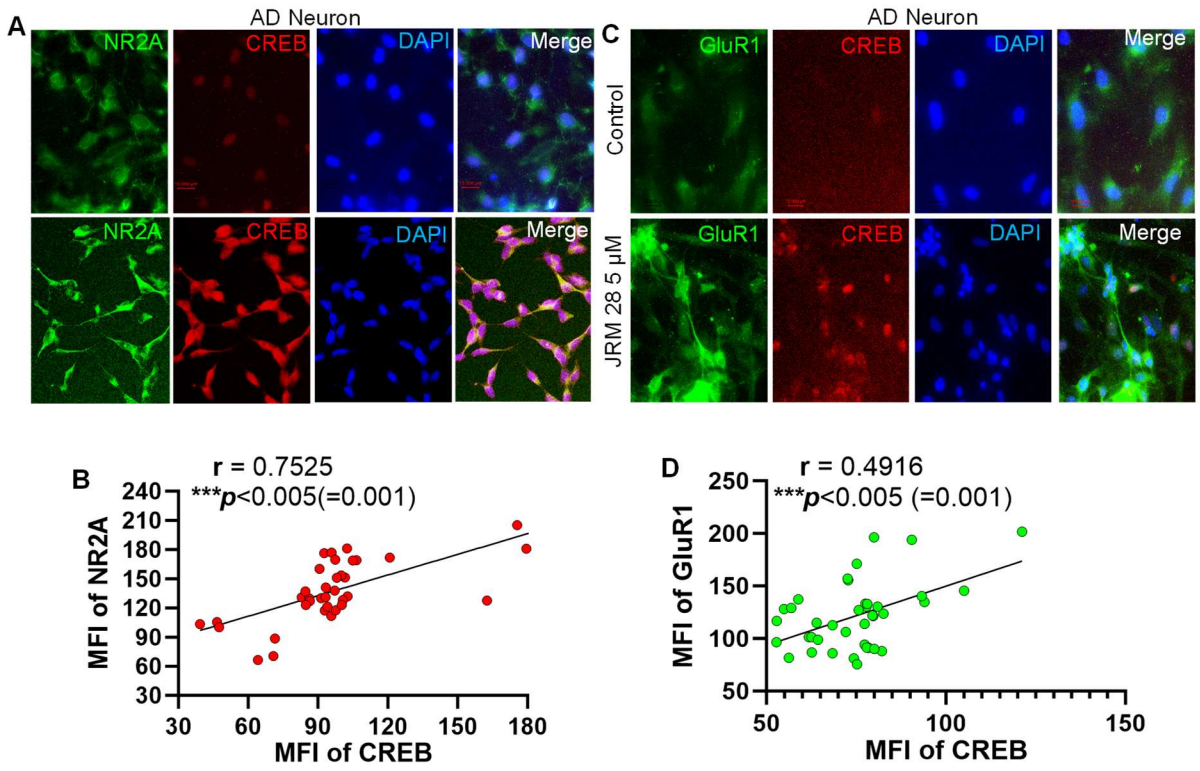


Figure 32: The effect of JRM-28-mediated activation of CREB on the upregulation of NR2A, and GluR1 and in-duction of metabotropic ionotropic calcium entry in AD neurons. AD neurons were differenti-ated from iPSC-derived neural stem cells (NSCs) as described under the method section followed by the treatment with 5 µM of JRM-28 for 48 hrs, and then analyzed for IF and calcium influx assay. (A) The representative image exhibits a dual IF analysis of NR2A (green) and CREB (red). Nuclei were stained with DAPI (blue). (B) A non-parametric Spearman correlation analysis of mean flu-orescence intensities (MFIs) was performed between CREB and NR2A. The resultant scatter plot displays a strong positive correlation (***p<0.005). A total of 30 random neurons were selected from 6 different images (3 images per group) in this analysis. MFI was calculated in ImageJ soft-ware, the raw values were recorded, and the derived dataset was analyzed for the normality test in GraphPad Prism 8 software. Spearman correlation analysis was decided once the dataset failed to pass the D'Agostino & Pearson normality test. MFI measurement was restricted to cell bodies only. (C) A representative dual IF image of GluR1 (green) and CREB (red). Nuclei were labeled with DAPI (blue). (D) A parametric Pearson correlation statistic of MFIs between CREB and GluR1 was performed after the normality test was successfully executed in GraphPad Prism 8 software. A total of 30 neurons from 6 independent images (3 images /group) were selected in this analysis. Results are confirmed after three different experiments.

basal dendrites in these AD neurons. Moreover, a Pearson correlation analysis (Figure 31D)

between the MFI of HDAC2 and the dendritic length of basal dendrites reiterated that the downregulation of HDAC2 is indeed involved in the augmentation of dendritic morphogenesis in these AD neurons. To further evaluate the effect of CREB on JRM-28-induced morphological

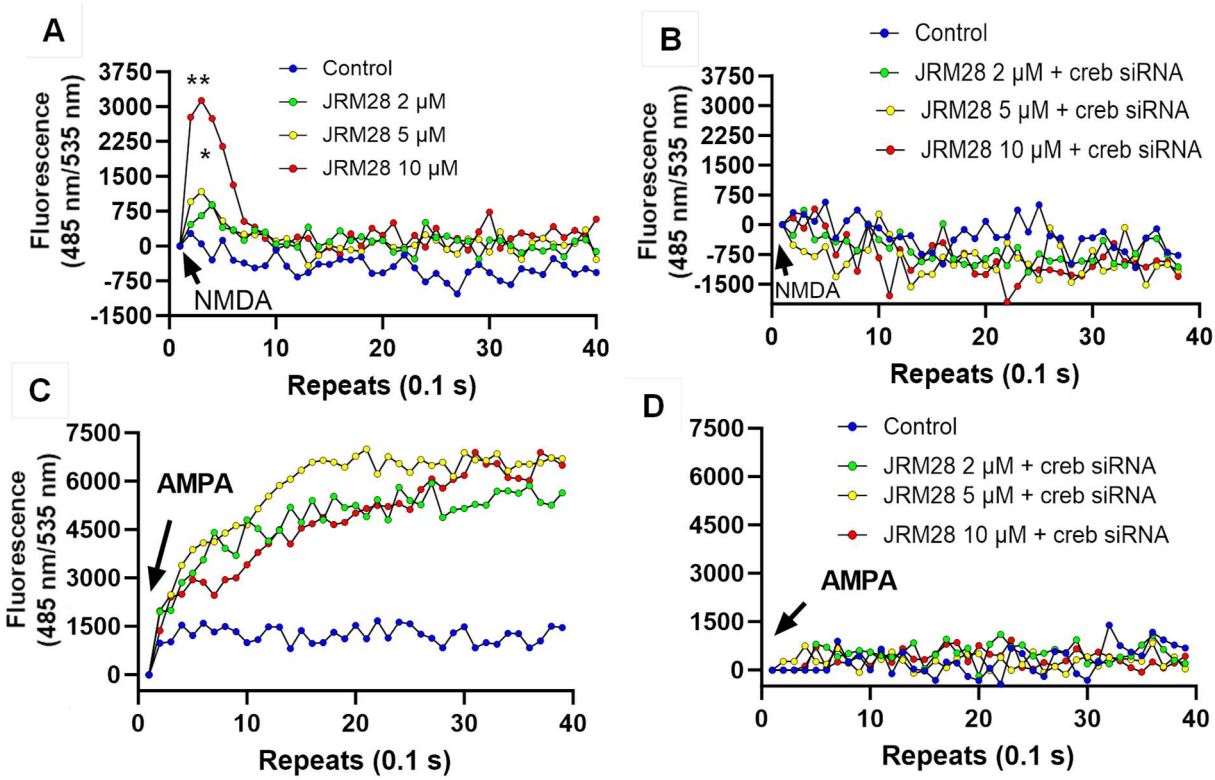


Figure 33: The effect of JRM-28-mediated activation of CREB on in-duction of metabotropic ionotropic calcium entry in AD neurons. (A) Metabotropic Ionotropic calcium assay was performed in AD neurons with increasing doses of JRM-28. Recording started 0.1 s after the addition of 20 µM NMDA via a dual pump autoinjector and the kinetic plot was recorded at Ex: Em 485:535 nm filter set at 0.1s interval for 100 readings. The result was normalized with the baseline and plotted as a logarithmic scale. *p<0.05 and **p<0.01 versus maximum fluorescence value of control reading. (C) AMPA-driven calcium influx assay in AD neurons treated with 2, 5, and 10 µM of JRM-28. The recording was performed at a 0.1 sec time interval for 100 repeats following the addition of 20 µM AMPA. (B) AD neurons were transfected with the creb siRNA for 24 hrs followed by the treatment with different doses of JRM-28 for another 24 hrs. After that, an NMDA-sensitive calcium influx assay was performed. (H) AMPA-sensitive calcium entry assay was measured in creb siRNA-transfected AD neurons after the treatment with increasing doses of JRM-28. Results are confirmed after three independent experiments.

plasticity, a dual IF analysis of CREB was performed with NMDA receptor subunit NR2A (Figure 32A) or AMPA receptor subunit GluR1 (Figure 32C). Interestingly, these immunolabeling studies followed by correlation analyses (Fig. 32B & 32D) clearly indicated that JRM-28-mediated upregulation of CREB truly augmented the expressions of metabotropic ionotropic calcium receptors in dendrites of AD neurons. While studying the dose-dependent effect of JRM-28 on metabotropic ionotropic calcium influx, we ob-served significant upregulations of both NMDA- (Figure 33A) and AMPA- (Figure 33C) driven calcium entry in AD neurons. According to that analysis, JRM-28 displayed a dose-dependent increase of NMDA-driven calcium entry significantly high at 5 μM dose with a maximum at 10 μM concentration. On the other hand, we observed a strong AMPA-driven calcium influx at 5 μM dose. To confirm the direct role of CREB in JRM-28-mediated calcium entry, we performed a similar calcium entry assay in creb siRNA-transfected AD neurons. Interestingly, knocking down of CREB expression by creb siRNA strongly attenuated both NMDA- (Figure 33B) and AMPA- (Figure 33D) induced calcium entry in JRM-28-treated AD neurons suggesting the essential role of CREB in JRM-28-mediated calcium entry in AD neurons.

Taken together, our current study highlights the discovery of a novel HDAC2 in-hibitor JRM-28, and its potential role in inducing neuronal plasticity via activation of CREB.

4.0. Discussion

Previous studies indicated that suppression of HDAC2 activity by small-molecule therapeutics might display beneficial effects in the improvement of neurocognitive function[150,151]and the amelioration of AD pathologies[152] such as the removal of amyloid plaque burden and the attenuation of Tau pathologies.[153] Although the molecular mechanism is still unclear, the role of HDAC2 suppression in inducing morphological plasticity such as promoting synaptic transmission and augmenting dendritic morphogenesis should be studied with prime importance. However, the major challenge is the highly overlapping structural similarities of all class-I HDACs, which makes it difficult to identify a selective inhibitor of HDAC2.

4.1. Synthesis

Based on the early synthesized lead compound MJM-1, we initially synthesized three series of analogs with ester, ketones and amide cap groups to develop HDAC2 selective inhibitors. The yields varied within the range of 60% to 80%. Cap groups with bulky hydrophobic moiety usually had lower yields which can be attributed by the unfavorable nucleophilic attack by the LDA, generated during the course of Aldol condensation reaction. After screening all the compounds against purified HDAC2, we selected four best inhibitors from each series (JRM-9, JRM-11 and JRM-20 including the MJM-1), and modified the disulfide linkers to the monosulfide moieties and conducted molecular docking study. The docking score interestingly showed better binding to the HDAC2 catalytic domain and motivated us to make the analogs which resulted in the formation of JRM-21 to JRM-24. In HDAC-2 inhibition study, the monosulfoxide JRM-20 (the N-methyl acetanilide cap group analog) showed the highest inhibition and led us to make the disulfoxide analog of JRM-20. Literature study and NMR analysis confirmed that the disulfide is chemically

very unstable and readily converted to the monosulfone compound (JRM-28).[140] The JRM-28 displayed the highest HDAC-2 inhibition among all the compounds that we have synthesized so far.

4.2. JRM-28 is a selective HDAC2 inhibitor

Previous studies indicated that suppression of HDAC2 activity by small-molecule therapeutics might display beneficial effects in the improvement of neurocognitive function[150,151] and the amelioration of AD pathologies[154] such as the removal of amyloid plaque burden[155] and the attenuation of Tau pathologies. Although the molecular mechanism is still unclear, the role of HDAC2 suppression in inducing morphological plasticity such as promoting synaptic transmission and augmenting dendritic morphogenesis should be studied with prime importance. However, the major challenge is the highly overlapping structural similarities of all class-I HDACs, which makes it difficult to identify a selective inhibitor of HDAC2. In our current manuscript, we report the synthesis and characterization of a novel HDAC2 inhibitor termed JRM-28 followed by evaluating its effect in promoting morphological plasticity in hippocampal neurons. JRM-28 is a macrocyclic compound, which is de-signed and synthesized to satisfy the structural determinants of a classical HDAC in-hibitor with an N-methyl acetalide “caphead” group, a lipophilic “linker”, and a sulfur-containing ZBG. Originally, JRM-28 was synthesized as a prodrug, which is a di-mer of two monomeric units with a disulfide linkage and one sulfur unit was oxidized twice. Based on 13CNMR, 1HNMR, and LC-MS analyses, it was found that upon re-duction, JRM-28 was derivatized to JRM-28a, a monomer with sulfonate (-SO2H) group, and JRM-28b, another monomer with sulfhydryl (-SH) group. both JRM-28a and 28b were evaluated for HDAC2 inhibition by luminescence and fluorimetric in-hibitor screening strategies. A dose-responsive

ligand binding assay with purified HDAC2 revealed that JRM-28a was a stronger inhibitor (IC50=0.28 μM) of HDAC2 than JRM-28b (IC50 =2.713 μM). Moreover, a fluorimetric binding assay with purified HDAC1, HDAC2, HDAC3, and HDAC6 followed by the comparative analyses of IC50 values and hillslopes of sigmoidal binding curves further indicated that JRM-28a could be a selective inhibitor only to HDAC2, but not other HDACs. An in-silico docking simulation study once more indicated that JRM-28a was strongly docked in the cata-lytic pocket of HDAC2, whereas weaker docking was observed while analyzing the interaction between JRM-28a and HDAC4, a class-II HDAC.

4.3. JRM-28 displays a strong neuroprotective response by inducing morphological plasticity in neurons

Before exploring the neuroprotective properties of JRM-28, different cellular as-says confirmed that a 5 μM dose of JRM-28 significantly attenuated the activation of HDAC2 without causing any cell death. While exploring the molecular changes in neurons, the most striking observation was the upregulated synthesis of apical den-drites in SHSY5Y neurons upon treatment with 5μM of JRM-28. Dendritic morpho-genesis is an integral mechanism of morphological plasticity. Being intrigued by the initial observation, we repeated the same experiment in E18 mouse primary hippo-campal neurons which further demonstrated that JRM-28 indeed induced dendritic morphogenesis in hippocampal neurons. When applied to the fully differentiated hippocampal neurons, we observed that JRM-28 strongly induced the maturation of dendritic spines. Dendritic spines are the home of metabotropic ionotropic calcium receptors playing a direct role in post-synaptic neurotransmission. Accordingly, we observed that JRM-28 not only upregulated expressions but also dose-dependently induced calcium influx through these receptors.

4.4. The JRM-28-mediated inactivation of HDAC2 triggers the transcriptional activation of CREB

A growing body of evidence[156,157] suggests that the transcriptional activation of CREB plays a central role in regulating morphological plasticity).[133] Several plasticity-associated genes contain multiple cAMP response elements (CRE) in their promoter region.[146,153,158] While studying the role of JRM-28 in the regulation of CREB, we observed that JRM-28 dose-dependently induced the expression and the transcriptional activity of CREB. Moreover, we observed a strong association between the JRM-28-mediated inactivation of HDAC2 and the upregulation of CREB suggesting the direct role of HDAC2 inactivation in the augmentation of CREB's transcriptional activity. However, Two other members of CREB family proteins including activating transcription factor-1 (ATF-1) and cAMP responsive element modulator (CREM) are also activated in response to several CREB-inducing molecular factors including cAMP, calcium, and mitogenic stimuli.[159] Therefore, along with the evaluation of the transcriptional activity of CREB, the effects of JRM-28 on the regulations of CREM and ATF-I were also scrutinized. Interestingly, JRM-28-mediated inactivation of HDAC2 was observed to upregulate the expression of CREB only, but not CREM and ATF-1.

4.5. JRM-28 upregulates neuronal plasticity in AD neurons

It is believed that neuronal plasticity decreases in neurons of the AD brain. Recent studies indicate that the markers of morphological plasticity such as spine density,[160] dendritic arbors, and post-synaptic neurotransmission are severely impaired in the hippocampal neurons of AD patients. Therefore, identifying a therapeutic strategy to induce morphological plasticity in AD is an important area of research.[160] To address this challenge, JRM-28 was applied to the AD neurons

generated from iPSC-derived NSCs of a 31-year-old female AD patient with an A246E mutation at the psen1 gene.

Here, we delineated that upon 48 hrs of stimulation with JRM-28, the molecular markers of post-synaptic neurons such as NR2A and GluR1 were strongly upregulated in AD neurons. As a result, we observed that JRM-28 stimulated the metabotropic ionotropic calcium entry in cultured AD neurons suggesting that similar to primary hippocampal neurons, JRM-28 is also capable of inducing neuronal plasticity in AD neurons. While exploring the molecular mechanism, we observed that JRM-28-mediated inactivation of HDAC2 induced the expression of CREB in AD neurons. The elevated nuclear translocation of CREB demonstrated its elevated transcriptional activity and as a result, the expressions of CREB-dependent proteins such as NR2A and GluR1 were upregulated. Moreover, JRM-28 was found to dose-dependently stimulate the NMDA- and AMPA-driven calcium entry in AD neurons suggesting that JRM-28 not only upregulated the expressions of proteins but also induced post-synaptic neurotransmission. The direct role of CREB in JRM-28-mediated neurotransmission was validated by a gene silencing study when a siRNA-mediated ablation of CREB strongly inhibited JRM-28-stimulated NMDA- and AMPA-driven calcium influx in AD neurons.

In summary, our current literature highlights the discovery of a novel small molecular compound that selectively inhibits HDAC2, but not other HDACs. By inhibiting HDAC2, JRM-28 stimulated the transcriptional activity of CREB and subsequently augmented the downstream events of structural plasticity including dendritic morphogenesis, spine maturation, and neurotransmission through metabotropic ionotropic calcium receptors.

References

1. Handy, D. E., Castro, R. & Loscalzo, J. Epigenetic Modifications. *Circulation* **123**, 2145–2156 (2011).

2. Fedorova, E. & Zink, D. Nuclear architecture and gene regulation. *Biochimica et Biophysica Acta (BBA) - Molecular Cell Research* **1783**, 2174–2184 (2008).

3. Campos, E. I. & Reinberg, D. Histones: Annotating Chromatin. *Annu Rev Genet* **43**, 559–599 (2009).

4. Avery, O. T., MacLeod, C. M. & McCarty, M. STUDIES ON THE CHEMICAL NATURE OF THE SUBSTANCE INDUCING TRANSFORMATION OF PNEUMOCOCCAL TYPES. *Journal of Experimental Medicine* **79**, 137–158 (1944).

5. HOTCHKISS, R. D. The quantitative separation of purines, pyrimidines, and nucleosides by paper chromatography. *J Biol Chem* **175**, 315–32 (1948).

6. Holliday, R. & Pugh, J. E. DNA modification mechanisms and gene activity during development. *Science* **187**, 226–32 (1975).

7. Goto, K. *et al.* Expression of DNA methyltransferase gene in mature and immature neurons as well as proliferating cells in mice. *Differentiation* **56**, 39–44 (1994).

8. Moore, L. D., Le, T. & Fan, G. DNA Methylation and Its Basic Function. *Neuropsychopharmacology* **38**, 23–38 (2013).

9. Kouzarides, T. Chromatin Modifications and Their Function. *Cell* **128**, 693–705 (2007).

10. Völkel, P. & Angrand, P.-O. The control of histone lysine methylation in epigenetic regulation. *Biochimie* **89**, 1–20 (2007).

11. Nitsch, S., Zorro Shahidian, L. & Schneider, R. Histone acylations and chromatin dynamics: concepts, challenges, and links to metabolism. *EMBO Rep* **22**, (2021).

12. Bannister, A. J. & Kouzarides, T. Regulation of chromatin by histone modifications. *Cell Res* **21**, 381–395 (2011).

13. Wang, G. G., Allis, C. D. & Chi, P. Chromatin remodeling and cancer, part II: ATP-dependent chromatin remodeling. *Trends Mol Med* **13**, 373–380 (2007).

14. Mikkelsen, T. S. *et al.* Genome-wide maps of chromatin state in pluripotent and lineage-committed cells. *Nature* **448**, 553–560 (2007).

15. Timmermann, S., Lehrmann, H., Polesskaya, A. & Harel-Bellan, A. Histone acetylation and disease. *Cellular and Molecular Life Sciences* **58**, 728–736 (2001).

16. Park, S.-Y. & Kim, J.-S. A short guide to histone deacetylases including recent progress on class II enzymes. *Exp Mol Med* **52**, 204–212 (2020).

17. Gregoretti, I., Lee, Y.-M. & Goodson, H. V. Molecular Evolution of the Histone Deacetylase Family: Functional Implications of Phylogenetic Analysis. *J Mol Biol* **338**, 17–31 (2004).

18. Ceccacci, E. & Minucci, S. Inhibition of histone deacetylases in cancer therapy: lessons from leukaemia. *Br J Cancer* **114**, 605–611 (2016).

19. Haberland, M., Montgomery, R. L. & Olson, E. N. The many roles of histone deacetylases in development and physiology: implications for disease and therapy. *Nat Rev Genet* **10**, 32–42 (2009).

20. Chuang, D.-M., Leng, Y., Marinova, Z., Kim, H.-J. & Chiu, C.-T. Multiple roles of HDAC inhibition in neurodegenerative conditions. *Trends Neurosci* **32**, 591–601 (2009).

21. Consalvi, S. *et al.* Histone Deacetylase Inhibitors in the Treatment of Muscular Dystrophies: Epigenetic Drugs for Genetic Diseases. *Molecular Medicine* **17**, 457–465 (2011).

22. Glozak, M. A. & Seto, E. Histone deacetylases and cancer. *Oncogene* **26**, 5420–5432 (2007).

23. Bjerling, P. *et al.* Functional Divergence between Histone Deacetylases in Fission Yeast by Distinct Cellular Localization and In Vivo Specificity. *Mol Cell Biol* **22**, 2170–2181 (2002).

24. Gao, L., Cueto, M. A., Asselbergs, F. & Atadja, P. Cloning and Functional Characterization of HDAC11, a Novel Member of the Human Histone Deacetylase Family. *Journal of Biological Chemistry* **277**, 25748–25755 (2002).

25. RUIJTER, A. J. M. de, GENNIP, A. H. van, CARON, H. N., KEMP, S. & KUILENBURG, A. B. P. van. Histone deacetylases (HDACs): characterization of the classical HDAC family. *Biochemical Journal* **370**, 737–749 (2003).

26. Somoza, J. R. *et al.* Structural Snapshots of Human HDAC8 Provide Insights into the Class I Histone Deacetylases. *Structure* **12**, 1325–1334 (2004).

27. Yang, F., Zhao, N., Ge, D. & Chen, Y. Next-generation of selective histone deacetylase inhibitors. *RSC Adv* **9**, 19571–19583 (2019).

28. Wang, X., Wei, X., Pang, Q. & Yi, F. Histone deacetylases and their inhibitors: molecular mechanisms and therapeutic implications in diabetes mellitus. *Acta Pharm Sin B* **2**, 387–395 (2012).

29. Astratenkova, I. V. & Rogozkin, V. A. The Role of Acetylation/Deacetylation of Histones and Transcription Factors in Regulating Metabolism in Skeletal Muscles. *Neurosci Behav Physiol* **49**, 281–288 (2019).

30. Park, S.-Y. *et al.* Structural basis of the specific interaction of SMRT corepressor with histone deacetylase 4. *Nucleic Acids Res* **46**, 11776–11788 (2018).

31. Seidel, C., Schnekenburger, M., Dicato, M. & Diederich, M. Histone deacetylase modulators provided by Mother Nature. *Genes Nutr* **7**, 357–367 (2012).

32. Mottamal, M., Zheng, S., Huang, T. & Wang, G. Histone Deacetylase Inhibitors in Clinical Studies as Templates for New Anticancer Agents. *Molecules* **20**, 3898–3941 (2015).

33. Yan Dai and Douglas V. Faller. Transcription Regulation by Class III Histone Deacetylases (HDACs)—Sirtuins. *Transl Oncogenomics* **1**, 53–65 (2008).

34. Yanginlar, C. & Logie, C. HDAC11 is a regulator of diverse immune functions. *Biochimica et Biophysica Acta (BBA) - Gene Regulatory Mechanisms* **1861**, 54–59 (2018).

35. Hanahan, D. & Weinberg, R. A. The Hallmarks of Cancer. *Cell* **100**, 57–70 (2000).

36. Ray, B. K., Dhar, S., Henry, C., Rich, A. & Ray, A. Epigenetic Regulation by Z-DNA Silencer Function Controls Cancer-Associated ADAM-12 Expression in Breast Cancer: Cross-talk between MeCP2 and NF1 Transcription Factor Family. *Cancer Res* **73**, 736–744 (2013).

37. Fraga, M. F. *et al.* Loss of acetylation at Lys16 and trimethylation at Lys20 of histone H4 is a common hallmark of human cancer. *Nat Genet* **37**, 391–400 (2005).

38. Bolden, J. E., Peart, M. J. & Johnstone, R. W. Anticancer activities of histone deacetylase inhibitors. *Nat Rev Drug Discov* **5**, 769–784 (2006).

39. Schlottmann, S. *et al.* Acetylation Increases EWS-FLI1 DNA Binding and Transcriptional Activity. *Front Oncol* **2**, (2012).

40. Xie, H. J. *et al.* HDAC1 Inactivation Induces Mitotic Defect and Caspase-Independent Autophagic Cell Death in Liver Cancer. *PLoS One* **7**, e34265 (2012).

41. Hayashi, A. *et al.* Type-specific roles of histone deacetylase (HDAC) overexpression in ovarian carcinoma: HDAC1 enhances cell proliferation and HDAC3 stimulates cell migration with downregulation of E-cadherin. *Int J Cancer* **127**, 1332–1346 (2010).

42. Yang, M., Zhang, Y. & Ren, J. Acetylation in cardiovascular diseases: Molecular mechanisms and clinical implications. *Biochimica et Biophysica Acta (BBA) - Molecular Basis of Disease* **1866**, 165836 (2020).

43. Marin-Husstege, M., Muggironi, M., Liu, A. & Casaccia-Bonnefil, P. Histone Deacetylase Activity Is Necessary for Oligodendrocyte Lineage Progression. *The Journal of Neuroscience* **22**, 10333–10345 (2002).

44. Zhang, L.-Y., Zhang, S.-Y., Wen, R., Zhang, T.-N. & Yang, N. Role of histone deacetylases and their inhibitors in neurological diseases. *Pharmacol Res* **208**, 107410 (2024).

45. Harrison, M. R., Georgiou, A. S., Spaink, H. P. & Cunliffe, V. T. The epigenetic regulator Histone Deacetylase 1 promotes transcription of a core neurogenic programme in zebrafish embryos. *BMC Genomics* **12**, 24 (2011).

46. Lagger, G. Essential function of histone deacetylase 1 in proliferation control and CDK inhibitor repression. *EMBO J* **21**, 2672–2681 (2002).

47. Chen, Y. *et al.* HDAC-mediated deacetylation of NF-κB is critical for Schwann cell myelination. *Nat Neurosci* **14**, 437–441 (2011).

48. Cunliffe, V. T. Histone deacetylase 1 is required to repress Notch target gene expression during zebrafish neurogenesis and to maintain the production of motoneurones in response to hedgehog signalling. *Development* **131**, 2983–2995 (2004).

49. MacDonald, J. L. & Roskams, A. J. Histone deacetylases 1 and 2 are expressed at distinct stages of neuro-glial development. *Developmental Dynamics* **237**, 2256–2267 (2008).

50. Ajamian, F., Suuronen, T., Salminen, A. & Reeben, M. Upregulation of class II histone deacetylases mRNA during neural differentiation of cultured rat hippocampal progenitor cells. *Neurosci Lett* **346**, 57–60 (2003).

51. Kim, A. H. *et al.* A Centrosomal Cdc20-APC Pathway Controls Dendrite Morphogenesis in Postmitotic Neurons. *Cell* **136**, 322–336 (2009).

52. Lang, B. *et al.* HDAC9 is implicated in schizophrenia and expressed specifically in post-mitotic neurons but not in adult neural stem cells. *Am J Stem Cells* **1**, 31–41 (2012).

53. Schneider, J. W. *et al.* Small-molecule activation of neuronal cell fate. *Nat Chem Biol* **4**, 408–410 (2008).

54. Bolger, T. A. & Yao, T.-P. Intracellular Trafficking of Histone Deacetylase 4 Regulates Neuronal Cell Death. *The Journal of Neuroscience* **25**, 9544–9553 (2005).

55. Xu, Y. *et al.* Low expression of the intestinal metabolite butyric acid and the corresponding memory pattern regulate HDAC4 to promote apoptosis in rat hippocampal neurons. *Ecotoxicol Environ Saf* **253**, 114660 (2023).

56. Liu, H., Hu, Q., Kaufman, A., D'Ercole, A. J. & Ye, P. Developmental expression of histone deacetylase 11 in the murine brain. *J Neurosci Res* **86**, 537–543 (2008).

57. Jarome, T. J. & Helmstetter, F. J. Protein degradation and protein synthesis in long-term memory formation. *Front Mol Neurosci* **7**, (2014).

58. Igaz, L. M., Vianna, M. R. M., Medina, J. H. & Izquierdo, I. Two Time Periods of Hippocampal mRNA Synthesis Are Required for Memory Consolidation of Fear-Motivated Learning. *The Journal of Neuroscience* **22**, 6781–6789 (2002).

59. Roth, S. Y., Denu, J. M. & Allis, C. D. Histone Acetyltransferases. *Annu Rev Biochem* **70**, 81–120 (2001).

60. Delcuve, G. P., Khan, D. H. & Davie, J. R. Roles of histone deacetylases in epigenetic regulation: emerging paradigms from studies with inhibitors. *Clin Epigenetics* **4**, 5 (2012).

61. Guan, J.-S. *et al.* HDAC2 negatively regulates memory formation and synaptic plasticity. *Nature* **459**, 55–60 (2009).

62. Borczyk, M., Śliwińska, M. A., Caly, A., Bernas, T. & Radwanska, K. Neuronal plasticity affects correlation between the size of dendritic spine and its postsynaptic density. *Sci Rep* **9**, 1693 (2019).

63. Segal, M. Dendritic spines and long-term plasticity. *Nat Rev Neurosci* **6**, 277–284 (2005).

64. Pérez-González, M. *et al.* Identifying the Main Functional Pathways Associated with Cognitive Resilience to Alzheimer's Disease. *Int J Mol Sci* **22**, 9120 (2021).

65. Sada, N. *et al.* Inhibition of HDAC increases BDNF expression and promotes neuronal rewiring and functional recovery after brain injury. *Cell Death Dis* **11**, 655 (2020).

66. Gräff, J. *et al.* An epigenetic blockade of cognitive functions in the neurodegenerating brain. *Nature* **483**, 222–226 (2012).

67. Babaei, P. NMDA and AMPA receptors dysregulation in Alzheimer's disease. *Eur J Pharmacol* **908**, 174310 (2021).

68. Butterfield, D. A. & Pocernich, C. B. The Glutamatergic System and Alzheimer???s Disease. *CNS Drugs* **17**, 641–652 (2003).

69. Palop, J. J. Epilepsy and Cognitive Impairments in Alzheimer Disease. *Arch Neurol* **66**, 435 (2009).

70. Paoletti, P., Bellone, C. & Zhou, Q. NMDA receptor subunit diversity: impact on receptor properties, synaptic plasticity and disease. *Nat Rev Neurosci* **14**, 383–400 (2013).

71. Köhr, G. NMDA receptor function: subunit composition versus spatial distribution. *Cell Tissue Res* **326**, 439–446 (2006).

72. Kullmann, D. M. & Lamsa, K. P. Long-term synaptic plasticity in hippocampal interneurons. *Nat Rev Neurosci* **8**, 687–699 (2007).

73. Liu, J., Chang, L., Song, Y., Li, H. & Wu, Y. The Role of NMDA Receptors in Alzheimer's Disease. *Front Neurosci* **13**, (2019).

74. Vizi, E. S., Kisfali, M. & Lőrincz, T. Role of nonsynaptic GluN2B-containing NMDA receptors in excitotoxicity: Evidence that fluoxetine selectively inhibits these receptors and may have neuroprotective effects. *Brain Res Bull* **93**, 32–38 (2013).

75. Léveillé, F. *et al.* Neuronal viability is controlled by a functional relation between synaptic and extrasynaptic NMDA receptors. *The FASEB Journal* **22**, 4258–4271 (2008).

76. O'Donovan, S. M., Sullivan, C. R. & McCullumsmith, R. E. The role of glutamate transporters in the pathophysiology of neuropsychiatric disorders. *NPJ Schizophr* **3**, 32 (2017).

77. Soni, N., Reddy, B. V. K. & Kumar, P. GLT-1 transporter: An effective pharmacological target for various neurological disorders. *Pharmacol Biochem Behav* **127**, 70–81 (2014).

78. Lu, W. *et al.* Subunit Composition of Synaptic AMPA Receptors Revealed by a Single-Cell Genetic Approach. *Neuron* **62**, 254–268 (2009).

79. Bassani, S., Valnegri, P., Beretta, F. & Passafaro, M. The GLUR2 subunit of AMPA receptors: Synaptic role. *Neuroscience* **158**, 55–61 (2009).

80. Lee, H.-K., Barbarosie, M., Kameyama, K., Bear, M. F. & Huganir, R. L. Regulation of distinct AMPA receptor phosphorylation sites during bidirectional synaptic plasticity. *Nature* **405**, 955–959 (2000).

81. Bolden, J. E., Peart, M. J. & Johnstone, R. W. Anticancer activities of histone deacetylase inhibitors. *Nat Rev Drug Discov* **5**, 769–784 (2006).

82. Li, Y. & Seto, E. HDACs and HDAC Inhibitors in Cancer Development and Therapy. *Cold Spring Harb Perspect Med* **6**, a026831 (2016).

83. Seto, E. & Yoshida, M. Erasers of Histone Acetylation: The Histone Deacetylase Enzymes. *Cold Spring Harb Perspect Biol* **6**, a018713–a018713 (2014).

84. Finnin, M. S. *et al.* Structures of a histone deacetylase homologue bound to the TSA and SAHA inhibitors. *Nature* **401**, 188–193 (1999).

85. Lauffer, B. E. L. *et al.* Histone Deacetylase (HDAC) Inhibitor Kinetic Rate Constants Correlate with Cellular Histone Acetylation but Not Transcription and Cell Viability. *Journal of Biological Chemistry* **288**, 26926–26943 (2013).

86. Wu, R., Lu, Z., Cao, Z. & Zhang, Y. Zinc Chelation with Hydroxamate in Histone Deacetylases Modulated by Water Access to the Linker Binding Channel. *J Am Chem Soc* **133**, 6110–6113 (2011).

87. Rajak, H. *et al.* A Structural Insight into Hydroxamic Acid Based Histone Deacetylase Inhibitors for the Presence of Anticancer Activity. *Curr Med Chem* **21**, 2642–2664 (2013).

88. Micelli, C. & Rastelli, G. Histone deacetylases: structural determinants of inhibitor selectivity. *Drug Discov Today* **20**, 718–735 (2015).

89. Zhou, H., Jiang, S., Chen, J. & Su, S. B. Suberoylanilide hydroxamic acid suppresses inflammation-induced neovascularization. *Can J Physiol Pharmacol* **92**, 879–885 (2014).

90. ZHANG, Z.-H. *et al.* Valproic acid inhibits tumor angiogenesis in mice transplanted with Kasumi-1 leukemia cells. *Mol Med Rep* **9**, 443–449 (2014).

91. Montgomery, R. L. *et al.* Maintenance of cardiac energy metabolism by histone deacetylase 3 in mice. *Journal of Clinical Investigation* **118**, 3588–3597 (2008).

92. Kenny, R. G., Ude, Z., Docherty, J. R. & Marmion, C. J. Vorinostat and Belinostat, hydroxamate-based anti-cancer agents, are nitric oxide donors. *J Inorg Biochem* **206**, 110981 (2020).

93. Peng, L. & Seto, E. Deacetylation of Nonhistone Proteins by HDACs and the Implications in Cancer. in 39–56 (2011). doi:10.1007/978-3-642-21631-2_3.

94. Shukla, S., Meeran, S. M. & Katiyar, S. K. Epigenetic regulation by selected dietary phytochemicals in cancer chemoprevention. *Cancer Lett* **355**, 9–17 (2014).

95. Bandolik, J. J., Hamacher, A., Schrenk, C., Weishaupt, R. & Kassack, M. U. Class I-Histone Deacetylase (HDAC) Inhibition is Superior to pan-HDAC Inhibition in Modulating Cisplatin Potency in High Grade Serous Ovarian Cancer Cell Lines. *Int J Mol Sci* **20**, 3052 (2019).

96. Chao, M.-W. *et al.* Combination treatment strategy for pancreatic cancer involving the novel HDAC inhibitor MPT0E028 with a MEK inhibitor beyond K-Ras status. *Clin Epigenetics* **11**, 85 (2019).

97. Cortiguera, M. G. *et al.* Suppression of BCL6 function by HDAC inhibitor mediated acetylation and chromatin modification enhances BET inhibitor effects in B-cell lymphoma cells. *Sci Rep* **9**, 16495 (2019).

98. Groselj, B. *et al.* Radiosensitization *In Vivo* by Histone Deacetylase Inhibition with No Increase in Early Normal Tissue Radiation Toxicity. *Mol Cancer Ther* **17**, 381–392 (2018).

99. Piekarz, R. L. *et al.* Phase II Multi-Institutional Trial of the Histone Deacetylase Inhibitor Romidepsin As Monotherapy for Patients With Cutaneous T-Cell Lymphoma. *Journal of Clinical Oncology* **27**, 5410–5417 (2009).

100. Garcia-Manero, G. *et al.* Phase 1 study of the histone deacetylase inhibitor vorinostat (suberoylanilide hydroxamic acid [SAHA]) in patients with advanced leukemias and myelodysplastic syndromes. *Blood* **111**, 1060–1066 (2008).

101. Gao, S., Li, X., Zang, J., Xu, W. & Zhang, Y. Preclinical and Clinical Studies of Chidamide (CS055/HBI-8000), An Orally Available Subtype-selective HDAC Inhibitor for Cancer Therapy. *Anticancer Agents Med Chem* **17**, (2017).

102. Finkler, N. J. *et al.* Phase II multicenter trial of the histone deactylase inhibitor (HDACi) belinostat, carboplatin and paclitaxel (BelCaP) in patients (pts) with

relapsed epithelial ovarian cancer (EOC). *Journal of Clinical Oncology* **26**, 5519–5519 (2008).

103. Guha, M. HDAC inhibitors still need a home run, despite recent approval. *Nat Rev Drug Discov* **14**, 225–226 (2015).

104. Suraweera, A., O'Byrne, K. J. & Richard, D. J. Combination Therapy With Histone Deacetylase Inhibitors (HDACi) for the Treatment of Cancer: Achieving the Full Therapeutic Potential of HDACi. *Front Oncol* **8**, (2018).

105. Wood, M. A., Hawk, J. D. & Abel, T. Combinatorial chromatin modifications and memory storage: A code for memory?: Figure 1. *Learning & Memory* **13**, 241–244 (2006).

106. Korzus, E., Rosenfeld, M. G. & Mayford, M. CBP Histone Acetyltransferase Activity Is a Critical Component of Memory Consolidation. *Neuron* **42**, 961–972 (2004).

107. Stefanko, D. P., Barrett, R. M., Ly, A. R., Reolon, G. K. & Wood, M. A. Modulation of long-term memory for object recognition via HDAC inhibition. *Proceedings of the National Academy of Sciences* **106**, 9447–9452 (2009).

108. Haettig, J. *et al.* HDAC inhibition modulates hippocampus-dependent long-term memory for object location in a CBP-dependent manner. *Learning & Memory* **18**, 71–79 (2011).

109. Fass, D. M. *et al.* Crebinostat: A novel cognitive enhancer that inhibits histone deacetylase activity and modulates chromatin-mediated neuroplasticity. *Neuropharmacology* **64**, 81–96 (2013).

110. Lopez-Atalaya, J. P., Ito, S., Valor, L. M., Benito, E. & Barco, A. Genomic targets, and histone acetylation and gene expression profiling of neural HDAC inhibition. *Nucleic Acids Res* **41**, 8072–8084 (2013).

111. Roozendaal, B. *et al.* Membrane-Associated Glucocorticoid Activity Is Necessary for Modulation of Long-Term Memory via Chromatin Modification. *The Journal of Neuroscience* **30**, 5037–5046 (2010).

112. Covington, H. E. *et al.* Antidepressant Actions of Histone Deacetylase Inhibitors. *The Journal of Neuroscience* **29**, 11451–11460 (2009).

113. Sung, Y. M. *et al.* Mercaptoacetamide-based class II HDAC inhibitor lowers Aβ levels and improves learning and memory in a mouse model of Alzheimer's disease. *Exp Neurol* **239**, 192–201 (2013).

114. Covington, H. E. *et al.* Antidepressant Actions of Histone Deacetylase Inhibitors. *The Journal of Neuroscience* **29**, 11451–11460 (2009).

115. Gräff, J. *et al.* Epigenetic Priming of Memory Updating during Reconsolidation to Attenuate Remote Fear Memories. *Cell* **156**, 261–276 (2014).

116. Wagner, F. F. *et al.* Kinetically selective inhibitors of histone deacetylase 2 (HDAC2) as cognition enhancers. *Chem Sci* **6**, 804–815 (2015).

117. Guan, J.-S. *et al.* HDAC2 negatively regulates memory formation and synaptic plasticity. *Nature* **459**, 55–60 (2009).

118. Morris, M. J., Mahgoub, M., Na, E. S., Pranav, H. & Monteggia, L. M. Loss of Histone Deacetylase 2 Improves Working Memory and Accelerates Extinction Learning. *The Journal of Neuroscience* **33**, 6401–6411 (2013).

119. 2024 Alzheimer's disease facts and figures. *Alzheimer's & Dementia* **20**, 3708–3821 (2024).

120. Huang, L.-K., Kuan, Y.-C., Lin, H.-W. & Hu, C.-J. Clinical trials of new drugs for Alzheimer disease: a 2020–2023 update. *J Biomed Sci* **30**, 83 (2023).

121. Alhazmi, H. A. & Albratty, M. An update on the novel and approved drugs for Alzheimer disease. *Saudi Pharmaceutical Journal* **30**, 1755–1764 (2022).

122. van Dyck, C. H. *et al.* Lecanemab in Early Alzheimer's Disease. *New England Journal of Medicine* **388**, 9–21 (2023).

123. Lindauer, A., Sexson, K. & Harvath, T. A. Medication Management for People with Dementia. *AJN, American Journal of Nursing* **117**, 60–64 (2017).

124. Cacabelos, R. Donepezil in Alzheimer's disease: From conventional trials to pharmacogenetics. *Neuropsychiatr Dis Treat* **3**, 303–33 (2007).

125. Su, Q. *et al.* Trichostatin A ameliorates Alzheimer's disease-related pathology and cognitive deficits by increasing albumin expression and Aβ clearance in APP/PS1 mice. *Alzheimers Res Ther* **13**, 7 (2021).

126. Zupkovitz, G. *et al.* Negative and Positive Regulation of Gene Expression by Mouse Histone Deacetylase 1. *Mol Cell Biol* **26**, 7913–7928 (2006).

127. He, R., Liu, B., Geng, B., Li, N. & Geng, Q. The role of HDAC3 and its inhibitors in regulation of oxidative stress and chronic diseases. *Cell Death Discov* **9**, 131 (2023).

128. Li, J. *et al.* Histone deacetylase 8 regulates cortactin deacetylation and contraction in smooth muscle tissues. *American Journal of Physiology-Cell Physiology* **307**, C288–C295 (2014).

129. Hanson, J. E. *et al.* SAHA Enhances Synaptic Function and Plasticity In Vitro but Has Limited Brain Availability In Vivo and Does Not Impact Cognition. *PLoS One* **8**, e69964 (2013).

130. Furumai, R. *et al.* FK228 (depsipeptide) as a natural prodrug that inhibits class I histone deacetylases. *Cancer Res* **62**, 4916–21 (2002).

131. Iwamoto, F. M. *et al.* A phase I/II trial of the histone deacetylase inhibitor romidepsin for adults with recurrent malignant glioma: North American Brain Tumor Consortium Study 03-03. *Neuro Oncol* **13**, 509–516 (2011).

132. Belayet, J. B. *et al.* Development of a Novel, Small-Molecule Brain-Penetrant Histone Deacetylase Inhibitor That Enhances Spatial Memory Formation in Mice. *J Med Chem* **65**, 3388–3403 (2022).

133. Roy, A. *et al.* Enhancement of Morphological Plasticity in Hippocampal Neurons by a Physically Modified Saline via Phosphatidylinositol-3 Kinase. *PLoS One* **9**, e101883 (2014).

134. Roy, A. *et al.* Regulation of Cyclic AMP Response Element Binding and Hippocampal Plasticity-Related Genes by Peroxisome Proliferator-Activated Receptor α. *Cell Rep* **4**, 724–737 (2013).

135. Gottschalk, G. *et al.* Elevated ATG13 in serum of patients with ME/CFS stimulates oxidative stress response in microglial cells via activation of receptor for advanced glycation end products (RAGE). *Molecular and Cellular Neuroscience* **120**, 103731 (2022).

136. B:urgi, H. B., Dunitz, J. D., Lehn, J. M. & Wipff, G. Stereochemistry of reaction paths at carbonyl centres. *Tetrahedron* **30**, 1563–1572 (1974).

137. Larraufie, M.-H. *et al.* Incorporation of metabolically stable ketones into a small molecule probe to increase potency and water solubility. *Bioorg Med Chem Lett* **25**, 4787–4792 (2015).

138. House, H. O. & Kramar, V. The Chemistry of Carbanions. V. The Enolates Derived from Unsymmetrical Ketones [1a]. *J Org Chem* **28**, 3362–3379 (1963).

139. Pinheiro, P. de S. M., Franco, L. S. & Fraga, C. A. M. The Magic Methyl and Its Tricks in Drug Discovery and Development. *Pharmaceuticals* **16**, 1157 (2023).

140. Zefirov, N. S., Zyk, N. V., Beloglazkina, E. K. & Kutateladze, A. G. Thiosulfonates: Synthesis, Reactions and Practical Applications. *Sulfur reports* **14**, 223–240 (1993).

141. Singh, R. & Whitesides, G. M. Reagents for rapid reduction of disulfide bonds in proteins. in 259–266 (1995). doi:10.1016/S1080-8914(06)80033-5.

142. Li, X., Gluth, A., Zhang, T. & Qian, W. Thiol redox proteomics: Characterization of thiol-based post-translational modifications. *Proteomics* **23**, (2023).

143. Fernandes, P. A. & Ramos, M. J. Theoretical Insights into the Mechanism for Thiol/Disulfide Exchange. *Chemistry – A European Journal* **10**, 257–266 (2004).

144. Tang, Q. & Maul, G. G. Mouse Cytomegalovirus Immediate-Early Protein 1 Binds with Host Cell Repressors To Relieve Suppressive Effects on Viral Transcription and Replication during Lytic Infection. *J Virol* **77**, 1357–1367 (2003).

145. Marzola, P., Melzer, T., Pavesi, E., Gil-Mohapel, J. & Brocardo, P. S. Exploring the Role of Neuroplasticity in Development, Aging, and Neurodegeneration. *Brain Sci* **13**, 1610 (2023).

146. Roy, A. *et al.* Regulation of Cyclic AMP Response Element Binding and Hippocampal Plasticity-Related Genes by Peroxisome Proliferator-Activated Receptor α. *Cell Rep* **4**, 724–737 (2013).

147. Roy, A. *et al.* HMG-CoA Reductase Inhibitors Bind to PPARα to Upregulate Neurotrophin Expression in the Brain and Improve Memory in Mice. *Cell Metab* **22**, 253–265 (2015).

148. Mijalkov, M. *et al.* Dendritic spines are lost in clusters in Alzheimer's disease. *Sci Rep* **11**, 12350 (2021).

149. Tzioras, M., McGeachan, R. I., Durrant, C. S. & Spires-Jones, T. L. Synaptic degeneration in Alzheimer disease. *Nat Rev Neurol* **19**, 19–38 (2023).

150. Ahmad Ganai, S., Ramadoss, M. & Mahadevan, V. Histone Deacetylase (HDAC) Inhibitors - emerging roles in neuronal memory, learning, synaptic plasticity and neural regeneration. *Curr Neuropharmacol* **14**, 55–71 (2016).

151. Singh, P. & Thakur, M. K. Histone Deacetylase 2 Inhibition Attenuates Downregulation of Hippocampal Plasticity Gene Expression during Aging. *Mol Neurobiol* **55**, 2432–2442 (2018).

152. Yang, W. *et al.* Effect of Trichostatin A on Gelsolin Levels, Proteolysis of Amyloid Precursor Protein, and Amyloid Beta-Protein Load in the Brain of Transgenic Mouse Model of Alzheimer's Disease. *Curr Alzheimer Res* **11**, 1002–1011 (2014).

153. Guzowski, J. F. & McGaugh, J. L. Antisense oligodeoxynucleotide-mediated disruption of hippocampal cAMP response element binding protein levels impairs consolidation of memory for water maze training. *Proceedings of the National Academy of Sciences* **94**, 2693–2698 (1997).

154. Yang, S., Zhang, R., Wang, G. & Zhang, Y. The development prospection of HDAC inhibitors as a potential therapeutic direction in Alzheimer's disease. *Transl Neurodegener* **6**, 19 (2017).

155. Liu, D. *et al.* Targeting the HDAC2/HNF-4A/miR-101b/AMPK Pathway Rescues Tauopathy and Dendritic Abnormalities in Alzheimer's Disease. *Molecular Therapy* **25**, 752–764 (2017).

156. Gottschalk, G. *et al.* Elevated ATG13 in serum of patients with ME/CFS stimulates oxidative stress response in microglial cells via activation of receptor for advanced glycation end products (RAGE). *Molecular and Cellular Neuroscience* **120**, 103731 (2022).

157. Roy, A. *et al.* Regulation of Cyclic AMP Response Element Binding and Hippocampal Plasticity-Related Genes by Peroxisome Proliferator-Activated Receptor α. *Cell Rep* **4**, 724–737 (2013).

158. Yin, J. C. P., Del Vecchio, M., Zhou, H. & Tully, T. CREB as a Memory Modulator: induced expression of a dCREB2 activator isoform enhances long-term memory in drosophila. *Cell* **81**, 107–115 (1995).

159. Mayr, B. & Montminy, M. Transcriptional regulation by the phosphorylation-dependent factor CREB. *Nat Rev Mol Cell Biol* **2**, 599–609 (2001).

160. Maiti, P., Manna, J., Ilavazhagan, G., Rossignol, J. & Dunbar, G. L. Molecular regulation of dendritic spine dynamics and their potential impact on synaptic plasticity and neurological diseases. *Neurosci Biobehav Rev* **59**, 208–237 (2015).

161. Ho, T. C. S., Chan, A. H. Y. & Ganesan, A. Thirty Years of HDAC Inhibitors: 2020 Insight and Hindsight. *J Med Chem* **63**, 12460–12484 (2020).

162. Hontecillas-Prieto, L. *et al.* Synergistic Enhancement of Cancer Therapy Using HDAC Inhibitors: Opportunity for Clinical Trials. *Front Genet* **11**, (2020).

Appendix A

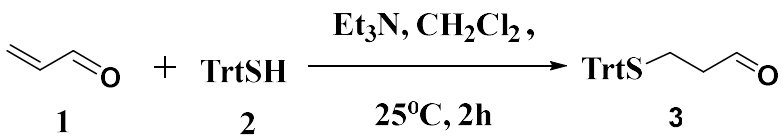
General Methods and Experimental

2.6.1. General Consideration

Under dry nitrogen conditions, unless otherwise stated, all reactions were performed following standard Schlenk techniques. Prior use, The reaction vessels were filled with nitrogen and dried under vacuum using a flame. Reagents and solvents were purchased from Sigma-Aldrich, Milwaukee. All ^{1}H and ^{13}C NMR spectra were recorded in $CDCl_3$ (internal standard: 7.26 ppm, ^{1}H; 77.16 ppm, ^{13}C) at room temperature with a Burker 500 MHz spectrometer. The chemical shifts are given in parts per million (ppm), while the coupling constants are given in Hertz (Hz). A singlet, a doublet, a triplet, a quadruplet, and a multiplet was abbreviated as s, d, t, q, and m respectively. ^{1}H NMR. ^{1}H NMR, ^{13}C NMR, and high-resolution mass spectrometry (HRMS) techniques were employed to characterize all new compounds. HRMS were obtained using electrospray ionization (ESI) technique. For column chromatography, silica gel (35-70 microns) was used. Thin layer chromatography (TLC) was performed on aluminium-backed plates precoated (0.25 mm) with Silica Gel 60 F254 with a suitable solvent system and was visualized using UV fluorescence and/or iodine chamber.

2.6.2. Experimental:

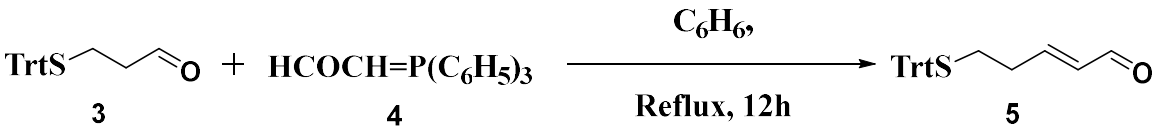
Synthesis of 3-(Tritylthio)propanal, 3:



1 2 3

A round bottom flask was charged with triphenylmethyl mercaptan, 2 (5.0 g, 18.1 mmol). The flask was put under argon and the contents of the flask were dissolved in dichloromethane (50 mL). Triethylamine (3.0 mL, 21.7 mmol, 1.2 equiv.) was added to the mixture and was stirred for additional 10 minutes. Acrolein, 1 (1.2 mL, 18.1 mmol) was added to the mixture dropwise and was stirred for 2 hours. Completion of the reaction was confirmed by thin-layer chromatography (TLC) using 15% ethyl acetate/hexane. The crude reaction was passed through a silica plug and then concentrated in-vacuo. Product 3 was purified by recrystallization with 10% ethyl acetate/hexane and collected 5.3 g with 88% yield 3. 3 was confirmed by comparing spectra to known NMR. ^{1}H NMR (500 MHz, $CDCl_3$) δ 9.58 (t, *J* = 1.6 Hz, 1H), 7.45 (dt, *J* = 5.1, 2.0 Hz, 7H), 7.31 (ddd, *J* = 14.4, 7.4, 5.1 Hz, 7H), 7.25 (ddd, *J* = 7.2, 4.0, 1.4 Hz, 3H), 2.51 – 2.46 (m, 2H), 2.42 – 2.37 (m, 2H).; ^{13}C NMR (126 MHz, $CDCl_3$) δ 200.33, 144.53, 129.56, 127.99, 126.78, 67.01, 42.69, 24.42.

Synthesis of (*E*)-5-(tritylthio)pent-2-enal, 5:

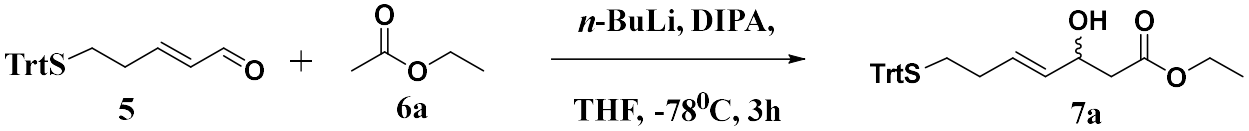


A round bottom flask was charged with 3 (5.0 g, 15.0 mmol, 1 equiv.) and 2-(triphenylphosphoranylidene)acetaldehyde, 4 (5.3 g, 16.6 mmol, 1.1 equiv.). The flask was put under argon and the contents of the flask were dissolved in benzene (100 mL). The solution was then refluxed overnight. When all starting materials were found to have disappeared, the reaction mixture was allowed to cool to room temperature and was then concentrated in vacuo. The crude product was separated via column chromatography and the column was run with an ethyl acetate/ hexane (1:7) solution until the product spot eluted. Then the product was purified by

recrystallization with toluene to give 3.8 g (70%) of pure product 5. Compound 5 was confirmed by comparing spectra to known NMR. ^{1}H NMR (500 MHz, $CDCl_3$) δ 9.45 (d, *J* = 7.8 Hz, 1H), 7.47 – 7.42 (m, 6H), 7.32 (dd, *J* = 8.5, 6.7 Hz, 6H), 7.25 (d, *J* = 7.2 Hz, 3H), 6.65 (dt, *J* = 15.7, 6.5 Hz, 1H), 6.03 – 5.97 (m, 1H), 2.38 (ddd, *J* = 9.7, 6.6, 2.3 Hz, 2H), 2.35 – 2.29 (m, 2H); ^{13}C NMR (126 MHz, $CDCl_3$) δ 193.75, 155.76, 144.58, 133.65, 129.54, 127.98, 126.80, 67.01, 31.73, 30.04.

Series 1: Ester Derivatives

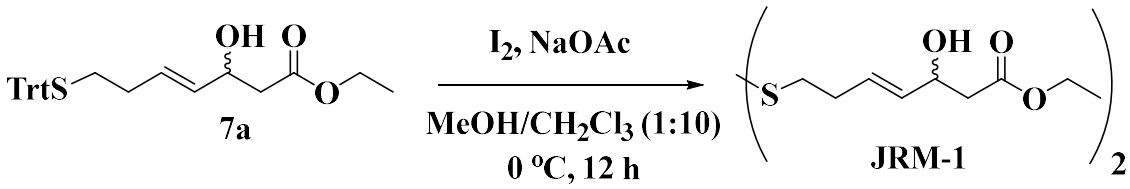
(E)-ethyl -3-hydroxy-7-(tritylthio)hept-4-enoate, 7a:



THF (50 mL) was taken in a round bottom flask under nitrogen condition and cooled over a dry ice bath. Later, diisopropylamine (DIPA) (4.70 mL, 33.46 mmol, 4 equiv.) was added into the round bottom flask. Then n-butyllithium (3.09 mL, 33.47 mmol, 4 equiv.) were added dropwise at -78°C and was stirred for 1 hour. Ethyl acetate, **6a** (2.86 mL, 29.28 mmol, 3.5 equiv.) was added at -78°C and was allowed to stir for additional 1 hour. Lastly, (E)-5-(tritylthio)pent-2-enal, **5** (3 g, 8.36 mmol, 1 equiv.) was added and the mixture was stirred for 1 hour under the same temperature. The reaction was quenched with a saturated solution of NH_4Cl (25 mL) and then concentrated in vacuo to remove THF. Then dichloromethane was added to aqueous mixture and the two phases were separated. After collecting the organic layer, the aqueous layer was extracted twice with dichloromethane and organic layers were combined. The organic layer was washed with $NaHCO_3$ solution, brine, then dried over anhydrous Na_2SO_4, and concentrated in vacuo. The residue was purified with flash column chromatography on silica gel (ethyl acetate/ hexane, 1:9) to afford 3 g (80%) of product, (E)-ethyl -3-hydroxy-7-(tritylthio)hept-4-enoate, **7a** as a white solid1H NMR

(300 MHz, CDCl3) δ 7.48 (d, J = 8.0 Hz, 6H), 7.33 (t, J = 7.5 Hz, 6H), 7.28 – 7.21 (m, 3H), 5.69 – 5.57 (m, 1H), 5.48 (dd, J = 15.5, 6.0 Hz, 1H), 4.50 (s, 1H), 4.19 (q, J = 7.0 Hz, 2H), 3.07 (s, 1H), 2.54 (d, J = 6.0 Hz, 2H), 2.27 (d, J = 7.2 Hz, 2H), 2.13 (dd, J = 13.8, 6.8 Hz, 2H), 1.29 (t, J = 7.0 Hz, 3H). 13C NMR (75 MHz, CDCl3) δ 172.24, 144.97, 132.20, 130.08, 129.65, 127.93, 126.66, 77.66, 77.24, 76.81, 68.63, 66.66, 60.75, 41.61, 31.55, 31.40, 14.27. HRMS (ESI+): Calculated (m/z) for $C_{28}H_{30}O_3S$ $(M+Na)^+$: 497.2121, Found 497.2129.

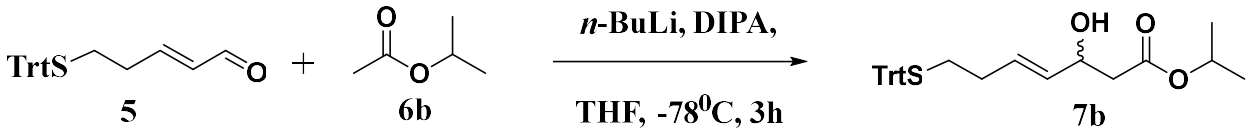
(4E,4'E)-diethyl 7,7'-disulfanediyl-bis(3-hydroxyhept-4-enoate), JRM-1:



10:1 solution of CH_2Cl_2/MeOH (15 mL) solution was prepared in a round bottom flask under vacuum. Iodine (0.85 g, 3.35 mmol, 1.0 equiv.) and sodium acetate (0.55 g, 6.7 mmol, 2.0 equiv.) were dissolved into that under nitrogen atmosphere at 0 °C. (E)-ethyl -3-hydroxy-7-(tritylthio)hept-4-enoate, **7a** (1.5 g, 3.35 mmol, 1.0 equiv.) was dissolved in a 10:1 solution of CH_2Cl_2/MeOH (10 mL) and was added dropwise over 20 minutes to the first solution containing iodine and sodium acetate using additional flask. This solution was then allowed to stir for additional 2 hour. The reaction was quenched by adding a saturated sodium thiosulfate ($Na_2S_2O_3$) solution until the mixture turned clear. Then, brine (5 mL) was added and the layers were separated. The aqueous layer was extracted with dichloromethane (3 x 15 mL) and then with ethyl acetate (3 x 15 mL). The residue was purified with flash column chromatography on silica gel hexane/ethyl acetate, 7:3) using triethyl amine (TEA) to afford 1 g (73% yield) of product, (4E,4'E)-diethyl 7,7'-disulfanediyl-bis(3-hydroxyhept-4-enoate), **JRM-1** as a white solid. 1H NMR (300 MHz, CDCl3) δ 5.77 (dt, J = 15.5, 6.7 Hz, 1H), 5.60 (dd, J = 15.5, 6.1 Hz, 1H), 4.53 (dd, J = 12.8, 5.7 Hz, 1H),

4.19 (q, J = 7.1 Hz, 2H), 2.74 (t, J = 7.3 Hz, 1H), 2.55 (dd, J = 6.1, 3.0 Hz, 2H), 2.45 (dd, J = 14.1, 6.9 Hz, 1H), 1.29 (t, J = 7.1 Hz, 3H) ^{13}C NMR (75 MHz, $CDCl_3$) δ 171.59, 132.79, 129.09, 81.22, 77.59, 77.16, 76.74, 68.66, 42.54, 38.09, 31.82, 28.08. HRMS (ESI+): Calculated (m/z) for $C_{18}H_{38}O_6S_2Na$ $(M+Na)^+$: 485.2002, Found 485.1995.

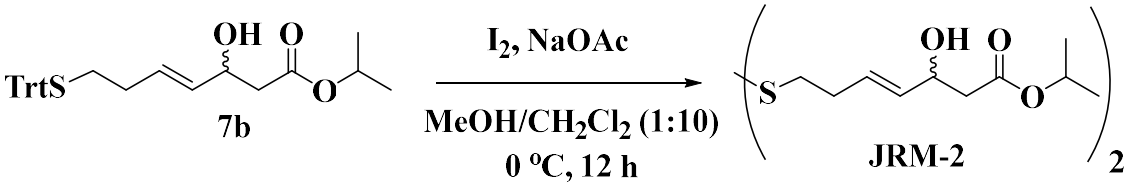
(E)-Isopropyl-3-hydroxy-7-(tritylthio)hept-4-enoate, 7b



THF (50 mL) was taken in a round bottom flask under nitrogen condition and cooled over a dry ice bath. Later, diisopropylamine (DIPA) (4.70 mL, 33.46 mmol, 4 equiv.) was added into the round bottom flask. Then n-butyllithium (3.09 mL, 33.47 mmol, 4 equiv.) were added dropwise at -78°C and was stirred for 1 hour. Isopropyl acetate, **6b** (3.43 mL, 29.28 mmol, 3.5 equiv.) was added at -78°C and was allowed to stir for additional 1 hour. Lastly, (E)-5-(tritylthio)pent-2-enal, **5** (3 g, 8.36 mmol, 1 equiv.) was added and the mixture was stirred for 1 hour under the same temperature. The reaction was quenched with a saturated solution of NH_4Cl (25 mL) and then concentrated in vacuo to remove THF. Then dichloromethane was added to aqueous mixture and the two phases were separated. After collecting the organic layer, the aqueous layer was extracted twice with dichloromethane and organic layers were combined. The organic layer was washed with $NaHCO_3$ solution, brine, then dried over anhydrous Na_2SO_4, and concentrated in vacuo. The residue was purified with flash column chromatography on silica gel (ethyl acetate/ hexane, 1:9) to afford 2.8 g (73%) of product, (E)-Isopropyl-3-hydroxy-7-(tritylthio)hept-4-enoate, **7b** as a white solid. ^{1}H NMR (500 MHz, $CDCl_3$) δ 7.45 – 7.41 (m, 6H), 7.30 (dd, *J* = 8.3, 7.0 Hz, 6H),

7.24 (dt, *J* = 9.2, 4.2 Hz, 3H), 5.60 (dtd, *J* = 7.6, 6.6, 0.9 Hz, 1H), 5.44 (dd, *J* = 15.4, 6.2 Hz, 1H), 5.10 – 5.02 (m, 1H), 4.45 (d, *J* = 4.3 Hz, 1H), 2.93 (s, 1H), 2.53 – 2.42 (m, 2H), 2.23 (t, *J* = 7.3 Hz, 2H), 2.10 (dd, *J* = 14.4, 7.2 Hz, 2H), 1.25 (d, *J* = 4.0 Hz, 6H). ^{13}C NMR (126 MHz, $CDCl_3$) δ 171.90, 144.91, 131.97, 130.13, 129.60, 127.87, 126.61, 77.30, 77.05, 76.79, 68.64, 68.29, 66.60, 41.66, 31.47, 31.37, 21.83. HRMS (ESI+): Calculated (m/z) for $C_{29}H_{32}O_3S$ $(M+Na)^+$: 497.2121, Found 497.2129.

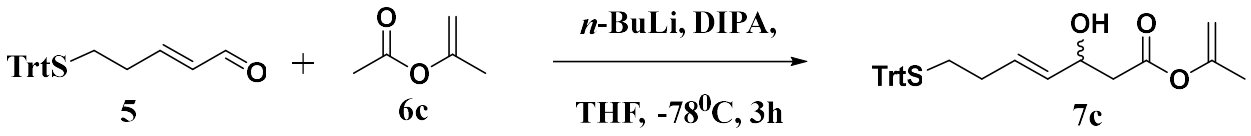
(4E,4'E)-diisopropyl 7,7'-disulfanediyl-bis(3-hydroxyhept-4-enoate), JRM-2



10:1 solution of CH_2Cl_2/MeOH (15 mL) solution was prepared in a round bottom flask under vacuum. Iodine (0.82 g, 3.25 mmol, 1.0 equiv.) and sodium acetate (0.53 g, 6.51 mmol, 2.0 equiv.) were dissolved into that under nitrogen atmosphere at 0 °C. (E)-Isopropyl-3-hydroxy-7-(tritylthio)hept-4-enoate, **7b** (1.0 g, 3.25 mmol, 1.0 equiv.) was dissolved in a 10:1 solution of CH_2Cl_2/MeOH (10 mL) and was added dropwise over 20 minutes to the first solution containing iodine and sodium acetate using additional flask. This solution was then allowed to stir for additional 2 hour. The reaction was quenched by adding a saturated sodium thiosulfate ($Na_2S_2O_3$) solution until the mixture turned clear. Then, brine (5 mL) was added and the layers were separated. The aqueous layer was extracted with dichloromethane (3 x 15 mL) and then with ethyl acetate (3 x 15 mL). The residue was purified with flash column chromatography on silica gel hexane/ethyl acetate, 7:3) using triethyl amine (TEA) to afford 1.1 g (78% yield) of product, (4E,4'E)-diisopropyl 7,7'-disulfanediyl-bis(3-hydroxyhept-4-enoate), **JRM-2** as a white solid. ^{1}H NMR (300 MHz, $CDCl_3$) δ 5.80 – 5.68 (m, 1H), 5.58 (dd, *J* = 15.6, 6.0 Hz, 1H), 5.12 – 4.98 (m, 1H),

4.50 (d, J = 5.5 Hz, 1H), 3.09 (s, 1H), 2.72 (t, J = 7.4 Hz, 2H), 2.54 – 2.37 (m, 4H), 1.25 (d, J = 6.3 Hz, 6H); ^{13}C NMR (75 MHz, $CDCl_3$) δ 171.82, 132.62, 129.40, 77.48, 77.05, 76.63, 68.62, 68.29, 41.73, 38.12, 31.83, 21.81. HRMS (ESI^+): Calculated (m/z) for C20 H34 O6 S2 $(M+Na)^+$: 457.1689, Found 457.1682.

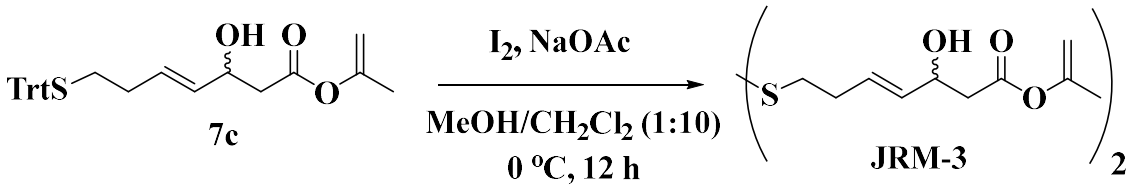
(E)Prop-1-en-2-yl-3-hydroxy-7-(tritylthio)hept-4-enoate, 7c



THF (50 mL) was taken in a round bottom flask under nitrogen condition and cooled over a dry ice bath. Later, diisopropylamine (DIPA) (4.70 mL, 33.46 mmol, 4 equiv.) was added into the round bottom flask. Then n-butyllithium (3.09 mL, 33.47 mmol, 4 equiv.) were added dropwise at -78°C and was stirred for 1 hour. Isopropenyl acetate, **6c** (6.6 mL, 29.28 mmol, 3.5 equiv.) was added at -78°C and was allowed to stir for additional 1 hour. Lastly, (E)-5-(tritylthio)pent-2-enal, **5** (3 g, 8.36 mmol, 1 equiv.) was added and the mixture was stirred for 1 hour under the same temperature. The reaction was quenched with a saturated solution of NH_4Cl (25 mL) and then concentrated in vacuo to remove THF. Then dichloromethane was added to aqueous mixture and the two phases were separated. After collecting the organic layer, the aqueous layer was extracted twice with dichloromethane and organic layers were combined. The organic layer was washed with $NaHCO_3$ solution, brine, then dried over anhydrous Na_2SO_4, and concentrated in vacuo. The residue was purified with flash column chromatography on silica gel (ethyl acetate/ hexane, 1:9) to afford 3 g (78%) of product, (E)Prop-1-en-2-yl-3-hydroxy-7-(tritylthio)hept-4-enoate, **7c** as a

white solid. ^{1}H NMR (300 MHz, $CDCl_3$) δ 7.45 (d, *J* = 7.4 Hz, 6H), 7.32 (t, *J* = 7.4 Hz, 6H), 7.25 (d, *J* = 7.0 Hz, 3H), 5.69 – 5.58 (m, 1H), 5.48 (dd, *J* = 15.5, 6.1 Hz, 1H), 4.73 (d, *J* = 7.1 Hz, 2H), 4.56 – 4.46 (m, 1H), 2.73 (d, *J* = 4.3 Hz, 1H), 2.61 (d, *J* = 6.2 Hz, 2H), 2.26 (t, *J* = 7.1 Hz, 2H), 2.12 (dd, *J* = 15.3, 8.3 Hz, 2H), 1.94 (s, 3H).; ^{13}C NMR (75 MHz, $CDCl_3$) δ 170.25, 152.76, 144.90, 131.85, 130.46, 129.61, 127.88, 126.63, 102.37, 77.50, 77.08, 76.65, 68.58, 66.63, 41.54, 31.36, 19.54, HRMS (ESI+): Calculated (m/z) for $C_{29}H_{30}O_6S_2$ $(M+Na)^+$: 497.2121, Found 497.2129.

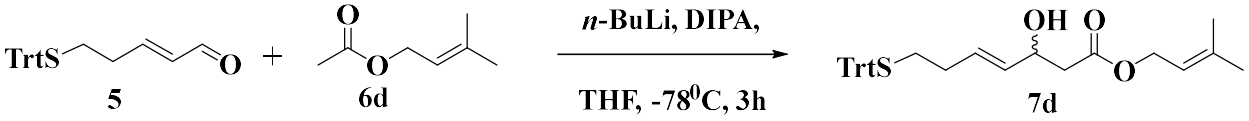
(4E,4'E)-di(prop-1-en-2-yl) 7,7'-disulfanediyl-bis(3-hydroxyhept-4-enoate), JRM-3



10:1 solution of CH_2Cl_2/MeOH (15 mL) solution was prepared in a round bottom flask under vacuum. Iodine (0.83 g, 3.27 mmol, 1.0 equiv.) and sodium acetate (0.53 g, 6.54 mmol, 2.0 equiv.) were dissolved into that under nitrogen atmosphere at 0 °C. (E)Prop-1-en-2-yl-3-hydroxy-7-(tritylthio)hept-4-enoate, **7c** (1.0 g, 2.1 mmol, 1.0 equiv.) was dissolved in a 10:1 solution of CH_2Cl_2/MeOH (10 mL) and was added dropwise over 20 minutes to the first solution containing iodine and sodium acetate using additional flask. This solution was then allowed to stir for additional 2 hour. The reaction was quenched by adding a saturated sodium thiosulfate ($Na_2S_2O_3$) solution until the mixture turned clear. Then, brine (5 mL) was added and the layers were separated. The aqueous layer was extracted with dichloromethane (3 x 15 mL) and then with ethyl acetate (3 x 15 mL). The residue was purified with flash column chromatography on silica gel hexane/ethyl acetate, 7:3) using triethyl amine (TEA) to afford 1.1 g (78% yield) of product, (4E,4'E)-di(prop-

1-en-2-yl) 7,7'-disulfanediyl-bis(3-hydroxyhept-4-enoate), J**RM-3** as a white solid. ^{1}H NMR (500 MHz, $CDCl_3$) δ 5.77 (dtd, *J* = 7.6, 6.6, 0.9 Hz, 1H), 5.61 (dd, *J* = 15.4, 6.3 Hz, 1H), 4.72 (dd, *J* = 8.0, 6.8 Hz, 2H), 4.55 (dd, *J* = 12.2, 6.1 Hz, 1H), 2.96 – 2.86 (m, 1H), 2.73 (t, *J* = 7.4 Hz, 2H), 2.64 – 2.61 (m, 2H), 2.44 (dd, *J* = 14.2, 6.9 Hz, 2H), 1.93 (s, 3H); ^{13}C NMR (126 MHz, $CDCl_3$) δ 170.20, 152.74, 132.48, 129.76, 102.38, 77.35, 77.09, 76.84, 68.60, 41.63, 38.06, 31.81, 19.53. HRMS (ESI^+): Calculated (m/z) for $C_{20}H_{30}O_6S_2Na$ $(M+Na)^+$: 485.2002, Found 485.1995.

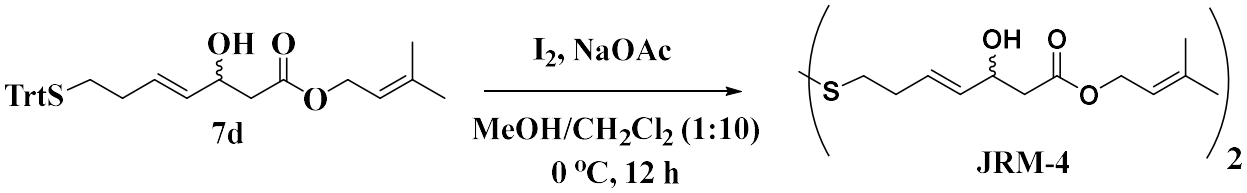
(E)-3-methylbut-2-en-1-yl-3-hydroxy-7-(tritylthio)hept-4-enoate, 7d



THF (50 mL) was taken in a round bottom flask under nitrogen condition and cooled over a dry ice bath. Later, diisopropylamine (DIPA) (4.70 mL, 33.46 mmol, 4 equiv.) was added into the round bottom flask. Then n-butyllithium (3.09 mL, 33.47 mmol, 4 equiv.) were added dropwise at -78°C and was stirred for 1 hour. Prenyl acetate, **6d** (4.09 mL, 29.28 mmol, 3.5 equiv.) was added at -78°C and was allowed to stir for additional 1 hour. Lastly, (E)-5-(tritylthio)pent-2-enal, **5** (3 g, 8.36 mmol, 1 equiv.) was added and the mixture was stirred for 1 hour under the same temperature. The reaction was quenched with a saturated solution of NH4Cl (25 mL) and then concentrated in vacuo to remove THF. Then dichloromethane was added to aqueous mixture and the two phases were separated. After collecting the organic layer, the aqueous layer was extracted twice with dichloromethane and organic layers were combined. The organic layer was washed with NaHCO3 solution, brine, then dried over anhydrous Na2SO4, and concentrated in vacuo. The residue was purified with flash column chromatography on silica gel (ethyl acetate/ hexane, 1:9) to afford 3.1 g (76%) of product, (E)-3-methylbut-2-en-1-yl-3-hydroxy-7-(tritylthio)hept-4-enoate**, 7d** as a

white solid. ^{1}H NMR (500 MHz, $CDCl_3$) δ 7.44 (dd, *J* = 8.4, 1.2 Hz, 6H), 7.31 (dd, *J* = 8.3, 6.9 Hz, 6H), 7.24 (ddd, *J* = 7.3, 3.8, 1.1 Hz, 3H), 5.60 (dtd, *J* = 7.7, 6.6, 1.0 Hz, 1H), 5.44 (dd, *J* = 15.4, 6.2 Hz, 1H), 5.36 (dddd, *J* = 7.3, 5.9, 2.8, 1.4 Hz, 1H), 4.64 (dd, *J* = 13.9, 6.3 Hz, 2H), 4.47 (dd, *J* = 11.2, 6.9 Hz, 1H), 2.60 – 2.41 (m, 1H), 2.23 (t, *J* = 7.2 Hz, 2H), 2.10 (dd, *J* = 14.4, 7.2 Hz, 2H), 1.79 (s, 3H), 1.73 (s, 3H); ^{13}C NMR (126 MHz, $CDCl_3$) δ 172.36, 144.89, 131.90, 130.19, 129.59, 127.85, 127.27, 126.59, 118.20, 77.27, 77.01, 76.76, 68.58, 66.58, 61.66, 53.42, 41.39, 31.35, 25.77, 18.03. HRMS (ESI+): Calculated (m/z) for $C_{31}H_{34}O_3S$ (M+Na)+ : 497.2121, Found 497.2129.

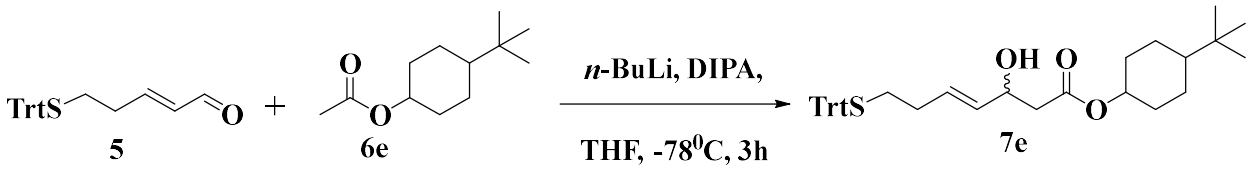
(4E,4'E)-bis(3-methylbut-2-en-1-yl) 7,7'-disulfanediyl-bis(3-hydroxyhept-4-enoate), JRM-4



10:1 solution of CH_2Cl_2/MeOH (15 mL) solution was prepared in a round bottom flask under vacuum. Iodine (0.78 g, 3.08 mmol, 1.0 equiv.) and sodium acetate (0.50 g, 6.16 mmol, 2.0 equiv.) were dissolved into that under nitrogen atmosphere at 0 °C. (E)-3-methylbut-2-en-1-yl-3-hydroxy-7-(tritylthio)hept-4-enoate, **16** (1.5 g, 3.08 mmol, 1.0 equiv.) was dissolved in a 10:1 solution of CH_2Cl_2/MeOH (10 mL) and was added dropwise over 20 minutes to the first solution containing iodine and sodium acetate using additional flask. This solution was then allowed to stir for additional 2 hour. The reaction was quenched by adding a saturated sodium thiosulfate ($Na_2S_2O_3$) solution until the mixture turned clear. Then, brine (5 mL) was added and the layers were separated. The aqueous layer was extracted with dichloromethane (3 x 15 mL) and then with ethyl acetate (3

x 15 mL). The residue was purified with flash column chromatography on silica gel hexane/ethyl acetate, 7:3) using triethyl amine (TEA) to afford 1.2 g (80% yield) of product, (4E,4'E)-diethyl 7,7'-disulfanediyl-bis(3-hydroxyhept-4-enoate), **17** as a white solid. ^{1}H NMR (500 MHz, $CDCl_3$) δ 5.76 – 5.70 (m, 1H), 5.57 (dd, *J* = 15.5, 6.2 Hz, 1H), 5.35 – 5.31 (m, 1H), 4.60 (d, *J* = 7.3 Hz, 2H), 4.52 – 4.47 (m, 1H), 3.08 (s, 1H), 2.71 (t, *J* = 7.4 Hz, 2H), 2.53 (dd, *J* = 6.0, 5.5 Hz, 2H), 2.42 (q, *J* = 7.1 Hz, 2H), 1.76 (s, 3H), 1.71 (s, 3H); ^{13}C NMR (126 MHz, $CDCl_3$) δ 172.25, 139.52, 132.61, 129.45, 118.24, 77.36, 77.11, 76.85, 68.58, 61.66, 41.51, 38.11, 31.84, 25.77, 18.03. HRMS (ESI+): Calculated (m/z) for C24 H38 O6 S2 $(M+H)^+$: 486.2182, Found 487.2176.

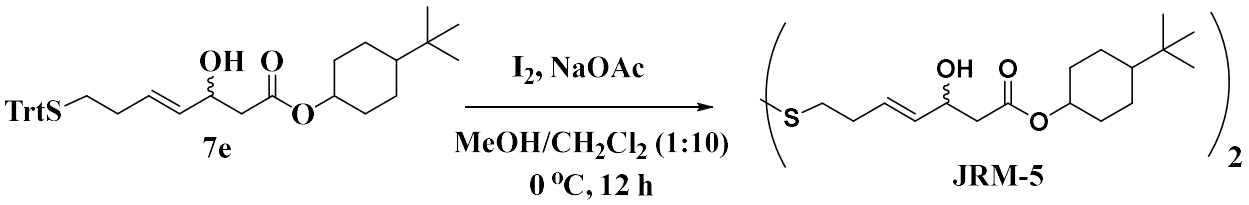
(E)-4-(tert-butyl)cyclohexyl-3-hydroxy-7-(tritylthio)hept-4-enoate, 7e



THF (50 mL) was taken in a round bottom flask under nitrogen condition and cooled over a dry ice bath. Later, diisopropylamine (DIPA) (4.70 mL, 33.46 mmol, 4 equiv.) was added into the round bottom flask. Then n-butyllithium (3.09 mL, 33.47 mmol, 4 equiv.) were added dropwise at -78°C and was stirred for 1 hour. 4-tert-Butylcyclohexyl acetate, **6e** (6.21 mL, 29.28 mmol, 3.5 equiv.) was added at -78°C and was allowed to stir for additional 1 hour. Lastly, (E)-5-(tritylthio)pent-2-enal, **5** (3 g, 8.36 mmol, 1 equiv.) was added and the mixture was stirred for 1 hour under the same temperature. The reaction was quenched with a saturated solution of NH_4Cl (25 mL) and then concentrated in vacuo to remove THF. Then dichloromethane was added to aqueous mixture and the two phases were separated. After collecting the organic layer, the aqueous layer was extracted twice with dichloromethane and organic layers were combined. The organic layer was washed with $NaHCO_3$ solution, brine, then dried over anhydrous Na_2SO_4, and

concentrated in vacuo. The residue was purified with flash column chromatography on silica gel (ethyl acetate/ hexane, 1:9) to afford 3.4 g (73%) of product, (E)-4-(tert-butyl)cyclohexyl-3-hydroxy-7-(tritylthio)hept-4-enoate, **7e** as a white solid. ^{1}H NMR (500 MHz, $CDCl_3$) δ 7.42 – 7.38 (m, 4H), 7.30 – 7.25 (m, 6H), 7.23 – 7.18 (m, 2H), 5.61 – 5.53 (m, 1H), 5.45 – 5.37 (m, 1H), 5.29 (s, 1H), 4.65 (tt, *J* = 11.3, 4.4 Hz, 1H), 4.45 – 4.39 (m, 1H), 2.52 – 2.48 (m, 1H), 2.47 – 2.43 (m, 1H), 2.23 – 2.18 (m, 1H), 2.06 (dt, *J* = 8.1, 4.2 Hz, 1H), 2.02 – 1.95 (m, 2H), 1.94 – 1.89 (m, 1H), 1.83 – 1.76 (m, 1H), 1.60 – 1.54 (m, 1H), 1.45 (ddd, *J* = 13.8, 7.8, 2.9 Hz, 1H), 1.34 – 1.19 (m, 2H), 1.13 – 0.95 (m, 3H), 0.86 – 0.84 (m, 9H); ^{13}C NMR (126 MHz, $CDCl_3$) δ 171.93, 144.91, 131.95, 130.10, 129.60, 127.87, 126.60, 77.28, 77.03, 76.77, 74.28, 68.64, 47.04, 41.66, 32.31, 32.08, 31.47, 31.37, 27.60, 27.46, 25.42. HRMS (ESI+): Calculated (m/z) for $C_{36}H_{44}O_3S$ $(M+Na)^+$: 497.2121, Found 497.2129.

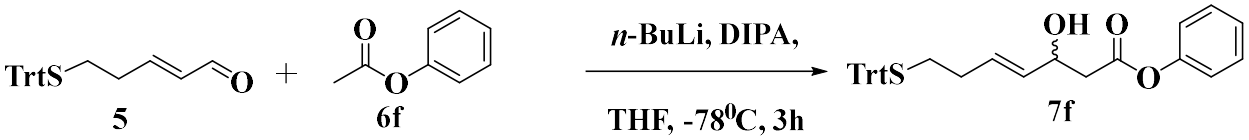
(E)-4-(tert-butyl)cyclohexyl-7-(((E)-7-((4-(tert-butyl)cyclohexyl)oxy)-5-hydroxy-7-oxohept-3-en-1-yl)disulfaneyl)-3-hydroxyhept-4-enoate, JRM-5



10:1 solution of CH_2Cl_2/MeOH (15 mL) solution was prepared in a round bottom flask under vacuum. Iodine (0.68 g, 2.7 mmol, 1.0 equiv.) and sodium acetate (0.44 g, 5.38 mmol, 2.0 equiv.) were dissolved into that under nitrogen atmosphere at 0 °C. (E)-4-(tert-butyl)cyclohexyl-3-hydroxy-7-(tritylthio)hept-4-enoate, **7e** (1.5 g, 2.7 mmol, 1.0 equiv.) was dissolved in a 10:1

solution of CH_2Cl_2/MeOH (10 mL) and was added dropwise over 20 minutes to the first solution containing iodine and sodium acetate using additional flask. This solution was then allowed to stir for additional 2 hour. The reaction was quenched by adding a saturated sodium thiosulfate ($Na_2S_2O_3$) solution until the mixture turned clear. Then, brine (5 mL) was added and the layers were separated. The aqueous layer was extracted with dichloromethane (3 x 15 mL) and then with ethyl acetate (3 x 15 mL). The residue was purified with flash column chromatography on silica gel hexane/ethyl acetate, 7:3) using triethyl amine (TEA) to afford 3.6 g (78% yield) of product, (E)-4-(tert-butyl)cyclohexyl-7-(((E)-7-((4-(tert-butyl)cyclohexyl)oxy)-5-hydroxy-7-oxohept-3-en-1-yl)disulfaneyl)-3-hydroxyhept-4-enoate, **JRM-5** as a white solid. ^{1}H NMR (500 MHz, $CDCl_3$) δ 5.78 – 5.71 (m, 1H), 5.63 – 5.55 (m, 1H), 4.68 (tt, *J* = 11.2, 4.4 Hz, 1H), 4.50 (dd, *J* = 11.9, 6.2 Hz, 1H), 2.73 (t, *J* = 7.3 Hz, 2H), 2.56 (dd, *J* = 9.7, 3.3 Hz, 1H), 2.52 (dd, *J* = 7.5, 6.4 Hz, 1H), 2.43 (dd, *J* = 14.0, 7.0 Hz, 2H), 2.06 – 1.99 (m, 2H), 1.95 (d, *J* = 14.5 Hz, 1H), 1.82 (d, *J* = 12.6 Hz, 2H), 1.60 (d, *J* = 12.4 Hz, 1H), 1.48 (dd, *J* = 16.8, 10.8 Hz, 1H), 1.38 – 1.22 (m, 3H), 1.16 – 1.06 (m, 2H), 1.04 – 0.96 (m, 1H), 0.86 (s, 9H); ^{13}C NMR (126 MHz, $CDCl_3$) δ 171.95, 132.57, 129.46, 77.28, 77.02, 76.77, 74.34, 68.65, 47.04, 41.70, 32.32, 32.10, 29.71, 27.59, 27.46, 25.43.HRMS (ESI+): Calculated (m/z) for C34 H58 O6 S2 $(M+Na)^+$: 649.3567, Found 649.3558.

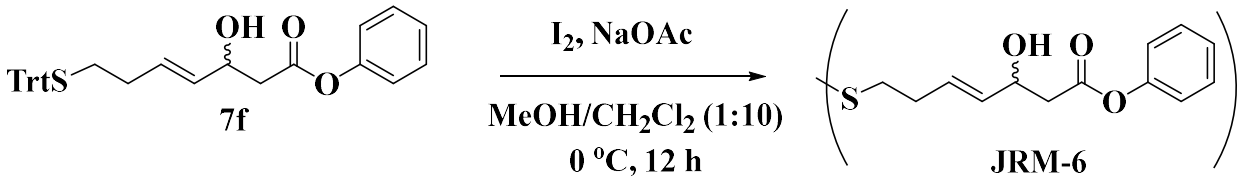
(E)-phenyl-3-hydroxy-7-(tritylthio)hept-4-enoate, 7f



THF (50 mL) was taken in a round bottom flask under nitrogen condition and cooled over a dry ice bath. Later, diisopropylamine (DIPA) (4.70 mL, 33.46 mmol, 4 equiv.) was added into the round bottom flask. Then n-butyllithium (3.09 mL, 33.47 mmol, 4 equiv.) were added dropwise at

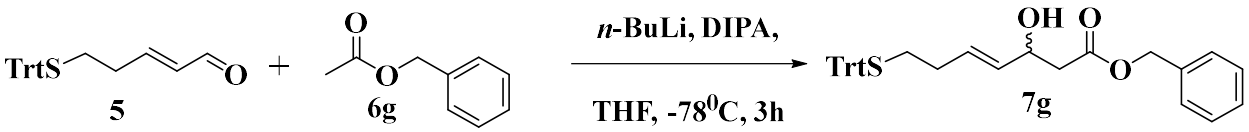
-78°C and was stirred for 1 hour. Phenyl acetate, **6f** (3.71 mL, 29.28 mmol, 3.5 equiv.) was added at -78°C and was allowed to stir for additional 1 hour. Lastly, (E)-5-(tritylthio)pent-2-enal, **5** (3 g, 8.36 mmol, 1 equiv.) was added and the mixture was stirred for 1 hour under the same temperature. The reaction was quenched with a saturated solution of NH_4Cl (25 mL) and then concentrated in vacuo to remove THF. Then dichloromethane was added to aqueous mixture and the two phases were separated. After collecting the organic layer, the aqueous layer was extracted twice with dichloromethane and organic layers were combined. The organic layer was washed with $NaHCO_3$ solution, brine, then dried over anhydrous Na_2SO_4, and concentrated in vacuo. The residue was purified with flash column chromatography on silica gel (ethyl acetate/ hexane, 1:9) to afford 3.2 g (77%) of product, (E)-phenyl-3-hydroxy-7-(tritylthio)hept-4-enoate, **7f** as a white solid. ^{1}H NMR (500 MHz, $CDCl_3$) δ 7.36 – 7.32 (m, 1H), 7.31 – 7.26 (m, 1H), 7.24 – 7.16 (m, 1H), 7.16 – 7.12 (m, 1H), 6.99 (dd, *J* = 8.7, 1.2 Hz, 1H), 5.60 – 5.53 (m, 1H), 5.42 (dd, *J* = 15.4, 6.3 Hz, 1H), 4.49 (ddd, *J* = 6.6, 6.2, 1.1 Hz, 1H), 2.70 – 2.66 (m, 1H), 2.19 – 2.12 (m, 1H), 2.07 – 2.00 (m, 1H); ^{13}C NMR (126 MHz, $CDCl_3$) δ 170.70, 150.37, 132.43, 130.01, 129.51, 126.09, 121.50, 77.29, 77.04, 76.78, 68.70, 41.70, 38.11, 31.84. HRMS (ESI+): Calculated (m/z) for $C_{32}H_{30}O_3S$ $(M+Na)^+$: 497.2121, Found 497.2129.

Diphenyl 7,7'-disulfanediyl(4E,4'E)-bis(3-hydroxyhept-4-enoate), JRM-6



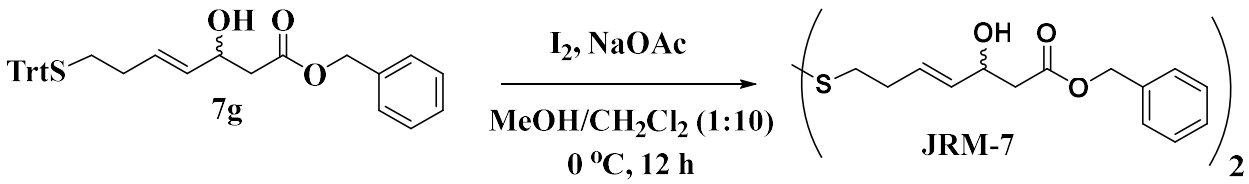
10:1 solution of CH_2Cl_2/MeOH (15 mL) solution was prepared in a round bottom flask under vacuum. Iodine (0.76 g, 3.03 mmol, 1.0 equiv.) and sodium acetate (0.50 g, 6.06 mmol, 2.0 equiv.) were dissolved into that under nitrogen atmosphere at 0 °C. (E)-phenyl-3-hydroxy-7-(tritylthio)hept-4-enoate, **22** (1.5 g, 3.03 mmol, 1.0 equiv.) was dissolved in a 10:1 solution of CH_2Cl_2/MeOH (10 mL) and was added dropwise over 20 minutes to the first solution containing iodine and sodium acetate using additional flask. This solution was then allowed to stir for additional 2 hour. The reaction was quenched by adding a saturated sodium thiosulfate ($Na_2S_2O_3$) solution until the mixture turned clear. Then, brine (5 mL) was added and the layers were separated. The aqueous layer was extracted with dichloromethane (3 x 15 mL) and then with ethyl acetate (3 x 15 mL). The residue was purified with flash column chromatography on silica gel hexane/ethyl acetate, 7:3) using triethyl amine (TEA) to afford 1.2 g (79% yield) of product, Diphenyl 7,7'-disulfanediyl(4E,4'E)-bis(3-hydroxyhept-4-enoate), **23** as a white solid. ^{1}H NMR (500 MHz, $CDCl_3$) δ 5.76 – 5.70 (m, 1H), 5.57 (dd, *J* = 15.5, 6.2 Hz, 1H), 5.35 – 5.31 (m, 1H), 4.60 (d, *J* = 7.3 Hz, 2H), 4.52 – 4.47 (m, 1H), 3.08 (s, 1H), 2.71 (t, *J* = 7.4 Hz, 2H), 2.53 (dd, *J* = 6.0, 5.5 Hz, 2H), 2.42 (q, *J* = 7.1 Hz, 2H), 1.76 (s, 3H), 1.71 (s, 3H); ^{13}C NMR (126 MHz, $CDCl_3$) δ 170.70, 150.37, 132.43, 130.01, 129.51, 126.09, 121.50, 77.29, 77.04, 76.78, 68.70, 41.70, 38.11, 31.84. HRMS (ESI+): Calculated (m/z) for $C_{26}H_{30}O_6S_2Na$ $(M+Na)^+$: 485.2002, Found 485.1995.

Benzyl (E)-3-hydroxy-7-(tritylthio)hept-4-enoate, 7g



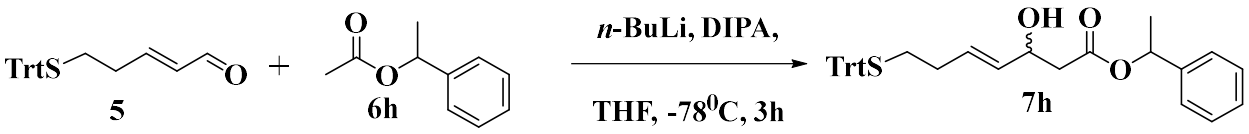
THF (50 mL) was taken in a round bottom flask under nitrogen condition and cooled over a dry ice bath. Later, diisopropylamine (DIPA) (4.70 mL, 33.46 mmol, 4 equiv.) was added into the round bottom flask. Then n-butyllithium (3.09 mL, 33.47 mmol, 4 equiv.) were added dropwise at -78°C and was stirred for 1 hour. Benzyl acetate, **6g** (4.17 mL, 29.28 mmol, 3.5 equiv.) was added at -78°C and was allowed to stir for additional 1 hour. Lastly, (E)-5-(tritylthio)pent-2-enal, **5** (3 g, 8.36 mmol, 1 equiv.) was added and the mixture was stirred for 1 hour under the same temperature. The reaction was quenched with a saturated solution of NH_4Cl (25 mL) and then concentrated in vacuo to remove THF. Then dichloromethane was added to aqueous mixture and the two phases were separated. After collecting the organic layer, the aqueous layer was extracted twice with dichloromethane and organic layers were combined. The organic layer was washed with $NaHCO_3$ solution, brine, then dried over anhydrous Na_2SO_4, and concentrated in vacuo. The residue was purified with flash column chromatography on silica gel (ethyl acetate/ hexane, 1:9) to afford 4 g (73%) of product, Benzyl (E)-3-hydroxy-7-(tritylthio)hept-4-enoate, **7g** as a white solid. ^{1}H NMR (500 MHz, $CDCl_3$) δ 7.44 (d, *J* = 7.5 Hz, 6H), 7.40 – 7.35 (m, 5H), 7.30 (dd, *J* = 13.3, 5.3 Hz, 7H), 7.25 – 7.21 (m, 3H), 5.60 (ddd, *J* = 13.6, 6.7, 3.3 Hz, 1H), 5.44 (dd, *J* = 15.4, 6.2 Hz, 1H), 5.20 – 5.13 (m, 2H), 4.49 (dd, *J* = 12.0, 6.5 Hz, 1H), 2.58 (dd, *J* = 6.2, 3.3 Hz, 2H), 2.23 (t, *J* = 7.5 Hz, 2H), 2.12 – 2.06 (m, 2H); ^{13}C NMR (126 MHz, $CDCl_3$) δ 172.06, 144.91, 135.59, 131.89, 130.34, 129.61, 128.64, 128.40, 128.29, 127.95, 127.88, 126.62, 68.63, 66.56, 41.49, 31.46, 31.34. HRMS (ESI+): Calculated (m/z) for $C_{33}H_{32}O_3S$ $(M+Na)^+$: 497.2121, Found 497.2129.

(4E,4'E)-dibenzyl 7,7'-disulfanediyl-bis(3-hydroxyhept-4-enoate), JRM-7



10:1 solution of CH_2Cl_2/MeOH (15 mL) solution was prepared in a round bottom flask under vacuum. Iodine (0.75 g, 2.94 mmol, 1.0 equiv.) and sodium acetate (0.45g, 5.9 mmol, 2.0 equiv.) were dissolved into that under nitrogen atmosphere at 0 °C. Benzyl (E)-3-hydroxy-7-(tritylthio)hept-4-enoate, **7g**(1.0 g, 2.1 mmol, 1.0 equiv.) was dissolved in a 10:1 solution of CH_2Cl_2/MeOH (10 mL) and was added dropwise over 20 minutes to the first solution containing iodine and sodium acetate using additional flask. This solution was then allowed to stir for additional 2 hour. The reaction was quenched by adding a saturated sodium thiosulfate ($Na_2S_2O_3$) solution until the mixture turned clear. Then, brine (5 mL) was added and the layers were separated. The aqueous layer was extracted with dichloromethane (3 x 15 mL) and then with ethyl acetate (3 x 15 mL). The residue was purified with flash column chromatography on silica gel hexane/ethyl acetate, 7:3) using triethyl amine (TEA) to afford 1.2 g (78% yield) of product, (4E,4'E)-dibenzyl 7,7'-disulfanediyl-bis(3-hydroxyhept-4-enoate), **JRM-7** as a white solid. ^{1}H NMR (500 MHz, $CDCl_3$) δ 7.38 (d, *J* = 5.4 Hz, 5H), 5.77 – 5.70 (m, 1H), 5.59 (dd, *J* = 15.5, 6.2 Hz, 1H), 5.17 (s, 2H), 4.55 (q, *J* = 6.2 Hz, 1H), 3.10 (s, 1H), 2.71 (t, *J* = 7.4 Hz, 2H), 2.61 (d, *J* = 6.2 Hz, 2H), 2.42 (dd, *J* = 14.1, 7.1 Hz, 2H); ^{13}C NMR (126 MHz, $CDCl_3$) δ 171.96, 135.64, 132.64, 129.58, 128.64, 128.41, 128.32, 77.47, 77.22, 76.96, 68.61, 66.56, 41.67, 38.09, 31.83. HRMS (ESI+): Calculated (m/z) for C28 H34 O6 S2 $(M+Na)^+$: 553.1689, Found 553.1682.

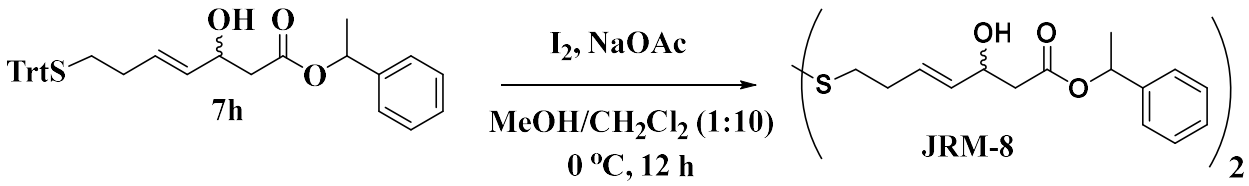
(E)-1-phenylethyl-3-hydroxy-7-(tritylthio)hept-4-enoate, 7h



THF (50 mL) was taken in a round bottom flask under nitrogen condition and cooled over a dry ice bath. Later, diisopropylamine (DIPA) (4.70 mL, 33.46 mmol, 4 equiv.) was added into the

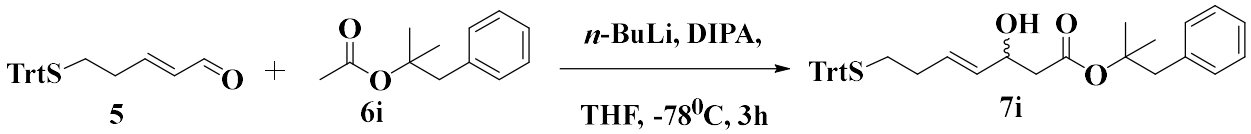
round bottom flask. Then n-butyllithium (3.09 mL, 33.47 mmol, 4 equiv.) were added dropwise at -78°C and was stirred for 1 hour. 1-Phenylethyl acetate, **6h** (4.6 mL, 29.28 mmol, 3.5 equiv.) was added at -78°C and was allowed to stir for additional 1 hour. Lastly, (E)-5-(tritylthio)pent-2-enal, **5** (3 g, 8.36 mmol, 1 equiv.) was added and the mixture was stirred for 1 hour under the same temperature. The reaction was quenched with a saturated solution of NH_4Cl (25 mL) and then concentrated in vacuo to remove THF. Then dichloromethane was added to aqueous mixture and the two phases were separated. After collecting the organic layer, the aqueous layer was extracted twice with dichloromethane and organic layers were combined. The organic layer was washed with NaHCO3 solution, brine, then dried over anhydrous Na_2SO_4, and concentrated in vacuo. The residue was purified with flash column chromatography on silica gel (ethyl acetate/ hexane, 1:9) to afford 3.3 g (75%) of product, (E)-1-tert-butoxy-4-hydroxy-8-(tritylthio)oct-5-en-2-one, **7h** as a white solid. ^{1}H NMR (500 MHz, $CDCl_3$) δ 7.45 – 7.41 (m, 5H), 7.38 – 7.34 (m, 3H), 7.33 – 7.27 (m, 7H), 7.23 (ddd, *J* = 7.2, 3.7, 1.0 Hz, 3H), 5.92 (q, *J* = 6.6 Hz, 1H), 5.60 – 5.53 (m, 1H), 5.42 (dt, *J* = 14.1, 6.5 Hz, 1H), 4.48 – 4.42 (m, 1H), 2.60 – 2.48 (m, 2H), 2.24 – 2.19 (m, 2H), 2.11 – 2.04 (m, 2H), 1.56 (dd, *J* = 6.6, 2.3 Hz, 3H); ^{13}C NMR (126 MHz, $CDCl_3$) δ 171.59, 144.90, 141.27, 131.84, 130.27, 129.60, 128.56, 128.02, 127.87, 126.61, 126.04, 77.29, 77.03, 76.78, 72.87, 68.64, 66.59, 41.68, 31.44, 31.34, 22.18. HRMS (ESI+): Calculated (m/z) for $C_{34}H_{34}O_3S$ (M+Na)+ : 497.2121, Found 497.2129.

1-phenylethyl(E)-3-hydroxy-7-(((E)-5-hydroxy-7-oxo-7-((S)-1-phenylethoxy)hept-3-en-1-yl)disulfaneyl)hept-4-enoate, JRM-8



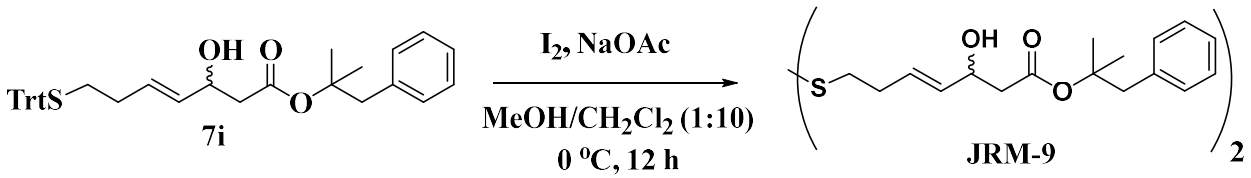
10:1 solution of CH_2Cl_2/MeOH (15 mL) solution was prepared in a round bottom flask under vacuum. Iodine (0.72 g, 2.86 mmol, 1.0 equiv.) and sodium acetate (0.47 g, 5.73 mmol, 2.0 equiv.) were dissolved into that under nitrogen atmosphere at 0 °C. (E)-ethyl -3-hydroxy-7-(tritylthio)hept-4-enoate, **7h** (1.5 g, 2.86 mmol, 1.0 equiv.) was dissolved in a 10:1 solution of CH_2Cl_2/MeOH (10 mL) and was added dropwise over 20 minutes to the first solution containing iodine and sodium acetate using additional flask. This solution was then allowed to stir for additional 2 hour. The reaction was quenched by adding a saturated sodium thiosulfate ($Na_2S_2O_3$) solution until the mixture turned clear. Then, brine (5 mL) was added and the layers were separated. The aqueous layer was extracted with dichloromethane (3 x 15 mL) and then with ethyl acetate (3 x 15 mL). The residue was purified with flash column chromatography on silica gel hexane/ethyl acetate, 7:3) using triethyl amine (TEA) to afford 1.2 g (75% yield) of product, 1-phenylethyl(E)-3-hydroxy-7-(((E)-5-hydroxy-7-oxo-7-((S)-1-phenylethoxy)hept-3-en-1-yl)disulfaneyl)hept-4-enoate, **JRM-8** as a white solid. ^{1}H NMR (500 MHz, $CDCl_3$) δ 7.28 (dd, *J* = 5.7, 2.3 Hz, 3H), 7.23 (ddt, *J* = 8.0, 3.5, 2.1 Hz, 1H), 7.19 (s, 1H), 5.85 (q, *J* = 6.6 Hz, 1H), 5.68 – 5.60 (m, 1H), 5.48 (ddd, *J* = 14.1, 12.3, 6.5 Hz, 1H), 4.46 – 4.40 (m, 1H), 2.61 (q, *J* = 7.7 Hz, 2H), 2.53 – 2.44 (m, 2H), 2.35 – 2.29 (m, 2H), 1.48 (d, *J* = 6.6 Hz, 3H13C NMR (126 MHz, CDCl3) δ 171.59, 144.90, 141.27, 131.84, 130.27, 129.60, 128.56, 128.02, 127.87, 126.61, 126.04, 77.29, 77.03, 76.78, 72.87, 68.64, 66.59, 41.68, 31.44, 31.34, 22.18. HRMS (ESI+): Calculated (m/z) for C30 H38 O6 S2 $(M+Na)^+$: 581.2002, Found 581.19947.

(E)-2-phenylpropan-2-yl-3-hydroxy-7-(tritylthio)hept-4-enoate, 7i



THF (50 mL) was taken in a round bottom flask under nitrogen condition and cooled over a dry ice bath. Later, diisopropylamine (DIPA) (4.70 mL, 33.46 mmol, 4 equiv.) was added into the round bottom flask. Then n-butyllithium (3.09 mL, 33.47 mmol, 4 equiv.) were added dropwise at -78°C and was stirred for 1 hour. 2-methyl-1-phenylpropan-2-yl acetate, **6i** (5.61 mL, 29.28 mmol, 3.5 equiv.) was added at -78°C and was allowed to stir for additional 1 hour. Lastly, (E)-5-(tritylthio)pent-2-enal (3 g, 8.36 mmol, 1 equiv.) was added and the mixture was stirred for 1 hour under the same temperature. The reaction was quenched with a saturated solution of NH_4Cl (25 mL) and then concentrated in vacuo to remove THF. Then dichloromethane was added to aqueous mixture and the two phases were separated. After collecting the organic layer, the aqueous layer was extracted twice with dichloromethane and organic layers were combined. The organic layer was washed with $NaHCO_3$ solution, brine, then dried over anhydrous Na_2SO_4, and concentrated in vacuo. The residue was purified with flash column chromatography on silica gel (ethyl acetate/ hexane, 1:9) to afford 3.3 g (72%) of product, (E)-1-tert-butoxy-4-hydroxy-8-(tritylthio)oct-5-en-2-one, **7i** as a white solid. ^{1}H NMR (500 MHz, $CDCl_3$) δ 7.40 (dt, *J* = 3.2, 1.9 Hz, 12H), 7.30 – 7.25 (m, 23H), 7.21 (ddd, *J* = 7.3, 3.8, 1.2 Hz, 7H), 5.61 – 5.53 (m, 2H), 5.41 (dd, *J* = 15.4, 6.2 Hz, 1H), 4.43 (dd, *J* = 11.2, 6.9 Hz, 1H), 4.18 – 4.12 (m, 4H), 2.82 (s, 2H), 2.51 – 2.43 (m, 3H), 2.20 (dd, *J* = 11.3, 4.0 Hz, 3H), 2.08 (t, *J* = 7.1 Hz, 3H), 1.27 – 1.23 (m, 6H); ^{13}C NMR (126 MHz, $CDCl_3$) δ 171.87, 144.95, 137.03, 132.07, 130.58, 130.03, 129.64, 128.09, 127.91, 126.64, 83.20, 77.37, 77.12, 76.87, 68.68, 66.63, 46.63, 42.58, 42.54, 31.51, 31.42, 26.08, 26.05. HRMS (ESI+): Calculated (m/z) for $C_{35}H_{36}O_3S$ (M+Na)+ : 497.2121, Found 497.2129.

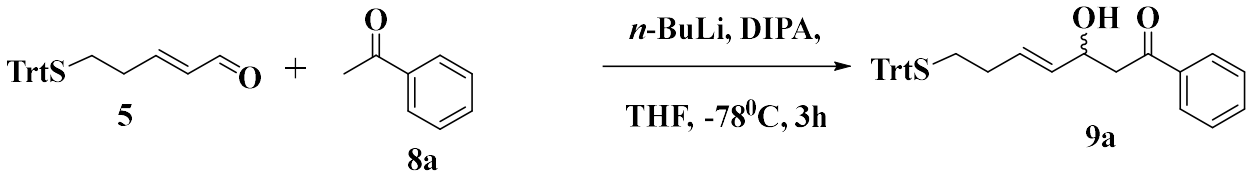
2-phenylpropan-2-yl (E)-3-hydroxy-7-(((E)-5-hydroxy-7-oxo-7-((2-phenylpropan-2-yl)oxy)hept-3-en-1-yl)disulfaneyl)hept-4-enoate, JRM-9



10:1 solution of CH_2Cl_2/MeOH (15 mL) solution was prepared in a round bottom flask under vacuum. Iodine (0.70 g, 2.8 mmol, 1.0 equiv.) and sodium acetate (0.45 g, 5.6 mmol, 2.0 equiv.) were dissolved into that under nitrogen atmosphere at 0 °C. (E)-2-phenylpropan-2-yl-3-hydroxy-7-(tritylthio)hept-4-enoate, **7i** (1.5 g, 2.8 mmol, 1.0 equiv.) was dissolved in a 10:1 solution of CH_2Cl_2/MeOH (10 mL) and was added dropwise over 20 minutes to the first solution containing iodine and sodium acetate using additional flask. This solution was then allowed to stir for additional 2 hour. The reaction was quenched by adding a saturated sodium thiosulfate ($Na_2S_2O_3$) solution until the mixture turned clear. Then, brine (5 mL) was added and the layers were separated. The aqueous layer was extracted with dichloromethane (3 x 15 mL) and then with ethyl acetate (3 x 15 mL). The residue was purified with flash column chromatography on silica gel hexane/ethyl acetate, 7:3) using triethyl amine (TEA) to afford 1.3 g (79% yield) of product, (4E,4'E)-diethyl 7,7'-disulfanediyl-bis(3-hydroxyhept-4-enoate), **JRM-9** as a white solid. ^{1}H NMR (500 MHz, $CDCl_3$) δ 7.32 – 7.28 (m, 2H), 7.27 – 7.23 (m, 1H), 7.21 – 7.18 (m, 2H), 5.75 – 5.67 (m, 1H), 5.60 – 5.54 (m, 1H), 4.47 (dd, *J* = 12.0, 6.1 Hz, 1H), 3.07 (s, 2H), 2.73 (dt, *J* = 11.8, 7.4 Hz, 2H), 2.48 (ddd, *J* = 10.3, 7.0, 5.0 Hz, 2H), 2.42 (dd, *J* = 13.9, 7.3 Hz, 2H), 2.18 (s, 5H); ^{13}C NMR (126 MHz, $CDCl_3$) δ 171.83, 136.99, 132.63, 130.55, 129.35, 128.05, 126.60, 77.33, 77.08, 76.83, 68.67, 46.61, 42.55, 38.10, 31.89, 30.93, 26.00. HRMS (ESI+): Calculated (m/z) for $C_{32}H_{42}O_6S_2Na$ $(M+Na)^+$: 485.2002, Found 485.1995.

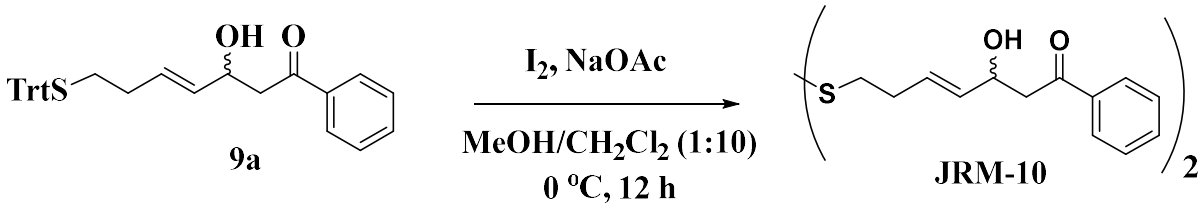
Series 2: Ketone Derivatives

(E)-3-hydroxy-1-phenyl-7-(tritylthio)hept-4-en-1-one, 9a



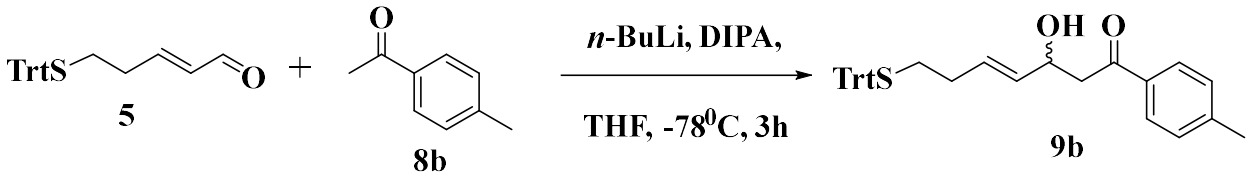
THF (50 mL) was taken in a round bottom flask under nitrogen condition and cooled over a dry ice bath. Later, diisopropylamine (DIPA) (4.70 mL, 33.46 mmol, 4 equiv.) was added into the round bottom flask. Then n-butyllithium (3.09 mL, 33.47 mmol, 4 equiv.) were added dropwise at -78°C and was stirred for 1 hour. Acetophenone, **8a** (3.41 mL, 29.28 mmol, 3.5 equiv.) was added at -78°C and was allowed to stir for additional 1 hour. Lastly, (E)-5-(tritylthio)pent-2-enal, **5** (3 g, 8.36 mmol, 1 equiv.) was added and the mixture was stirred for 1 hour under the same temperature. The reaction was quenched with a saturated solution of NH_4Cl (25 mL) and then concentrated in vacuo to remove THF. Then dichloromethane was added to aqueous mixture and the two phases were separated. After collecting the organic layer, the aqueous layer was extracted twice with dichloromethane and organic layers were combined. The organic layer was washed with $NaHCO_3$ solution, brine, then dried over anhydrous Na_2SO_4, and concentrated in vacuo. The residue was purified with flash column chromatography on silica gel (ethyl acetate/ hexane, 1:9) to afford 3.1 g (77%) of product, (E)-1-tert-butoxy-4-hydroxy-8-(tritylthio)oct-5-en-2-one, **9a** as a white solid. ^1H NMR ($CDCl_3$, 500 MHz): δ (ppm) 7.46 (d, J = 5.0 Hz, 6H), 7.32 (t, J = 7.5 Hz, 6H), 7.25 (t, J = 7.5 Hz, 3H), 5.64-5.58 (m, 1H), 5.45 (dd, J = 15.0, 5.0 Hz, 1H), 4.43 (s, 1H), 3.09 (s, 1H), 2.48-2.42 (m, 2H), 2.25 (t, J = 5.0 Hz, 2H), 2.13 (t, J = 7.0 Hz, 2H), 149 (s, 9H); ^{13}C NMR ($CDCl_3$, 125 MHz): δ (ppm) 171.8, 144.9, 132.1, 129.9, 129.6, 127.9, 126.6, 81.3, 68.7, 66.6, 42.4, 31.5, 31.4, 28.2. HRMS (ESI+): Calculated (m/z) for $C_{32}H_{30}O_2S$ $(M+Na)^+$: 497.2121, Found 497.2129.

(4E,4'E)-7,7'-disulfanediylbis(3-hydroxy-1-phenylhept-4-en-1-one), JRM-10



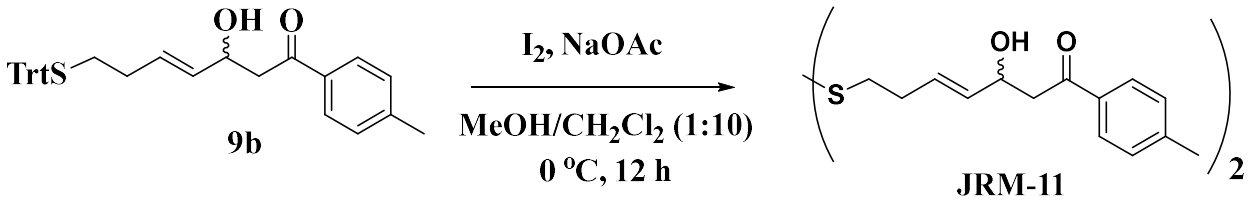
10:1 solution of CH_2Cl_2/MeOH (15 mL) solution was prepared in a round bottom flask under vacuum. Iodine (0.27 g, 2.1 mmol, 1.0 equiv.) and sodium acetate (0.17 g, 0.464 mmol, 2.0 equiv.) were dissolved into that under nitrogen atmosphere at 0 °C. (E)-ethyl -3-hydroxy-7-(tritylthio)hept-4-enoate, **9a** (1.0 g, 2.09 mmol, 1.0 equiv.) was dissolved in a 10:1 solution of CH_2Cl_2/MeOH (10 mL) and was added dropwise over 20 minutes to the first solution containing iodine and sodium acetate using additional flask. This solution was then allowed to stir for additional 2 hour. The reaction was quenched by adding a saturated sodium thiosulfate ($Na_2S_2O_3$) solution until the mixture turned clear. Then, brine (5 mL) was added and the layers were separated. The aqueous layer was extracted with dichloromethane (3 x 15 mL) and then with ethyl acetate (3 x 15 mL). The residue was purified with flash column chromatography on silica gel hexane/ethyl acetate, 7:3) using triethyl amine (TEA) to afford 0.8 g (81% yield) of product, (4E,4'E)-diethyl 7,7'-disulfanediyl-bis(3-hydroxyhept-4-enoate), **JRM-10** as a white solid. ^{1}H NMR ($CDCl_3$, 500 MHz): δ (ppm) 5.70-5.60 (m, 1H), 5.48 (dd, J = 15.0, 6.0 Hz, 1H), 4.38 (q, J = 6.0 Hz, 1H), 3.3 (s, 1H), 2.64 (t, J = 7.5 Hz, 2H), 2.38-2.31 (m, 4H), 1.38 (s, 9H); ^{13}C NMR ($CDCl_3$, 125 MHz): δ (ppm) 171.6, 132.8, 129.1, 81.2, 68.7, 42.5, 38.1, 31.8, 28.1. HRMS (ESI+): Calculated (m/z) for $C_{26}H_{30}O_4S_2Na$ $(M+Na)^+$: 485.2002, Found 485.1995.

(E)-3-hydroxy-1-(p-tolyl)-7-(tritylthio)hept-4-en-1-one, 9b



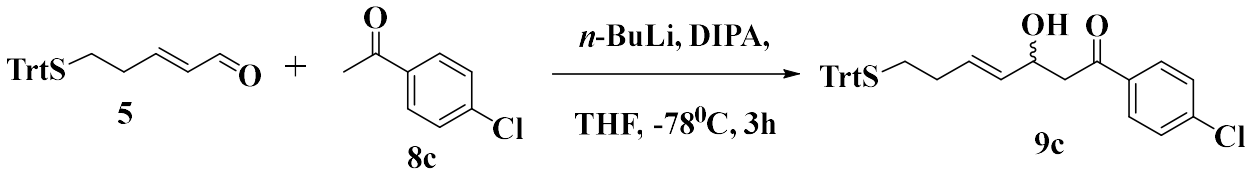
THF (50 mL) was taken in a round bottom flask under nitrogen condition and cooled over a dry ice bath. Later, diisopropylamine (DIPA) (4.70 mL, 33.46 mmol, 4 equiv.) was added into the round bottom flask. Then n-butyllithium (3.09 mL, 33.47 mmol, 4 equiv.) were added dropwise at -78°C and was stirred for 1 hour. 4′-Methylacetophenone, **8b** (3.91 mL, 29.28 mmol, 5 equiv.) was added at -78°C and was allowed to stir for additional 1 hour. Lastly, (E)-5-(tritylthio)pent-2-enal, **5** (3 g, 8.36 mmol, 1 equiv.) was added and the mixture was stirred for 1 hour under the same temperature. The reaction was quenched with a saturated solution of NH_4Cl (25 mL) and then concentrated in vacuo to remove THF. Then dichloromethane was added to aqueous mixture and the two phases were separated. After collecting the organic layer, the aqueous layer was extracted twice with dichloromethane and organic layers were combined. The organic layer was washed with $NaHCO_3$ solution, brine, then dried over anhydrous Na_2SO_4, and concentrated in vacuo. The residue was purified with flash column chromatography on silica gel (ethyl acetate/ hexane, 1:9) to afford 3.1 g (75%) of product, (E)-3-hydroxy-1-(p-tolyl)-7-(tritylthio)hept-4-en-1-one, **9b** as a white solid. ^1H NMR ($CDCl_3$, 500 MHz): δ (ppm) 7.46 (d, J = 5.0 Hz, 6H), 7.32 (t, J = 7.5 Hz, 6H), 7.25 (t, J = 7.5 Hz, 3H), 5.64-5.58 (m, 1H), 5.45 (dd, J = 15.0, 5.0 Hz, 1H), 4.43 (s, 1H), 3.09 (s, 1H), 2.48-2.42 (m, 2H), 2.25 (t, J = 5.0 Hz, 2H), 2.13 (t, J = 7.0 Hz, 2H), 149 (s, 9H); ^{13}C NMR ($CDCl_3$, 125 MHz): δ (ppm) 171.8, 144.9, 132.1, 129.9, 129.6, 127.9, 126.6, 81.3, 68.7, 66.6, 42.4, 31.5, 31.4, 28.2. HRMS (ESI+): Calculated (m/z) for $C_{33}H_{32}O_2S$ $(M+Na)^+$: 497.2121, Found 497.2129.

(4E,4'E)-7,7'-disulfanediylbis(3-hydroxy-1-(p-tolyl)hept-4-en-1-one), JRM-11



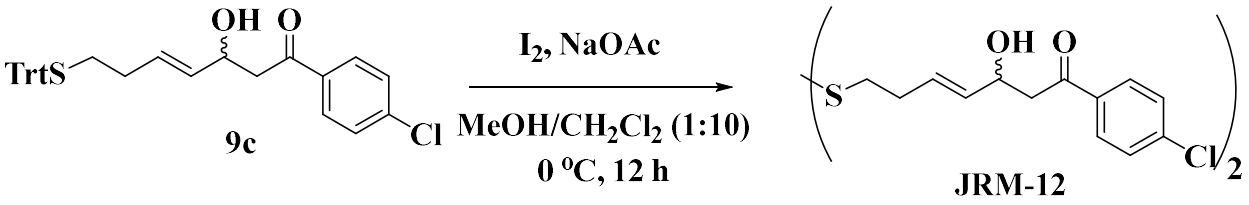
10:1 solution of CH_2Cl_2/MeOH (15 mL) solution was prepared in a round bottom flask under vacuum. Iodine (0.77 g, 3.04 mmol, 1.0 equiv.) and sodium acetate (0.50 g, 6.08 mmol, 2.0 equiv.) were dissolved into that under nitrogen atmosphere at 0 °C. (E)-3-hydroxy-1-(p-tolyl)-7-(tritylthio)hept-4-en-1-one, **9b** (1.5 g, 3.04 mmol, 1.0 equiv.) was dissolved in a 10:1 solution of CH_2Cl_2/MeOH (10 mL) and was added dropwise over 20 minutes to the first solution containing iodine and sodium acetate using additional flask. This solution was then allowed to stir for additional 2 hour. The reaction was quenched by adding a saturated sodium thiosulfate ($Na_2S_2O_3$) solution until the mixture turned clear. Then, brine (5 mL) was added and the layers were separated. The aqueous layer was extracted with dichloromethane (3 x 15 mL) and then with ethyl acetate (3 x 15 mL). The residue was purified with flash column chromatography on silica gel hexane/ethyl acetate, 7:3) using triethyl amine (TEA) to afford 1.2 g (80% yield) of product, (4E,4'E)-7,7'-disulfanediylbis(3-hydroxy-1-(p-tolyl)hept-4-en-1-one), **JRM-11** as a white solid. ^{1}H NMR ($CDCl_3$, 500 MHz): δ (ppm) 5.70-5.60 (m, 1H), 5.48 (dd, J = 15.0, 6.0 Hz, 1H), 4.38 (q, J = 6.0 Hz, 1H), 3.3 (s, 1H), 2.64 (t, J = 7.5 Hz, 2H), 2.38-2.31 (m, 4H), 1.38 (s, 9H); ^{13}C NMR (126 MHz, $CDCl_3$) δ 198.85, 140.15, 135.02, 132.72, 129.57, 129.47, 129.07, 77.28, 77.03, 76.77, 68.41, 45.17, 38.17, 31.92. HRMS (ESI+): Calculated (m/z) for $C_{28}H_{34}O_4S_2Na$ $(M+Na)^+$: 485.2002, Found 485.1995.

(E)-1-(4-chlorophenyl)-3-hydroxy-7-(tritylthio)hept-4-en-1-one, 9c



THF (50 mL) was taken in a round bottom flask under nitrogen condition and cooled over a dry ice bath. Later, diisopropylamine (DIPA) (4.70 mL, 33.46 mmol, 4 equiv.) was added into the round bottom flask. Then n-butyllithium (3.09 mL, 33.47 mmol, 4 equiv.) were added dropwise at -78°C and was stirred for 1 hour. 4′-Chloroacetophenone, **8c** (3.8 mL, 29.28 mmol, 3.5 equiv.) was added at -78°C and was allowed to stir for additional 1 hour. Lastly, (E)-5-(tritylthio)pent-2-enal, **5** (3 g, 8.36 mmol, 1 equiv.) was added and the mixture was stirred for 1 hour under the same temperature. The reaction was quenched with a saturated solution of NH_4Cl (25 mL) and then concentrated in vacuo to remove THF. Then dichloromethane was added to aqueous mixture and the two phases were separated. After collecting the organic layer, the aqueous layer was extracted twice with dichloromethane and organic layers were combined. The organic layer was washed with $NaHCO_3$ solution, brine, then dried over anhydrous Na_2SO_4, and concentrated in vacuo. The residue was purified with flash column chromatography on silica gel (ethyl acetate/ hexane, 1:9) to afford 3.1 g (75%) of product, (E)-1-(4-chlorophenyl)-3-hydroxy-7-(tritylthio)hept-4-en-1-one, **9c** as a white solid. ^{1}H NMR (500 MHz, $CDCl_3$) δ 7.87 (d, J = 8.5 Hz, 2H), 7.43 – 7.38 (m, 7H), 7.32 – 7.25 (m, 7H), 7.21 (dt, J = 9.3, 4.3 Hz, 3H), 5.62 (dtd, J = 15.5, 6.6, 1.1 Hz, 1H), 5.49 (dd, J = 15.4, 6.3 Hz, 1H), 4.65 (ddd, J = 7.2, 6.3, 0.9 Hz, 1H), 3.09 (d, J = 5.5 Hz, 2H), 2.26 – 2.18 (m, 2H), 2.15 – 2.03 (m, 2H).; ^{13}C NMR (126 MHz, $CDCl_3$) δ 198.87, 144.91, 140.08, 135.05, 132.11, 130.09, 129.61, 129.56, 129.04, 127.87, 126.62, 77.29, 77.03, 76.78, 68.40, 66.60, 45.14, 31.46, 31.41. HRMS (ESI+): Calculated (m/z) for $C_{32}H_{29}ClO_2S$ $(M+Na)^+$: 497.2121, Found 497.2129.

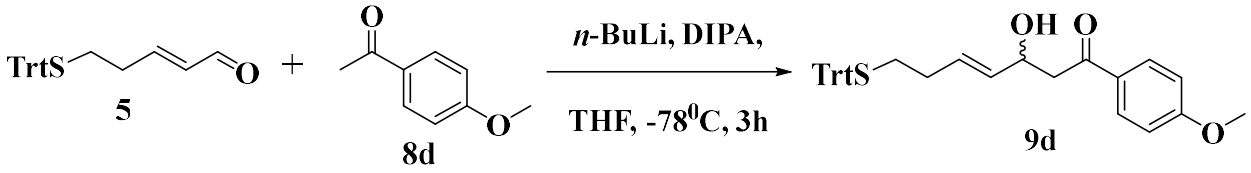
(4E,4'E)-7,7'-disulfanediylbis(1-(4-chlorophenyl)-3-hydroxyhept-4-en-1-one), JRM-12



10:1 solution of CH_2Cl_2/MeOH (15 mL) solution was prepared in a round bottom flask under vacuum. Iodine (0.27 g, 2.1 mmol, 1.0 equiv.) and sodium acetate (0.17 g, 0.464 mmol, 2.0 equiv.) were dissolved into that under nitrogen atmosphere at 0 °C. (E)-1-(4-chlorophenyl)-3-hydroxy-7-(tritylthio)hept-4-en-1-one, **9c** (1.5 g, 2.92 mmol, 1.0 equiv.) was dissolved in a 10:1 solution of CH_2Cl_2/MeOH (10 mL) and was added dropwise over 20 minutes to the first solution containing iodine and sodium acetate using additional flask. This solution was then allowed to stir for additional 2 hour. The reaction was quenched by adding a saturated sodium thiosulfate ($Na_2S_2O_3$) solution until the mixture turned clear. Then, brine (5 mL) was added and the layers were separated. The aqueous layer was extracted with dichloromethane (3 x 15 mL) and then with ethyl acetate (3 x 15 mL). The residue was purified with flash column chromatography on silica gel hexane/ethyl acetate, 7:3) using triethyl amine (TEA) to afford 1.2 g (76% yield) of product, (4E,4'E)-7,7'-disulfanediylbis(1-(4-chlorophenyl)-3-hydroxyhept-4-en-1-one), **JRM-12** as a white solid. ^{1}H NMR (500 MHz, $CDCl_3$) δ 7.82 (d, *J* = 8.5 Hz, 2H), 7.38 (d, *J* = 8.5 Hz, 2H), 5.73 (dtd, *J* = 7.6, 6.5, 1.0 Hz, 1H), 5.59 (dd, *J* = 15.5, 6.2 Hz, 1H), 4.66 (dd, *J* = 11.9, 6.0 Hz, 1H), 3.08 (d, *J* = 5.8 Hz, 2H), 2.68 (t, *J* = 7.5 Hz, 2H), 2.38 (dd, *J* = 14.2, 7.1 Hz, 2H).; ^{13}C NMR (126 MHz, $CDCl_3$) δ 198.85, 140.15, 135.02, 132.72, 129.57, 129.47, 129.07, 77.28, 77.03, 76.78, 68.41, 45.17, 38.17,

31.92. HRMS (ESI+): Calculated (m/z) for C26 H28 O4 S2 Cl2 $(M+Na)^+$: 561.0698, Found 561.0690.

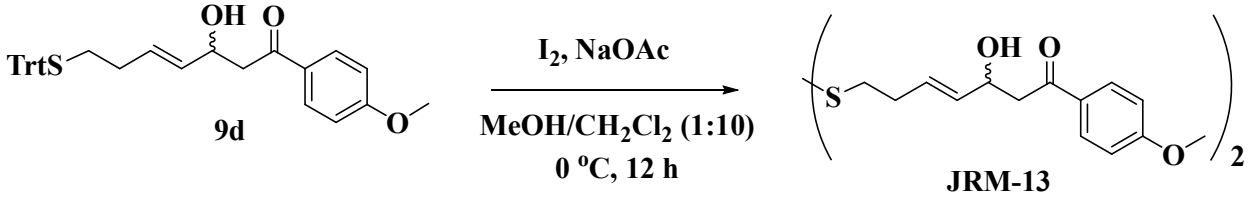
(E)-3-hydroxy-1-(4-methoxyphenyl)-7-(tritylthio)hept-4-en-1-one, 9d



THF (50 mL) was taken in a round bottom flask under nitrogen condition and cooled over a dry ice bath. Later, diisopropylamine (DIPA) (4.70 mL, 33.46 mmol, 4 equiv.) was added into the round bottom flask. Then n-butyllithium (3.09 mL, 33.47 mmol, 4 equiv.) were added dropwise at -78°C and was stirred for 1 hour. 4′-Methoxyacetophenone, **8d** (4.4 g, 29.28 mmol, 3.5 equiv.) was added at -78°C and was allowed to stir for additional 1 hour. Lastly, (E)-5-(tritylthio)pent-2-enal, **5** (3 g, 8.36 mmol, 1 equiv.) was added and the mixture was stirred for 1 hour under the same temperature. The reaction was quenched with a saturated solution of NH_4Cl (25 mL) and then concentrated in vacuo to remove THF. Then dichloromethane was added to aqueous mixture and the two phases were separated. After collecting the organic layer, the aqueous layer was extracted twice with dichloromethane and organic layers were combined. The organic layer was washed with $NaHCO_3$ solution, brine, then dried over anhydrous Na_2SO_4, and concentrated in vacuo. The residue was purified with flash column chromatography on silica gel (ethyl acetate/ hexane, 1:9) to afford 2.9 g (68%) of product, (E)-3-hydroxy-1-(4-methoxyphenyl)-7-(tritylthio)hept-4-en-1-one, **9d** as a white solid. ^{1}H NMR (500 MHz, $CDCl_3$) δ 7.91 (d, *J* = 8.8 Hz, 1H), 7.41 (dd, *J* = 8.5, 1.2 Hz, 3H), 7.32 – 7.24 (m, 3H), 7.21 (dt, *J* = 9.2, 4.4 Hz, 1H), 6.93 (d, *J* = 9.0 Hz, 1H), 5.65 – 5.58 (m, 1H), 5.49 (dd, *J* = 15.4, 6.1 Hz, 1H), 4.66 – 4.60 (m, 1H), 3.87 (s, 2H), 3.08 (qd, *J* = 17.4, 5.9 Hz, 1H), 2.25 – 2.18 (m, 1H), 2.15 – 2.03 (m, 1H); ^{13}C NMR (126 MHz, $CDCl_3$) δ 198.91,

163.91, 144.92, 132.26, 130.50, 129.81, 129.76, 129.61, 127.88, 126.61, 113.85, 77.31, 77.05, 76.80, 68.56, 66.56, 55.55, 44.57, 31.46, 29.73. HRMS (ESI+): Calculated (m/z) for $C_{33}H_{32}O_3S$ $(M+Na)^+$: 497.2121, Found 497.2129.

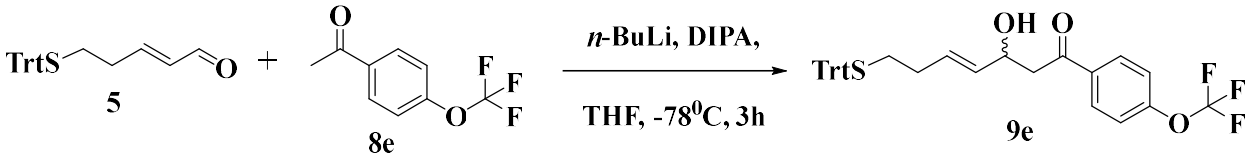
(4E,4'E)-7,7'-disulfanediylbis(3-hydroxy-1-(4-methoxyphenyl)hept-4-en-1-one), JRM-13



10:1 solution of CH_2Cl_2/MeOH (15 mL) solution was prepared in a round bottom flask under vacuum. Iodine (0.74 g, 2.92 mmol, 1.0 equiv.) and sodium acetate (0.74 g, 5.84 mmol, 2.0 equiv.) were dissolved into that under nitrogen atmosphere at 0 °C. (E)-3-hydroxy-1-(4-methoxyphenyl)-7-(tritylthio)hept-4-en-1-one, **9d** (1.0 g, 1.96 mmol, 1.0 equiv.) was dissolved in a 10:1 solution of CH_2Cl_2/MeOH (10 mL) and was added dropwise over 20 minutes to the first solution containing iodine and sodium acetate using additional flask. This solution was then allowed to stir for additional 2 hour. The reaction was quenched by adding a saturated sodium thiosulfate ($Na_2S_2O_3$) solution until the mixture turned clear. Then, brine (5 mL) was added and the layers were separated. The aqueous layer was extracted with dichloromethane (3 x 15 mL) and then with ethyl acetate (3 x 15 mL). The residue was purified with flash column chromatography on silica gel hexane/ethyl acetate, 7:3) using triethyl amine (TEA) to afford 0.9 g (86 % yield) of product, (4E,4'E)-7,7'-disulfanediylbis(3-hydroxy-1-(4-methoxyphenyl)hept-4-en-1-one), **JRM-13** as a white solid. ^{1}H NMR (500 MHz, $CDCl_3$) δ 7.94 (d, *J* = 8.9 Hz, 2H), 6.95 (d, *J* = 8.9 Hz, 2H), 5.80 (dtd, *J* = 7.4, 6.5, 0.8 Hz, 1H), 5.68 (dd, *J* = 15.5, 6.1 Hz, 1H), 4.72 (s, 1H), 3.88 (s, 3H), 3.14 (qd, *J* = 17.3, 6.0

Hz, 2H), 2.75 (t, J = 7.6 Hz, 2H), 2.46 (dd, J = 14.3, 7.0 Hz, 2H); ^{13}C NMR (126 MHz, $CDCl_3$) δ 198.78, 163.92, 132.95, 130.50, 129.79, 129.12, 113.86, 77.33, 77.08, 76.82, 68.59, 55.54, 44.65, 38.22, 31.98. HRMS (ESI+): Calculated (m/z) for C28 H34 O6 S2Na (M+Na)$^+$: 553.16890, Found 553.1682.

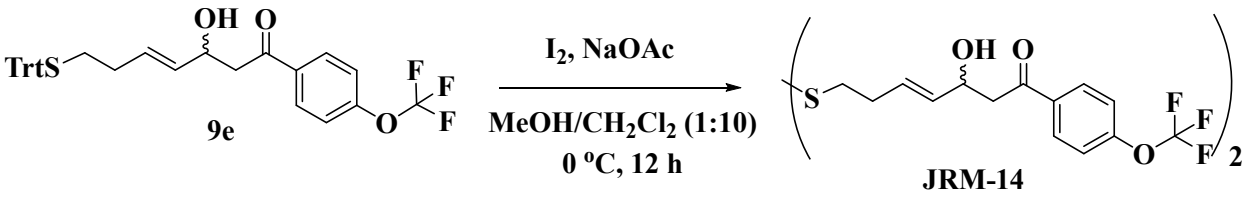
(E)-3-hydroxy-1-(4-(trifluoromethoxy)phenyl)-7-(tritylthio)hept-4-en-1-one, 9e



THF (50 mL) was taken in a round bottom flask under nitrogen condition and cooled over a dry ice bath. Later, diisopropylamine (DIPA) (4.70 mL, 33.46 mmol, 4 equiv.) was added into the round bottom flask. Then n-butyllithium (3.09 mL, 33.47 mmol, 4 equiv.) were added dropwise at -78°C and was stirred for 1 hour. 4′-(Trifluoromethoxy)acetophenone, **8e** (5.97 g, 29.28 mmol, 3.5 equiv.) was added at -78°C and was allowed to stir for additional 1 hour. Lastly, (E)-5-(tritylthio)pent-2-enal, **5** (3 g, 8.36 mmol, 1 equiv.) was added and the mixture was stirred for 1 hour under the same temperature. The reaction was quenched with a saturated solution of NH_4Cl (25 mL) and then concentrated in vacuo to remove THF. Then dichloromethane was added to aqueous mixture and the two phases were separated. After collecting the organic layer, the aqueous layer was extracted twice with dichloromethane and organic layers were combined. The organic layer was washed with $NaHCO_3$ solution, brine, then dried over anhydrous Na_2SO_4, and concentrated in vacuo. The residue was purified with flash column chromatography on silica gel (ethyl acetate/ hexane, 1:9) to afford 3.1 g (66%) of product, (E)-3-hydroxy-1-(4-(trifluoromethoxy)phenyl)-7-(tritylthio)hept-4-en-1-one, **9e** as a white solid. ^{1}H NMR (500 MHz,

$CDCl_3$) δ 7.98 (d, *J* = 8.8 Hz, 2H), 7.40 (dd, *J* = 8.4, 1.3 Hz, 6H), 7.28 (dd, *J* = 12.3, 5.1 Hz, 8H), 7.23 – 7.18 (m, 3H), 5.62 (dtd, *J* = 15.5, 6.6, 1.2 Hz, 1H), 5.50 (dd, *J* = 15.4, 6.3 Hz, 1H), 3.13 – 3.09 (m, 2H), 2.25 – 2.20 (m, 2H), 2.14 – 2.06 (m, 2H); ^{13}C NMR (126 MHz, $CDCl_3$) δ 198.50, 144.90, 134.93, 132.09, 130.21, 130.15, 129.60, 127.87, 126.61, 120.42, 77.27, 77.02, 76.77, 68.40, 66.60, 45.22, 31.40, 29.71. HRMS (ESI+): Calculated (m/z) for $C_{33}H_{29}F_3O_3S$ $(M+Na)^+$: 497.2121, Found 497.2129.

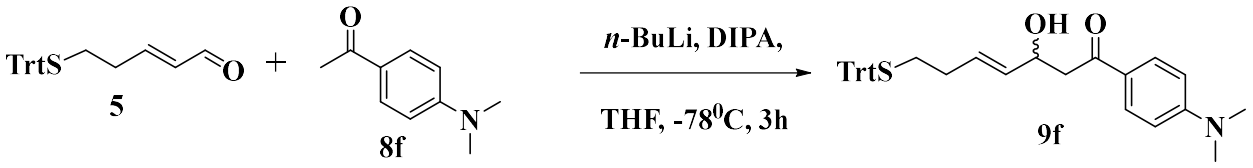
(4E,4'E)-7,7'-disulfanediylbis(3-hydroxy-1-(4-(trifluoromethoxy)phenyl)hept-4-en-1-one), JRM-14



10:1 solution of CH_2Cl_2/MeOH (15 mL) solution was prepared in a round bottom flask under vacuum. Iodine (0.67 g, 2.66 mmol, 1.0 equiv.) and sodium acetate (0.43 g, 5.33 mmol, 2.0 equiv.) were dissolved into that under nitrogen atmosphere at 0 °C. (E)-3-hydroxy-1-(4-(trifluoromethoxy)phenyl)-7-(tritylthio)hept-4-en-1-one, **93** (1.0 g, 1.77 mmol, 1.0 equiv.) was dissolved in a 10:1 solution of CH_2Cl_2/MeOH (10 mL) and was added dropwise over 20 minutes to the first solution containing iodine and sodium acetate using additional flask. This solution was then allowed to stir for additional 2 hour. The reaction was quenched by adding a saturated sodium thiosulfate ($Na_2S_2O_3$) solution until the mixture turned clear. Then, brine (5 mL) was added and the layers were separated. The aqueous layer was extracted with dichloromethane (3 x 15 mL) and then with ethyl acetate (3 x 15 mL). The residue was purified with flash column chromatography on silica gel hexane/ethyl acetate, 7:3) using triethyl amine (TEA) to afford 1 g (88% yield) of

product, (4E,4'E)-7,7'-disulfanediylbis(3-hydroxy-1-(4-(trifluoromethoxy)phenyl)hept-4-en-1-one), **JRM-14** as a white solid. ^{1}H NMR (500 MHz, $CDCl_3$) δ 7.94 (d, *J* = 8.8 Hz, 2H), 7.23 (dd, *J* = 9.0, 1.0 Hz, 2H), 5.74 (dtd, *J* = 15.5, 6.6, 1.1 Hz, 1H), 5.60 (dd, *J* = 15.5, 6.2 Hz, 1H), 4.67 (ddd, *J* = 7.2, 6.4, 1.0 Hz, 1H), 3.10 (d, *J* = 5.6 Hz, 2H), 2.68 (t, *J* = 7.6 Hz, 2H), 2.39 (q, *J* = 7.0 Hz, 2H); ^{13}C NMR (126 MHz, $CDCl_3$) δ 198.49, 152.98, 134.89, 132.70, 130.23, 129.52, 120.45, 77.27, 77.02, 76.77, 68.41, 45.24, 38.16, 31.91, 29.71. HRMS (ESI+): Calculated (m/z) for $C_{28}H_{28}F_6O_6S_2Na$ $(M+Na)^+$: 485.2002, Found 485.1995.

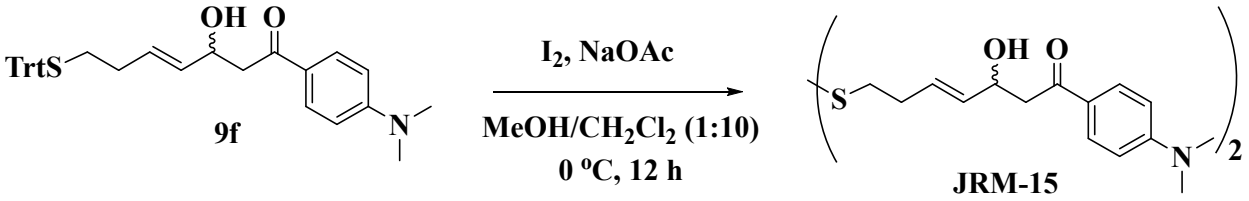
(E)-1-(4-(dimethylamino)phenyl)-3-hydroxy-7-(tritylthio)hept-4-en-1-one, 9f



THF (50 mL) was taken in a round bottom flask under nitrogen condition and cooled over a dry ice bath. Later, diisopropylamine (DIPA) (4.70 mL, 33.46 mmol, 4 equiv.) was added into the round bottom flask. Then n-butyllithium (3.09 mL, 33.47 mmol, 4 equiv.) were added dropwise at -78°C and was stirred for 1 hour. 1-[4-(Dimethylamino)phenyl]ethenone, **8f** (4.78 g, 29.28 mmol, 3.5 equiv.) was added at -78°C and was allowed to stir for additional 1 hour. Lastly, (E)-5-(tritylthio)pent-2-enal, **5** (3 g, 8.36 mmol, 1 equiv.) was added and the mixture was stirred for 1 hour under the same temperature. The reaction was quenched with a saturated solution of NH_4Cl (25 mL) and then concentrated in vacuo to remove THF. Then dichloromethane was added to aqueous mixture and the two phases were separated. After collecting the organic layer, the aqueous layer was extracted twice with dichloromethane and organic layers were combined. The organic layer was washed with $NaHCO_3$ solution, brine, then dried over anhydrous Na_2SO_4, and concentrated in vacuo. The residue was purified with flash column chromatography on silica gel

(ethyl acetate/ hexane, 1:9) to afford 3.2 g (73%) of product, (E)-1-(4-(dimethylamino)phenyl)-3-hydroxy-7-(tritylthio)hept-4-en-1-one, **9f** as a white solid. ^{1}H NMR (500 MHz, $CDCl_3$) δ 7.77 (d, *J* = 9.2 Hz, 2H), 7.34 (dd, *J* = 8.5, 1.3 Hz, 6H), 7.19 (dd, *J* = 7.4, 1.3 Hz, 6H), 7.14 (dt, *J* = 9.3, 4.3 Hz, 3H), 6.60 (d, *J* = 9.2 Hz, 2H), 4.56 – 4.50 (m, 1H), 3.05 – 3.00 (m, 1H), 2.99 (s, 6H), 2.89 (dd, *J* = 17.2, 8.9 Hz, 1H), 2.02 (dddd, *J* = 11.1, 4.8, 3.4, 1.5 Hz, 1H).; ^{13}C NMR (126 MHz, $CDCl_3$) δ 198.42, 153.53, 144.95, 132.53, 130.43, 129.62, 129.51, 127.86, 126.58, 110.97, 77.29, 77.04, 76.78, 68.81, 66.57, 43.90, 40.22, 31.55, 31.49, 29.72.

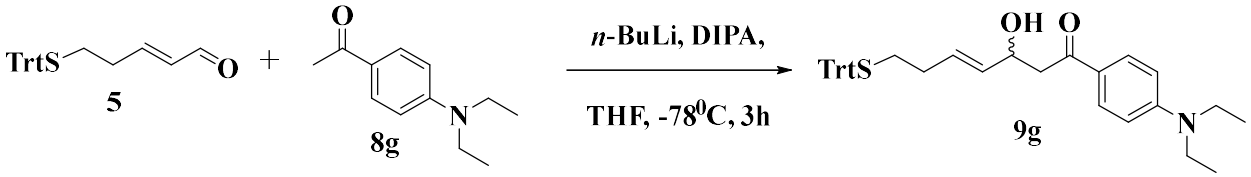
(4E,4'E)-7,7'-disulfanediylbis(1-(4-(dimethylamino)phenyl)-3-hydroxyhept-4-en-1-one), JRM-15



10:1 solution of CH_2Cl_2/MeOH (15 mL) solution was prepared in a round bottom flask under vacuum. Iodine (0.72 g, 2.87 mmol, 1.0 equiv.) and sodium acetate (0.47 g, 5.75 mmol, 2.0 equiv.) were dissolved into that under nitrogen atmosphere at 0 °C. (E)-1-(4-(dimethylamino)phenyl)-3-hydroxy-7-(tritylthio)hept-4-en-1-one, **9f** (1.5 g, 2.87 mmol, 1.0 equiv.) was dissolved in a 10:1 solution of CH_2Cl_2/MeOH (10 mL) and was added dropwise over 20 minutes to the first solution containing iodine and sodium acetate using additional flask. This solution was then allowed to stir for additional 2 hour. The reaction was quenched by adding a saturated sodium thiosulfate ($Na_2S_2O_3$) solution until the mixture turned clear. Then, brine (5 mL) was added and the layers were separated. The aqueous layer was extracted with dichloromethane (3 x 15 mL) and then with ethyl acetate (3 x 15 mL). The residue was purified with flash column chromatography on silica

gel hexane/ethyl acetate, 7:3) using triethyl amine (TEA) to afford 1.1 g (69% yield) of product, (4E,4'E)-7,7'-disulfanediylbis(1-(4-(dimethylamino)phenyl)-3-hydroxyhept-4-en-1-one), **JRM-15** as a white solid. ^{1}H NMR (500 MHz, $CDCl_3$) δ 7.85 (d, *J* = 9.0 Hz, 2H), 6.63 (d, *J* = 9.2 Hz, 2H), 5.77 (dt, *J* = 15.8, 6.5 Hz, 1H), 5.66 (dd, *J* = 15.4, 6.1 Hz, 1H), 4.70 – 4.64 (m, 1H), 3.14 (dd, *J* = 17.1, 3.0 Hz, 1H), 3.06 (s, 6H), 3.04 – 2.96 (m, 1H), 2.77 – 2.68 (m, 2H), 2.44 (dd, *J* = 14.5, 7.1 Hz, 2H); ^{13}C NMR (126 MHz, $CDCl_3$) δ 198.38, 153.75, 133.16, 130.45, 128.85, 124.58, 110.66, 77.32, 77.07, 76.82, 68.88, 43.88, 40.03, 38.28, 32.05. HRMS (ESI^+): Calculated (m/z) for $C_{30}H_{40}N_2O_4S_2Na$ $(M+Na)^+$: 485.2002, Found 485.1995.

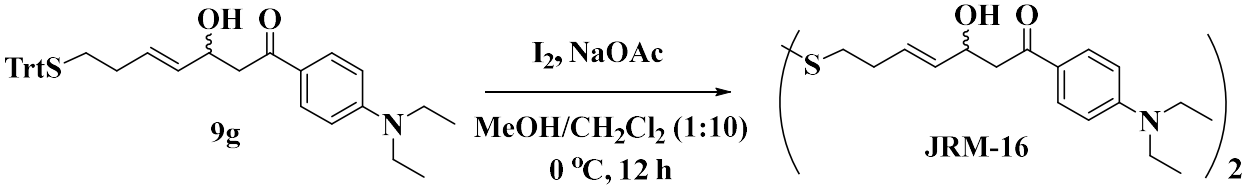
(E)-1-(4-(diethylamino)phenyl)-3-hydroxy-7-(tritylthio)hept-4-en-1-one, 9g



THF (50 mL) was taken in a round bottom flask under nitrogen condition and cooled over a dry ice bath. Later, diisopropylamine (DIPA) (4.70 mL, 33.46 mmol, 4 equiv.) was added into the round bottom flask. Then n-butyllithium (3.09 mL, 33.47 mmol, 4 equiv.) were added dropwise at -78°C and was stirred for 1 hour. 4′-Diethylaminoacetophenone, **8g** (5.60 g, 29.28 mmol, 3.5 equiv.) was added at -78°C and was allowed to stir for additional 1 hour. Lastly, (E)-5-(tritylthio)pent-2-enal (3 g, 8.36 mmol, 1 equiv.) was added and the mixture was stirred for 1 hour under the same temperature. The reaction was quenched with a saturated solution of NH_4Cl (25 mL) and then concentrated in vacuo to remove THF. Then dichloromethane was added to aqueous mixture and the two phases were separated. After collecting the organic layer, the aqueous layer

was extracted twice with dichloromethane and organic layers were combined. The organic layer was washed with $NaHCO_3$ solution, brine, then dried over anhydrous Na_2SO_4, and concentrated in vacuo. The residue was purified with flash column chromatography on silica gel (ethyl acetate/ hexane, 1:9) to afford 3.3 g (72%) of product, (E)-1-(4-(diethylamino)phenyl)-3-hydroxy-7-(tritylthio)hept-4-en-1-one, **9g** as a white solid. ^{1}H NMR (500 MHz, $CDCl_3$) δ 7.85 (d, J = 9.1 Hz, 2H), 7.45 (dd, J = 8.3, 1.0 Hz, 5H), 7.31 (t, J = 7.6 Hz, 6H), 7.23 (t, J = 7.3 Hz, 3H), 6.65 (d, J = 8.9 Hz, 2H), 5.67 – 5.61 (m, 1H), 5.53 (dd, J = 15.4, 6.1 Hz, 1H), 4.65 – 4.60 (m, 1H), 3.84 (s, 1H), 3.45 (q, J = 7.1 Hz, 4H), 3.12 (dd, J = 17.1, 2.9 Hz, 1H), 3.00 – 2.94 (m, 1H), 2.26 (t, J = 7.2 Hz, 2H), 2.16 – 2.10 (m, 2H), 1.23 (t, J = 7.1 Hz, 6H); ^{13}C NMR (126 MHz, $CDCl_3$) δ 198.14, 144.98, 132.64, 130.78, 129.63, 129.56, 129.43, 127.93, 127.88, 126.59, 77.35, 77.09, 76.84, 68.89, 66.58, 44.64, 43.72, 31.58, 31.51, 12.52. HRMS (ESI+): Calculated (m/z) for $C_{36}H_{39}NO_2S$ $(M+Na)^+$: 497.2121, Found 497.2129.

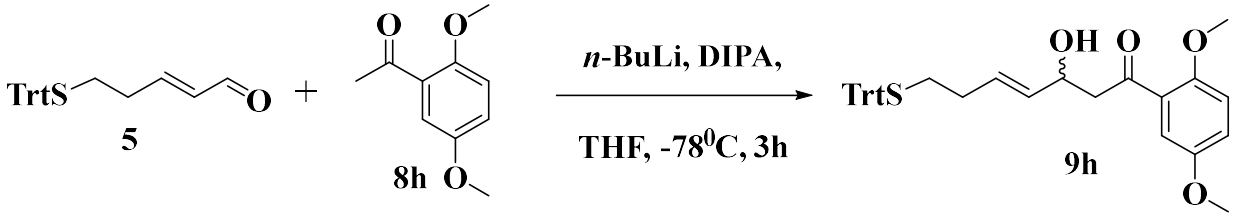
(4E,4'E)-7,7'-disulfanediylbis(1-(4-(diethylamino)phenyl)-3-hydroxyhept-4-en-1-one), JRM-16



10:1 solution of CH_2Cl_2/MeOH (15 mL) solution was prepared in a round bottom flask under vacuum. Iodine (0.70 g, 2.72 mmol, 1.0 equiv.) and sodium acetate (0.44 g, 5.45 mmol, 2.0 equiv.) were dissolved into that under nitrogen atmosphere at 0 °C. (E)-1-(4-(diethylamino)phenyl)-3-hydroxy-7-(tritylthio)hept-4-en-1-one, **9g** (1.0 g, 1.8 mmol, 1.0 equiv.) was dissolved in a 10:1 solution of CH_2Cl_2/MeOH (10 mL) and was added dropwise over 20 minutes to the first solution

containing iodine and sodium acetate using additional flask. This solution was then allowed to stir for additional 2 hour. The reaction was quenched by adding a saturated sodium thiosulfate ($Na_2S_2O_3$) solution until the mixture turned clear. Then, brine (5 mL) was added and the layers were separated. The aqueous layer was extracted with dichloromethane (3 x 15 mL) and then with ethyl acetate (3 x 15 mL). The residue was purified with flash column chromatography on silica gel hexane/ethyl acetate, 7:3) using triethyl amine (TEA) to afford 1.2 g (72% yield) of product, (4E,4'E)-7,7'-disulfanediylbis(1-(4-(diethylamino)phenyl)-3-hydroxyhept-4-en-1-one), **JRM-15**6as a white solid. ^{1}H NMR (500 MHz, $CDCl_3$) δ 7.83 (d, *J* = 9.1 Hz, 2H), 6.62 (d, *J* = 9.1 Hz, 2H), 5.77 (dtd, *J* = 15.2, 6.6, 1.0 Hz, 1H), 5.66 (dd, *J* = 15.4, 6.1 Hz, 1H), 4.66 (s, 1H), 3.88 (s, 1H), 3.42 (q, *J* = 7.1 Hz, 4H), 3.14 (dd, *J* = 17.0, 3.0 Hz, 1H), 2.99 (dd, *J* = 17.0, 8.9 Hz, 1H), 2.74 (t, *J* = 7.2 Hz, 2H), 2.44 (dd, *J* = 14.6, 7.1 Hz, 2H), 1.20 (t, *J* = 7.1 Hz, 6H)., ^{13}C NMR (126 MHz, $CDCl_3$) δ 198.13, 151.57, 133.18, 130.79, 128.84, 123.92, 110.22, 77.30, 77.04, 76.79, 68.95, 44.60, 43.70, 38.28, 32.06, 12.50. HRMS (ESI+): Calculated (m/z) for $C_{34}H_{48}N_2O_4S_2Na$ $(M+Na)^+$: 485.2002, Found 485.1995.

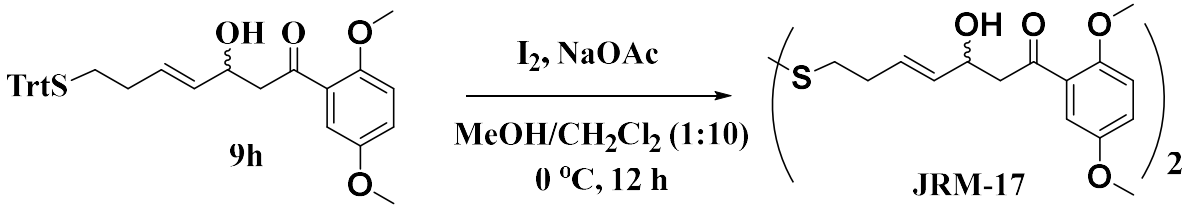
(E)-1-(2,5-dimethoxyphenyl)-3-hydroxy-7-(tritylthio)hept-4-en-1-one, 9h



THF (50 mL) was taken in a round bottom flask under nitrogen condition and cooled over a dry ice bath. Later, diisopropylamine (DIPA) (5.27 g, 29.28 mmol, 4 equiv.) was added into the round bottom flask. Then n-butyllithium (3.09 mL, 33.47 mmol, 4 equiv.) were added dropwise at -78°C and was stirred for 1 hour. 2′,5′-Dimethoxyacetophenone, **8h** (6.6 mL, 48.9 mmol, 3.5 equiv.) was

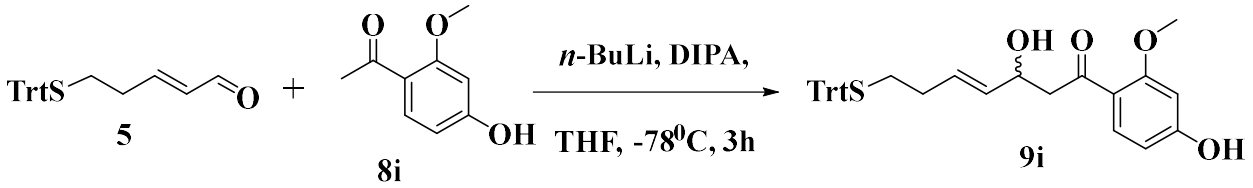
added at -78°C and was allowed to stir for additional 1 hour. Lastly, (E)-5-(tritylthio)pent-2-enal, **5** (3 g, 8.36 mmol, 1 equiv.) was added and the mixture was stirred for 1 hour under the same temperature. The reaction was quenched with a saturated solution of NH_4Cl (25 mL) and then concentrated in vacuo to remove THF. Then dichloromethane was added to aqueous mixture and the two phases were separated. After collecting the organic layer, the aqueous layer was extracted twice with dichloromethane and organic layers were combined. The organic layer was washed with $NaHCO_3$ solution, brine, then dried over anhydrous Na_2SO_4, and concentrated in vacuo. The residue was purified with flash column chromatography on silica gel (ethyl acetate/ hexane, 1:9) to afford 0.8 g (72%) of product (E)-1-(2,5-dimethoxyphenyl)-3-hydroxy-7-(tritylthio)hept-4-en-1-one, **9h** as a white solid. ^{1}H NMR (500 MHz, $CDCl_3$) δ 7.33 (dt, *J* = 3.2, 1.8 Hz, 6H), 7.23 – 7.21 (m, 1H), 7.21 – 7.17 (m, 6H), 7.16 – 7.10 (m, 3H), 6.97 (dd, *J* = 9.0, 3.2 Hz, 1H), 6.83 (d, *J* = 9.0 Hz, 1H), 5.52 (dtd, *J* = 15.5, 6.6, 1.1 Hz, 1H), 5.41 (dd, *J* = 15.4, 6.1 Hz, 1H), 4.55 – 4.49 (m, 1H), 3.75 (s, 3H), 3.71 (s, 3H), 3.16 (dd, *J* = 18.0, 3.0 Hz, 1H), 3.04 (dd, *J* = 18.0, 8.9 Hz, 1H), 2.18 – 2.12 (m, 2H), 2.10 – 1.97 (m, 2H).; ^{13}C NMR (126 MHz, $CDCl_3$) δ 201.74, 153.48, 144.95, 132.63, 129.61, 129.44, 127.86, 126.58, 120.94, 113.69, 113.22, 77.29, 77.03, 76.78, 68.75, 66.54, 56.02, 55.83, 50.46, 31.43, 29.72.HRMS (ESI+): Calculated (m/z) for $C_{30}H_{38}O_4S$ $(M+Na)^+$: 497.2121, Found 497.2129.

(4E,4'E)-7,7'-disulfanediylbis(1-(2,5-dimethoxyphenyl)-3-hydroxyhept-4-en-1-one), JRM-17



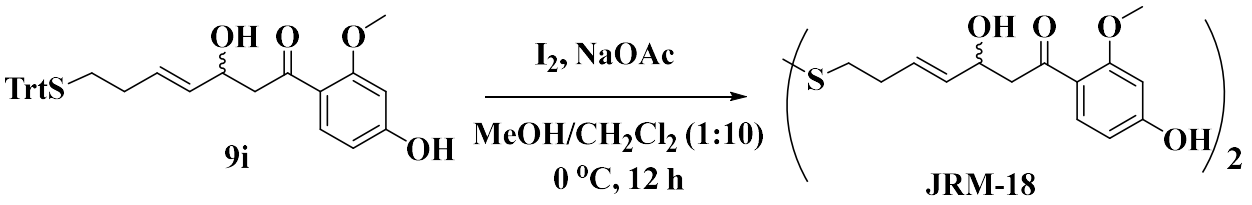
10:1 solution of CH_2Cl_2/MeOH (15 mL) solution was prepared in a round bottom flask under vacuum. Iodine (0.70 g, 2.78 mmol, 1.0 equiv.) and sodium acetate (0.45 g, 5.56 mmol, 2.0 equiv.) were dissolved into that under nitrogen atmosphere at 0 °C. (E)-1-(2,5-dimethoxyphenyl)-3-hydroxy-7-(tritylthio)hept-4-en-1-one, **54** (1.5 g, 2.78 mmol, 1.0 equiv.) was dissolved in a 10:1 solution of CH_2Cl_2/MeOH (10 mL) and was added dropwise over 20 minutes to the first solution containing iodine and sodium acetate using additional flask. This solution was then allowed to stir for additional 2 hour. The reaction was quenched by adding a saturated sodium thiosulfate ($Na_2S_2O_3$) solution until the mixture turned clear. Then, brine (5 mL) was added and the layers were separated. The aqueous layer was extracted with dichloromethane (3 x 15 mL) and then with ethyl acetate (3 x 15 mL). The residue was purified with flash column chromatography on silica gel hexane/ethyl acetate, 7:3) using triethyl amine (TEA) to afford 1.1 g (67% yield) of product, (4E,4'E)-7,7'-disulfanediylbis(1-(2,5-dimethoxyphenyl)-3-hydroxyhept-4-en-1-one), **JRM-17** as a white solid. ^{1}H NMR (500 MHz, $CDCl_3$) δ 7.31 (d, *J* = 3.2 Hz, 1H), 7.07 (dd, *J* = 9.0, 3.2 Hz, 1H), 6.93 (d, *J* = 9.0 Hz, 1H), 4.68 (s, 1H), 4.14 (q, *J* = 7.1 Hz, 1H), 3.89 (s, 3H), 3.81 (s, 3H), 3.30 (dd, *J* = 17.9, 3.1 Hz, 1H), 3.18 (dd, *J* = 17.9, 8.7 Hz, 1H), 2.76 (t, *J* = 7.6 Hz, 2H), 2.46 (dd, *J* = 14.4, 7.0 Hz, 2H), 2.06 (s, 1H), 1.28 (t, *J* = 7.1 Hz, 2H); ^{13}C NMR (126 MHz, $CDCl_3$) δ 201.69, 153.58, 153.48, 133.19, 128.83, 127.65, 120.94, 113.73, 113.23, 77.29, 77.04, 76.78, 68.77, 56.07, 55.84, 50.47, 38.28, 32.02. HRMS (ESI^+): Calculated (m/z) for $C_{30}H_{38}O_8S_2Na$ $(M+Na)^+$: 485.2002, Found 485.1995.

(E)-3-hydroxy-1-(3-hydroxy-4-methoxyphenyl)-7-(tritylthio)hept-4-en-1-one, 9i



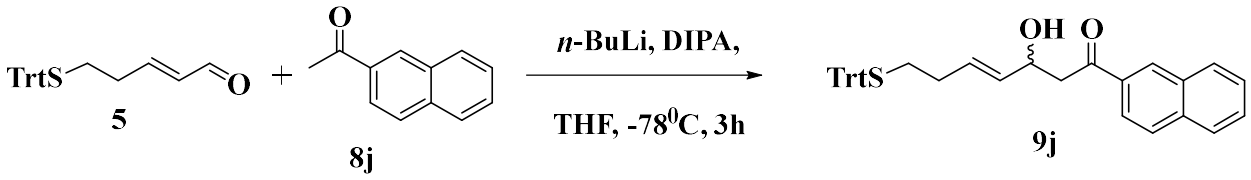
THF (50 mL) was taken in a round bottom flask under nitrogen condition and cooled over a dry ice bath. Later, diisopropylamine (DIPA) (4.70 mL, 33.46 mmol, 4 equiv.) was added into the round bottom flask. Then n-butyllithium (3.09 mL, 33.47 mmol, 4 equiv.) were added dropwise at -78°C and was stirred for 1 hour. 3′-Hydroxy-4′-methoxyacetophenone, **8i** (5.27 g, 29.28 mmol, 3.5 equiv.) was added at -78°C and was allowed to stir for additional 1 hour. Lastly, (E)-5-(tritylthio)pent-2-enal (3 g, 8.36 mmol, 1 equiv.) was added and the mixture was stirred for 1 hour under the same temperature. The reaction was quenched with a saturated solution of NH_4Cl (25 mL) and then concentrated in vacuo to remove THF. Then dichloromethane was added to aqueous mixture and the two phases were separated. After collecting the organic layer, the aqueous layer was extracted twice with dichloromethane and organic layers were combined. The organic layer was washed with $NaHCO_3$ solution, brine, then dried over anhydrous Na_2SO_4, and concentrated in vacuo. The residue was purified with flash column chromatography on silica gel (ethyl acetate/ hexane, 1:9) to afford 3.6 g (78%) of product, (E)-3-hydroxy-1-(3-hydroxy-4-methoxyphenyl)-7-(tritylthio)hept-4-en-1-one, **9i** as a white solid. ^{1}H NMR (500 MHz, $CDCl_3$) δ 7.51 (dd, *J* = 7.3, 1.7 Hz, 2H), 7.42 – 7.39 (m, 7H), 7.30 – 7.25 (m, 9H), 7.20 (t, *J* = 7.3 Hz, 3H), 6.94 (d, *J* = 8.6 Hz, 1H), 6.10 (d, *J* = 9.1 Hz, 1H), 5.65 – 5.59 (m, 1H), 5.50 (dd, *J* = 15.4, 6.2 Hz, 1H), 4.63 (t, *J* = 7.1 Hz, 1H), 3.93 (s, 3H), 3.30 (d, *J* = 3.4 Hz, 1H), 3.08 (qd, *J* = 17.3, 6.0 Hz, 2H), 2.24 – 2.20 (m, 2H), 2.10 (dd, *J* = 15.4, 7.6 Hz, 2H); ^{13}C NMR (126 MHz, $CDCl_3$) δ 198.77, 150.84, 146.66, 144.92, 132.29, 129.82, 129.59, 127.85, 126.59, 123.78, 113.90, 109.62, 77.27, 77.01, 76.76, 68.64, 66.56, 56.08, 44.44, 31.43, 29.71. HRMS (ESI+): Calculated (m/z) for $C_{33}H_{32}O_4S$ $(M+Na)^+$: 497.2121, Found 497.2129.

(4E,4'E)-7,7'-disulfanediylbis(3-hydroxy-1-(3-hydroxy-4-methoxyphenyl)hept-4-en-1-one), JRM-18



10:1 solution of CH_2Cl_2/MeOH (15 mL) solution was prepared in a round bottom flask under vacuum. Iodine (0.72 g, 2.85 mmol, 1.0 equiv.) and sodium acetate (0.17 g, 5.71 mmol, 2.0 equiv.) were dissolved into that under nitrogen atmosphere at 0 °C. (E)-3-hydroxy-1-(3-hydroxy-4-methoxyphenyl)-7-(tritylthio)hept-4-en-1-one, **9i** (1.5 g, 2.85 mmol, 1.0 equiv.) was dissolved in a 10:1 solution of CH_2Cl_2/MeOH (10 mL) and was added dropwise over 20 minutes to the first solution containing iodine and sodium acetate using additional flask. This solution was then allowed to stir for additional 2 hour. The reaction was quenched by adding a saturated sodium thiosulfate ($Na_2S_2O_3$) solution until the mixture turned clear. Then, brine (5 mL) was added and the layers were separated. The aqueous layer was extracted with dichloromethane (3 x 15 mL) and then with ethyl acetate (3 x 15 mL). The residue was purified with flash column chromatography on silica gel hexane/ethyl acetate, 7:3) using triethyl amine (TEA) to afford 1.2 g (75% yield) of product, (4E,4'E)-7,7'-disulfanediylbis(3-hydroxy-1-(3-hydroxy-4-methoxyphenyl)hept-4-en-1-one), **JRM-18** as a white solid. ^{1}H NMR (500 MHz, $CDCl_3$) δ 7.46 – 7.41 (m, 2H), 6.85 (d, J = 8.2 Hz, 1H), 5.74 – 5.66 (m, 1H), 5.58 (dd, J = 15.5, 6.2 Hz, 1H), 4.65 – 4.60 (m, 1H), 3.85 (s, 3H), 3.10 – 3.00 (m, 2H), 2.64 (t, J = 7.4 Hz, 2H), 2.35 (dd, J = 14.1, 6.9 Hz, 2H).; ^{13}C NMR (126 MHz, $CDCl_3$) δ 198.79, 151.04, 146.83, 132.84, 129.58, 129.26, 123.83, 114.11, 109.80, 77.35, 77.09, 76.84, 68.79, 56.08, 44.43, 38.15, 31.93. HRMS (ESI^+): Calculated (m/z) for C28 H34 O8 S2 $(M+Na)^+$: 585.15873, Found 585.1587.

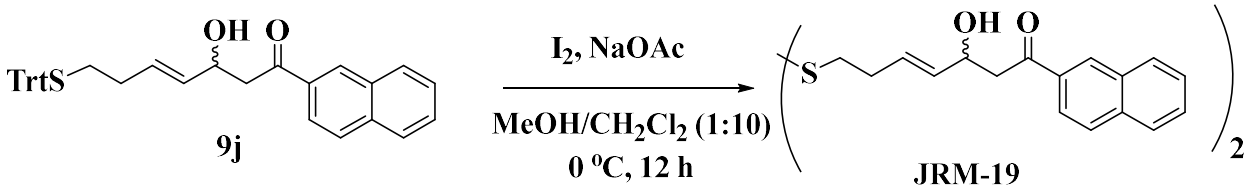
(E)-3-hydroxy-1-(naphthalen-2-yl)-7-(tritylthio)hept-4-en-1-one, 9j



THF (50 mL) was taken in a round bottom flask under nitrogen condition and cooled over a dry ice bath. Later, diisopropylamine (DIPA) (4.70 mL, 33.46 mmol, 4 equiv.) was added into the round bottom flask. Then n-butyllithium (3.09 mL, 33.47 mmol, 4 equiv.) were added dropwise at -78°C and was stirred for 1 hour. 2-Acetonaphthone, **8j** (4.98 g, 29.28 mmol, 3.5 equiv.) was added at -78°C and was allowed to stir for additional 1 hour. Lastly, (E)-5-(tritylthio)pent-2-enal (3 g, 8.36 mmol, 1 equiv.) was added and the mixture was stirred for 1 hour under the same temperature. The reaction was quenched with a saturated solution of NH_4Cl (25 mL) and then concentrated in vacuo to remove THF. Then dichloromethane was added to aqueous mixture and the two phases were separated. After collecting the organic layer, the aqueous layer was extracted twice with dichloromethane and organic layers were combined. The organic layer was washed with $NaHCO_3$ solution, brine, then dried over anhydrous Na_2SO_4, and concentrated in vacuo. The residue was purified with flash column chromatography on silica gel (ethyl acetate/ hexane, 1:9) to afford 3.2 g (72%) of product, (E)-3-hydroxy-1-(naphthalen-2-yl)-7-(tritylthio)hept-4-en-1-one, **9j** as a white solid. ^{1}H NMR (500 MHz, $CDCl_3$) δ 8.45 (s, 1H), 8.00 (dd, J = 8.6, 1.7 Hz, 1H), 7.95 (d, J = 8.1 Hz, 1H), 7.88 (dd, J = 8.3, 5.4 Hz, 2H), 7.63 – 7.59 (m, 1H), 7.58 – 7.54 (m, 1H), 7.41 (d, J = 7.3 Hz, 6H), 7.28 (t, J = 7.6 Hz, 7H), 7.20 (t, J = 7.3 Hz, 3H), 5.69 – 5.62 (m, 1H), 5.55 (dd, J = 15.4, 6.2 Hz, 1H), 4.72 (dd, J = 10.7, 7.0 Hz, 1H), 3.27 (t, J = 6.0 Hz, 2H), 2.24 (dd, J = 11.5, 4.3 Hz, 2H), 2.14 – 2.07 (m, 2H); ^{13}C NMR (126 MHz, $CDCl_3$) δ 200.24, 144.92, 135.82, 134.02, 132.45, 132.23, 130.18, 130.00, 129.68, 129.62, 128.80, 128.63, 127.90, 127.85, 126.96, 126.63, 123.59,

77.32, 77.06, 76.81, 68.56, 66.59, 45.14, 31.47. HRMS (ESI+): Calculated (m/z) for $C_{36}H_{32}O_2S$ $(M+Na)^+$: 497.2121, Found 497.2129.

(4E,4'E)-7,7'-disulfanediylbis(3-hydroxy-1-(naphthalen-2-yl)hept-4-en-1-one), JRM-19

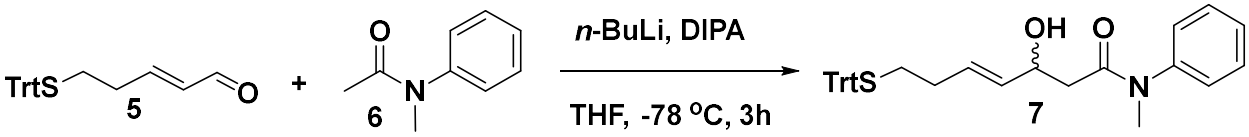


10:1 solution of CH_2Cl_2/MeOH (15 mL) solution was prepared in a round bottom flask under vacuum. Iodine (0.72 g, 2.83 mmol, 1.0 equiv.) and sodium acetate (0.46 g, 5.674 mmol, 2.0 equiv.) were dissolved into that under nitrogen atmosphere at 0 °C. (E)-3-hydroxy-1-(naphthalen-2-yl)-7-(tritylthio)hept-4-en-1-one, **9j** (1.5 g, 2.83 mmol, 1.0 equiv.) was dissolved in a 10:1 solution of CH_2Cl_2/MeOH (10 mL) and was added dropwise over 20 minutes to the first solution containing iodine and sodium acetate using additional flask. This solution was then allowed to stir for additional 2 hour. The reaction was quenched by adding a saturated sodium thiosulfate ($Na_2S_2O_3$) solution until the mixture turned clear. Then, brine (5 mL) was added and the layers were separated. The aqueous layer was extracted with dichloromethane (3 x 15 mL) and then with ethyl acetate (3 x 15 mL). The residue was purified with flash column chromatography on silica gel hexane/ethyl acetate, 7:3) using triethyl amine (TEA) to afford 1.1 g (68% yield) of product, (4E,4'E)-7,7'-disulfanediylbis(3-hydroxy-1-(naphthalen-2-yl)hept-4-en-1-one), **JRM-19** as a white solid. δ H (500 MHz, CDCl3) 8.49 (1 H, s), 8.04 (1 H, dd, J 8.6, 1.8), 7.99 (1 H, d, J 8.0), 7.93 – 7.88 (2 H, m), 7.66 – 7.62 (1 H, m), 7.60 – 7.56 (1 H, m), 5.89 – 5.83 (1 H, m), 5.75 (1 H, dd, J 15.5, 6.1), 4.82 (1 H, dd, J 10.7, 7.0), 3.40 – 3.30 (2 H, m), 2.79 (2 H, t, J 7.2), 2.50 (2 H, dd, J 14.4, 7.0); ^{13}C NMR (126 MHz, $CDCl_3$) δ 200.17, 135.82, 134.03, 132.87, 132.46, 130.17, 129.67, 129.36,

128.79, 128.63, 127.83, 126.96, 123.58, 77.29, 77.03, 76.78, 68.60, 45.18, 38.23, 32.00. HRMS (ESI+): Calculated (m/z) for C34 H34 O4 S2 $(M+Na)^+$: 593.17907, Found 593.1781.

Series 3: Amide

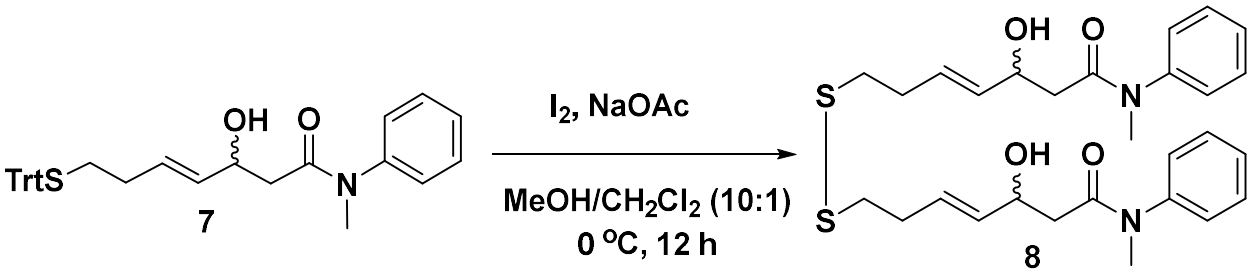
(*E*)-3-hydroxy-*N*-methyl-*N*-phenyl-7-(tritylthio)hept-4-enamide, 7



Under nitrogen, 50mL of THF (50mL) was poured into a round bottom flask and cooled on dry ice. Later, diisopropylamine (DIPA) (4.70 mL, 33.46 mmol, 4 equiv.) was added into the round bottom flask. In the next step, n-butyllithium (3.09 mL, 33.47 mmol, 4 equiv.) was added dropwise at -78°C and stirred for 1 hour.was added at -78°C and was allowed to stir for additional 1 hour. Lastly, (*E*)-5-(tritylthio)pent-2-enal, 5 (3 g, 8.36 mmol, 1 equiv.) was added and the mixture was stirred for 1 hour under the same temperature. As a final step, the reaction was quenched using 25 mL of NH4Cl (40%) and concentrated in vacuo to remove THF. During the workup, dichloromethane was added to the aqueous mixture, and two phases were separated. Following the collection of the organic layer, dichloromethane was used twice to extract the aqueous layer before the organic layers were combined. The organic layer was washed with $NaHCO_3$ solution, brine, then dried over anhydrous Na_2SO_4, and concentrated in vacuo. The residue was purified with flash column chromatography on silica gel (ethyl acetate/ hexane, 1:9) to afford 3.2 g (75%) of product, (*E*)-3-hydroxy-*N*-methyl-*N*-phenyl-7-(tritylthio)hept-4-enamide, 7 as a white solid. ^{1}H NMR (500

MHz, $CDCl_3$) δ 7.44 – 7.36 (m, 1H), 7.28 (dd, J = 9.4, 6.0 Hz, 1H), 7.24 – 7.19 (m, 1H), 7.17 (dd, J = 5.8, 3.5 Hz, 1H), 5.50 (dt, J = 15.8, 6.7 Hz, 1H), 5.30 (dd, J = 15.4, 5.9 Hz, 1H), 4.41 – 4.34 (m, 1H), 3.27 (s, 3H), 2.26 (dd, J = 16.3, 3.1 Hz, 1H), 2.21 (d, J = 8.3 Hz, 1H), 2.17 (t, J = 5.9 Hz, 1H), 2.09 – 2.00 (m, 1H). ^{13}C NMR (126 MHz, $CDCl_3$) δ 172.40, 144.91, 143.32, 132.21, 129.95, 129.59, 129.46, 128.13, 127.84, 127.24, 126.57, 68.96, 66.52, 40.30, 37.11, 31.45, 29.72, HRMS (ESI+): Calculated (m/z) for $C_{33}H_{33}NO_2S$ $(M+Na)^+$: 530.21242, Found 530.21372.

(4*E*,4'*E*)-7,7'-disulfanediylbis(3-hydroxy-*N*-methyl-*N*-phenylhept-4-enamide), 8 (JRM-20)

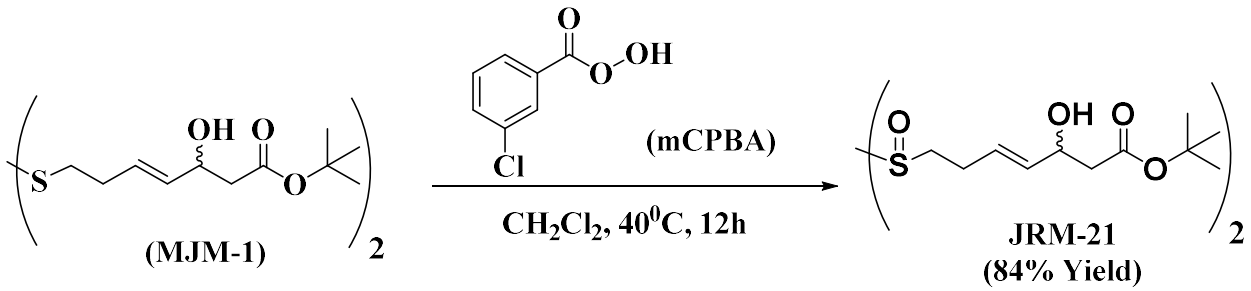


10:1 solution of CH_2Cl_2/MeOH (15 mL) solution was prepared in a round bottom flask under vacuum. Iodine (0.72 g, 2.83 mmol, 1.0 equiv.) and sodium acetate (0.46 g, 5.674 mmol, 2.0 equiv.) were dissolved into that under nitrogen atmosphere at 0 °C. Compound 7(1 g, 1.97 mmol, 1.0 equiv.) was dissolved in a 10:1 solution of CH_2Cl_2/MeOH (10 mL) and was added dropwise over 20 minutes to the first solution containing iodine and sodium acetate using an additional flask. This solution was then allowed to stir for additional 2 hours. The reaction was quenched by adding a saturated sodium thiosulfate ($Na_2S_2O_3$) solution until the mixture turned clear. Then, brine (5 mL) was added, and the layers were separated. The aqueous layer was extracted with dichloromethane (3 x 15 mL) and then with ethyl acetate (3 x 15 mL). The crude was purified with flash column chromatography on silica gel using hexane/ethyl acetate mobile phase to afford 0.8 g (76% yield) of product, 8 as a white solid. ^{1}H NMR (500 MHz, CDCl3) δ 7.46 – 7.41 (m, 1H), 7.39 – 7.34 (m,

1H), 7.20 – 7.15 (m, 1H), 5.67 – 5.59 (m, 1H), 5.42 (dd, *J* = 15.4, 6.1 Hz, 1H), 4.45 – 4.38 (m, 1H), 3.28 (s, 3H), 2.65 (dd, *J* = 11.4, 4.2 Hz, 1H), 2.37 – 2.28 (m, 1H), 2.27 – 2.17 (m, 1H). ^{13}C NMR (126 MHz, $CDCl_3$) δ 172.35, 143.29, 132.75, 129.98, 128.86, 128.17, 127.23, 68.95, 40.39, 38.11, 37.16, 31.92. HRMS (ESI+): Calculated (m/z) for C28 H36 N2 O4 S2 $(M+H)^+$: 529.21893, Found 529.22028.

Series 4: Sulfoxide Derivatives

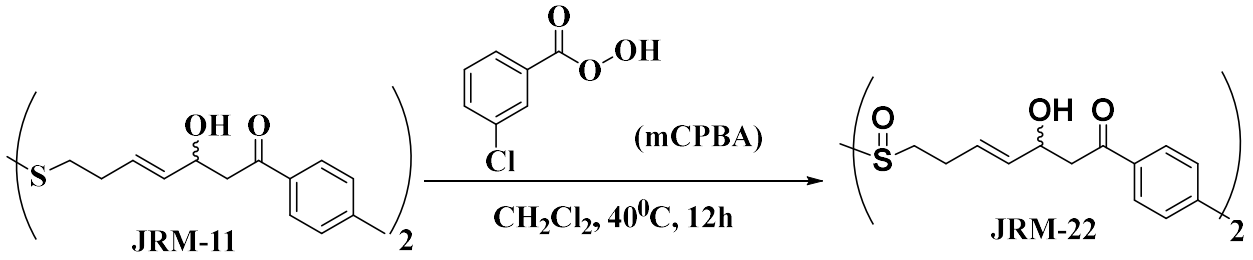
JRM-21



In a charged three-neck round bottom flask, a solution of **MJM-1** (0.7 g, 0.151 mmol, 1 equiv.) dissolved in 20 mL DCM was added under nitrogen condition. Then, mCPBA (26.1 mg, 0.151 mmol, 1.1 equiv.) dissolved in DCM was added to the round bottom flask dropwise. When the addition was done, the reaction was continued under reflux condition for 1.5 hours. The completion of reaction was confirmed by taking TLC at hexane/ethyl acetate, 7:3). The residue was purified with flash column chromatography on silica gel hexane/ethyl acetate, 7:3) using triethyl amine (TEA) to afford 0.8 g (84% yield) of product, (4E,4'E)-7,7'-disulfanediylbis(3-hydroxy-1-(naphthalen-2-yl)hept-4-en-1-one), **JRM-21** as a white solid. ^{1}H NMR ($CDCl_3$, 500 MHz): δ (ppm) 5.70-5.60 (m, 1H), 5.48 (dd, J = 15.0, 6.0 Hz, 1H), 4.38 (q, J = 6.0 Hz, 1H), 3.3 (s, 1H), 2.64 (t, J = 7.5 Hz, 2H), 2.38-2.31 (m, 4H), 1.38 (s, 9H); ^{13}C NMR ($CDCl_3$, 125 MHz): δ (ppm)

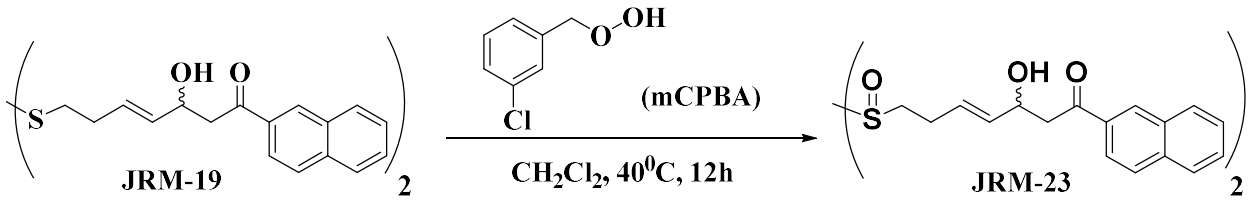
171.6, 132.8, 129.1, 81.2, 68.7, 42.5, 38.1, 31.8, 28.1. HRMS (ESI+): Calculated (m/z) for $C_{34}H_{34}O_4S_2Na$ $(M+Na)^+$: 485.2002, Found 485.1995.

1H S-((E)-5-hydroxy-7-oxo-7-(p-tolyl)hept-3-en-1-yl) (E)-5-hydroxy-7-oxo-7-(p-tolyl)hept-3-ene-1-sulfinothioate, JRM-22



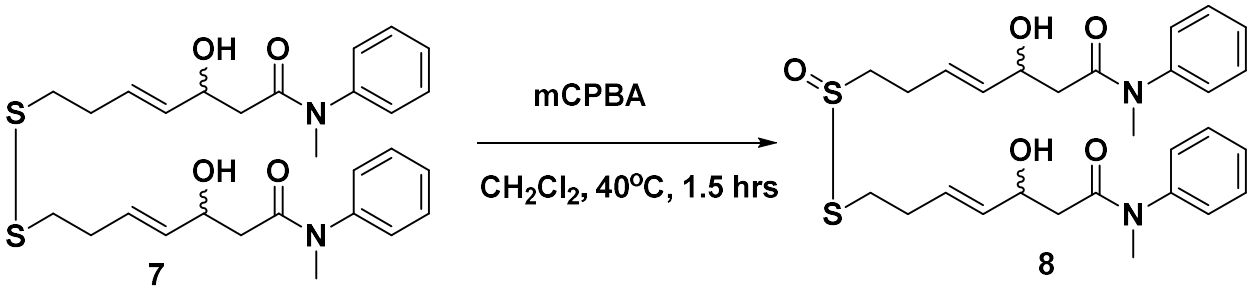
In a charged three-neck round bottom flask, a solution of (4E,4'E)-7,7'-disulfanediylbis(3-hydroxy-1-(p-tolyl)hept-4-en-1-one), **37** (0.7 g, 1.40 mmol, 1 equiv.) dissolved in 20 mL DCM was added under nitrogen condition. Then, mCPBA (26.1 mg, 0.0151 mmol, 1.1 equiv.) dissolved in DCM was added to the round bottom flask dropwise. When the addition was done, the reaction was continued under reflux condition for 1.5 hours. The completion of reaction was confirmed by taking TLC at hexane/ethyl acetate, 7:3). The residue was purified with flash column chromatography on silica gel hexane/ethyl acetate, 7:3) using triethyl amine (TEA) to afford 0.5 g (70% yield) of product, (4E,4'E)-7,7'-disulfanediylbis(3-hydroxy-1-(naphthalen-2-yl)hept-4-en-1-one), **37S** as a white solid. ^{1}H NMR (500 MHz, $CDCl_3$) δ 7.87 (dd, *J* = 8.2, 2.1 Hz, 2H), 7.31 – 7.27 (m, 3H), 5.87 – 5.79 (m, 1H), 5.78 – 5.72 (m, 1H), 4.78 – 4.73 (m, 1H), 3.30 – 3.11 (m, 4H), 2.62 (dd, *J* = 14.9, 6.6 Hz, 1H), 2.59 – 2.52 (m, 1H), 2.44 (s, 3H); ^{13}C NMR (126 MHz, $CDCl_3$) δ 199.82, 144.69, 134.15, 129.44, 128.56, 128.28, 127.13, 68.20, 55.25, 44.75, 33.48, 32.92, 26.20, 21.71.HRMS (ESI+): Calculated (m/z) for $C_{34}H_{34}O_4S_2Na$ $(M+Na)^+$: 485.2002, Found 485.1995.

S-((E)-5-hydroxy-7-(naphthalen-2-yl)-7-oxohept-3-en-1-yl)-(E)-5-hydroxy-7-(naphthalen-2-yl)-7-oxohept-3-ene-1-sulfinothioate, JRM-23



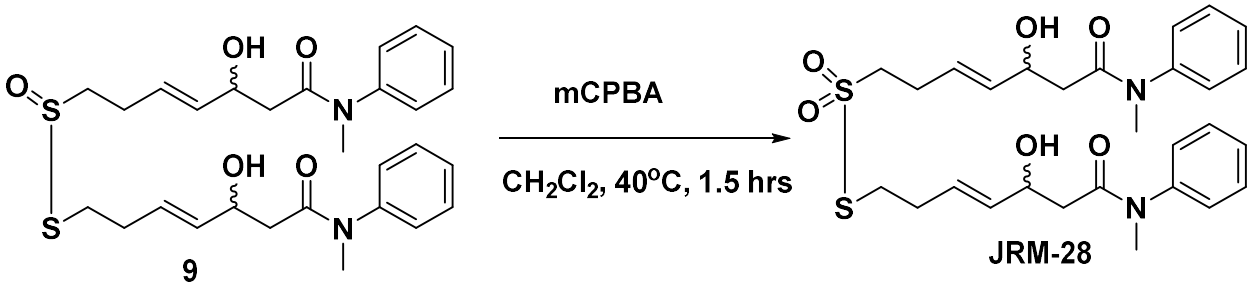
In a charged three-neck round bottom flask, a solution of (4E,4'E)-7,7'-disulfanediylbis(3-hydroxy-1-(naphthalen-2-yl)hept-4-en-1-one), **61** (0.7 g, 0.151 mmol, 1 equiv.) dissolved in 20 mL DCM was added under nitrogen condition. Then, mCPBA (26.1 mg, 0.151 mmol, 1.1 equiv.) dissolved in DCM was added to the round bottom flask dropwise. When the addition was done, the reaction was continued under reflux condition for 1.5 hours. The completion of reaction was confirmed by taking TLC at hexane/ethyl acetate, 7:3). The residue was purified with flash column chromatography on silica gel hexane/ethyl acetate, 7:3) using triethyl amine (TEA) to afford 0.5 g (70% yield) of product, (4E,4'E)-7,7'-disulfanediylbis(3-hydroxy-1-(naphthalen-2-yl)hept-4-en-1-one), **61B** as a white solid. ^{1}H NMR (500 MHz, $CDCl_3$) δ 8.03 (ddd, *J* = 21.9, 12.0, 5.1 Hz, 2H), 7.95 – 7.88 (m, 2H), 7.67 – 7.56 (m, 2H), 7.28 (s, 1H), 5.91 – 5.83 (m, 1H), 5.83 – 5.74 (m, 1H), 4.83 (d, *J* = 5.3 Hz, 1H), 3.41 – 3.30 (m, 2H), 3.30 – 3.17 (m, 2H), 2.71 – 2.52 (m, 2H); ^{13}C NMR ($CDCl_3$, 125 MHz): δ (ppm) (126 MHz, $CDCl_3$) δ 172.25, 143.22, 133.97, 133.82, 133.69, 130.04, 128.26, 127.90, 127.79, 127.21, 126.81, 113.93, 68.63, 55.16, 40.39, 40.27, 37.15, 33.52, 32.31, 26.01. HRMS (ESI+): Calculated (m/z) for $C_{34}H_{34}O_4S_2Na$ $(M+Na)^+$: 485.2002, Found 485.1995.

***S*-((*E*)-5-hydroxy-7-(methyl(phenyl)amino)-7-oxohept-3-en-1-yl) (*E*)-5-hydroxy-7-(methyl(phenyl)amino)-7-oxohept-3-ene-1-sulfinothioate, 9**



In a charged three-neck round bottom flask, a solution of JRM-20 (0.7 g, 0.151 mmol, 1 equiv.) dissolved in 20 mL DCM was added under nitrogen condition. Then, mCPBA (26.1 mg, 0.151 mmol, 1.1 equiv.) dissolved in DCM was added to the round bottom flask dropwise. When the addition was done, the reaction was continued under reflux condition for 1.5 hours. The completion of reaction was confirmed by taking TLC at hexane/ethyl acetate, 7:3). The residue was purified with flash column chromatography on silica gel hexane/ethyl acetate to afford 0.8 g (84% yield) of product, 9 as a brown solid. ^{1}H NMR (500 MHz, $CDCl_3$) δ 7.40 – 7.34 (m, 1H), 7.30 (td, *J* = 7.6, 3.2 Hz, 1H), 7.14 – 7.08 (m, 1H), 5.64 – 5.53 (m, 1H), 5.41 (ddd, *J* = 21.5, 10.8, 3.6 Hz, 1H), 4.41 – 4.34 (m, 1H), 3.21 (s, 2H), 3.07 (dd, *J* = 8.1, 5.6 Hz, 1H), 3.02 – 2.96 (m, 1H), 2.43 (dd, *J* = 15.5, 7.8 Hz, 1H), 2.40 – 2.32 (m, 1H), 2.20 (ddd, *J* = 16.3, 5.5, 2.6 Hz, 1H), 2.17 – 2.08 (m, 1H).; ^{13}C NMR (126 MHz, $CDCl_3$) δ 172.26, 143.28, 143.22, 133.82, 133.69, 130.03, 128.25, 127.90, 127.21, 126.81, 68.76, 68.62, 55.16, 40.39, 40.27, 37.15, 33.49, 32.33, 26.01. HRMS (ESI+): Calculated (m/z) for $C_{38}H_{36N2}O_5S_2Na$ $(M+H)^+$: 545.2138, Found 545.2133.

Synthesis of *S*-((*E*)-5-hydroxy-7-(methyl(phenyl)amino)-7-oxohept-3-en-1-yl) (*E*)-5-hydroxy-7-(methyl(phenyl)amino)-7-oxohept-3-ene-1-sulfonothioate, JRM-28

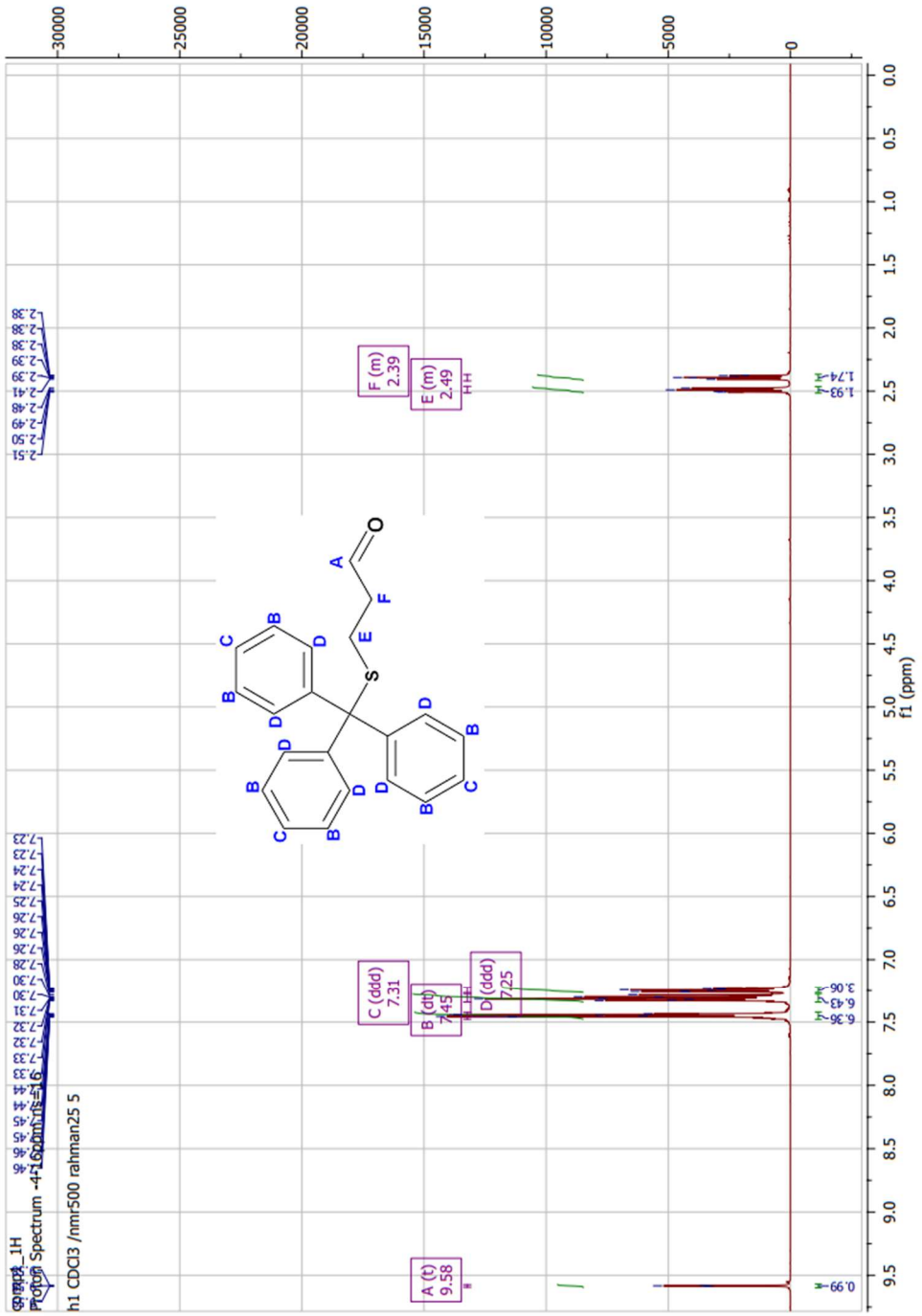


In a charged three-neck round bottom flask, a solution of compound **9** (70 mg, 0.151 mmol, 1 equiv.) dissolved in 20 mL DCM was added under nitrogen condition. Then, mCPBA (52 mg, 0.51 mmol, 2 equiv.) dissolved in DCM was added to the round bottom flask dropwise. When the addition was done, the reaction was continued under reflux condition for 1.5 hours. The completion of reaction was confirmed by taking TLC at hexane/ethyl acetate, 7:3). The residue was purified with flash column chromatography on silica gel hexane/ethyl acetate, 7:3) using triethyl amine (TEA) to afford 0.7 g (93% yield) of product, (4E,4'E)-7,7'-disulfanediylbis(3-hydroxy-1-(naphthalen-2-yl)hept-4-en-1-one), **JRM-28** as a light brown solid. 1H NMR (500 MHz, CDCl3) δ 7.49 – 7.43 (m, 1H), 7.42 – 7.37 (m, 1H), 7.20 (dd, *J* = 5.3, 4.4 Hz, 1H), 5.69 – 5.60 (m, 1H), 5.53 – 5.45 (m, 1H), 4.45 (dd, *J* = 8.9, 5.2 Hz, 1H), 3.34 – 3.30 (m, 1H), 3.30 (s, 3H), 3.13 (t, *J* = 7.3 Hz, 1H), 2.60 – 2.54 (m, 1H), 2.42 (dd, *J* = 14.3, 7.1 Hz, 1H), 2.33 – 2.27 (m, 1H), 2.24 – 2.18 (m, 1H); ^{13}C NMR (126 MHz, $CDCl_3$) δ 172.24, 172.19, 143.22, 143.20, 134.24, 134.15, 130.05, 128.28, 128.26, 127.21, 125.78, 68.57, 67.98, 61.74, 40.25, 40.21, 37.16, 32.36, 26.26, 25.62. HRMS (ESI+): Calculated (m/z) for $C_{28}H_{36}N_2O_6S_2$ $(M+H)^+$: 561.2087, Found 561.2090.

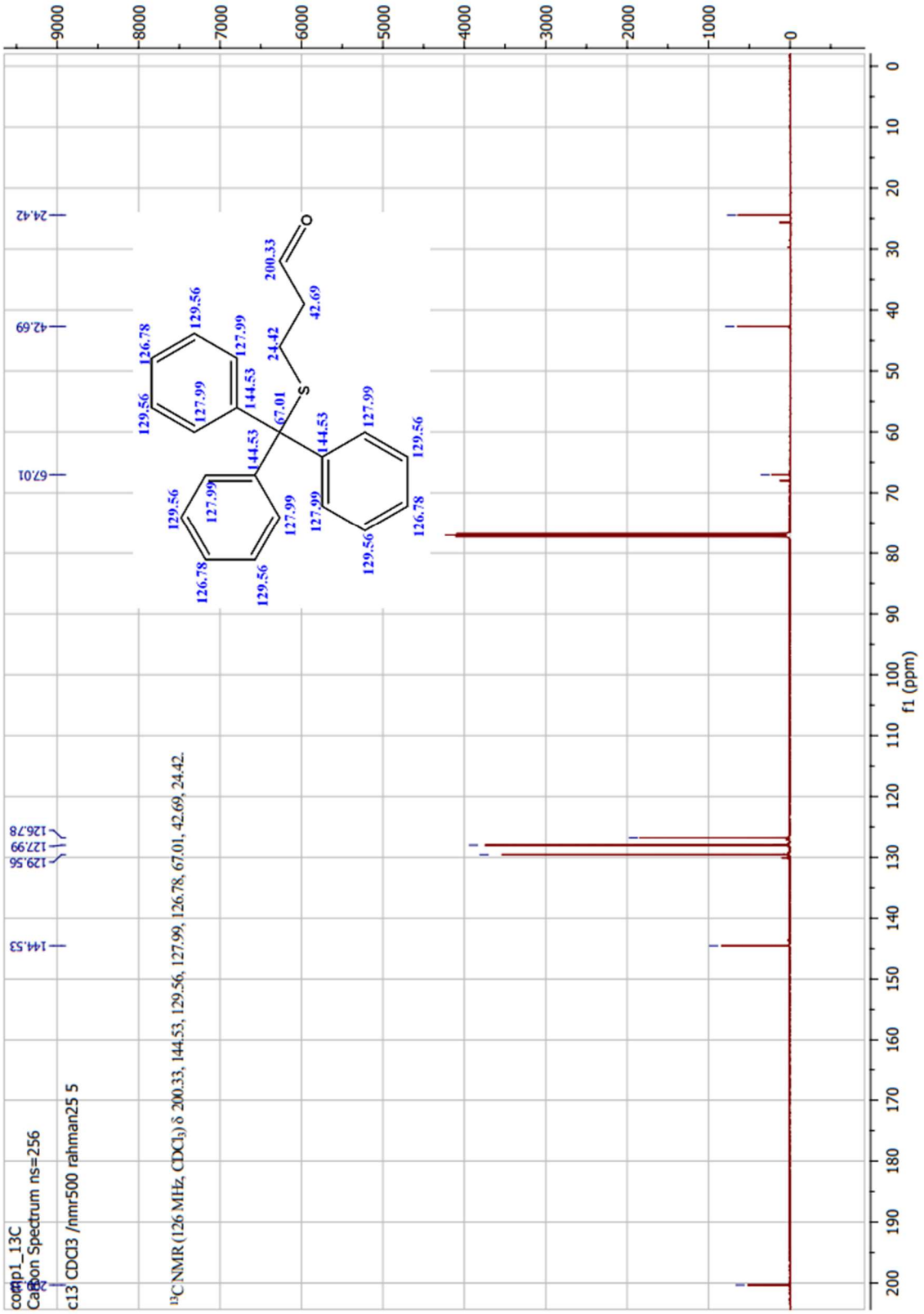
Appendix B

Supporting Information

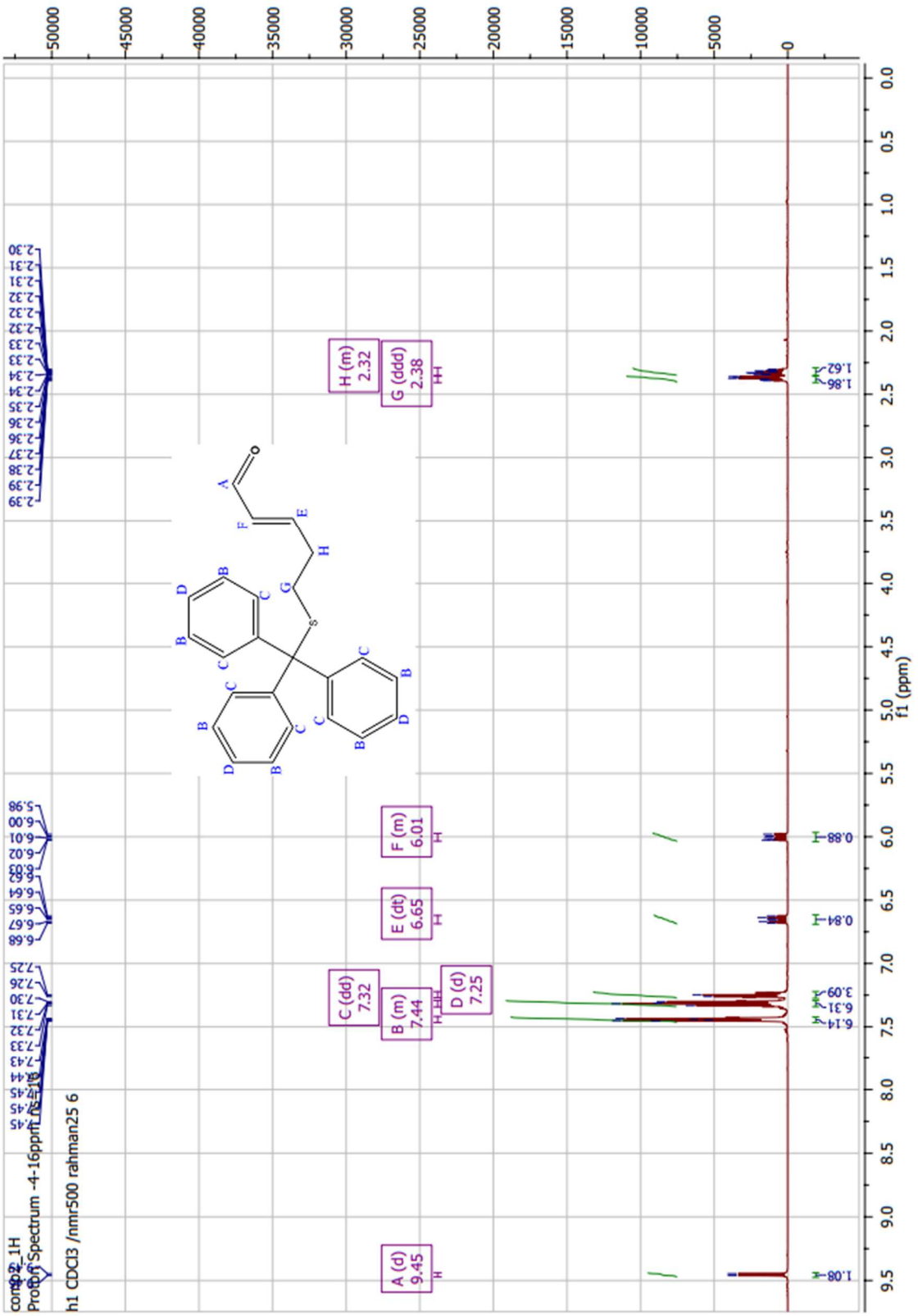
^{1}H NMR Spectrum of Compound 3(300 MHz, $CDCl_3$)



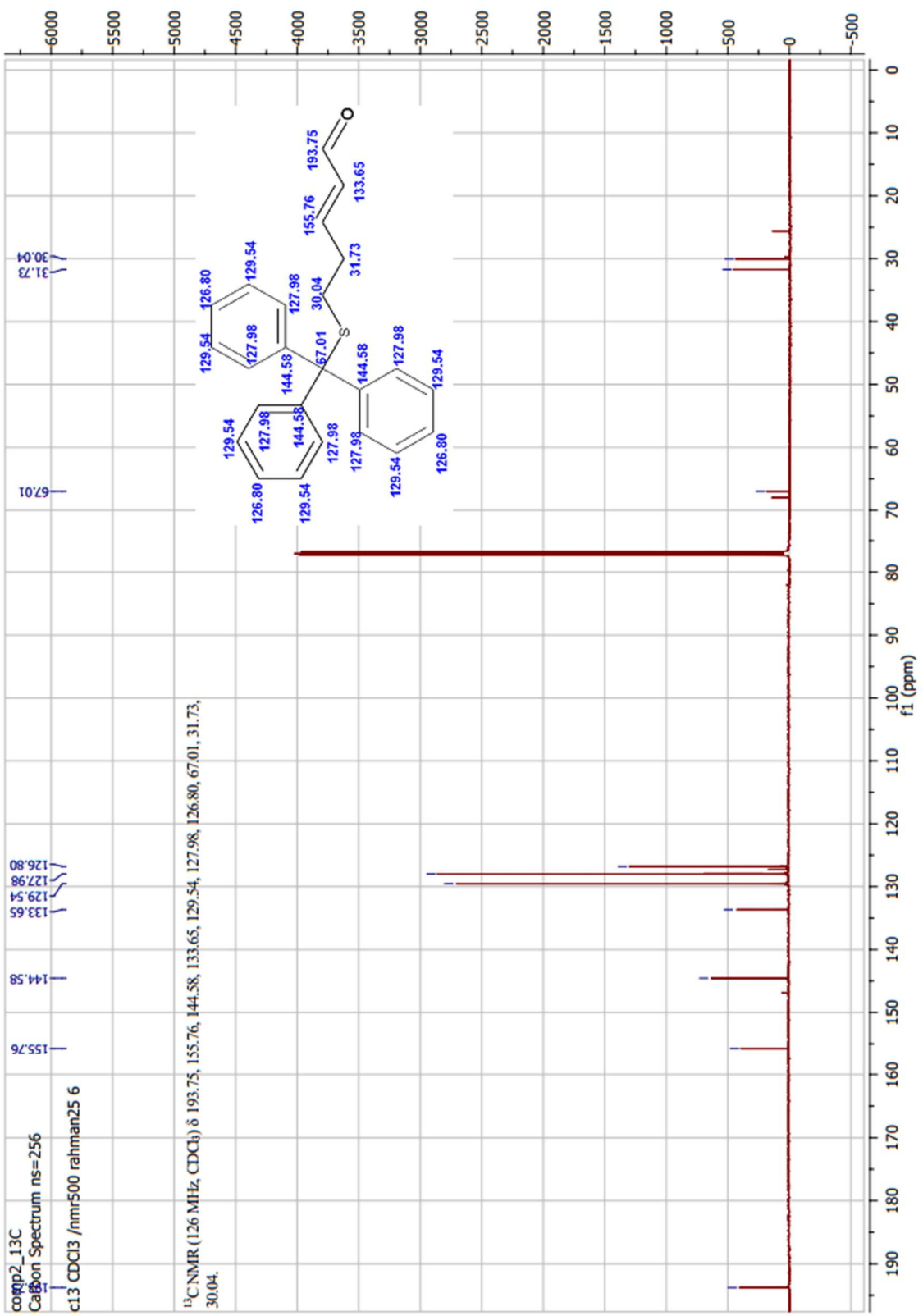
$^{13}C\{1H\}$ (proton-decoupled carbon) NMR Spectrum of Compound 3(125MHz, $CDCl_3$)



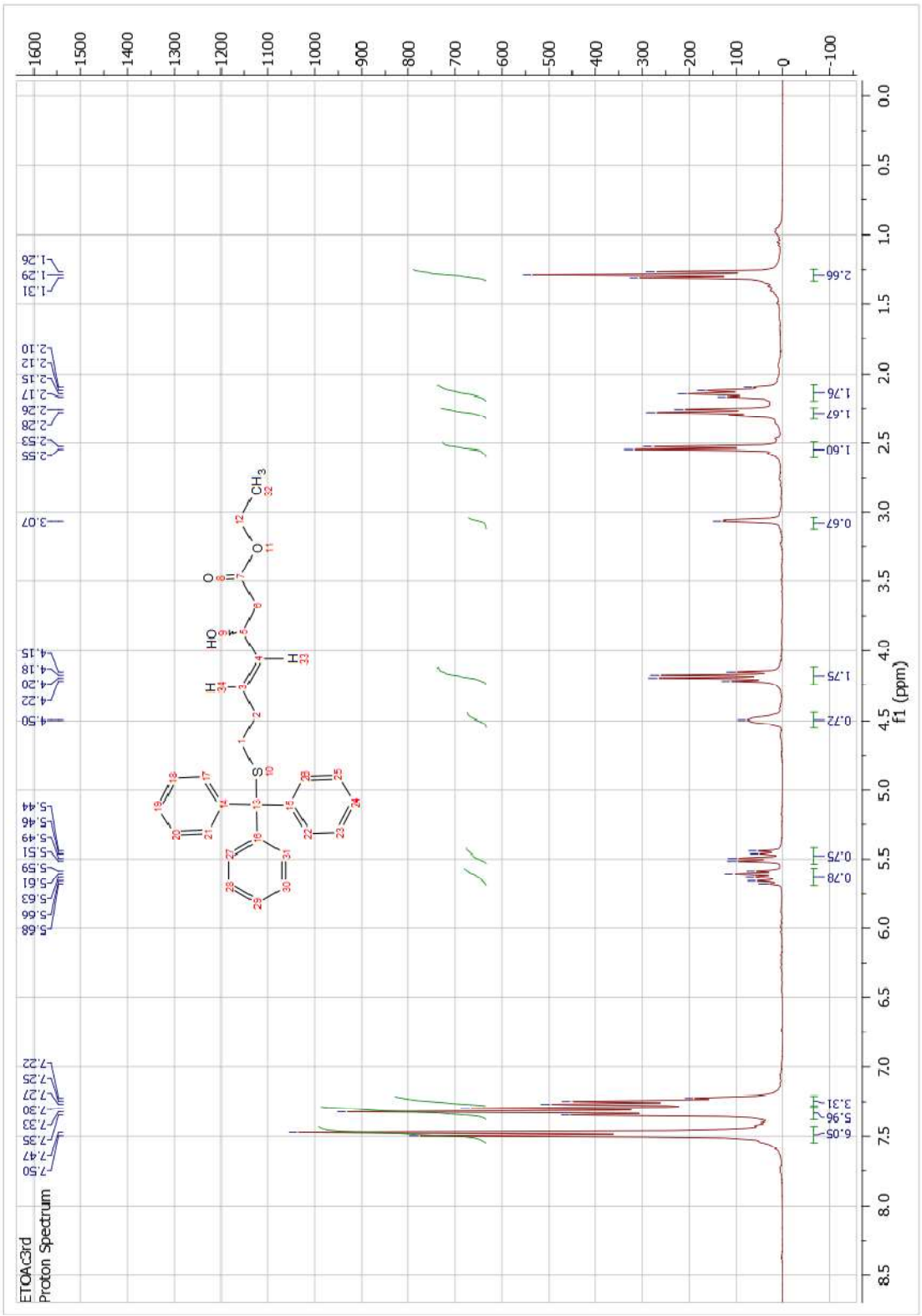
^{1}H NMR Spectrum of Compound 5 (500 MHz, $CDCl_3$)



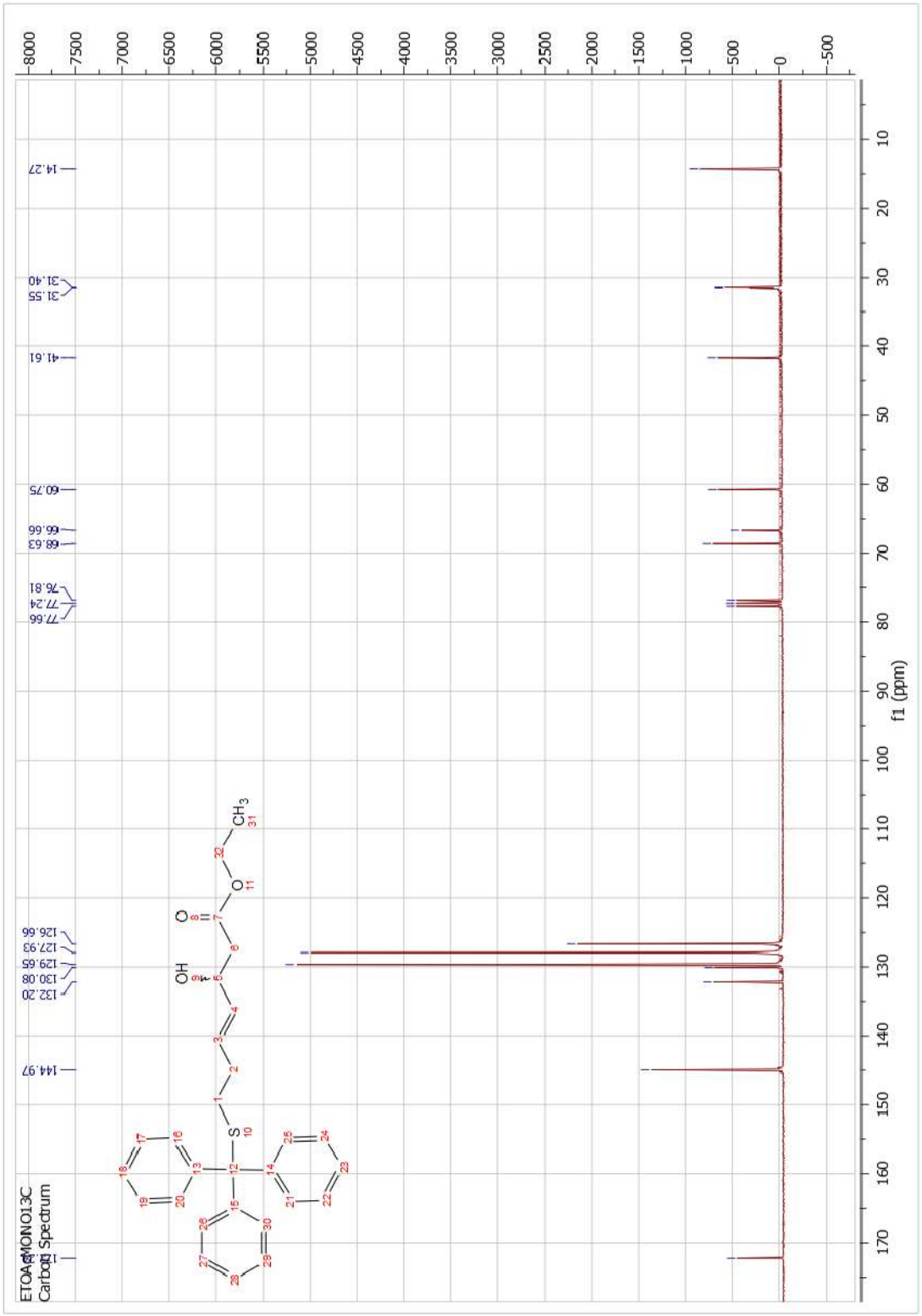
$^{13}C\{1H\}$ (proton-decoupled carbon) NMR Spectrum of Compound 5(125MHz, $CDCl_3$)



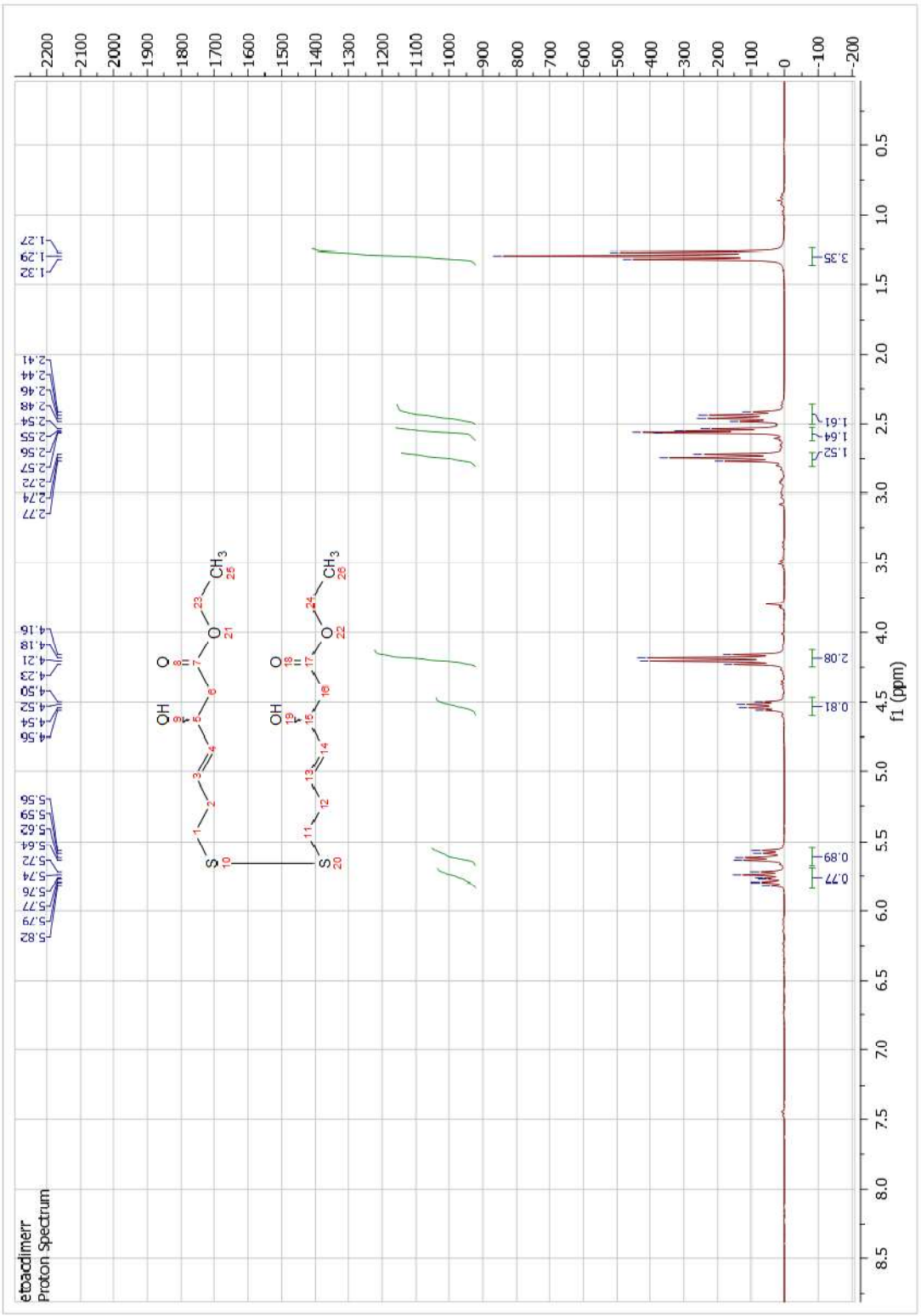
^{1}H NMR Spectrum of (E)-ethyl -3-hydroxy-7-(tritylthio)hept-4-enoate, 7a (500 MHz, $CDCl_3$)



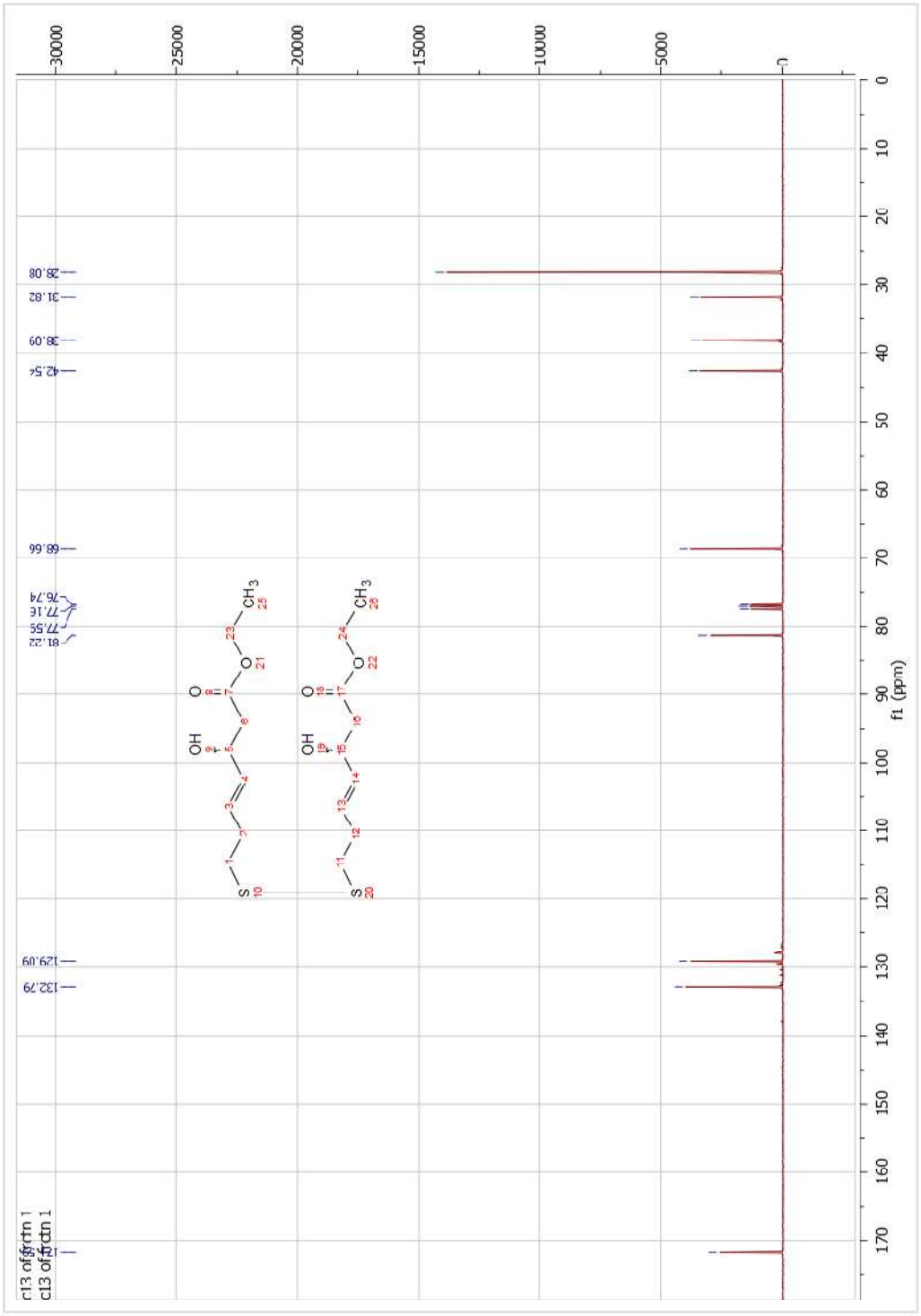
$^{13}C\{1H\}$ (proton-decoupled carbon) NMR Spectrum of (E)-ethyl -3-hydroxy-7-(tritylthio)hept-4-enoate, 7a (500 MHz, $CDCl_3$)



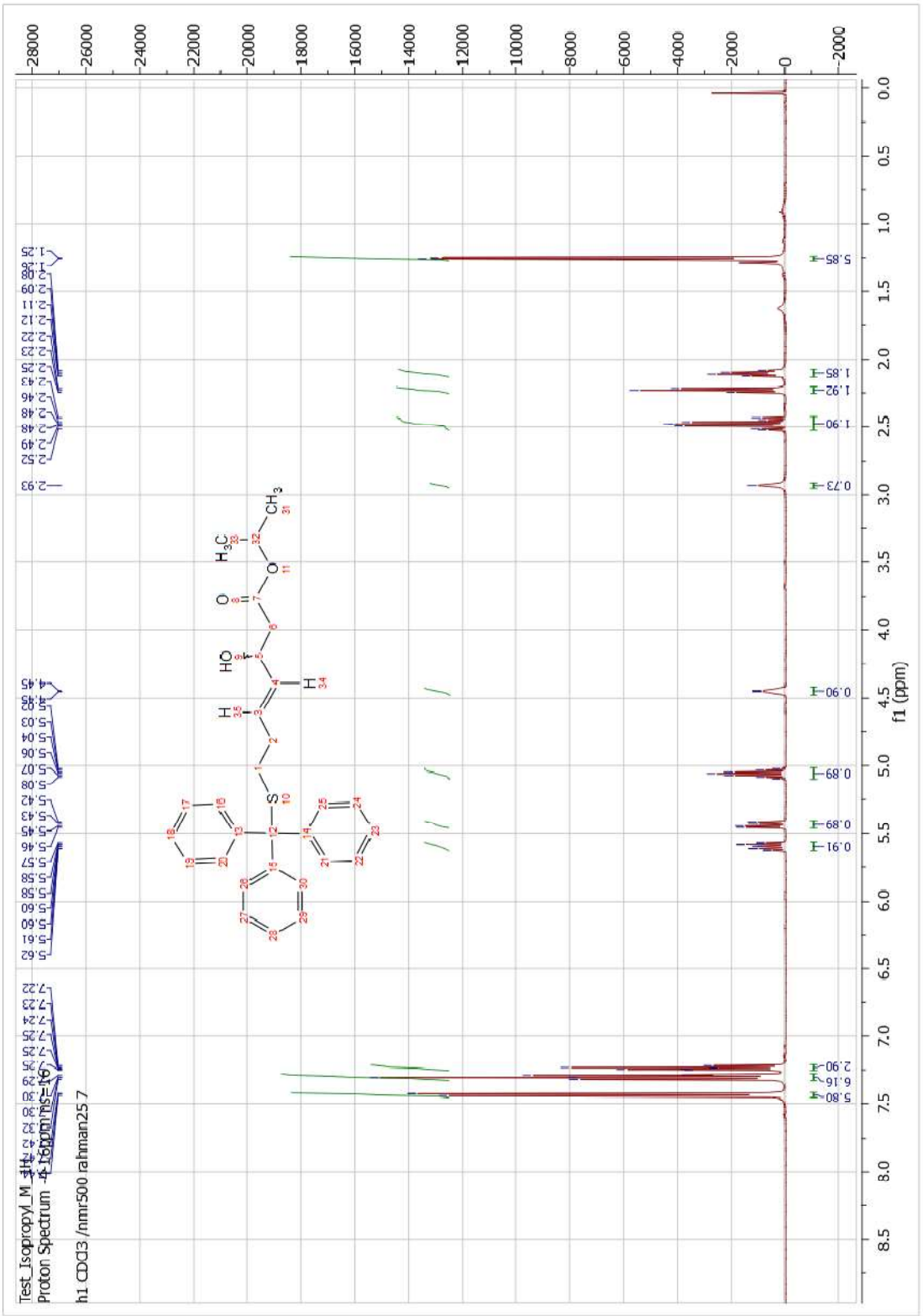
^{1}H NMR Spectrum of (4E,4'E)-diethyl 7,7'-disulfanediyl-bis(3-hydroxyhept-4-enoate), JRM-1



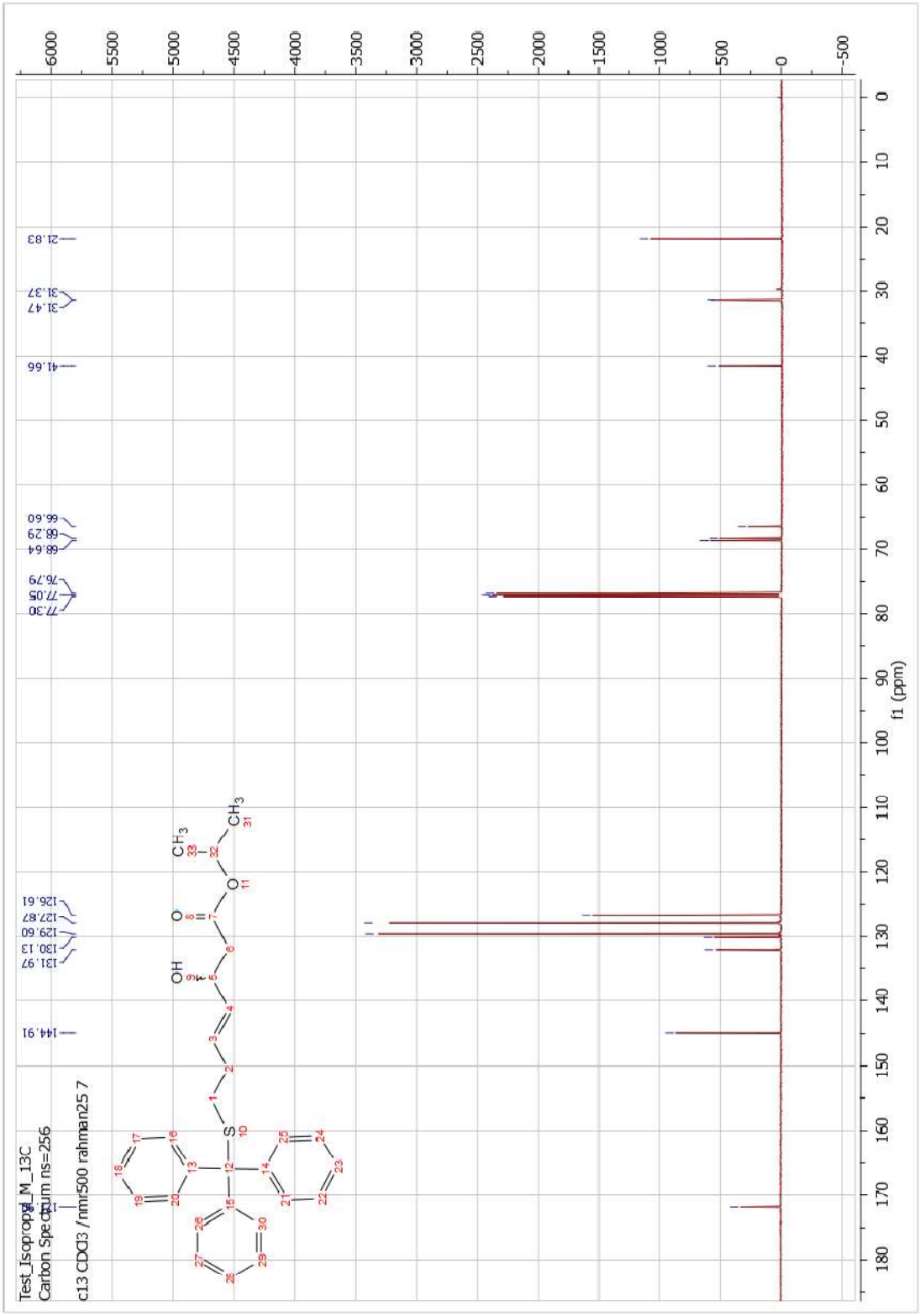
$^{13}C\{1H\}$ (proton-decoupled carbon) NMR Spectrum of (4E,4'E)-diethyl 7,7'-disulfanediyl-bis(3-hydroxyhept-4-enoate), JRM-1



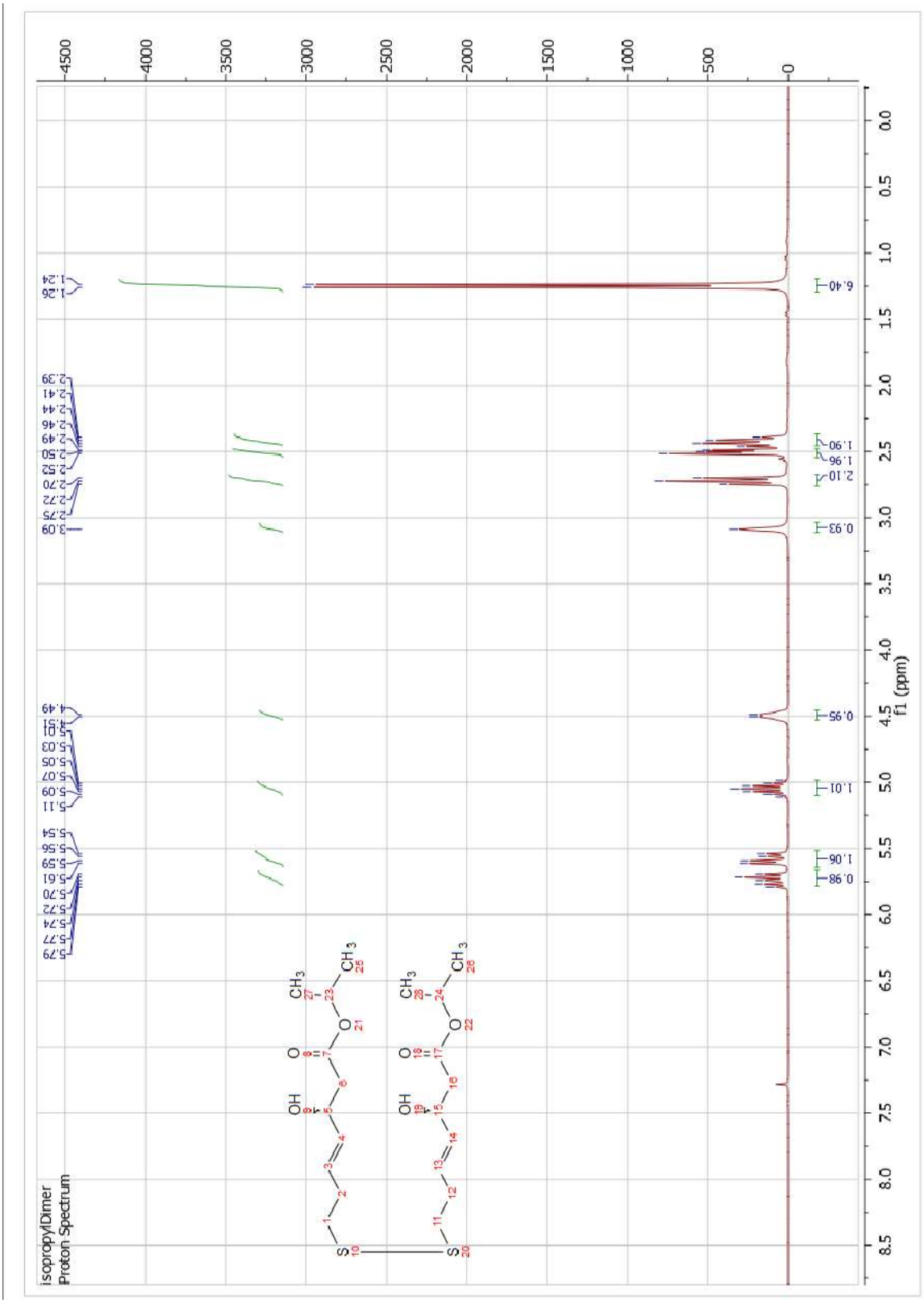
1H (E)-Isopropyl-3-hydroxy-7-(tritylthio)hept-4-enoate, 7b



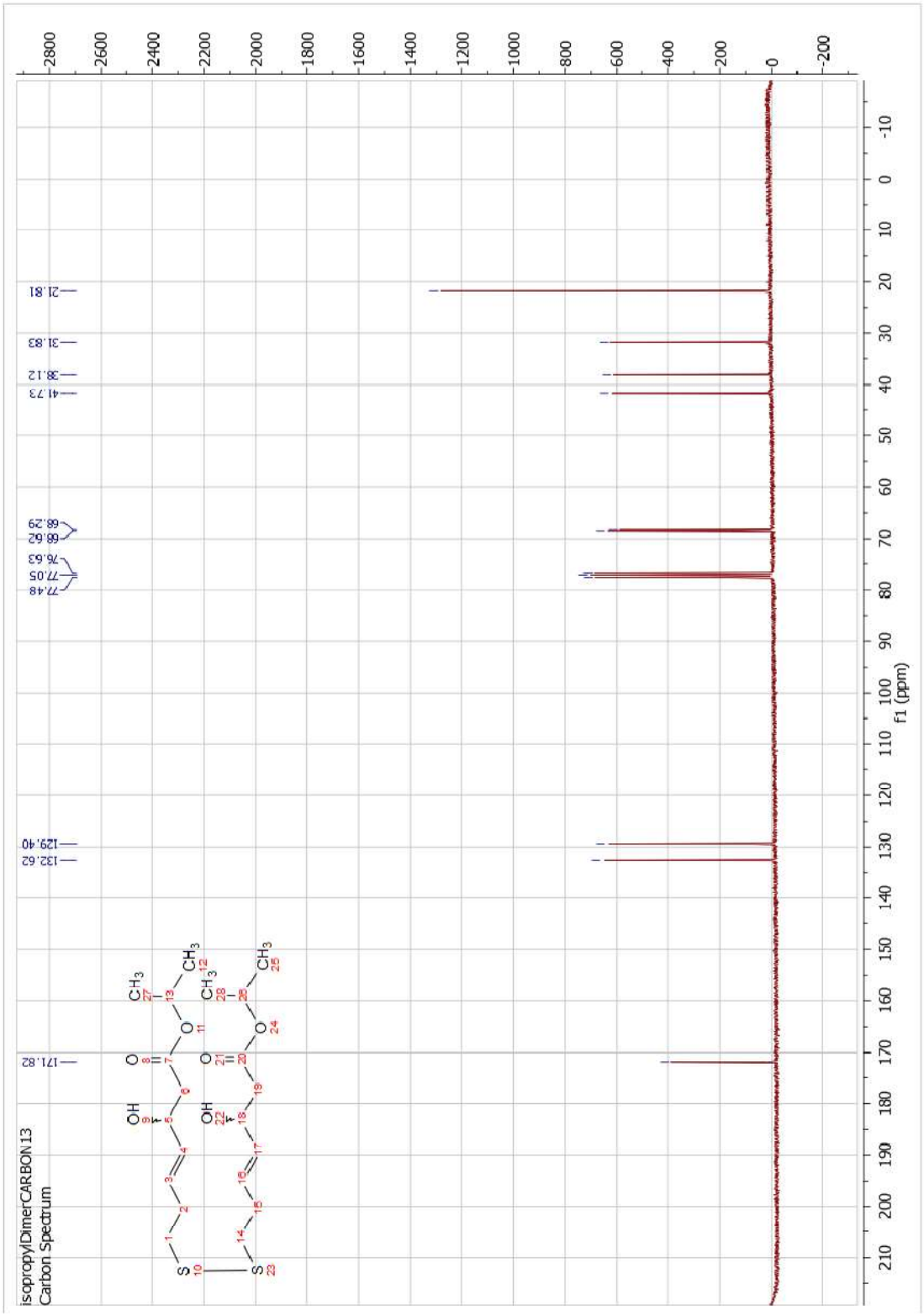
$^{13}C\{1H\}$ (proton-decoupled carbon) NMR Spectrum of (E)-Isopropyl-3-hydroxy-7-(tritylthio)hept-4-enoate, 7b



^{1}H NMR Spectrum of (4E,4'E)-diisopropyl 7,7'-disulfanediyl-bis(3-hydroxyhept-4-enoate), JRM-2



$^{13}C\{1H\}$ (proton-decoupled carbon) NMR Spectrum of (4E,4'E)-diisopropyl 7,7'-disulfanediyl-bis(3-hydroxyhept-4-enoate), JRM-2

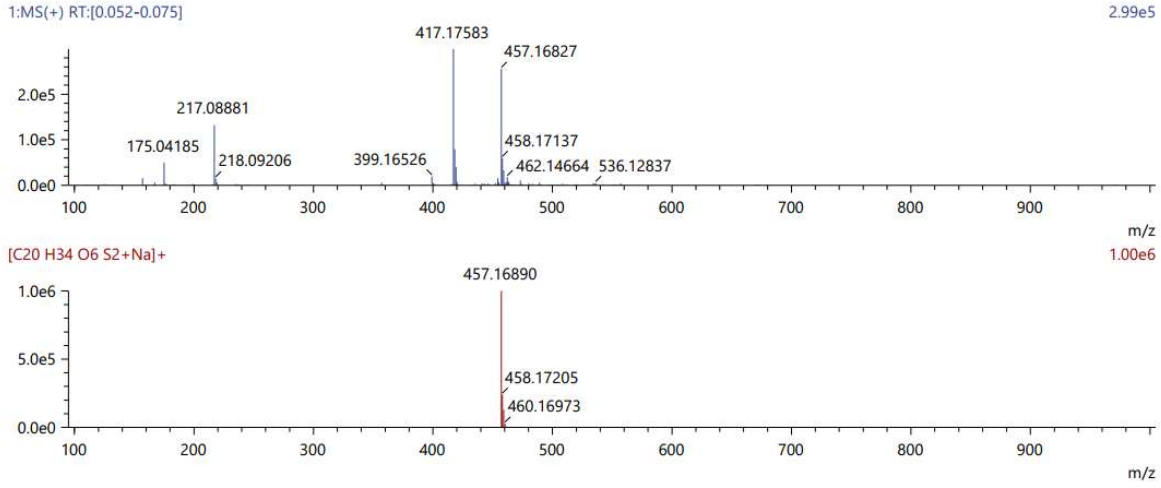


HRMS (4E,4'E)-diisopropyl 7,7'-disulfanediyl-bis(3-hydroxyhept-4-enoate), JRM-2

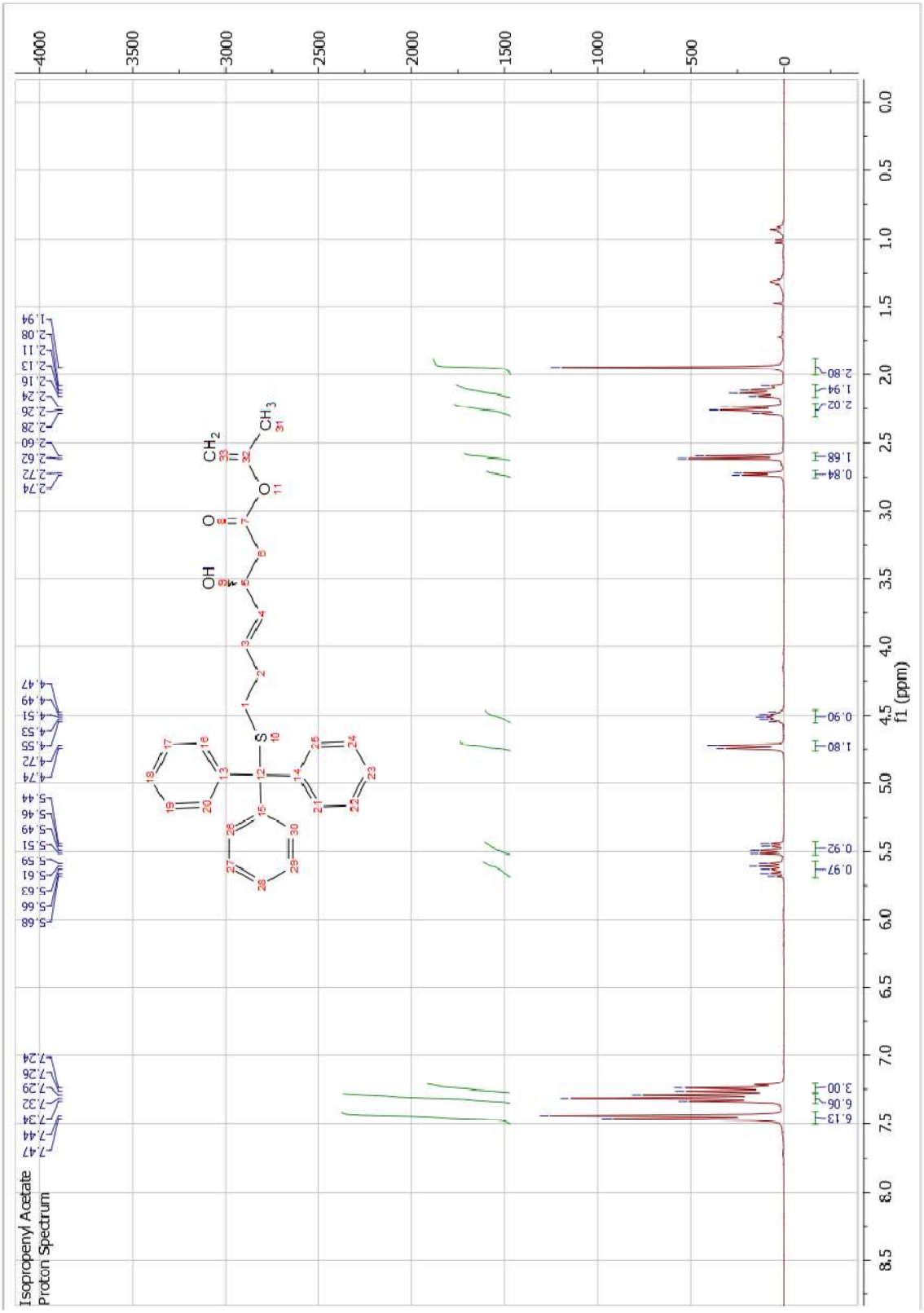
Jawad HRMS.lcb

Formula Predictor Result	**C20 H34 O6 S2**
Mass	457.16827
Error Margin	5 ppm
DBE Range	0 - 1000
Electron Ions	Both configurations
HC Ratio	Not Used
Nitrogen Rule	Used

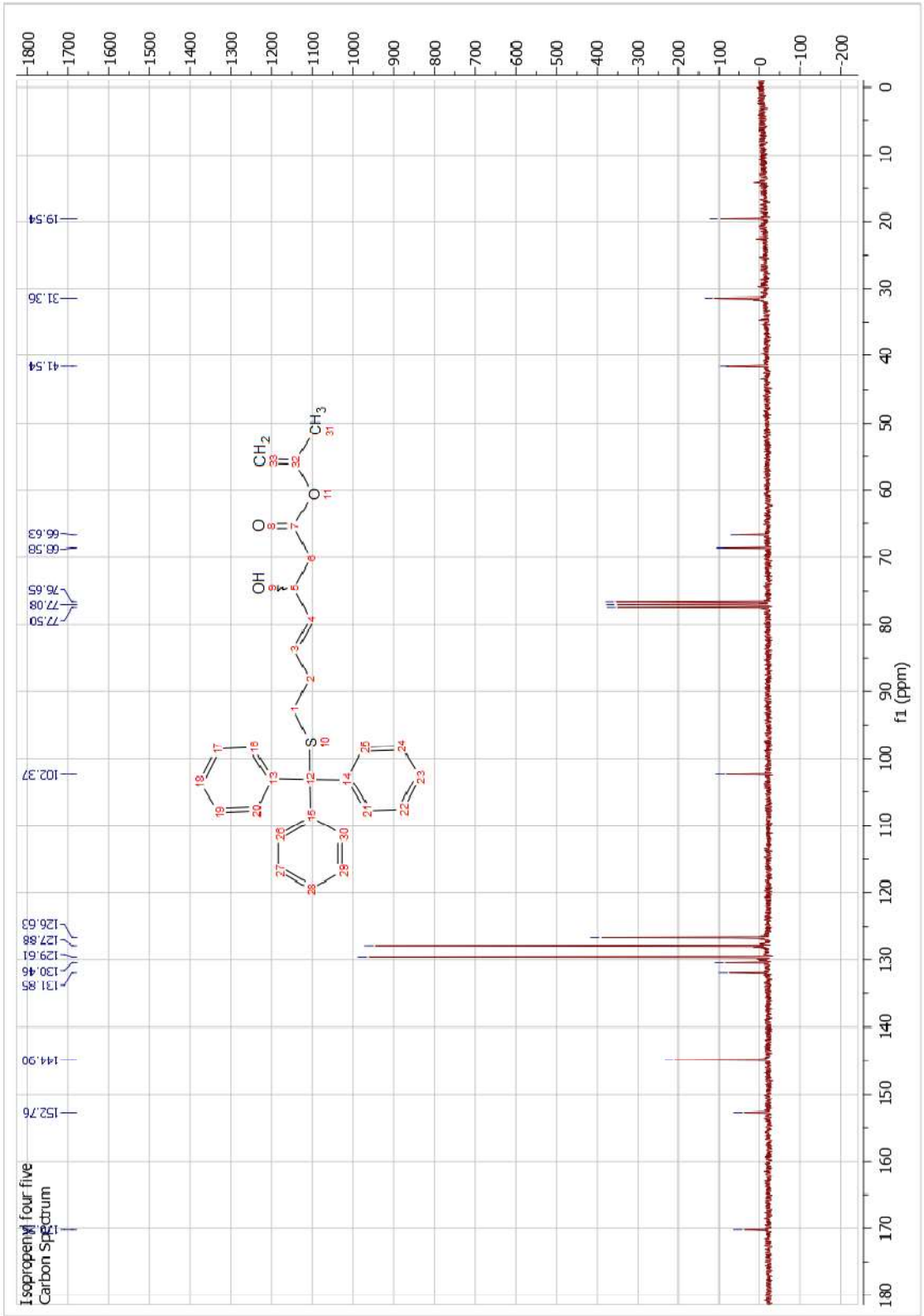
Score	Pred. (M)	Pred. m/z	Meas. m/z	Diff. (mDa)	Formulae (M)	Ion	Diff. (ppm)	Iso Score	DBE
74.09	434.17968	457.16890	457.16827	-0.63	C20 H34 O6 S2	[M+Na]+	-1.378	71.95	4.0



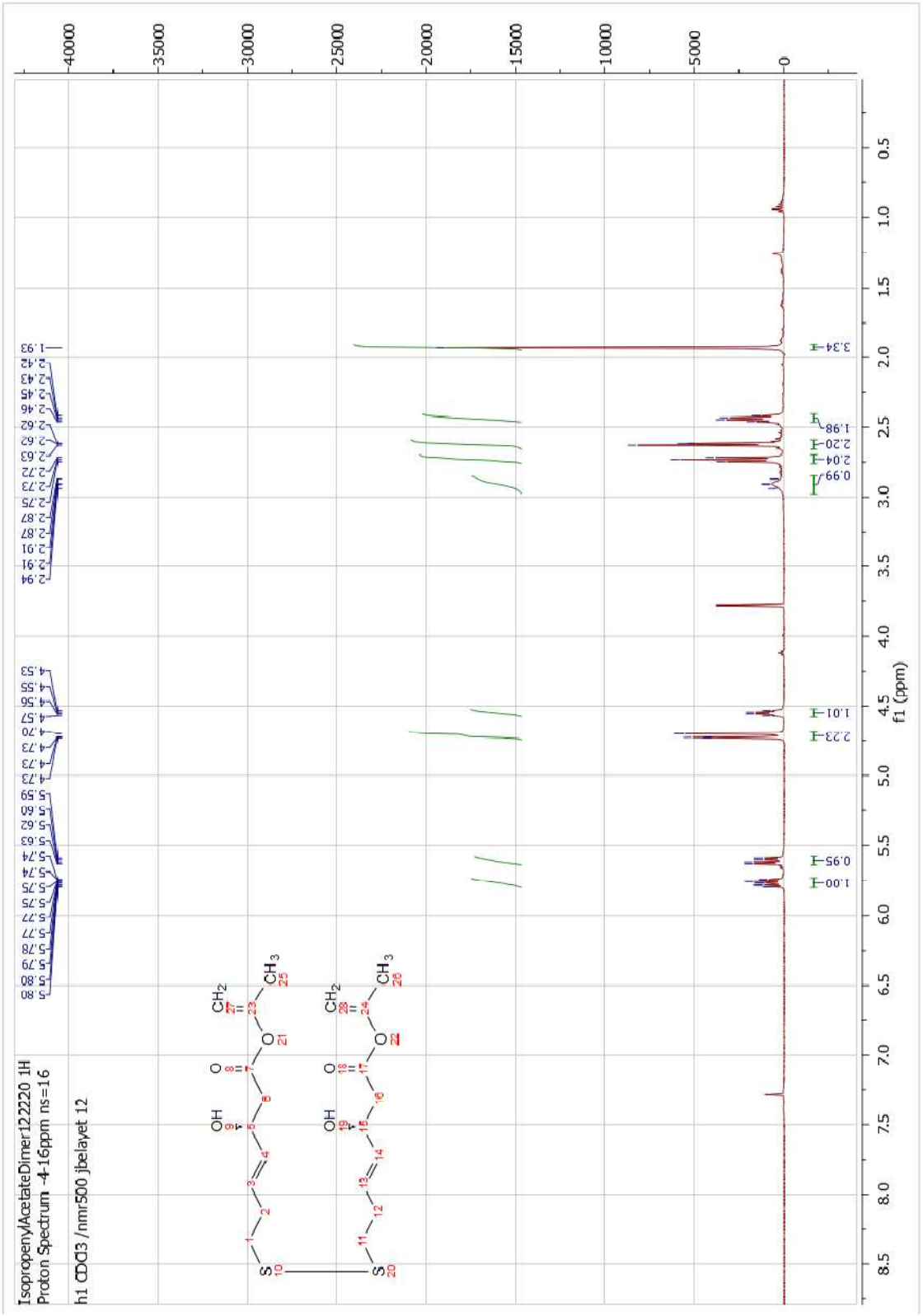
^{1}H NMR Spectrum of (E)Prop-1-en-2-yl-3-hydroxy-7-(tritylthio)hept-4-enoate, 7c



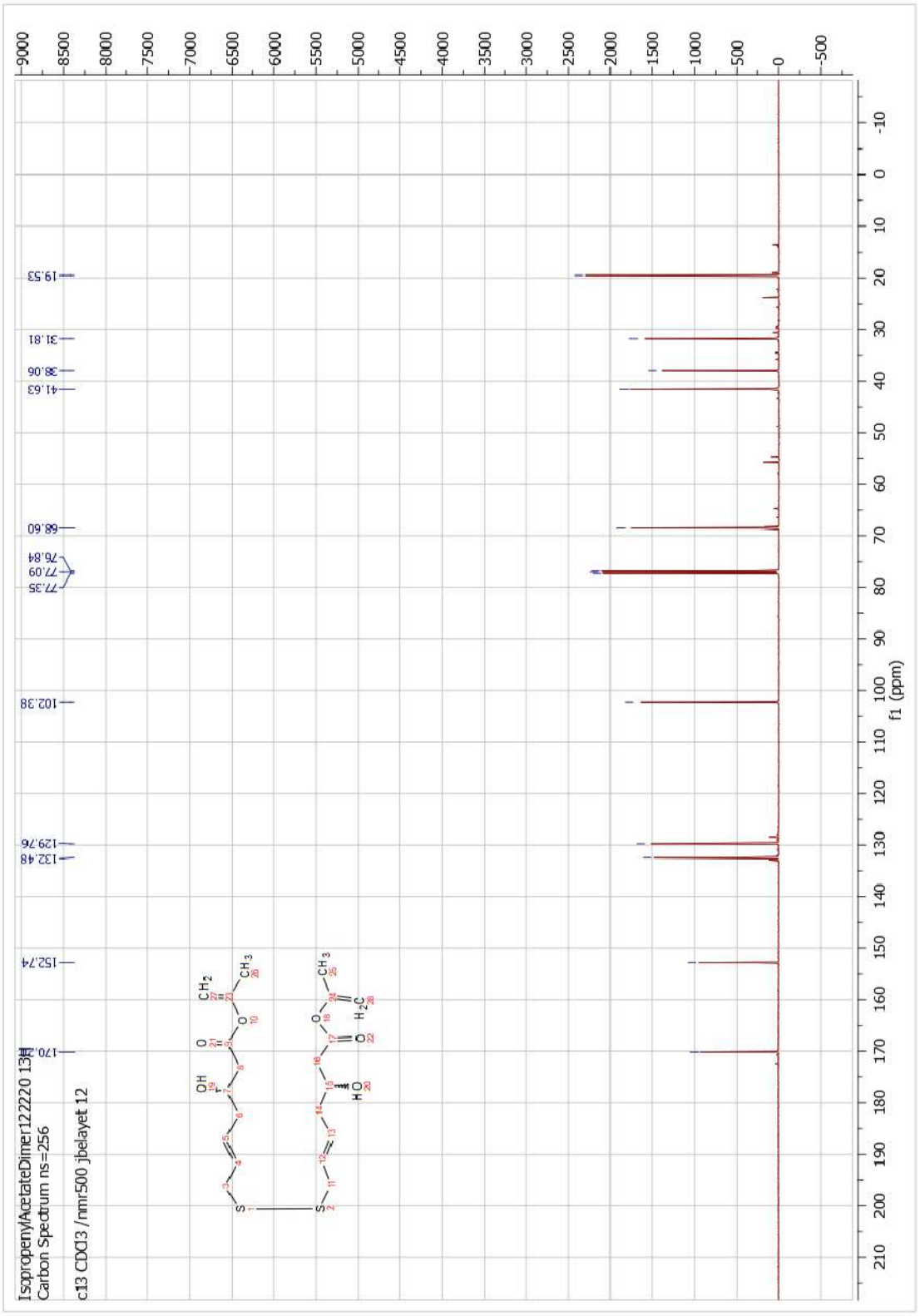
$^{13}C\{1H\}$ (proton-decoupled carbon) NMR Spectrum of (E)Prop-1-en-2-yl-3-hydroxy-7-(tritylthio)hept-4-enoate, 7c



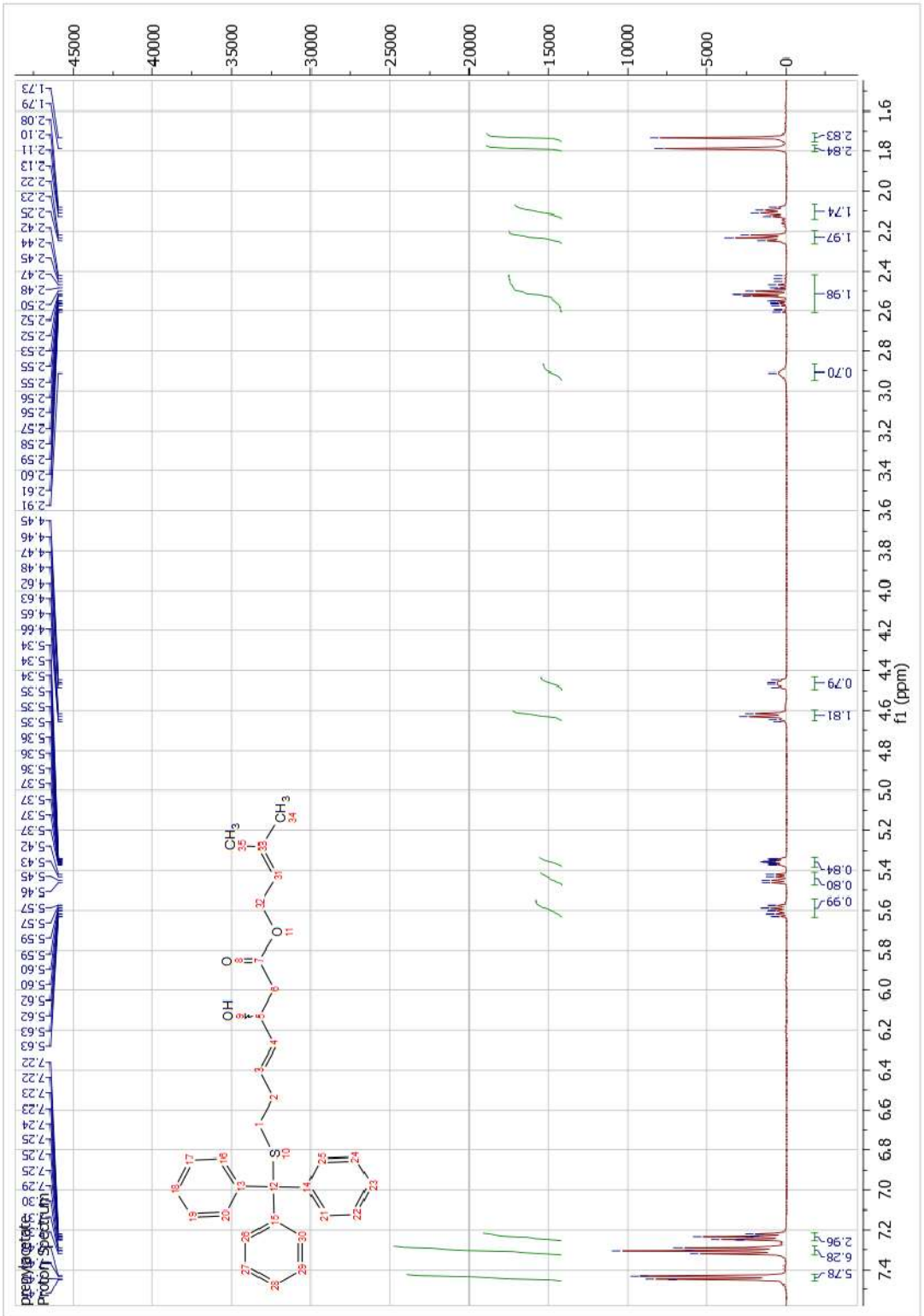
^{1}H NMR Spectrum of (4E,4'E)-di(prop-1-en-2-yl) 7,7'-disulfanediyl-bis(3-hydroxyhept-4-enoate), JRM-3



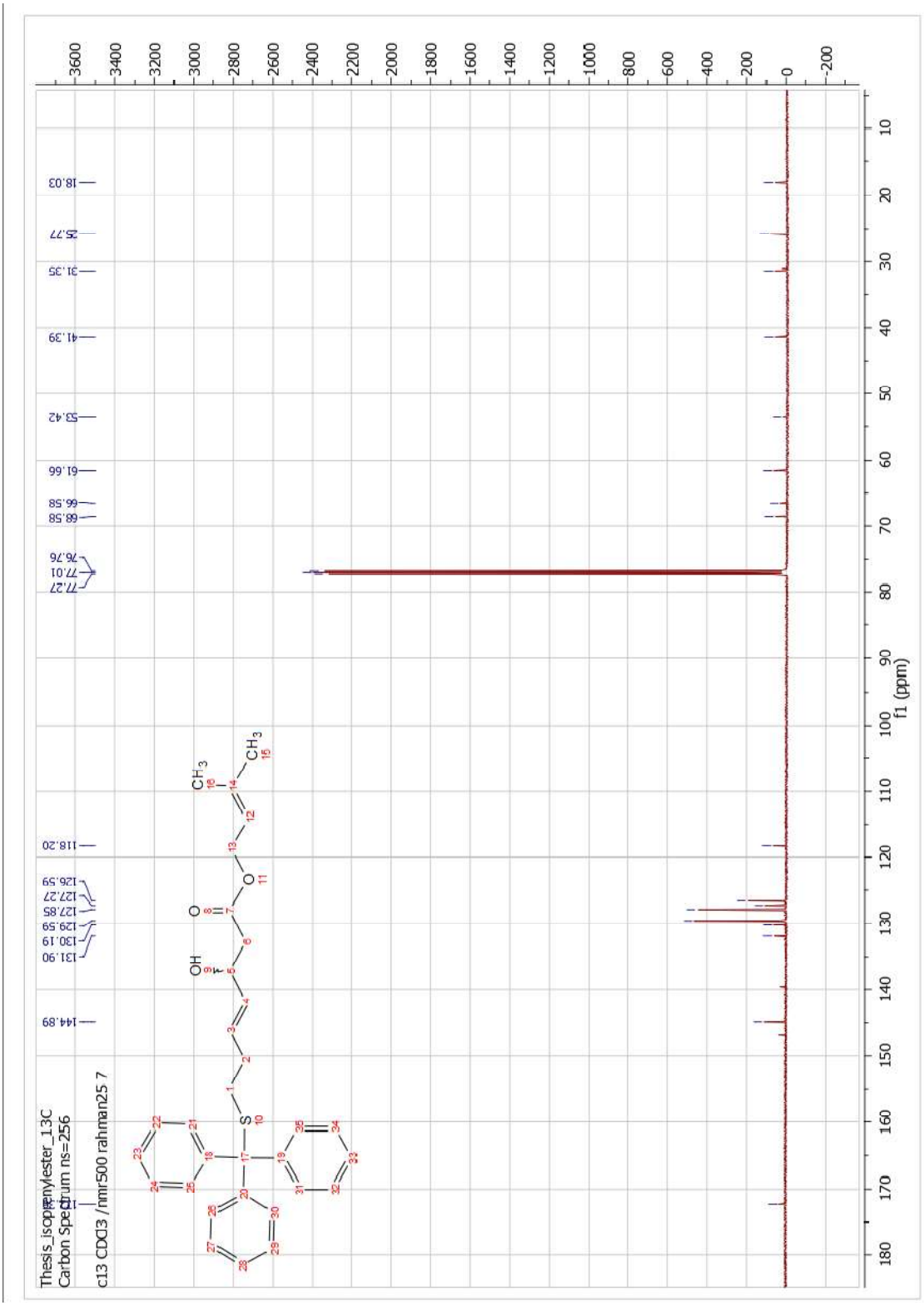
$^{13}C\{1H\}$ (proton-decoupled carbon) NMR Spectrum of (4E,4'E)-di(prop-1-en-2-yl) 7,7'-disulfanediyl-bis(3-hydroxyhept-4-enoate), JRM-3



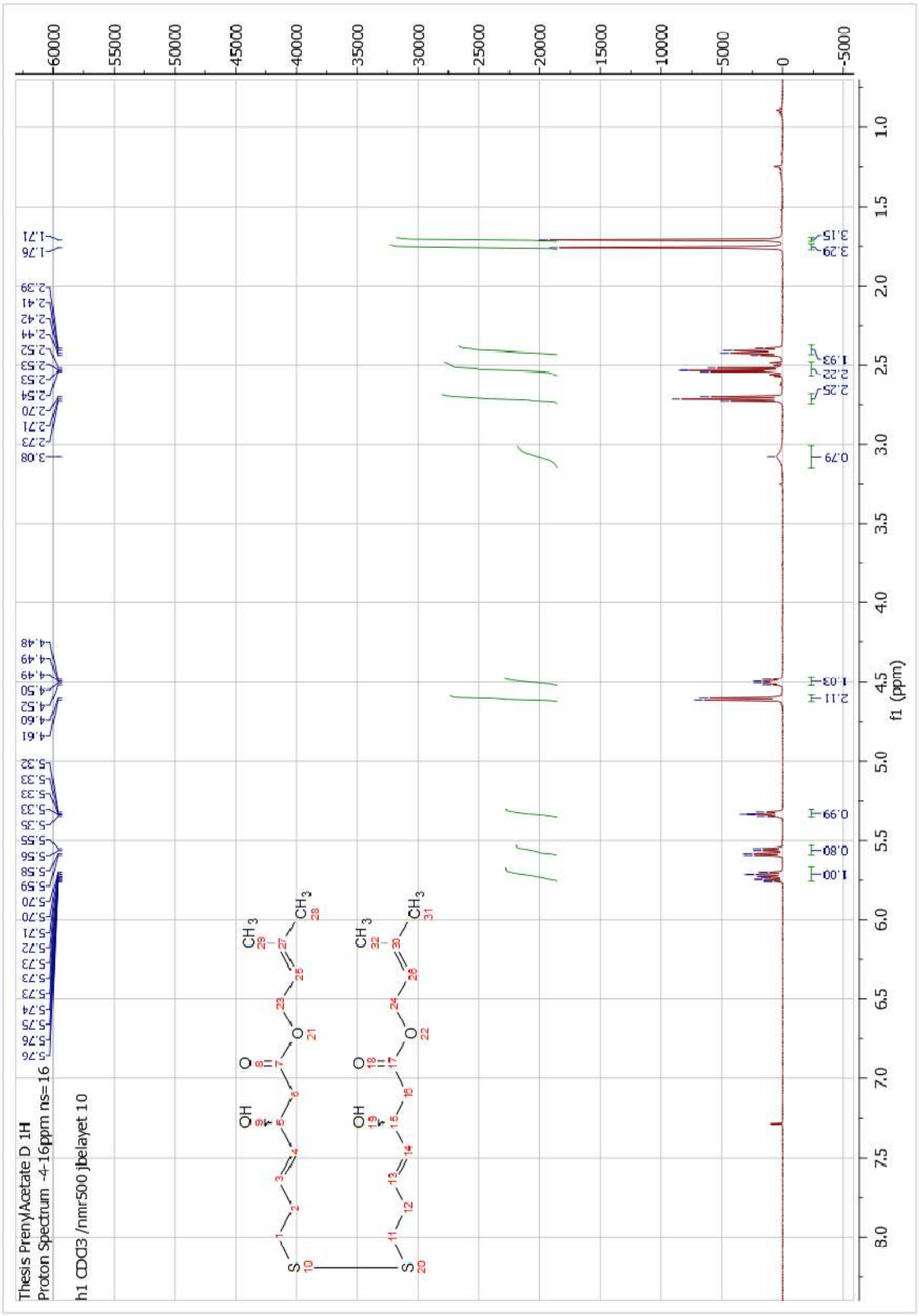
^{1}H NMR Spectrum of (E)-3-methylbut-2-en-1-yl-3-hydroxy-7-(tritylthio)hept-4-enoate, 7d



$^{13}C\{1H\}$ (proton-decoupled carbon) NMR Spectrum of (E)-3-methylbut-2-en-1-yl-3-hydroxy-7-(tritylthio)hept-4-enoate, 7d



^{1}H NMR Spectrum of (4E,4'E)-bis(3-methylbut-2-en-1-yl) 7,7'-disulfanediyl-bis(3-hydroxyhept-4-enoate), JRM-4

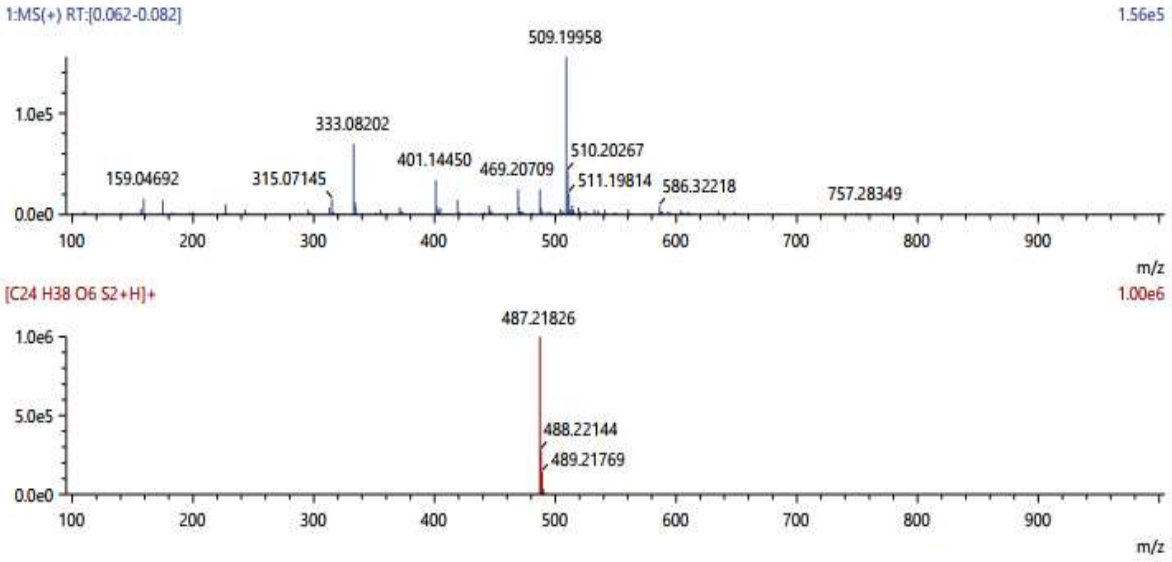


HRMS of (4E,4'E)-bis(3-methylbut-2-en-1-yl) 7,7'-disulfanediyl-bis(3-hydroxyhept-4-enoate), JRM-4

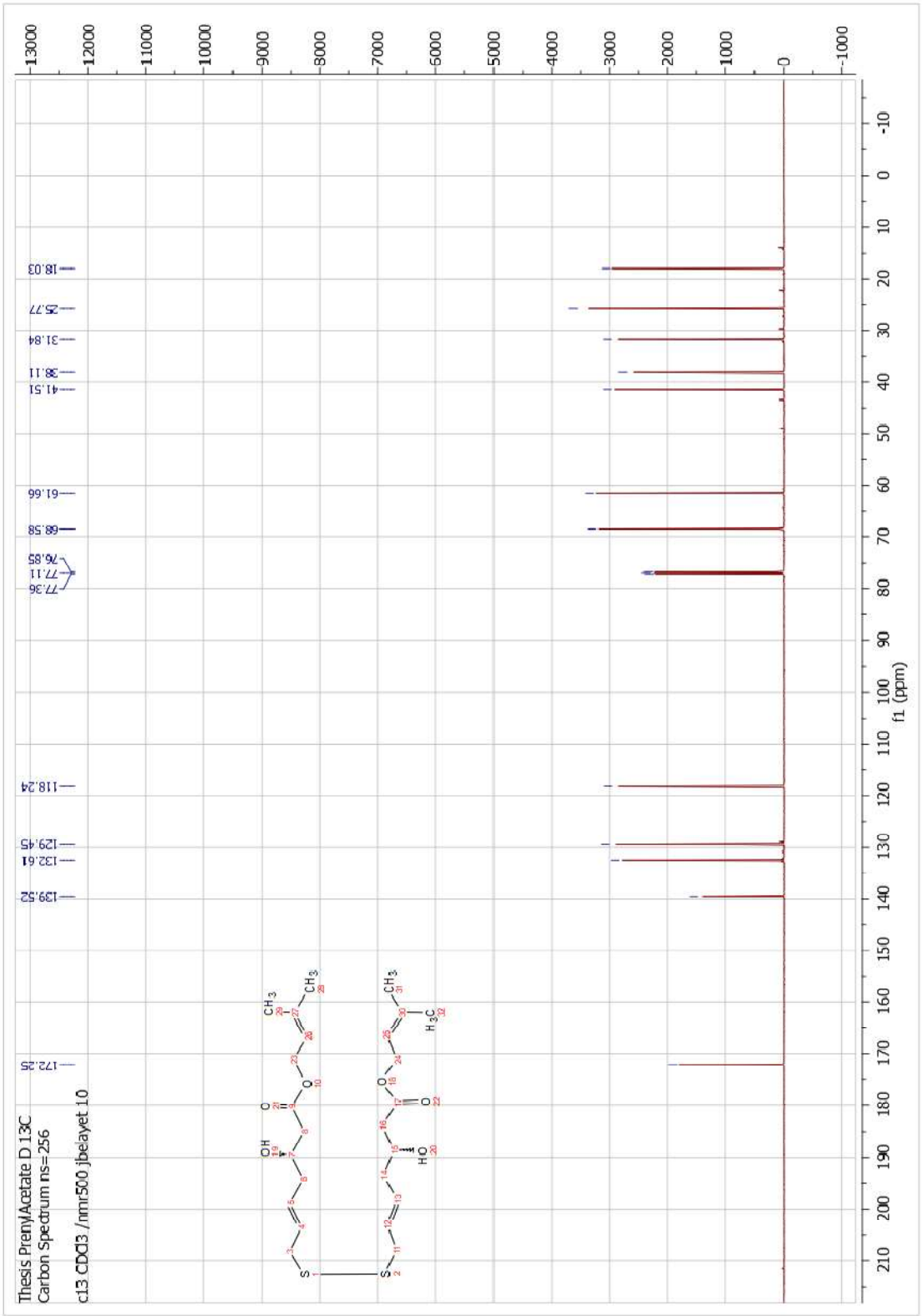
Jawad HRMS.lcb

Formula Predictor Result	**C24 H38 O6 S2**
Mass	487.21762
Error Margin	5 ppm
DBE Range	0 - 1000
Electron Ions	Both configurations
HC Ratio	Not Used
Nitrogen Rule	Used

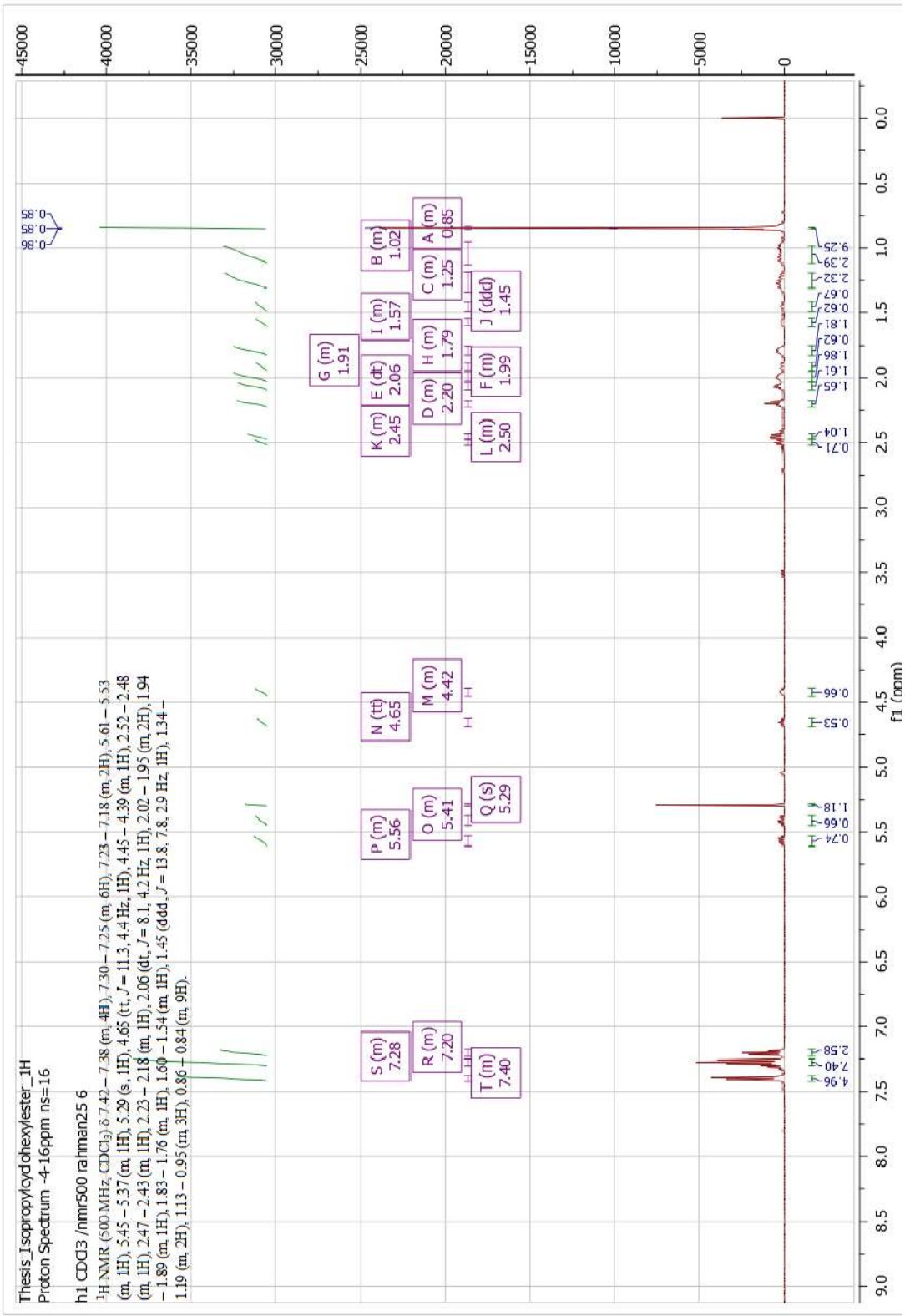
Score	Pred. (M)	Pred. m/z	Meas. m/z	Diff. (mDa)	Formulae (M)	Ion	Diff. (ppm)	Iso Score	DBE
82.19	486.21098	487.21826	487.21762	-0.64	C24 H38 O6 S2	[M+H]+	-1.314	80.91	6.0



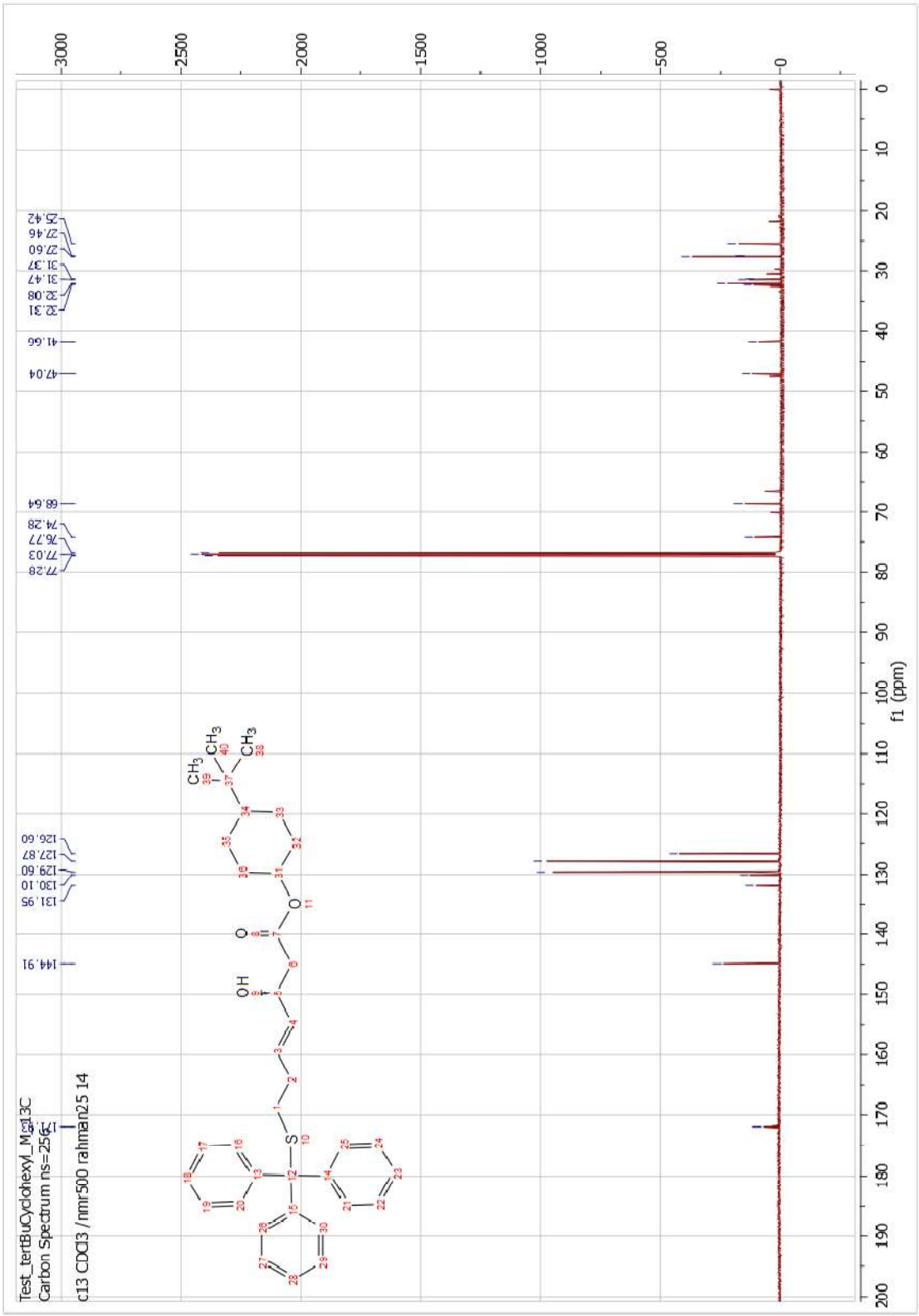
$^{13}C\{1H\}$ (proton-decoupled carbon) NMR Spectrum of (4E,4'E)-bis(3-methylbut-2-en-1-yl) 7,7'-disulfanediyl-bis(3-hydroxyhept-4-enoate), JRM-4



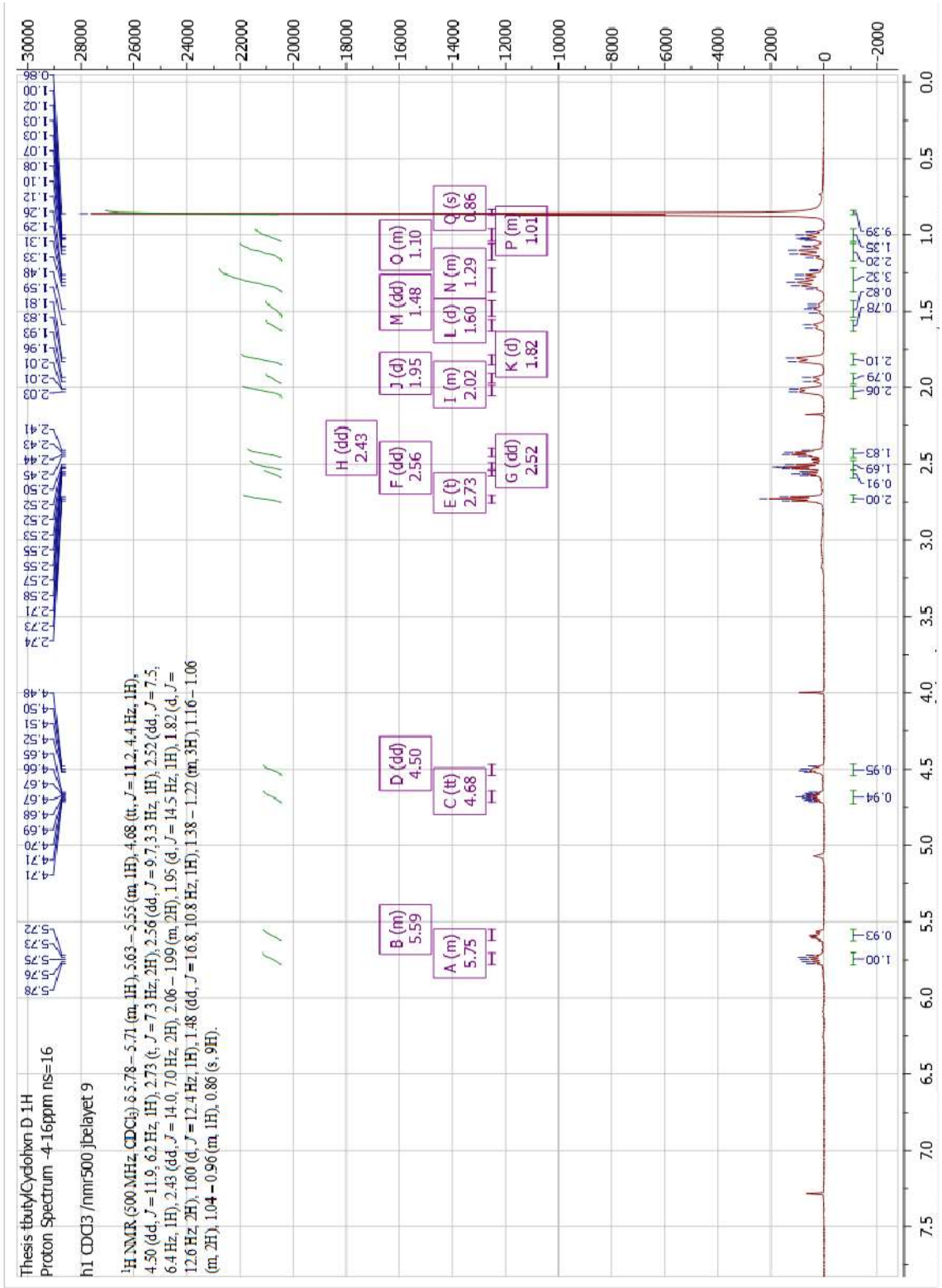
^{1}H NMR Spectrum of (E)-4-(tert-butyl)cyclohexyl-3-hydroxy-7-(tritylthio)hept-4-enoate, 7e



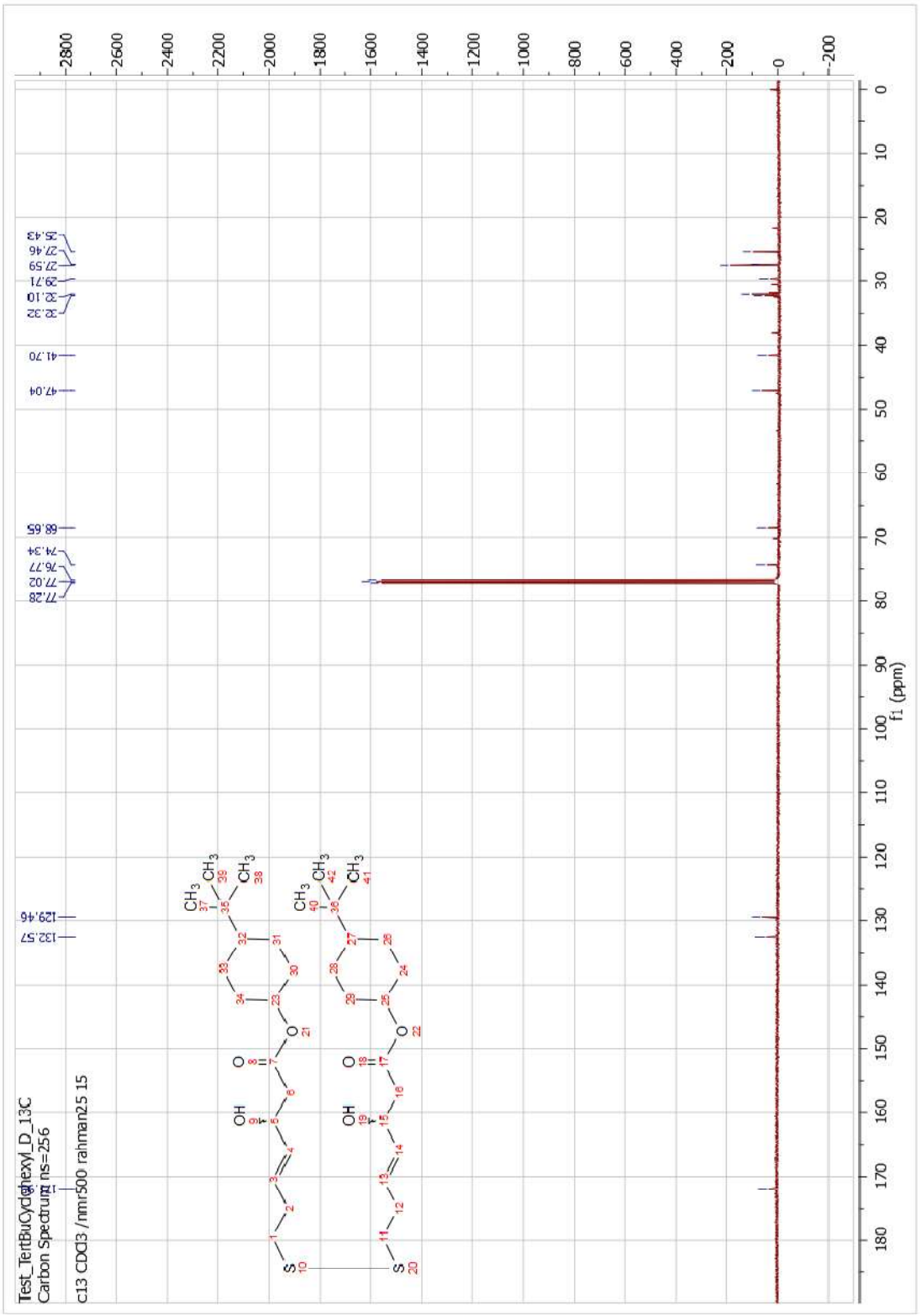
$^{13}C\{1H\}$ (proton-decoupled carbon) NMR Spectrum of (E)-4-(tert-butyl)cyclohexyl-3-hydroxy-7-(tritylthio)hept-4-enoate, 7e



^{1}H NMR Spectrum of (E)-4-(tert-butyl)cyclohexyl-7-(((E)-7-((4-(tert-butyl)cyclohexyl)oxy)-5-hydroxy-7-oxohept-3-en-1-yl)disulfaneyl)-3-hydroxyhept-4-enoate, JRM-5



$^{13}C\{1H\}$ (proton-decoupled carbon) NMR Spectrum of (E)-4-(tert-butyl)cyclohexyl-7-(((E)-7-((4-(tert-butyl)cyclohexyl)oxy)-5-hydroxy-7-oxohept-3-en-1-yl)disulfaneyl)-3-hydroxyhept-4-enoate, JRM-5

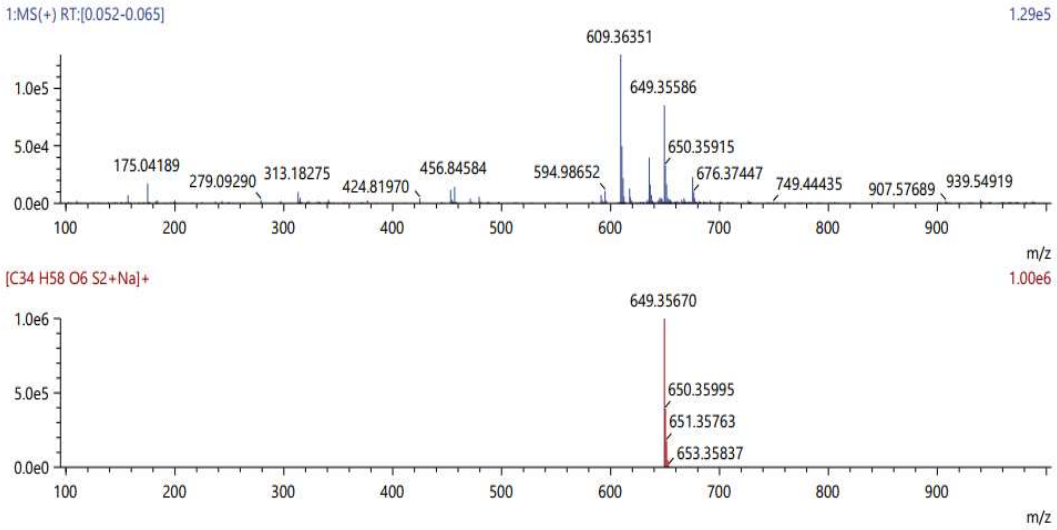


HRMS (E)-4-(tert-butyl)cyclohexyl-7-(((E)-7-((4-(tert-butyl)cyclohexyl)oxy)-5-hydroxy-7-oxohept-3-en-1-yl)disulfaneyl)-3-hydroxyhept-4-enoate, JRM-5

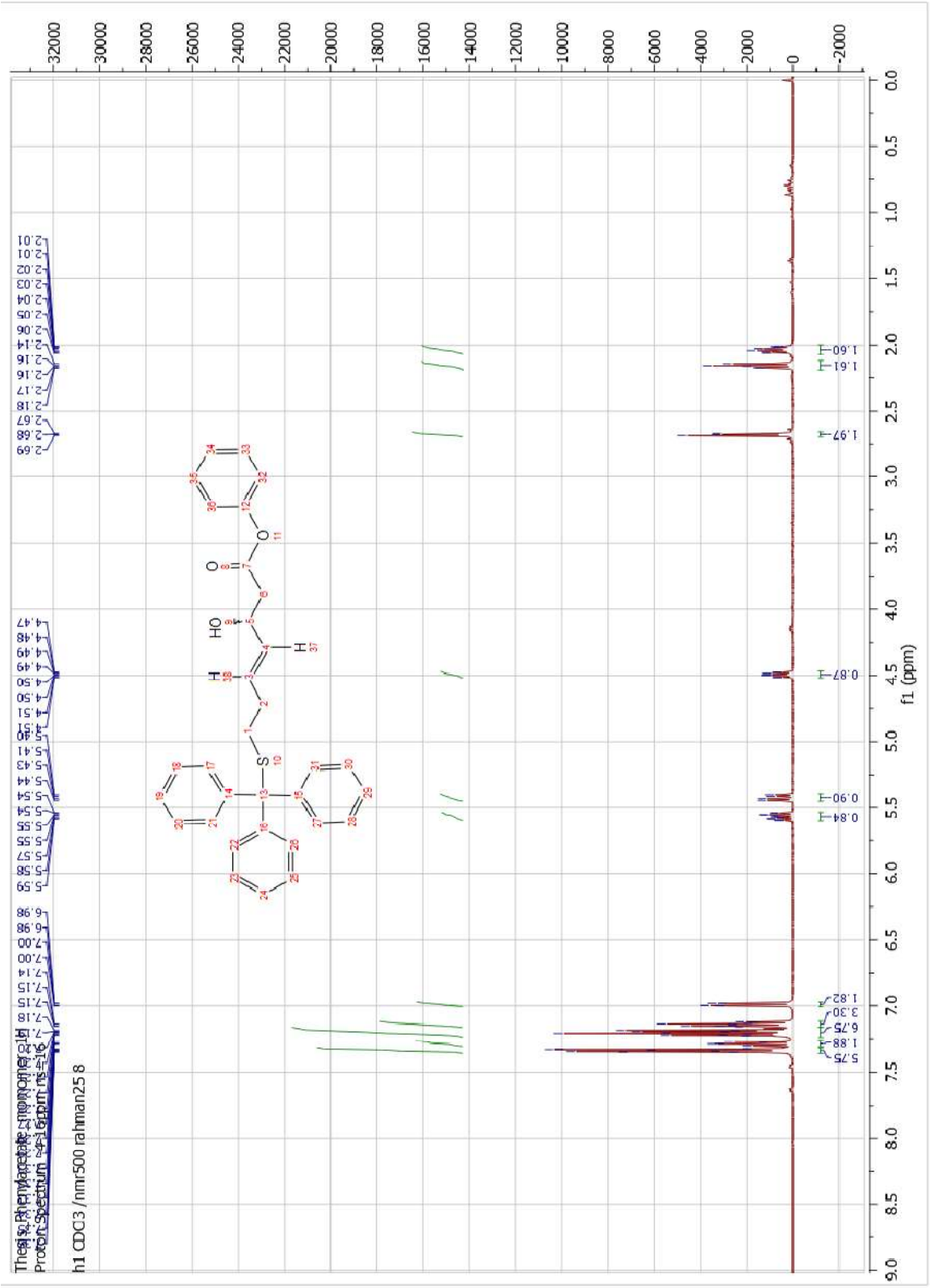
Jawad HRMS.lcb

Formula Predictor Result	**C34 H58 O6 S2**
Mass	649.35586
Error Margin	5 ppm
DBE Range	0 - 1000
Electron Ions	Both configurations
HC Ratio	Not Used
Nitrogen Rule	Used

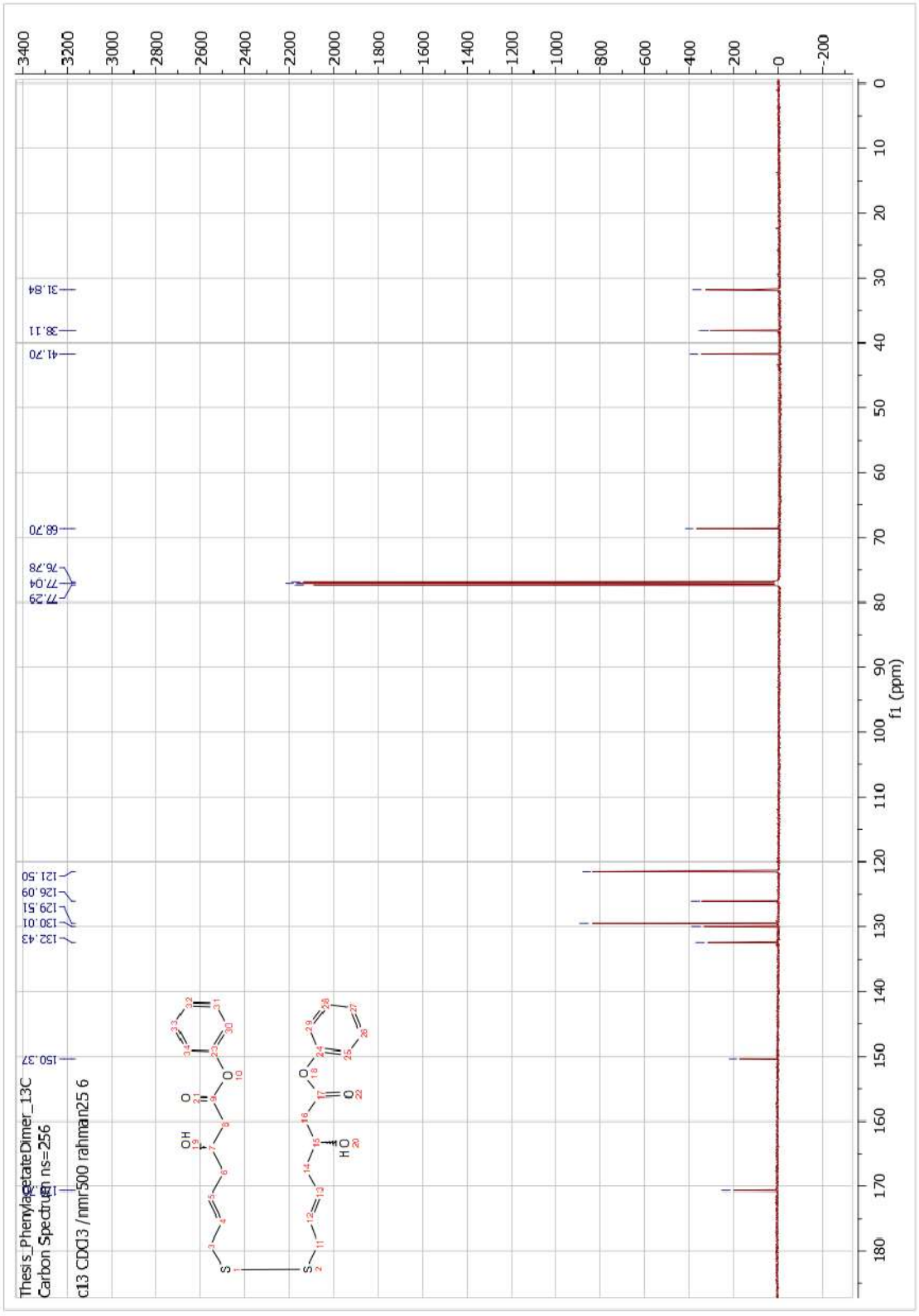
Score	Pred. (M)	Pred. m/z	Meas. m/z	Diff. (mDa)	Formulae (M)	Ion	Diff. (ppm)	Iso Score	DBE
94.21	626.36748	649.35670	649.35586	-0.84	C34 H58 O6 S2	[M+Na]+	-1.294	94.26	6.0



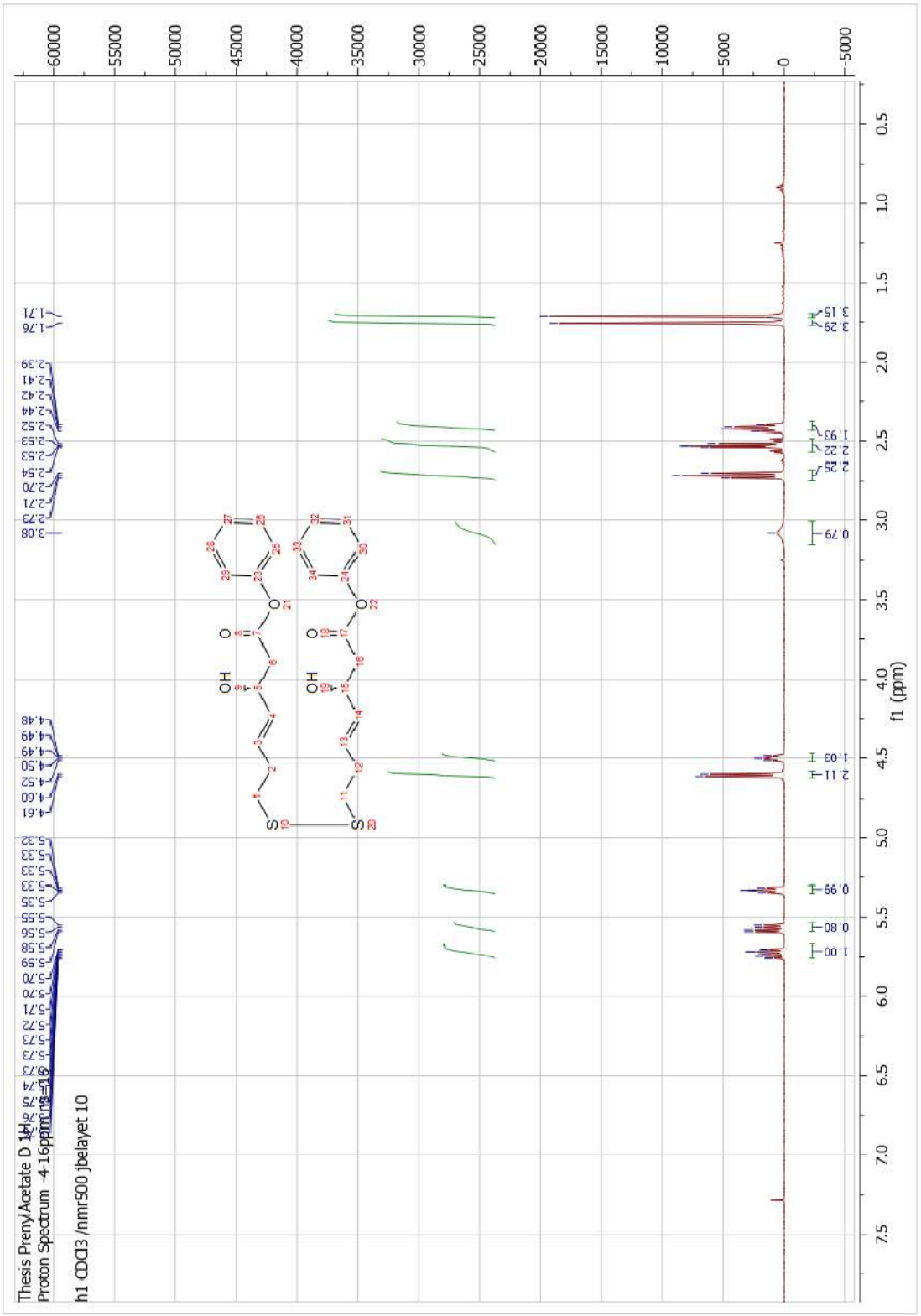
^{1}H NMR Spectrum of (E)-phenyl-3-hydroxy-7-(tritylthio)hept-4-enoate, 6f



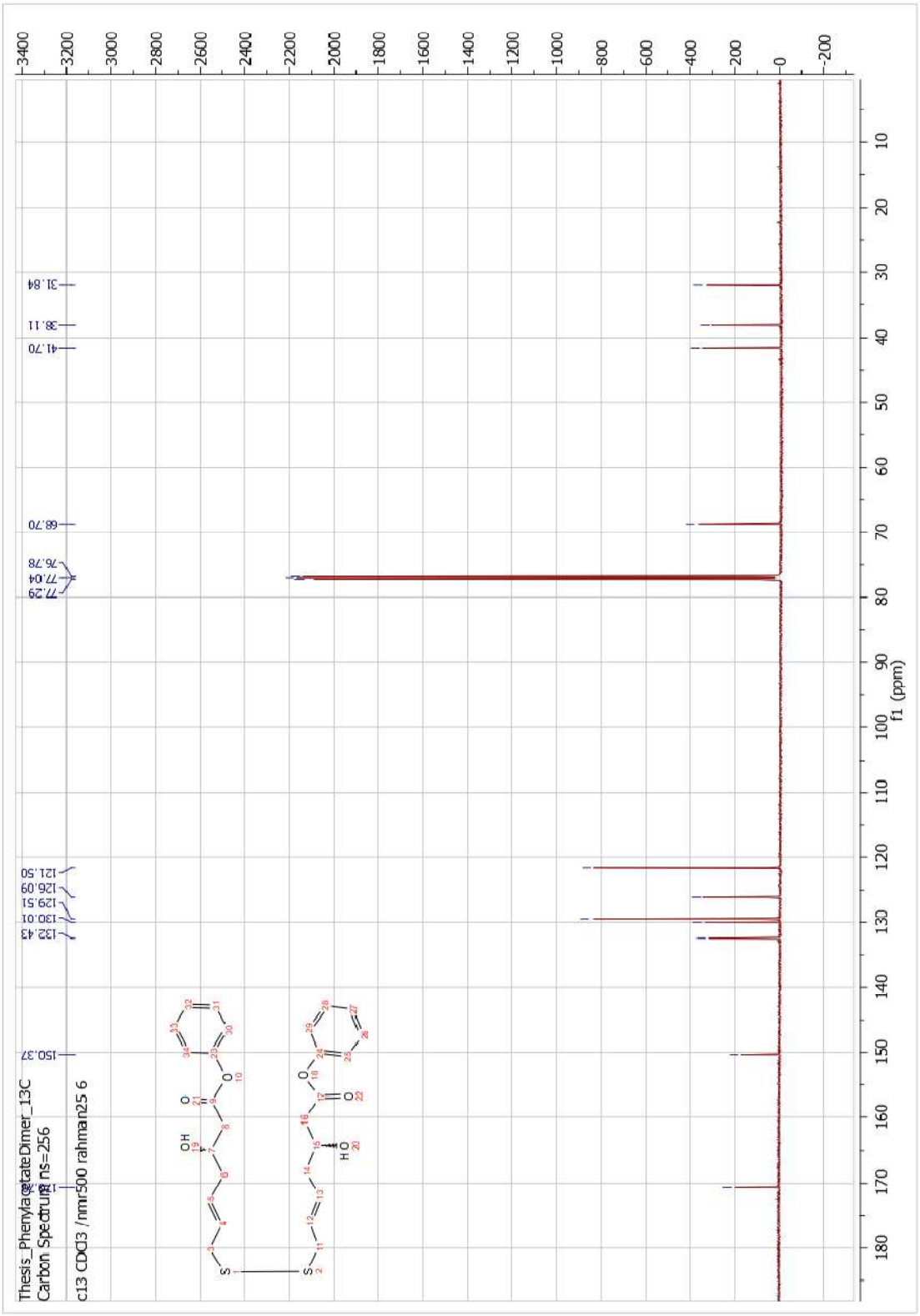
$^{13}C\{1H\}$ (proton-decoupled carbon) NMR Spectrum of (E)-phenyl-3-hydroxy-7-(tritylthio)hept-4-enoate, 6f



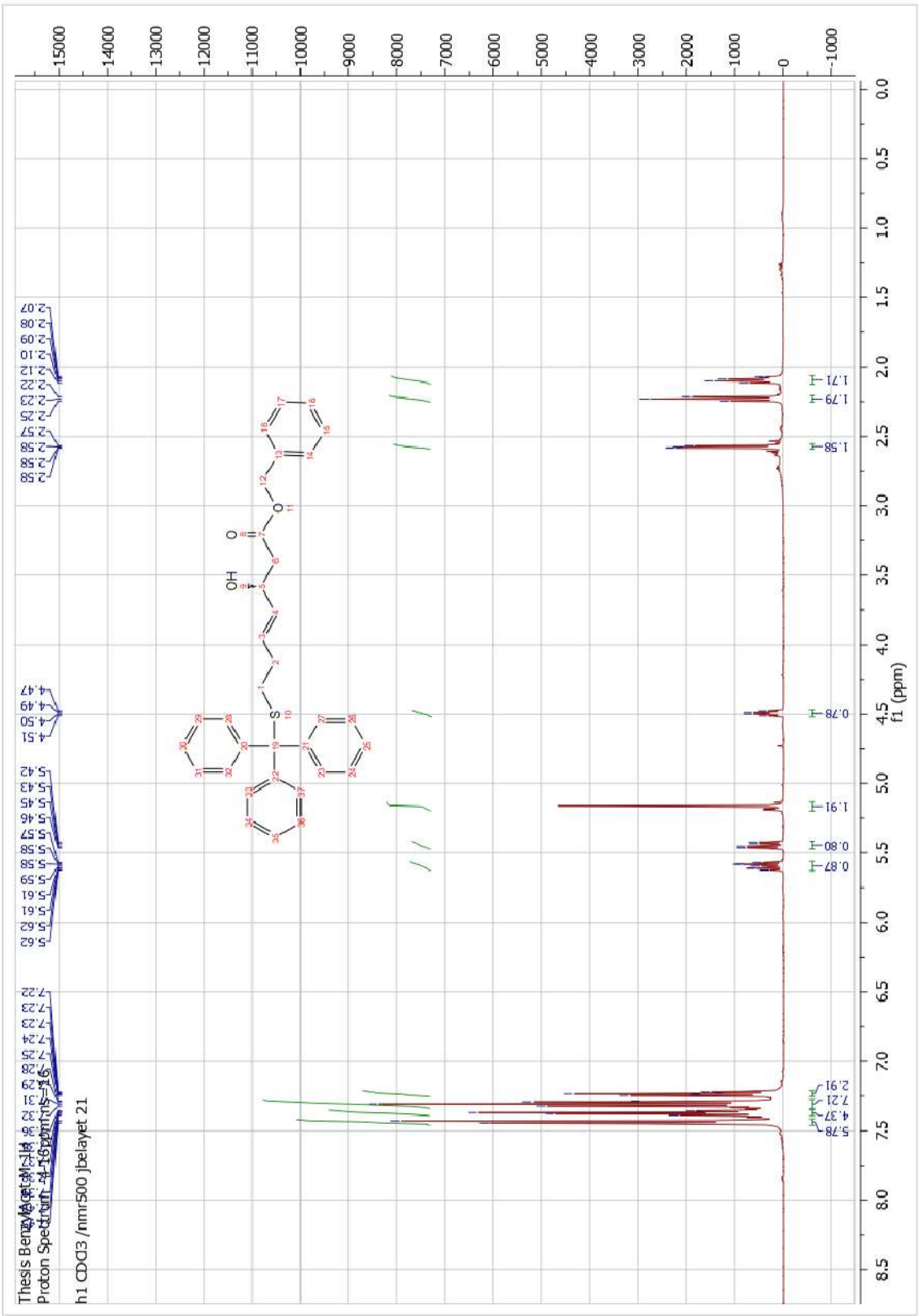
^{1}H NMR Spectrum of Diphenyl 7,7'-disulfanediyl(4E,4'E)-bis(3-hydroxyhept-4-enoate), JRM-6



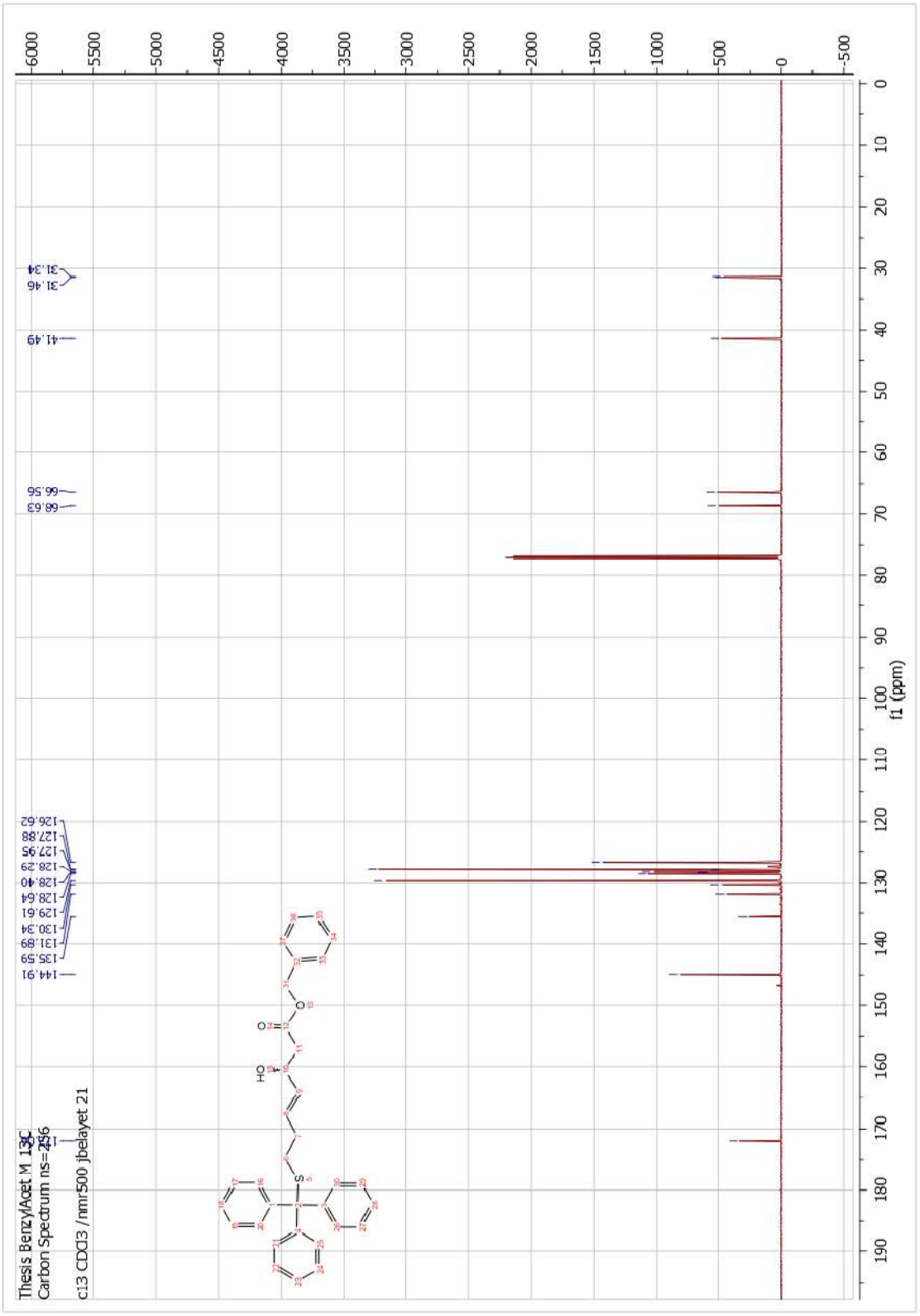
$^{13}C\{1H\}$ (proton-decoupled carbon) NMR Spectrum of NMR Spectrum of Diphenyl 7,7'-disulfanediyl(4E,4'E)-bis(3-hydroxyhept-4-enoate), JRM-6



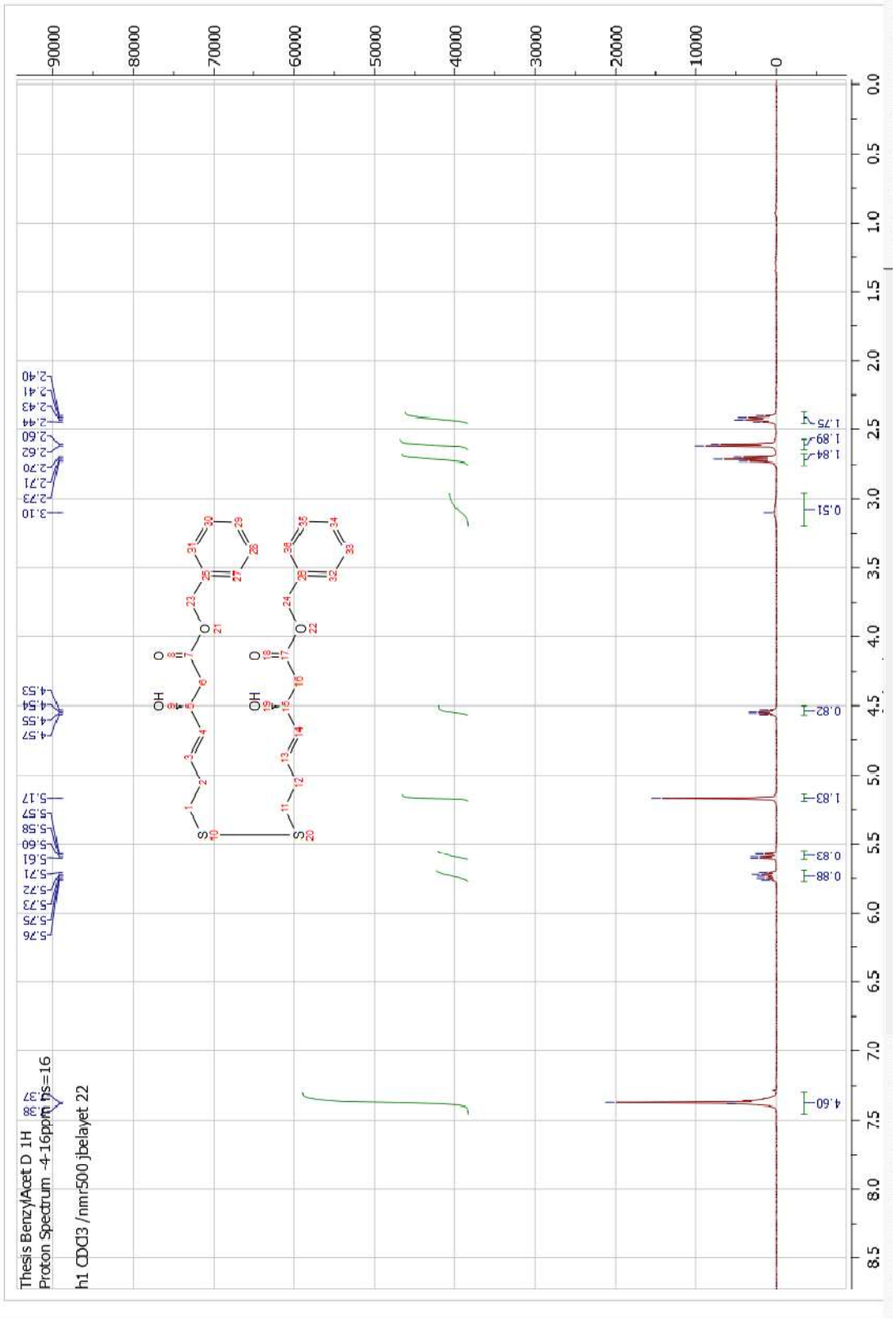
1H NMR spectrum of Benzyl (E)-3-hydroxy-7-(tritylthio)hept-4-enoate, 7g



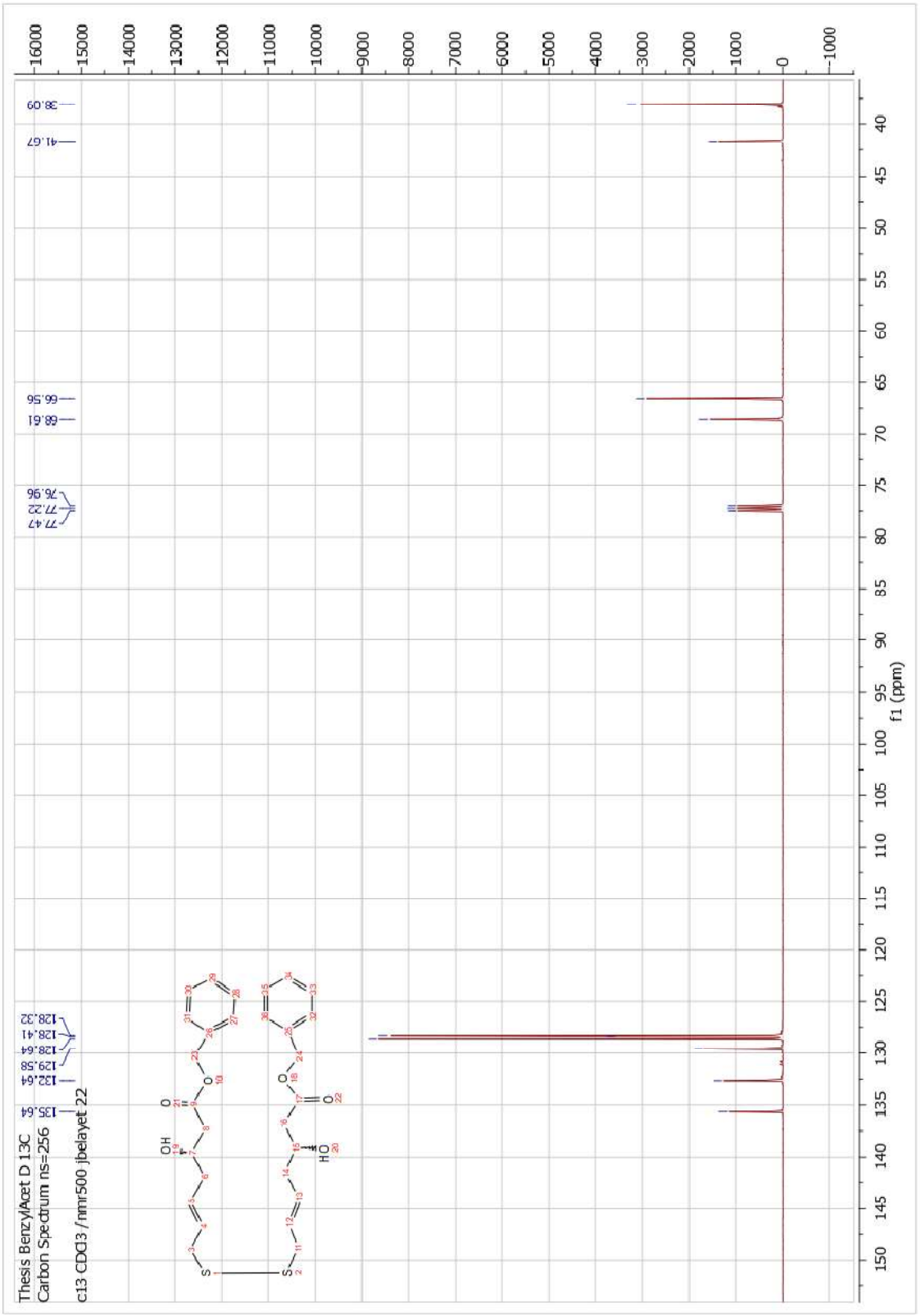
$^{13}C\{1H\}$ (proton-decoupled carbon) NMR Spectrum of Benzyl (E)-3-hydroxy-7-(tritylthio)hept-4-enoate, 7g



^{1}H NMR Spectrum of (4E,4'E)-dibenzyl 7,7'-disulfanediyl-bis(3-hydroxyhept-4-enoate), JRM-7



$^{13}C\{1H\}$ (proton-decoupled carbon) NMR Spectrum of (4E,4'E)-dibenzyl 7,7'-disulfanediyl-bis(3-hydroxyhept-4-enoate), JRM-7

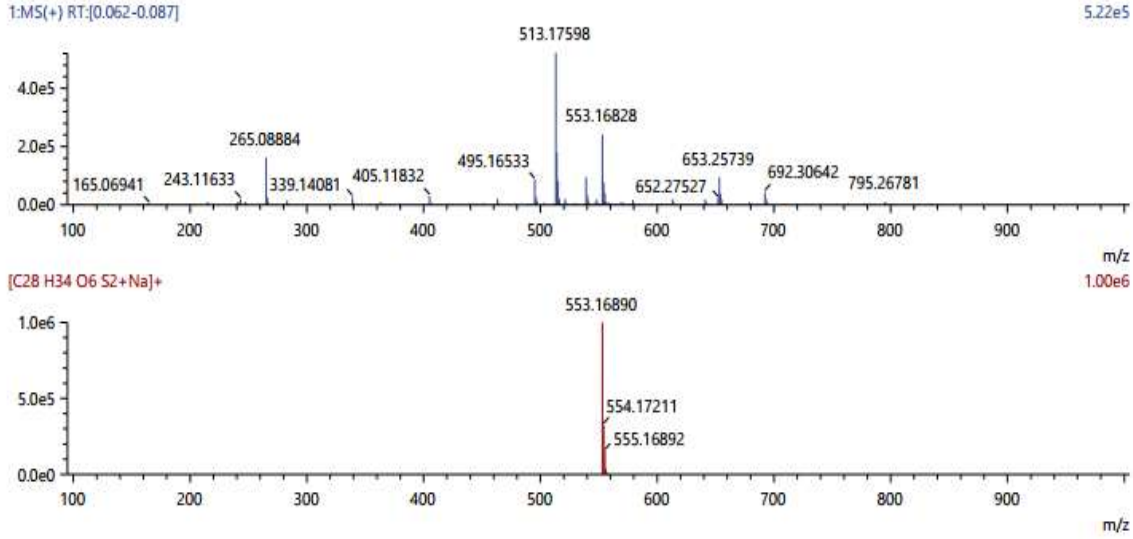


HRMS (4E,4'E)-dibenzyl 7,7'-disulfanediyl-bis(3-hydroxyhept-4-enoate), JRM-7

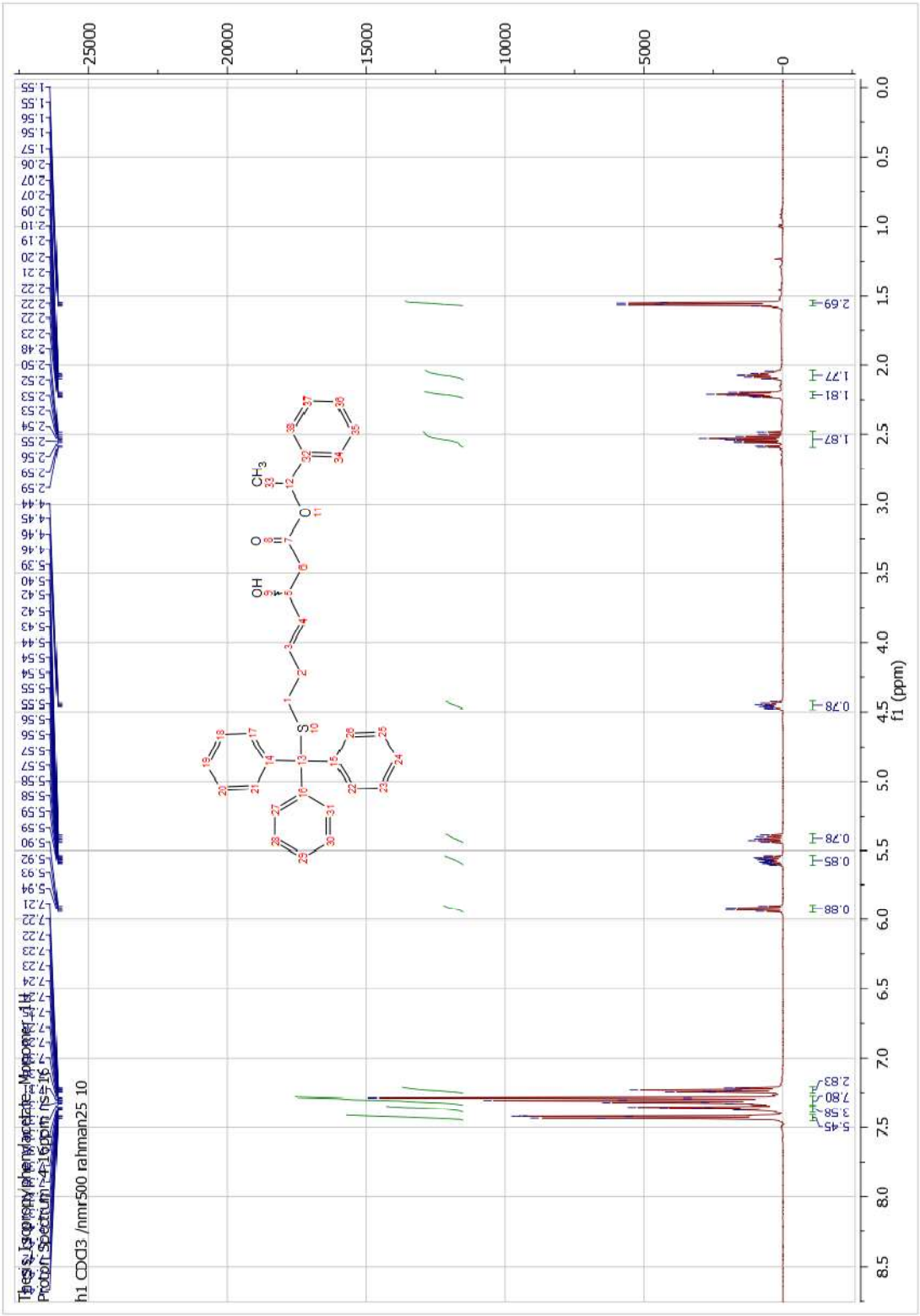
Jawad HRMS.lcb

Formula Predictor Result	**C28 H34 O6 S2**
Mass	553.16828
Error Margin	5 ppm
DBE Range	0 - 1000
Electron Ions	Both configurations
HC Ratio	Not Used
Nitrogen Rule	Used

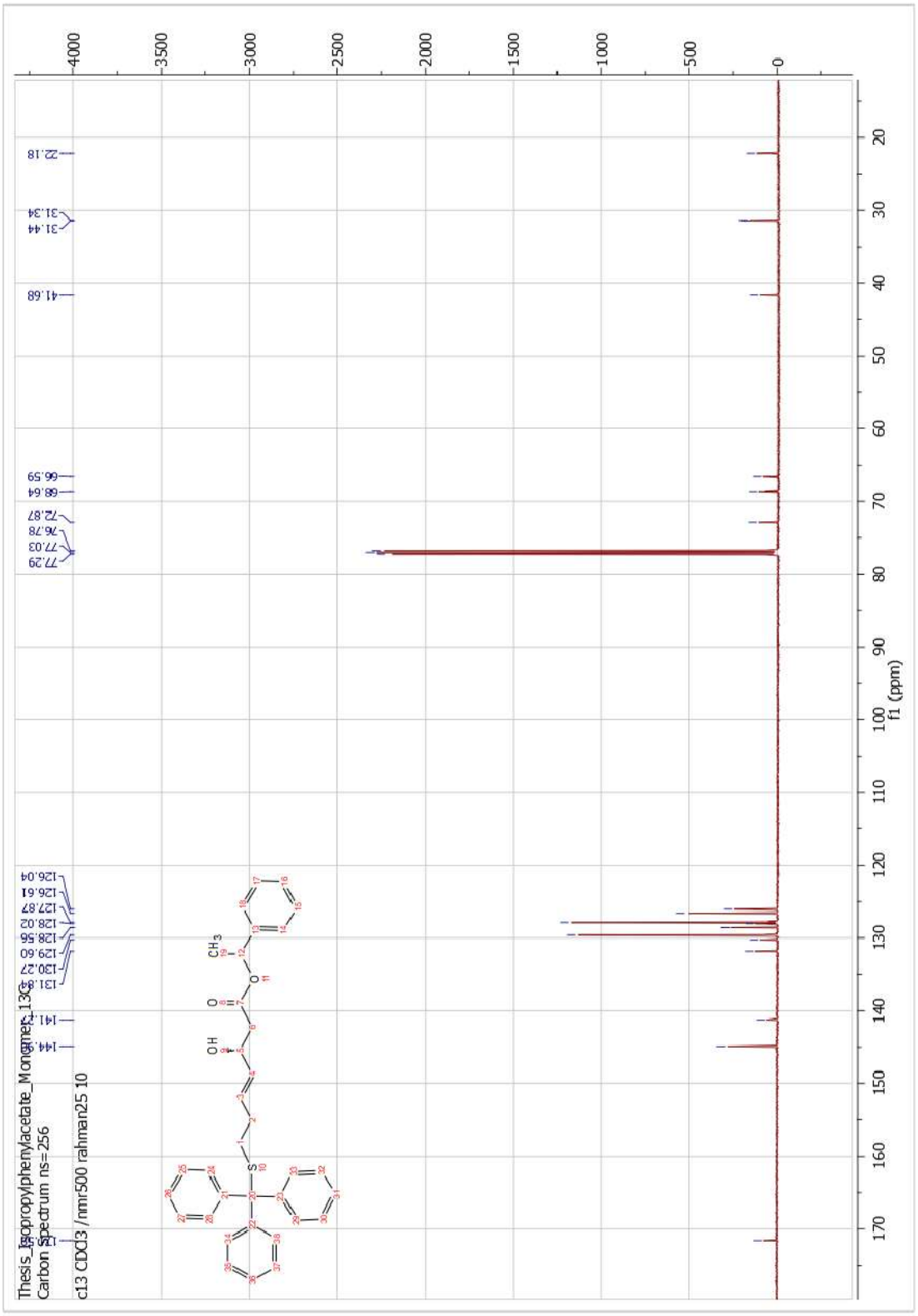
Score	Pred. (M)	Pred. m/z	Meas. m/z	Diff. (mDa)	Formulae (M)	Ion	Diff. (ppm)	Iso Score	DBE
96.32	530.17968	553.16890	553.16828	-0.62	C28 H34 O6 S2	[M+Na]+	-1.121	96.49	12.0



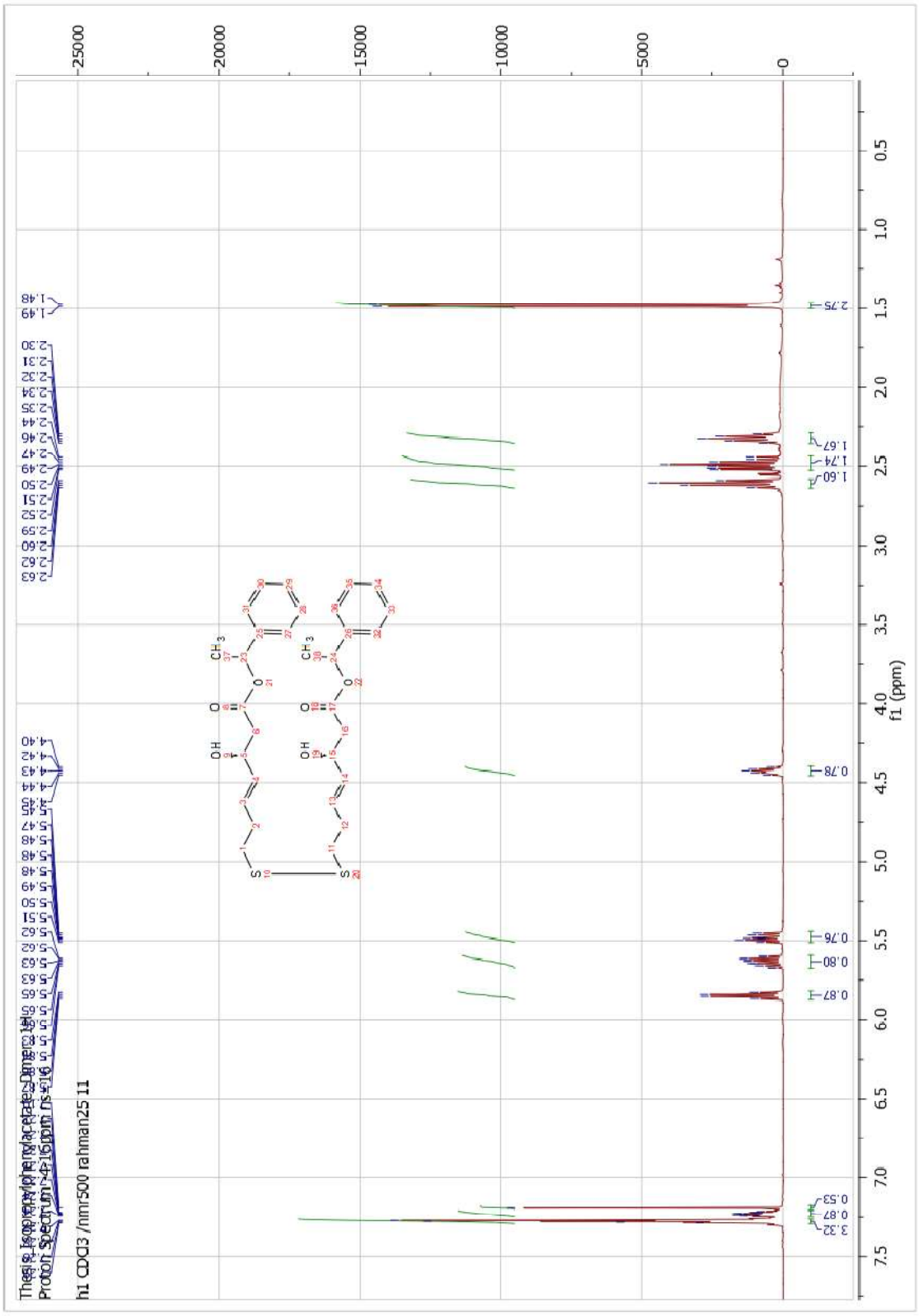
^{1}H NMR Spectrum of (E)-1-phenylethyl-3-hydroxy-7-(tritylthio)hept-4-enoate, 7h



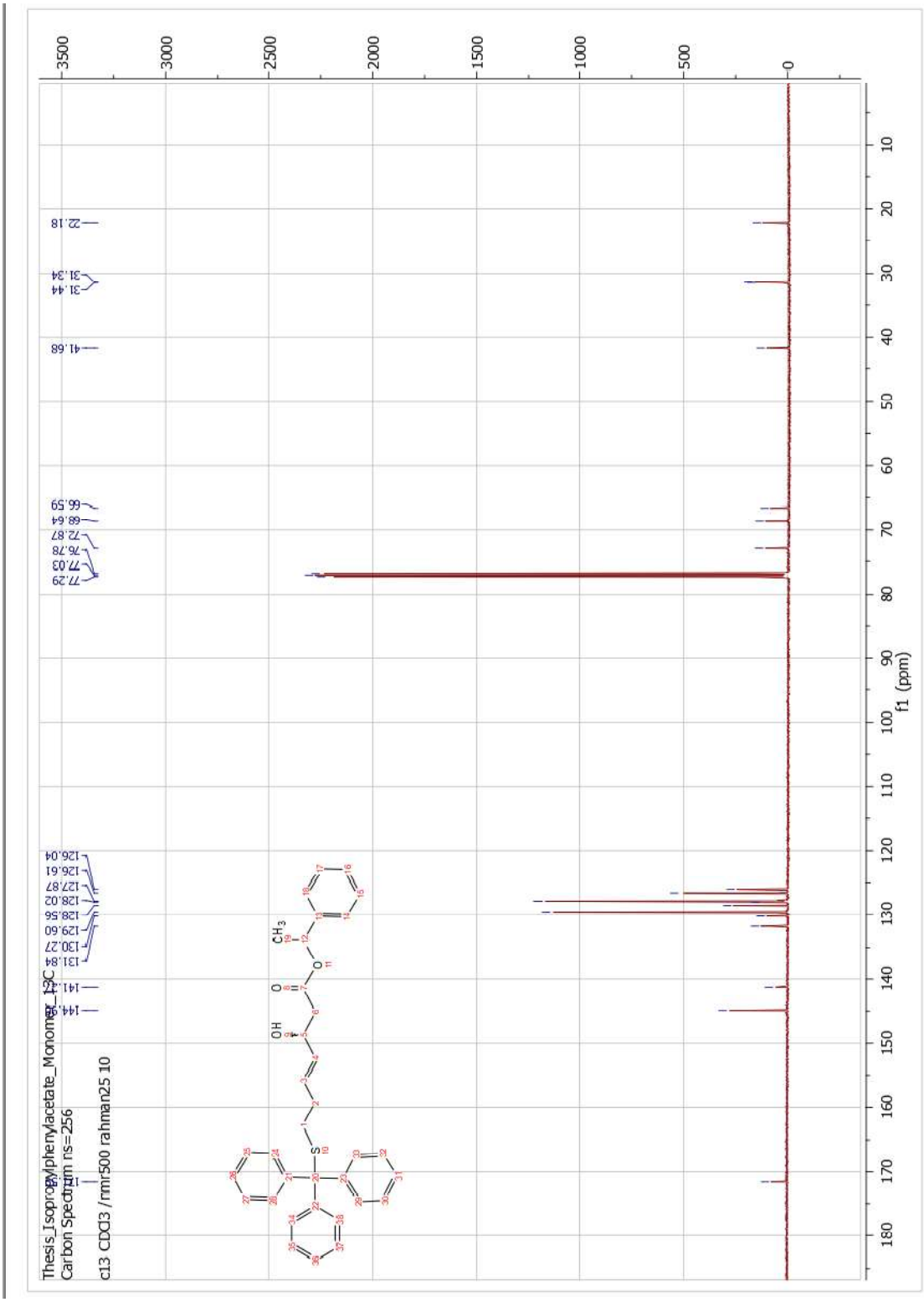
$^{13}C\{1H\}$ (proton-decoupled carbon) NMR Spectrum of (E)-1-phenylethyl-3-hydroxy-7-(tritylthio)hept-4-enoate, 7h



^{1}H NMR Spectrum of 1-phenylethyl(E)-3-hydroxy-7-(((E)-5-hydroxy-7-oxo-7-((S)-1-phenylethoxy)hept-3-en-1-yl)disulfaneyl)hept-4-enoate, JRM-8



$^{13}C\{1H\}$ (proton-decoupled carbon) NMR Spectrum of 1-phenylethyl(E)-3-hydroxy-7-(((E)-5-hydroxy-7-oxo-7-((S)-1-phenylethoxy)hept-3-en-1-yl)disulfaneyl)hept-4-enoate, 7i

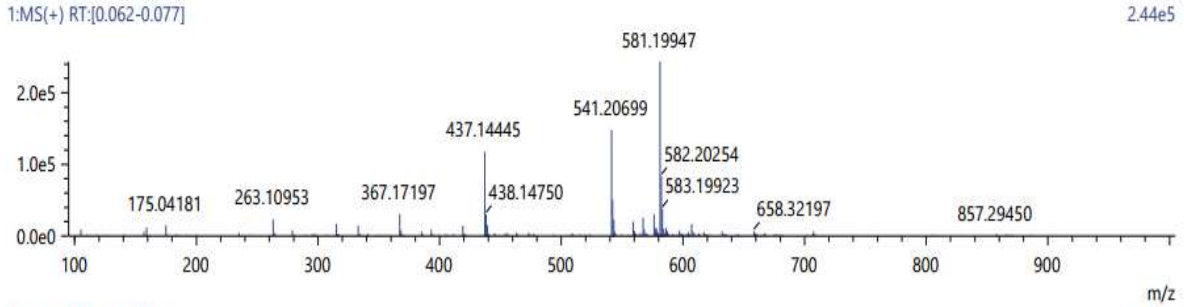


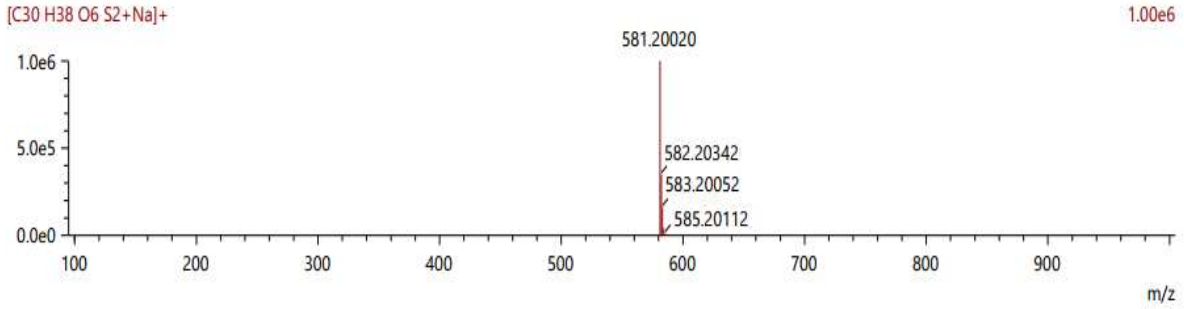
HRMS 1-phenylethyl(E)-3-hydroxy-7-(((E)-5-hydroxy-7-oxo-7-((S)-1-phenylethoxy)hept-3-en-1-yl)disulfaneyl)hept-4-enoate, JRM-8

Jawad HRMS.lcb

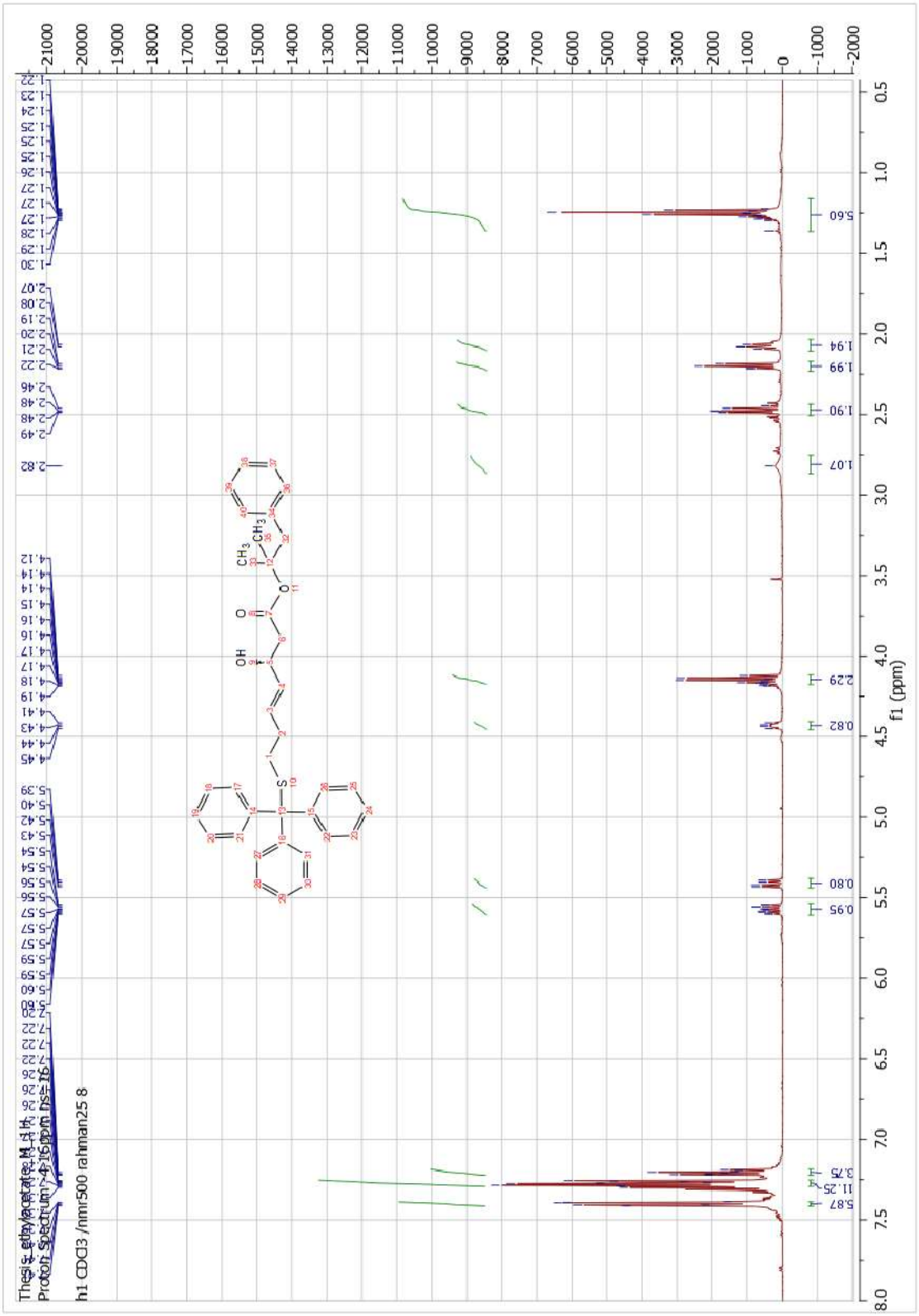
Formula Predictor Result	**C30 H38 O6 S2**
Mass	581.19947
Error Margin	5 ppm
DBE Range	0 - 1000
Electron Ions	Both configurations
HC Ratio	Not Used
Nitrogen Rule	Used

Score	Pred. (M)	Pred. m/z	Meas. m/z	Diff. (mDa)	Formulae (M)	Ion	Diff. (ppm)	Iso Score	DBE
74.02	558.21098	581.20020	581.19947	-0.73	C30 H38 O6 S2	[M+Na]+	-1.256	71.80	12.0

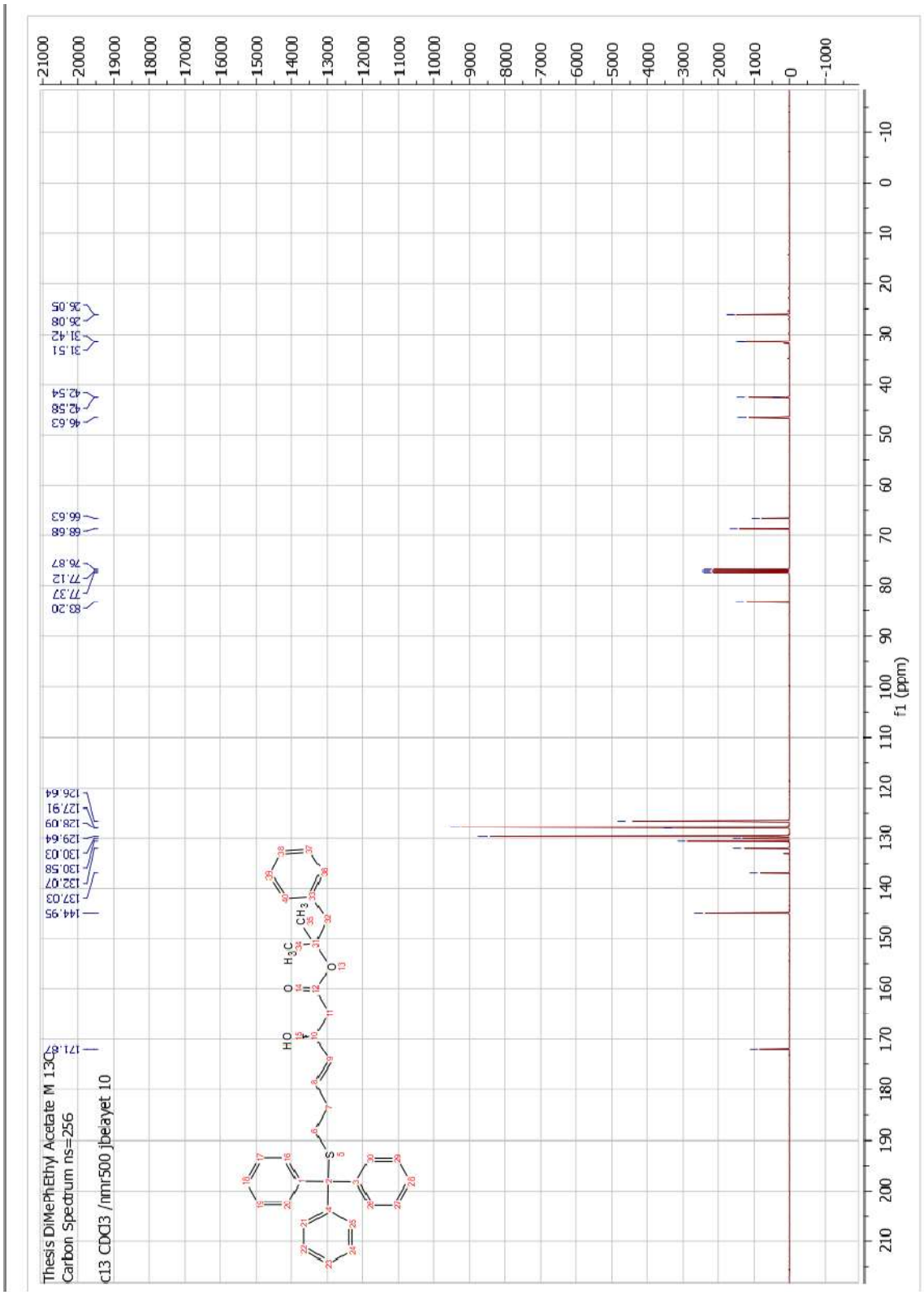




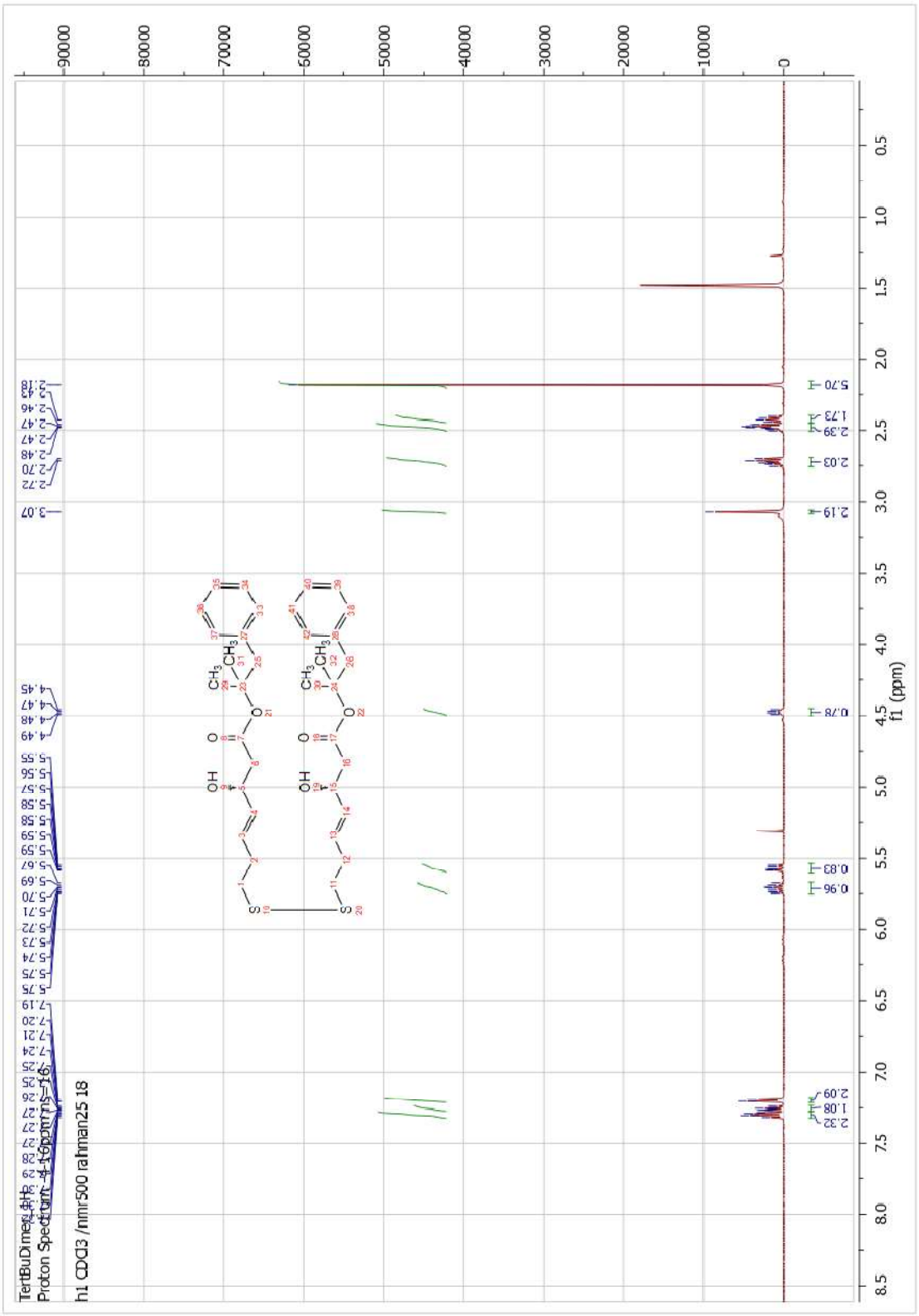
^{1}H NMR Spectrum of (E)-2-phenylpropan-2-yl-3-hydroxy-7-(tritylthio)hept-4-enoate, 7i



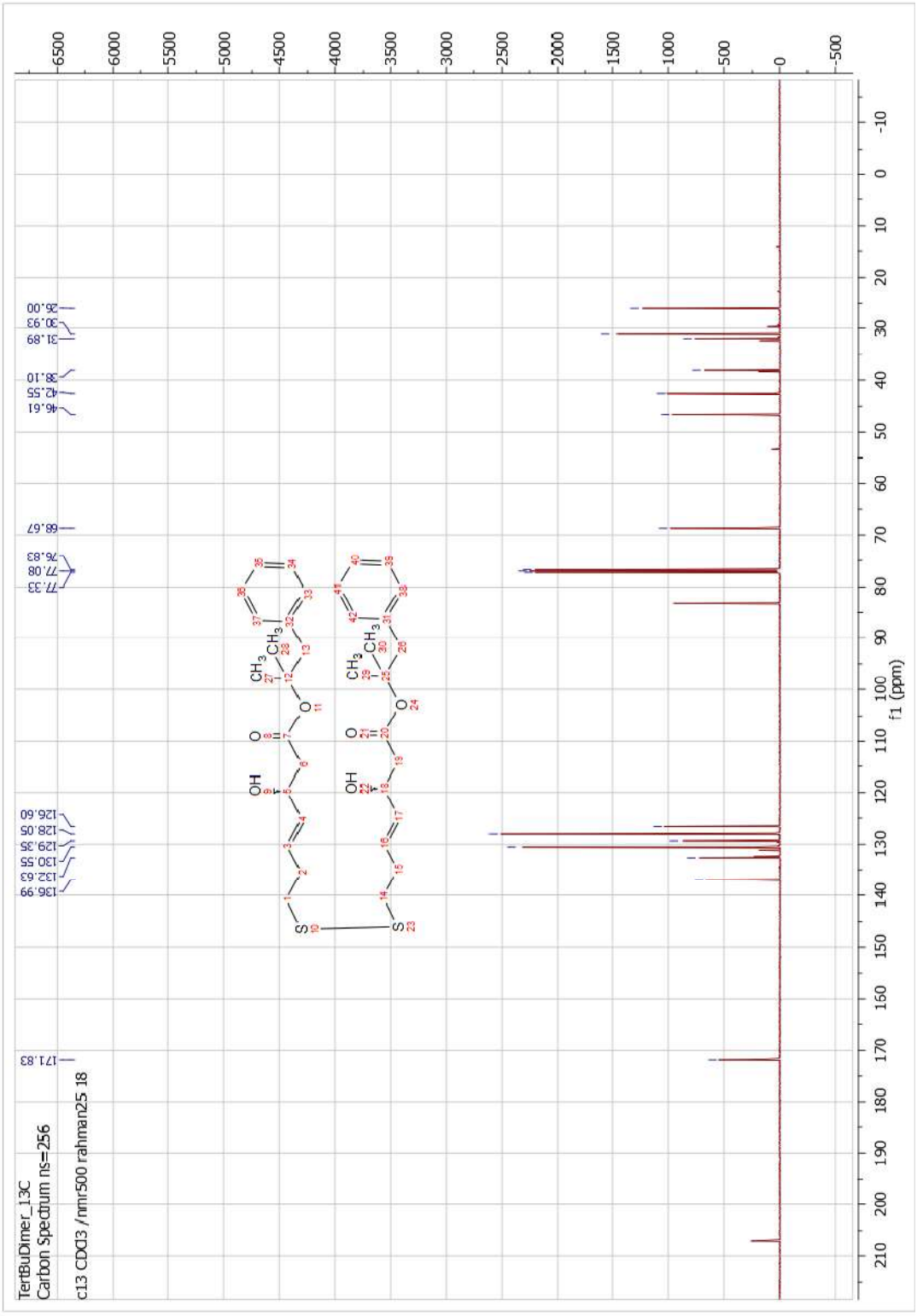
$^{13}C\{1H\}$ (proton-decoupled carbon) NMR Spectrum of (E)-2-phenylpropan-2-yl-3-hydroxy-7-(tritylthio)hept-4-enoate, 7i



^{1}H NMR Spectrum of 2-phenylpropan-2-yl (E)-3-hydroxy-7-(((E)-5-hydroxy-7-oxo-7-((2-phenylpropan-2-yl)oxy)hept-3-en-1-yl)disulfaneyl)hept-4-enoate, JRM-9

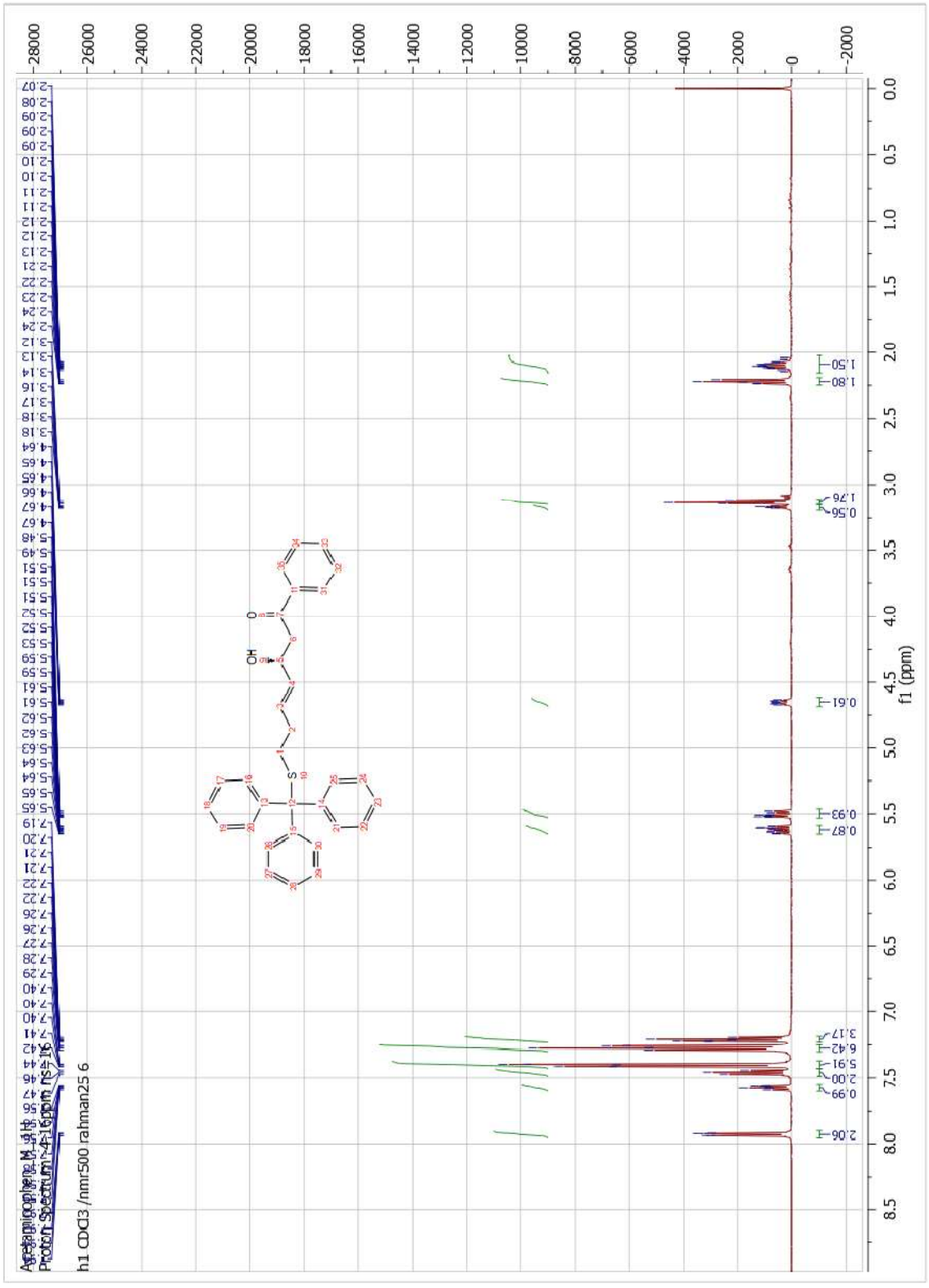


$^{13}C\{1H\}$ (proton-decoupled carbon) NMR Spectrum of 2-phenylpropan-2-yl (E)-3-hydroxy-7-(((E)-5-hydroxy-7-oxo-7-((2-phenylpropan-2-yl)oxy)hept-3-en-1-yl)disulfaneyl)hept-4-enoate, JRM-9

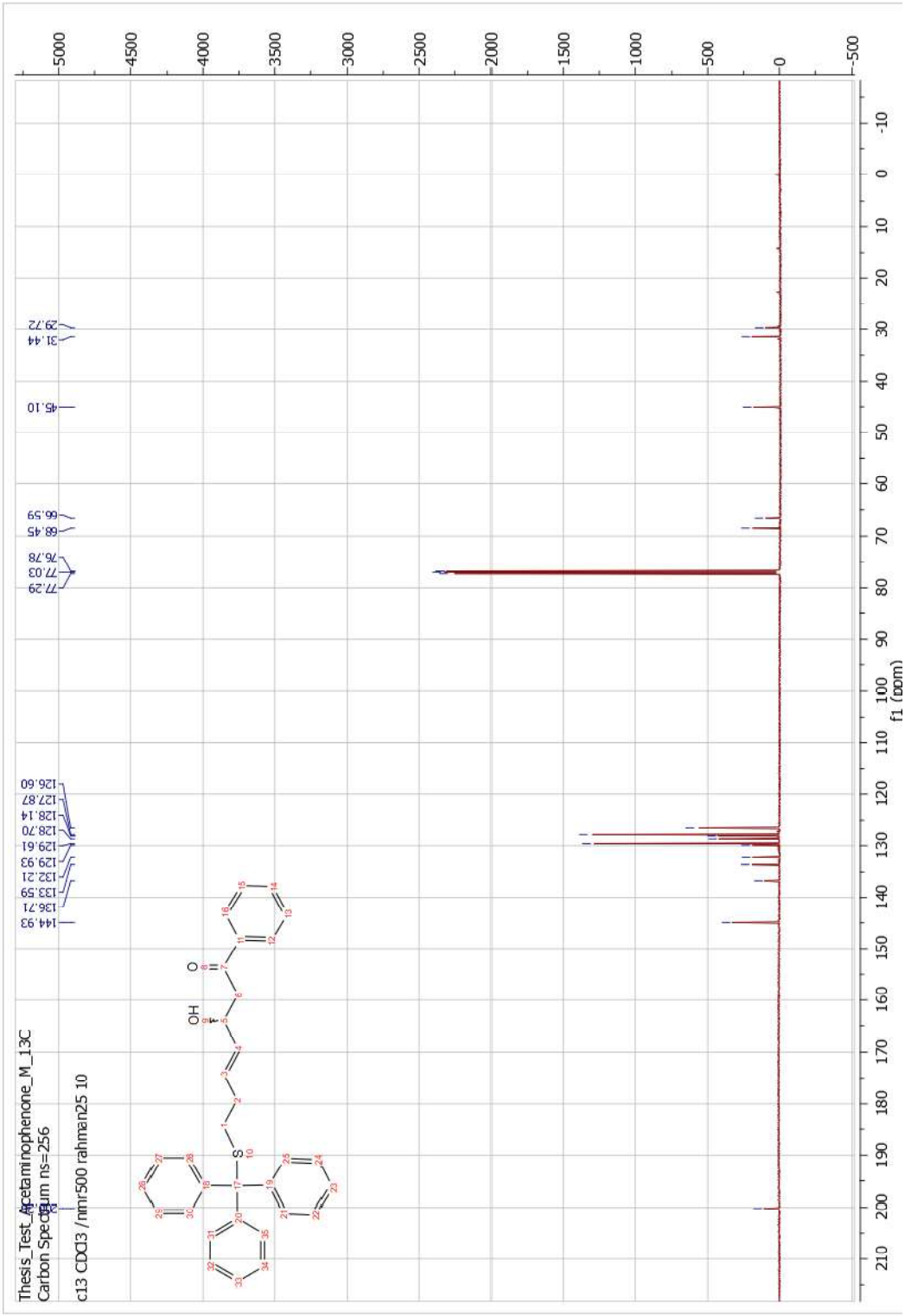


Ketone Derivatives

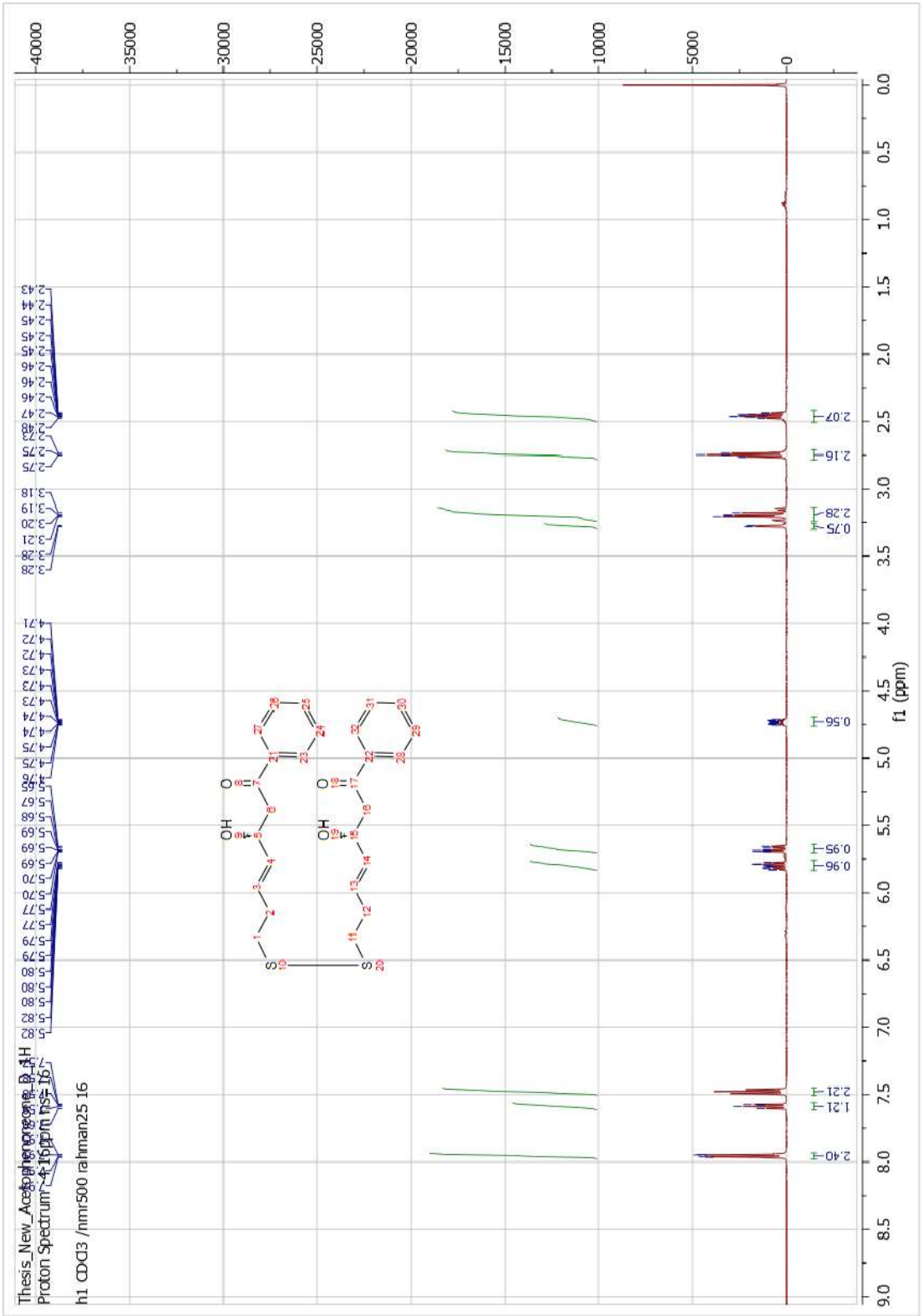
^{1}H NMR Spectrum of (E)-3-hydroxy-1-phenyl-7-(tritylthio)hept-4-en-1-one, 9a



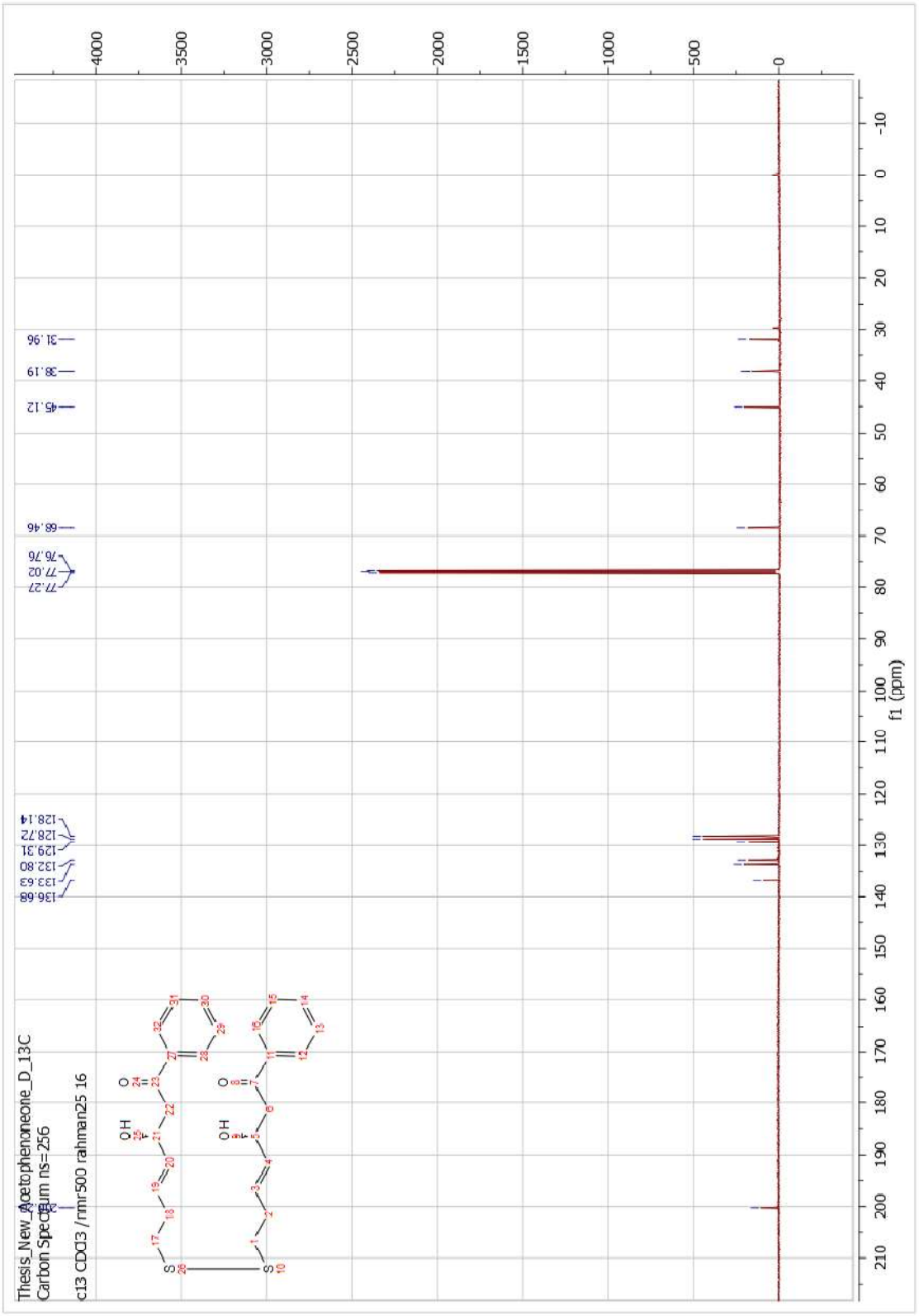
$^{13}C\{1H\}$ (proton-decoupled carbon) NMR Spectrum of (E)-3-hydroxy-1-phenyl-7-(tritylthio)hept-4-en-1-one, 9a



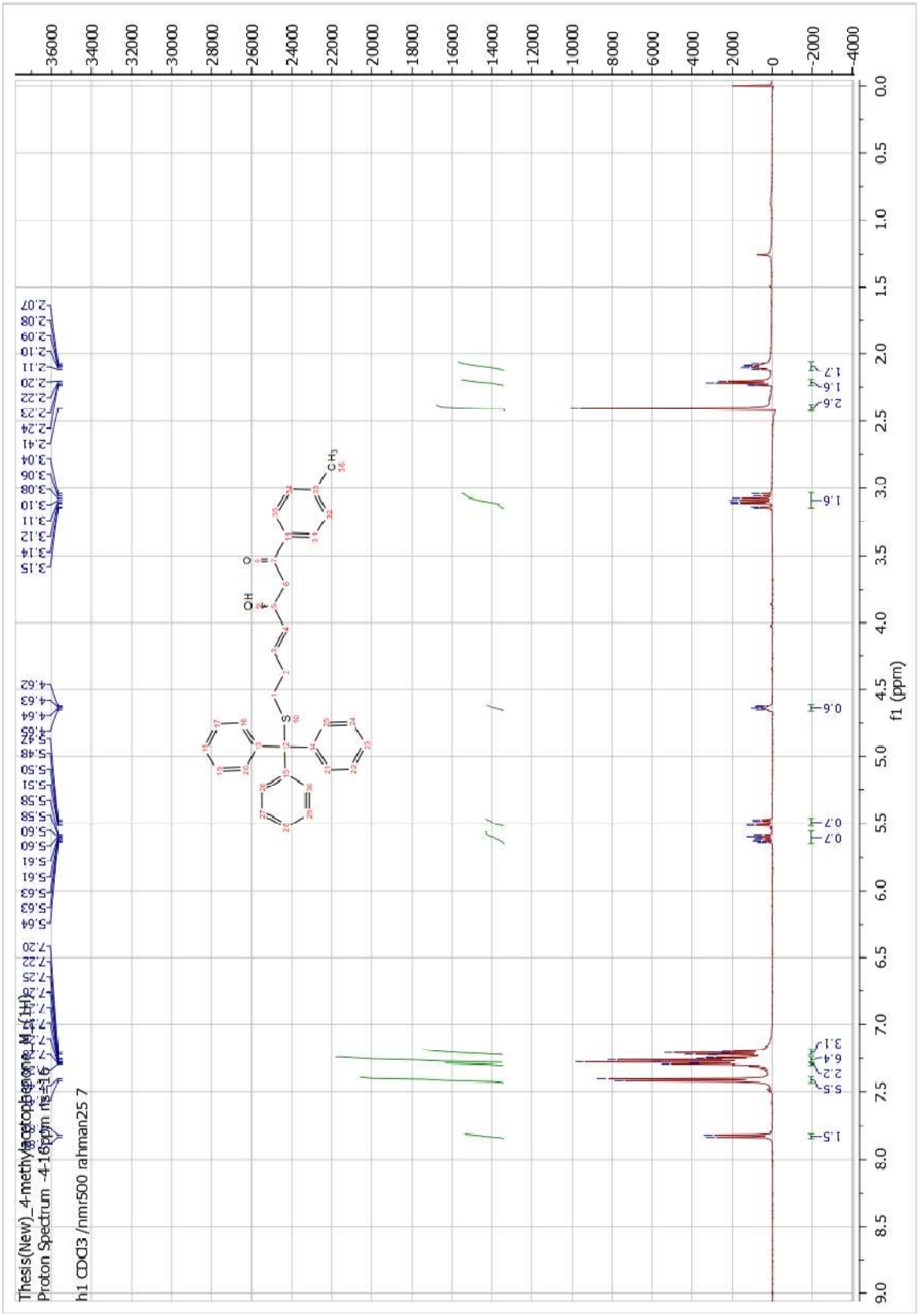
^{1}H NMR Spectrum of (4E,4'E)-7,7'-disulfanediylbis(3-hydroxy-1-phenylhept-4-en-1-one), JRM-10



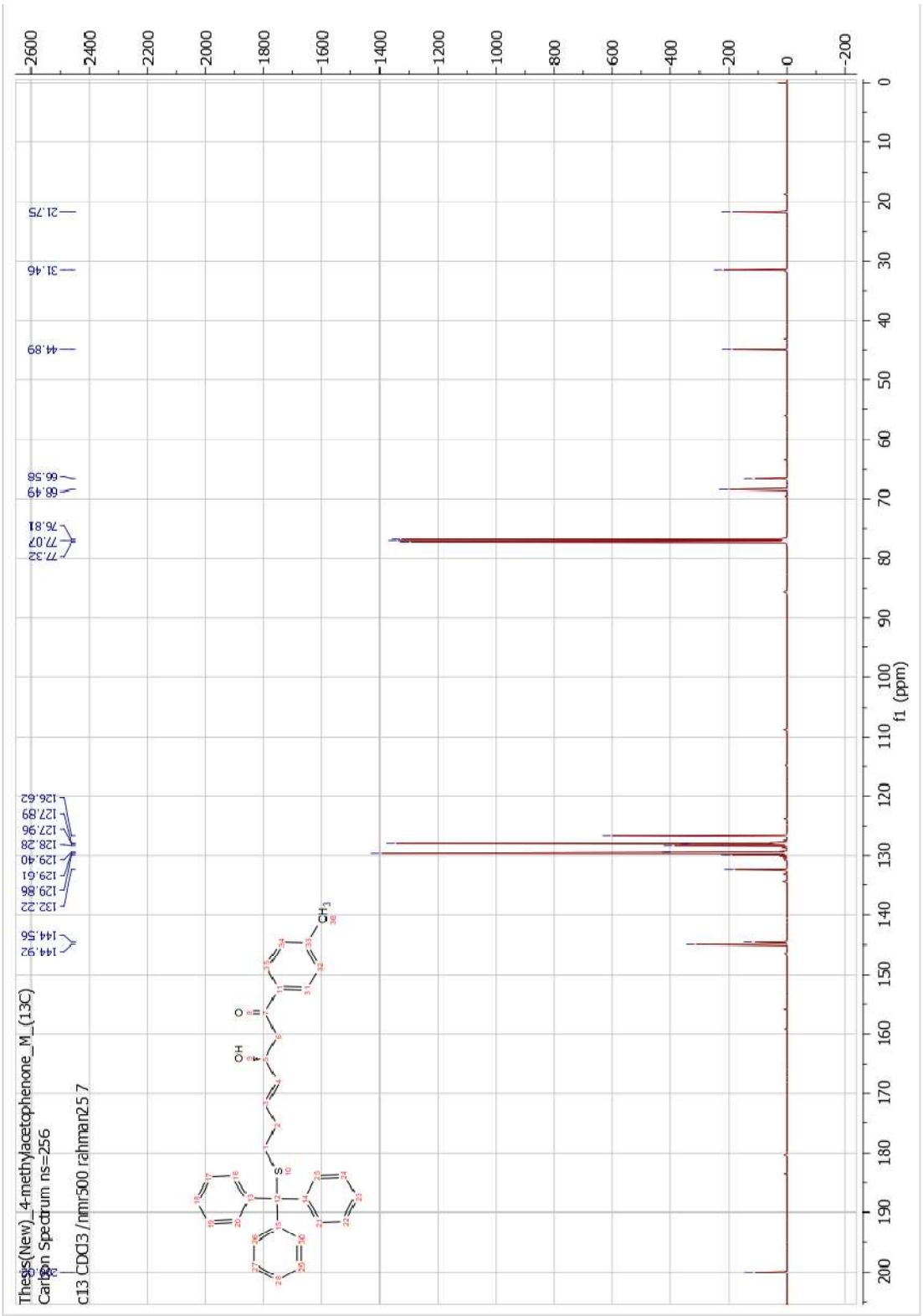
$^{13}C\{1H\}$ (proton-decoupled carbon) NMR Spectrum of (4E,4'E)-7,7'-disulfanediylbis(3-hydroxy-1-phenylhept-4-en-1-one), JRM-10



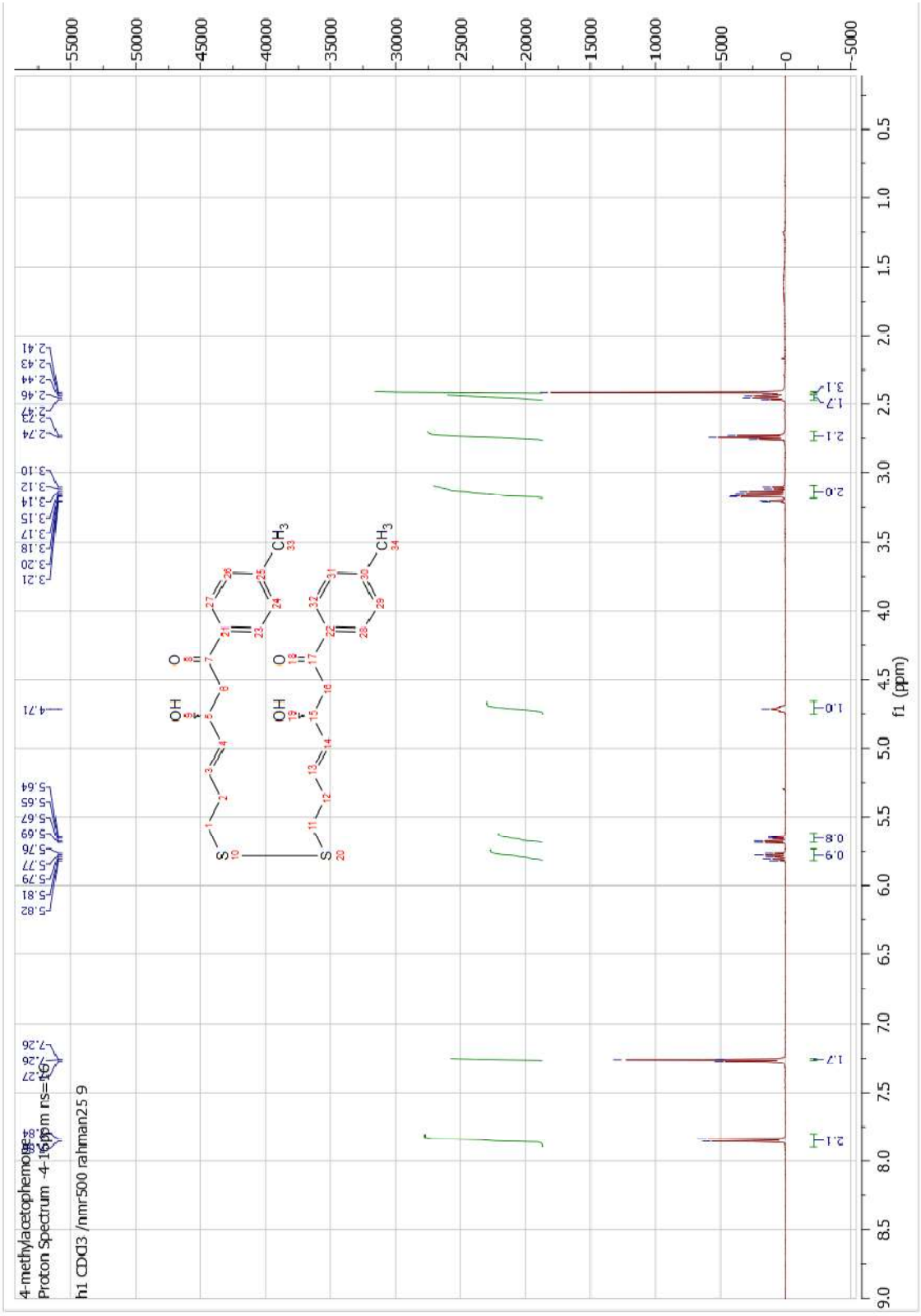
^{1}H NMR Spectrum of (E)-3-hydroxy-1-(p-tolyl)-7-(tritylthio)hept-4-en-1-one, 9b



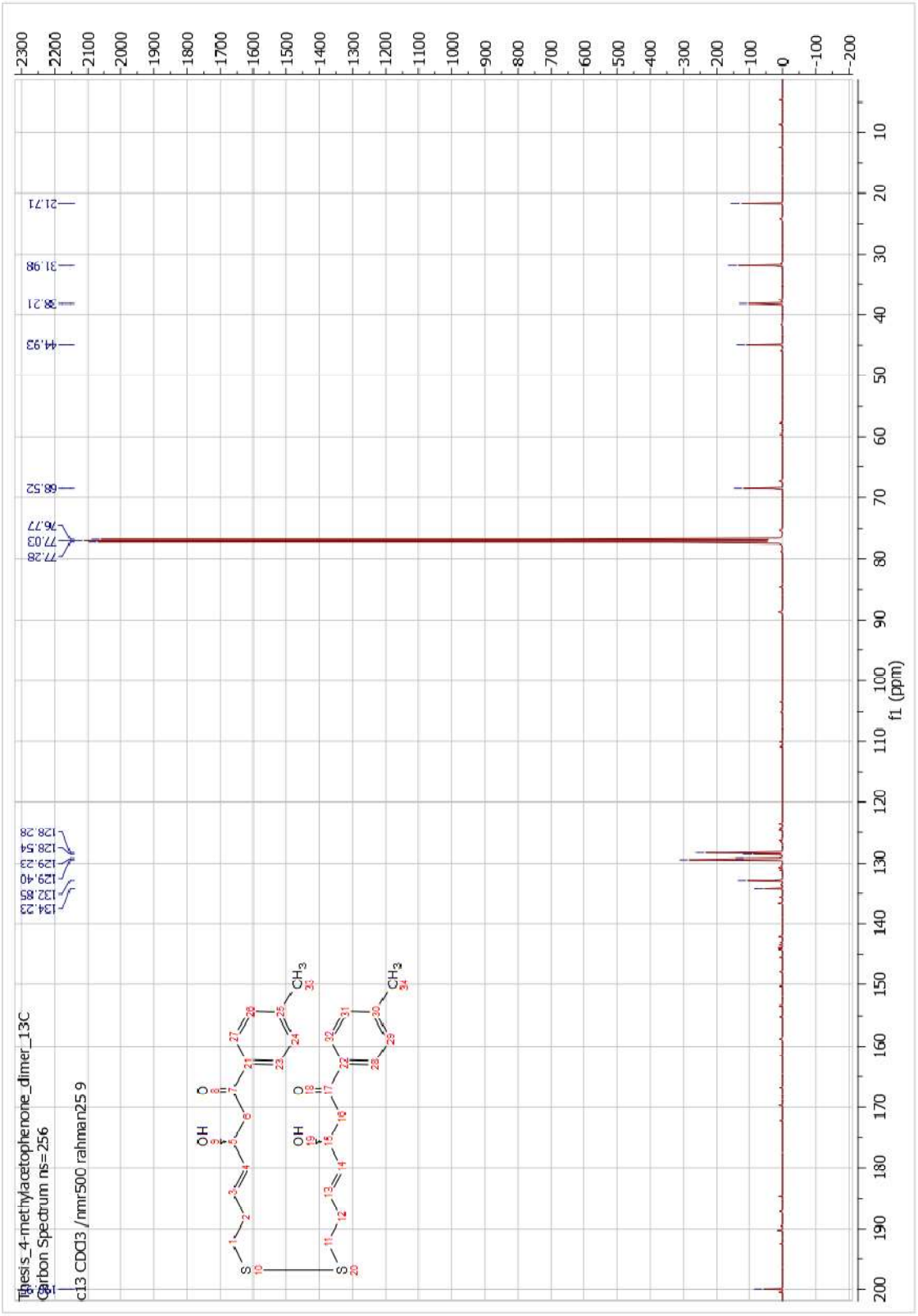
$^{13}C\{1H\}$ (proton-decoupled carbon) NMR Spectrum of (E)-3-hydroxy-1-(p-tolyl)-7-(tritylthio)hept-4-en-1-one, 9b



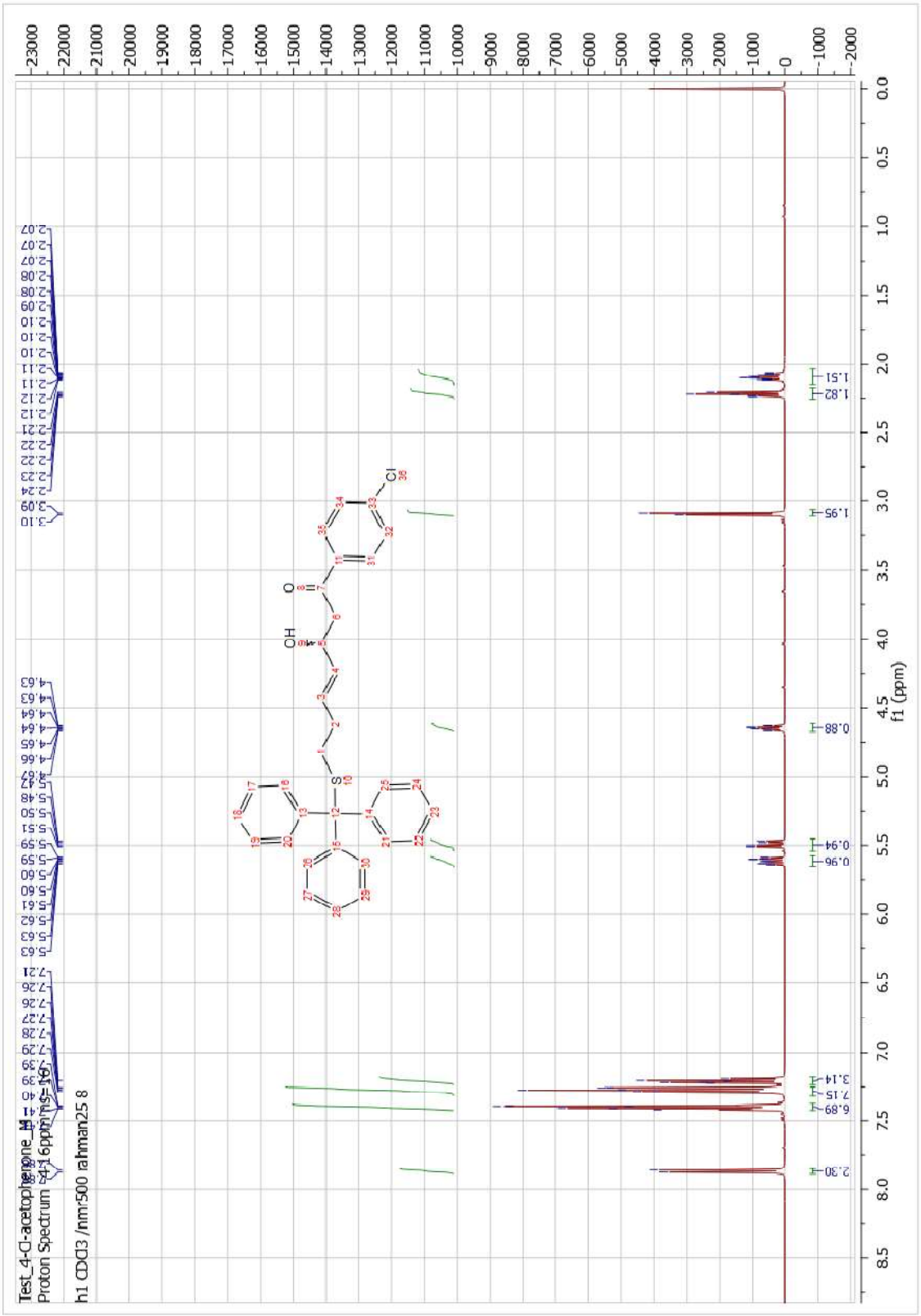
^{1}H NMR Spectrum of (4E,4'E)-7,7'-disulfanediylbis(3-hydroxy-1-(p-tolyl)hept-4-en-1-one), JRM-11



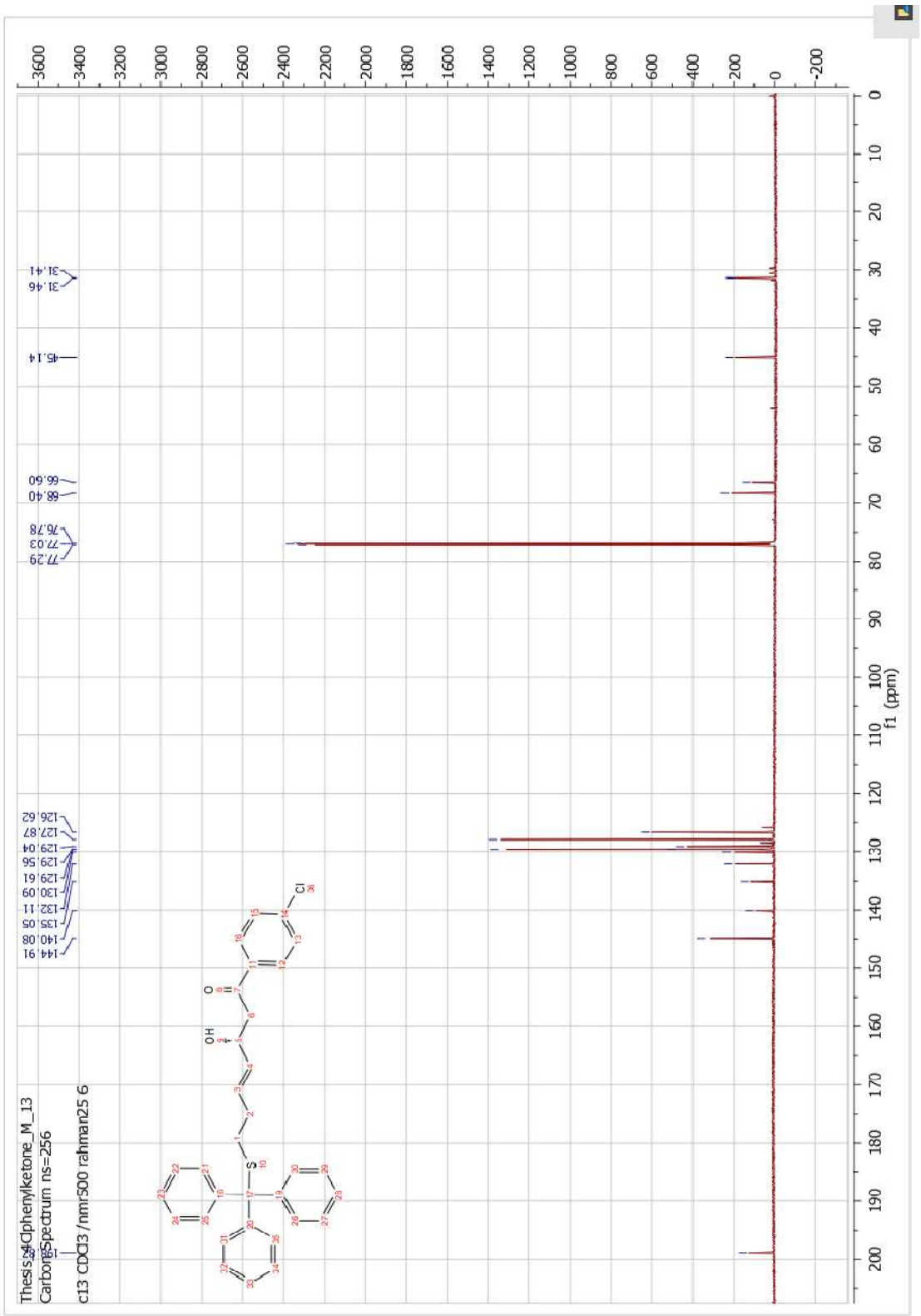
$^{13}C\{1H\}$ (proton-decoupled carbon) NMR Spectrum of (4E,4'E)-7,7'-disulfanediylbis(3-hydroxy-1-(p-tolyl)hept-4-en-1-one), 37



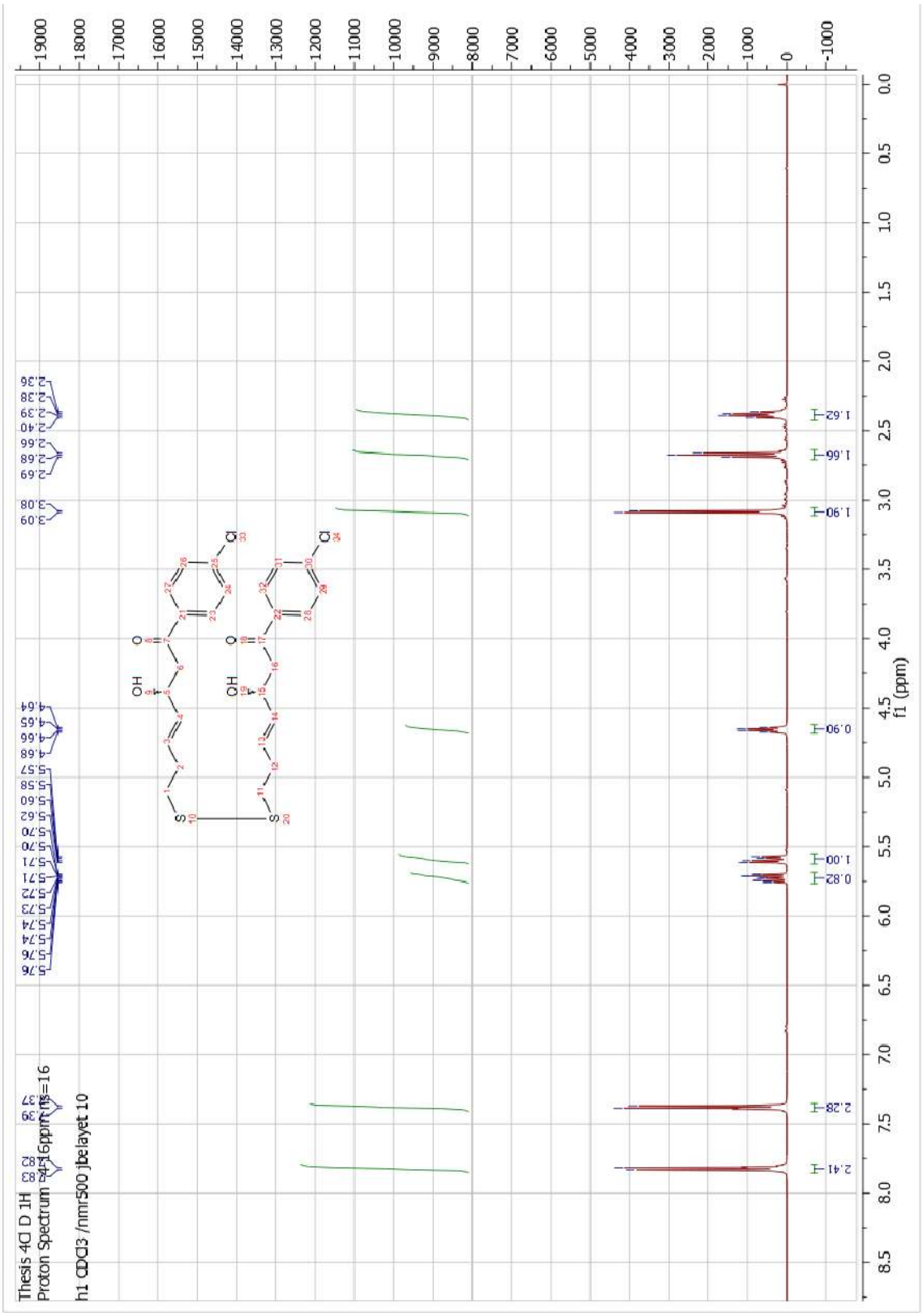
^{1}H NMR Spectrum of (E)-1-(4-chlorophenyl)-3-hydroxy-7-(tritylthio)hept-4-en-1-one, 9c



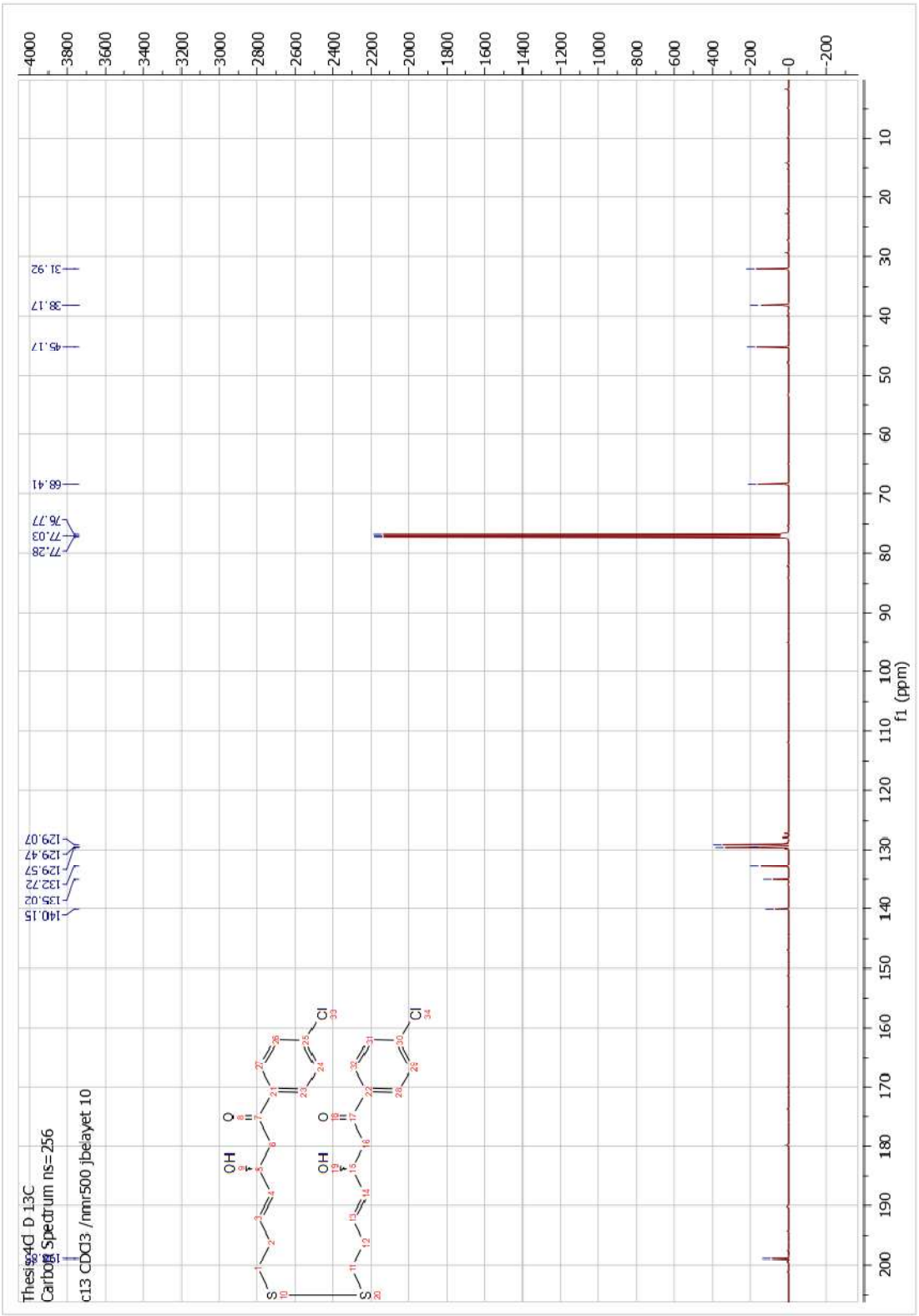
$^{13}C\{1H\}$ (proton-decoupled carbon) NMR Spectrum of (E)-1-(4-chlorophenyl)-3-hydroxy-7-(tritylthio)hept-4-en-1-one, 9c



^{1}H NMR Spectrum of (4E,4'E)-7,7'-disulfanediylbis(1-(4-chlorophenyl)-3-hydroxyhept-4-en-1-one), JRM-12



$^{13}C\{1H\}$ (proton-decoupled carbon) NMR Spectrum of (4E,4'E)-7,7'-disulfanediylbis(1-(4-chlorophenyl)-3-hydroxyhept-4-en-1-one), JRM-12

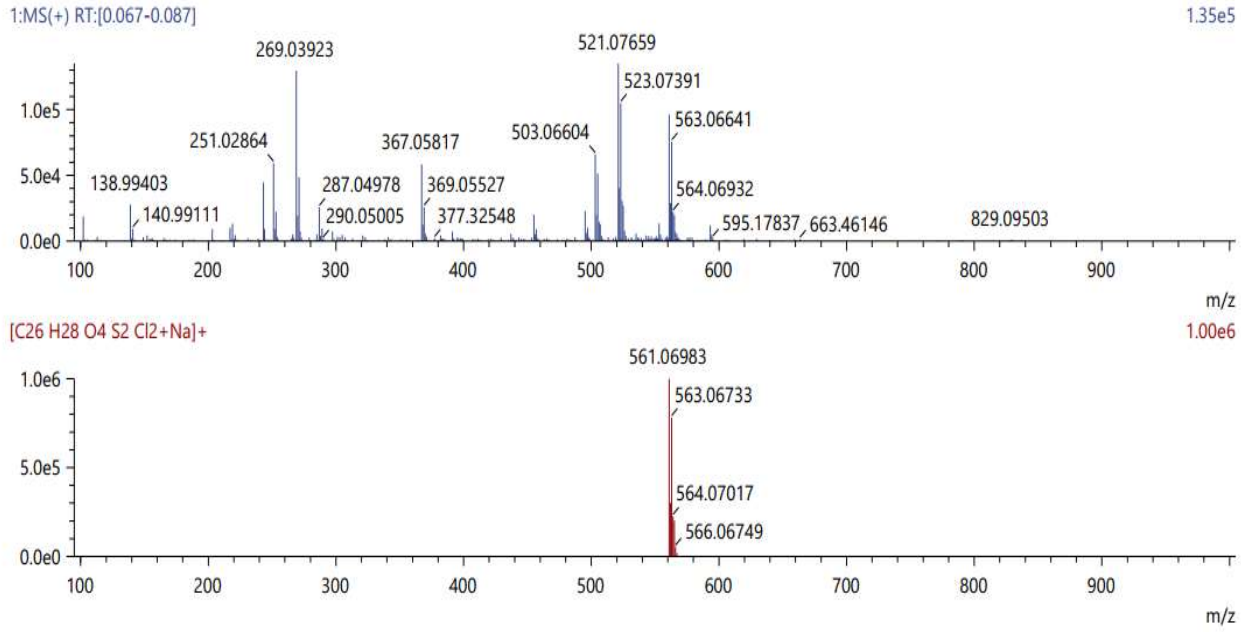


HRMS (4E,4'E)-7,7'-disulfanediylbis(1-(4-chlorophenyl)-3-hydroxyhept-4-en-1-one), JRM-12

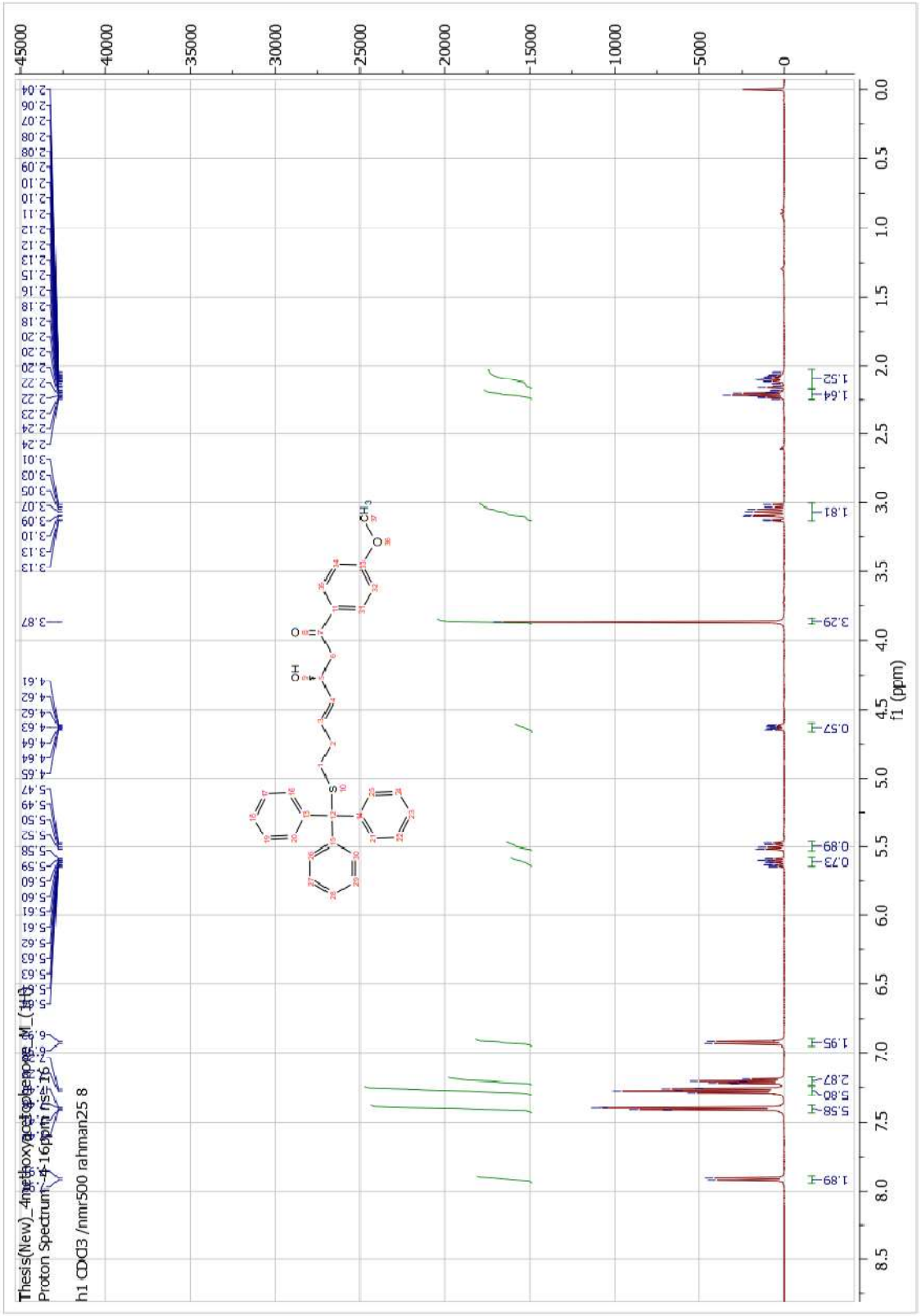
Jawad HRMS.lcb

Formula Predictor Result	**C26 H28 O4 S2 Cl2**
Mass	561.069
Error Margin	5 ppm
DBE Range	0 - 1000
Electron Ions	Both configurations
HC Ratio	Not Used
Nitrogen Rule	Used

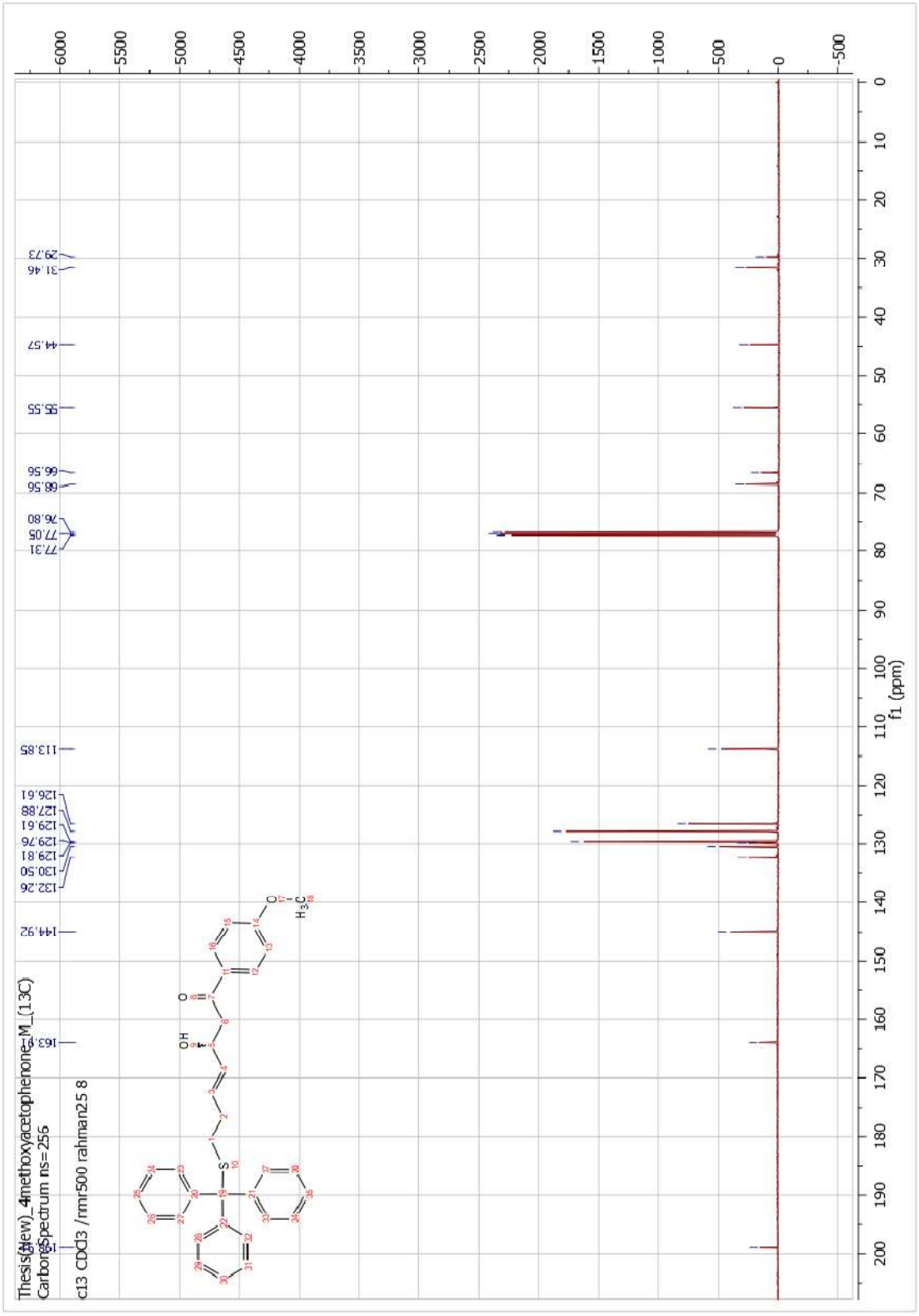
Score	Pred. (M)	Pred. m/z	Meas. m/z	Diff. (mDa)	Formulae (M)	Ion	Diff. (ppm)	Iso Score	DBE
75.24	538.08061	561.06983	561.06900	-0.83	C26 H28 O4 S2 Cl2	[M+Na]+	-1.479	84.41	12.0



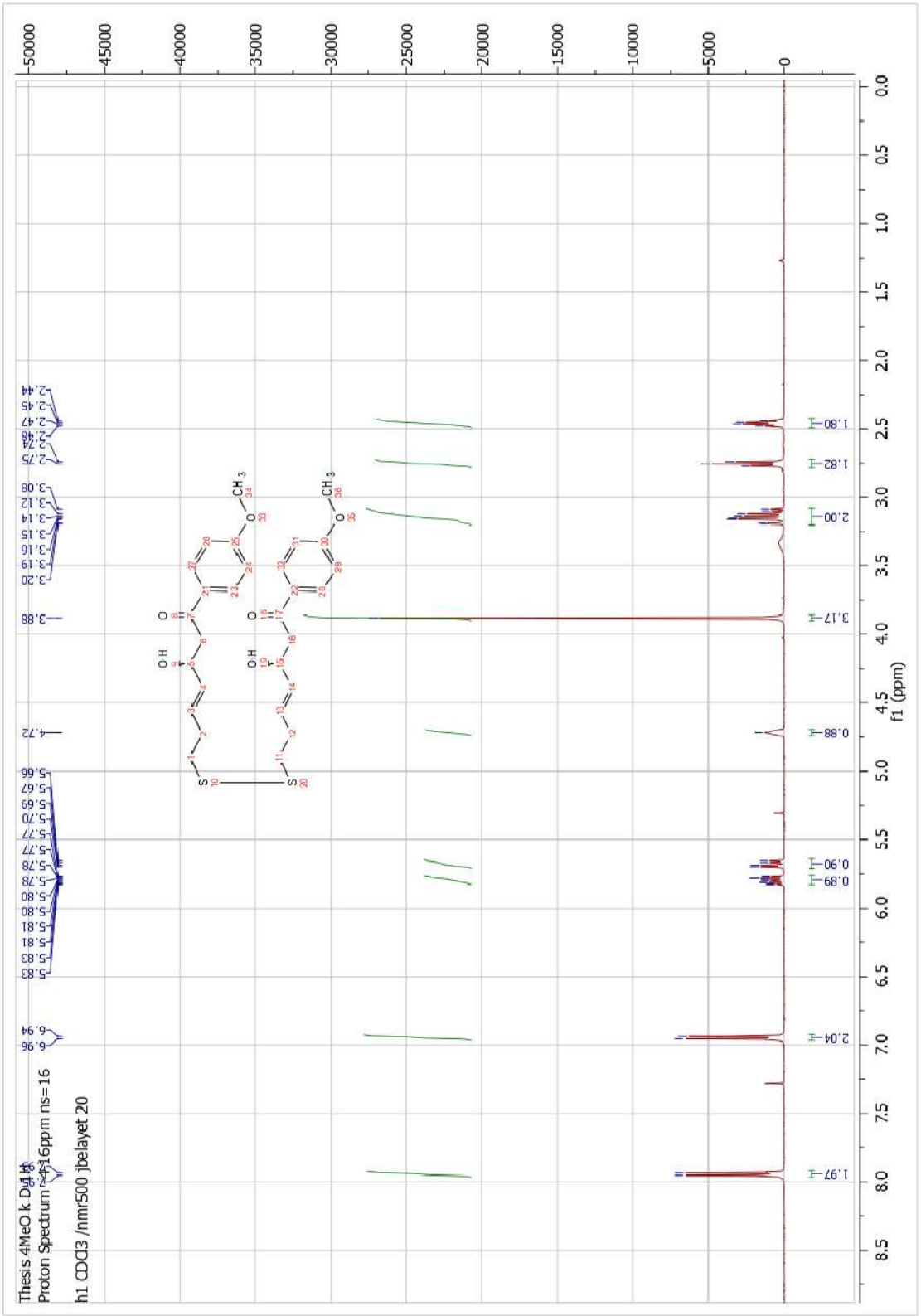
^{1}H NMR Spectrum of (E)-3-hydroxy-1-(4-methoxyphenyl)-7-(tritylthio)hept-4-en-1-one, 9d



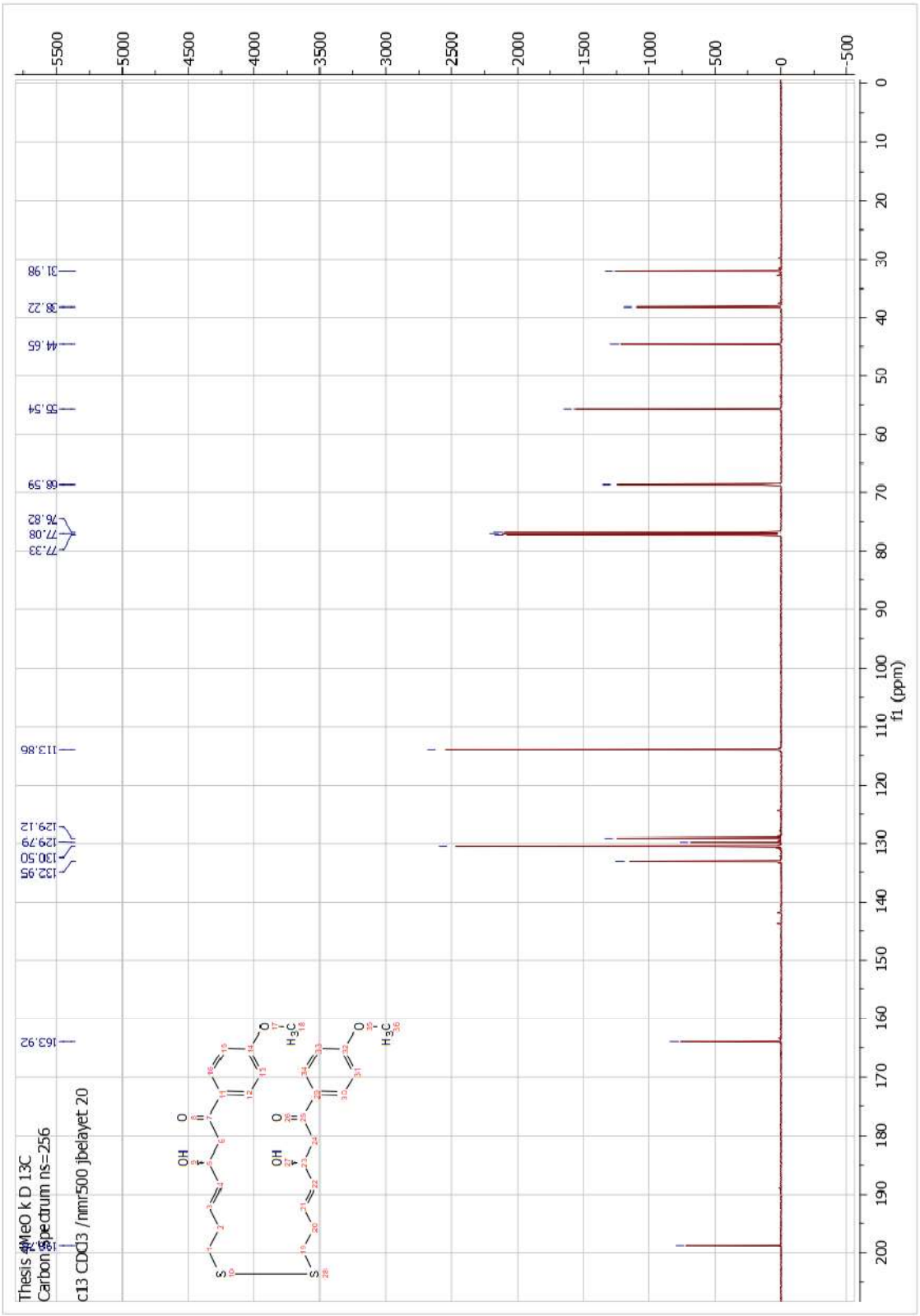
$^{13}C\{1H\}$ (proton-decoupled carbon) NMR Spectrum of (E)-3-hydroxy-1-(4-methoxyphenyl)-7-(tritylthio)hept-4-en-1-one, 9d



^{1}H NMR Spectrum of (4E,4'E)-7,7'-disulfanediylbis(3-hydroxy-1-(4-methoxyphenyl)hept-4-en-1-one), JRM-13



$^{13}C\{1H\}$ (proton-decoupled carbon) NMR Spectrum of (4E,4'E)-7,7'-disulfanediylbis(3-hydroxy-1-(4-methoxyphenyl)hept-4-en-1-one), JRM-13

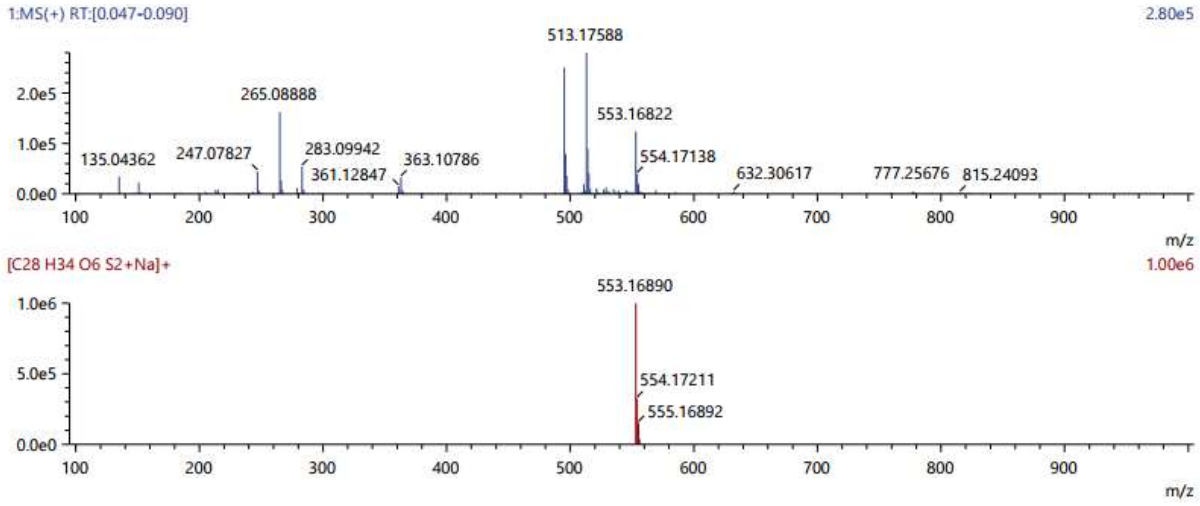


HRMS (4E,4'E)-7,7'-disulfanediylbis(3-hydroxy-1-(4-methoxyphenyl)hept-4-en-1-one), JRM-13

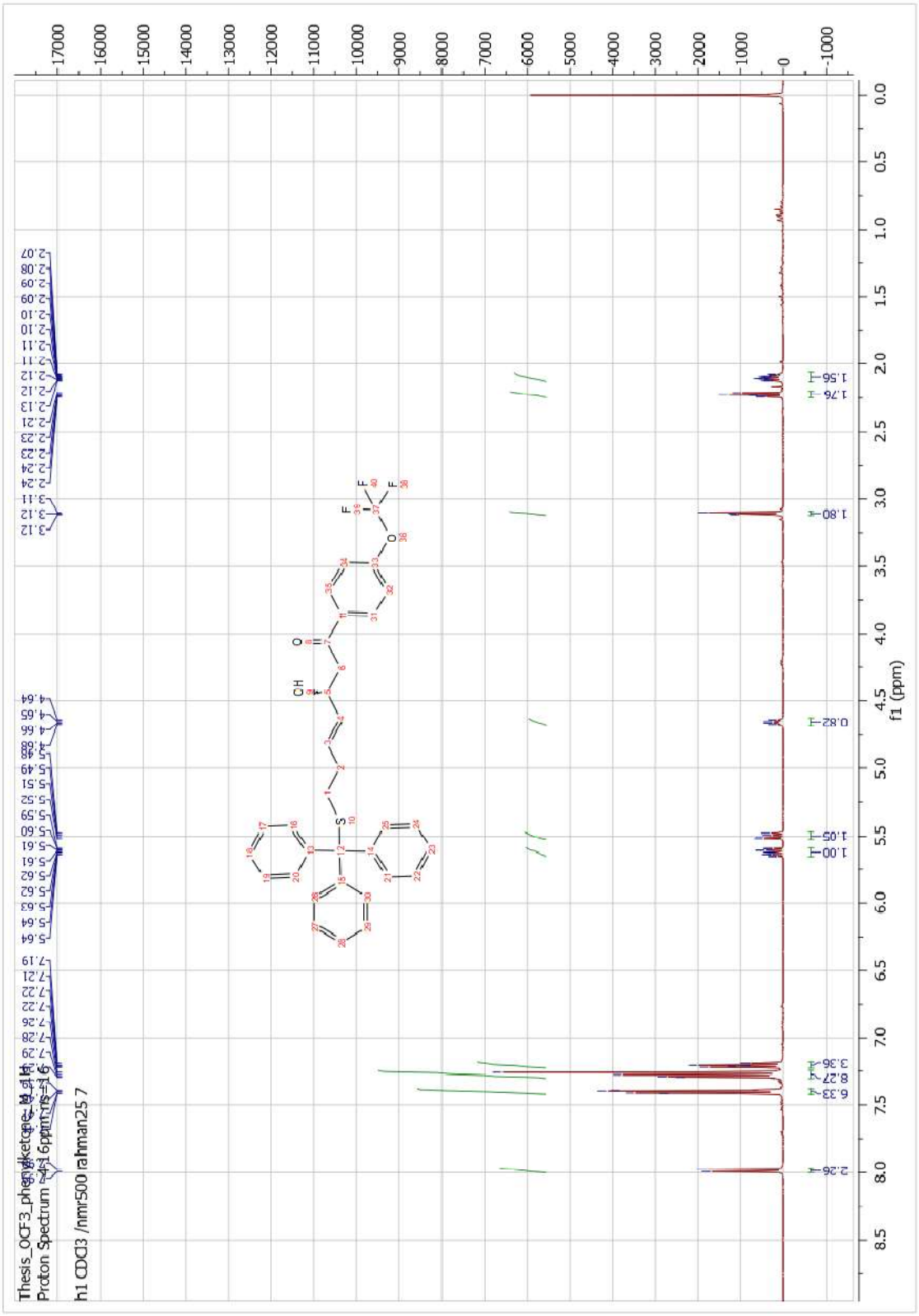
Jawad HRMS.lcb

Formula Predictor Result	**C28 H34 O6 S2**
Mass	553.16822
Error Margin	5 ppm
DBE Range	0 - 1000
Electron Ions	Both configurations
HC Ratio	Not Used
Nitrogen Rule	Used

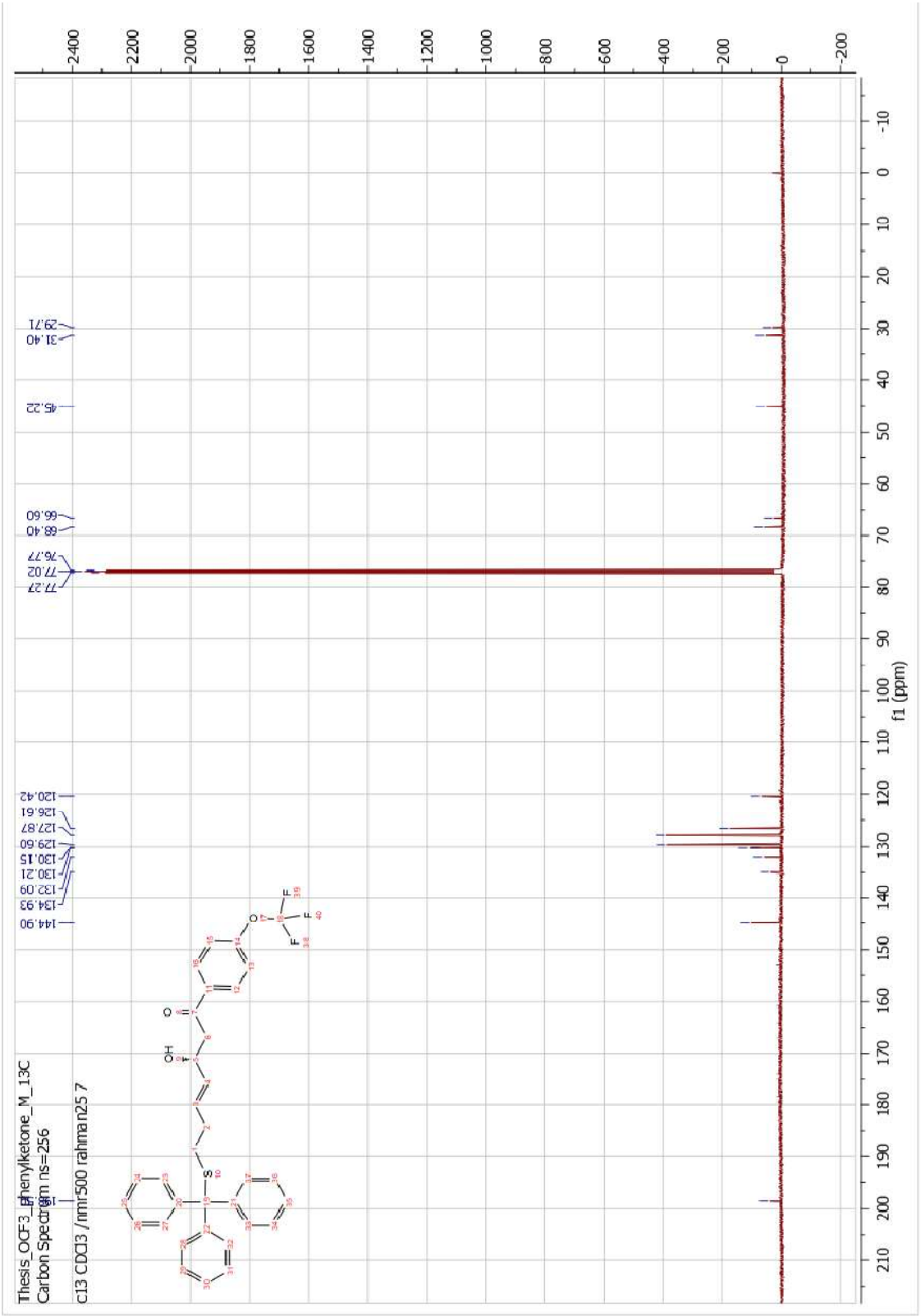
Score	Pred. (M)	Pred. m/z	Meas. m/z	Diff. (mDa)	Formulae (M)	Ion	Diff. (ppm)	Iso Score	DBE
88.51	530.17968	553.16890	553.16822	-0.68	C28 H34 O6 S2	[M+Na]+	-1.229	87.89	12.0



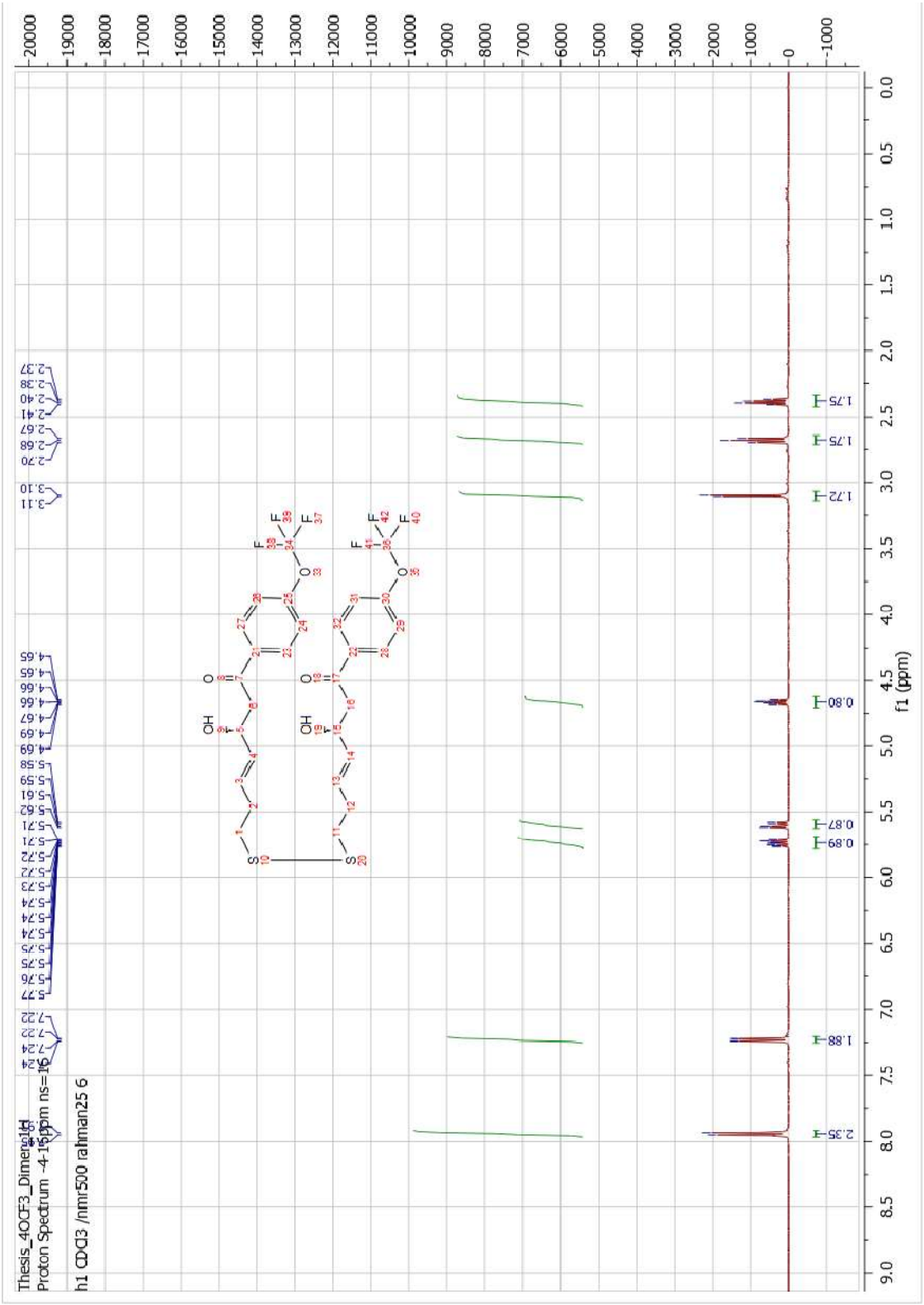
^{1}H NMR Spectrum of (E)-3-hydroxy-1-(4-(trifluoromethoxy)phenyl)-7-(tritylthio)hept-4-en-1-one, 9e



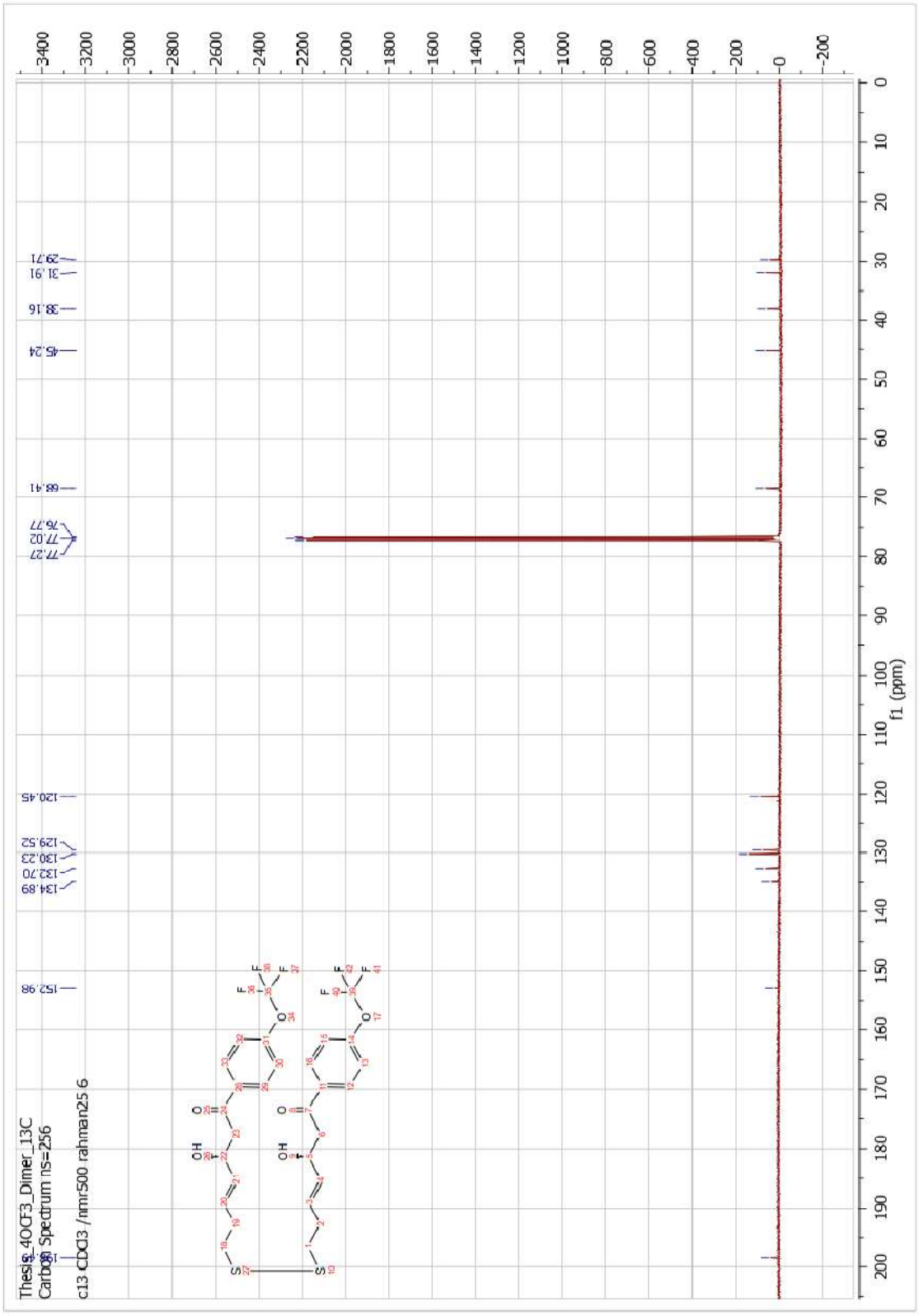
$^{13}C\{1H\}$ (proton-decoupled carbon) NMR Spectrum of (E)-3-hydroxy-1-(4-(trifluoromethoxy)phenyl)-7-(tritylthio)hept-4-en-1-one, 9e



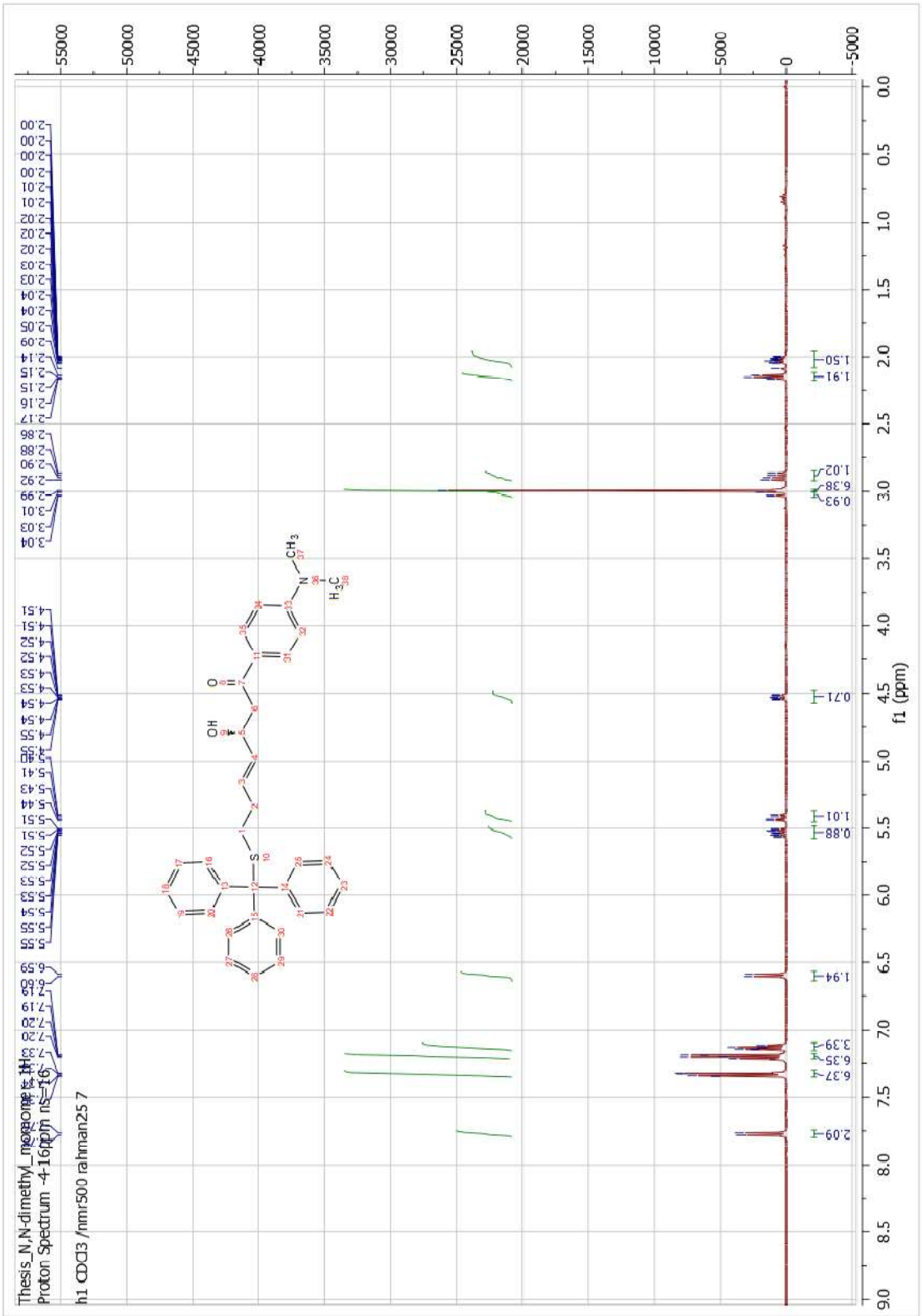
^{1}H NMR Spectrum of (4E,4'E)-7,7'-disulfanediylbis(3-hydroxy-1-(4-(trifluoromethoxy)phenyl)hept-4-en-1-one), JRM-14



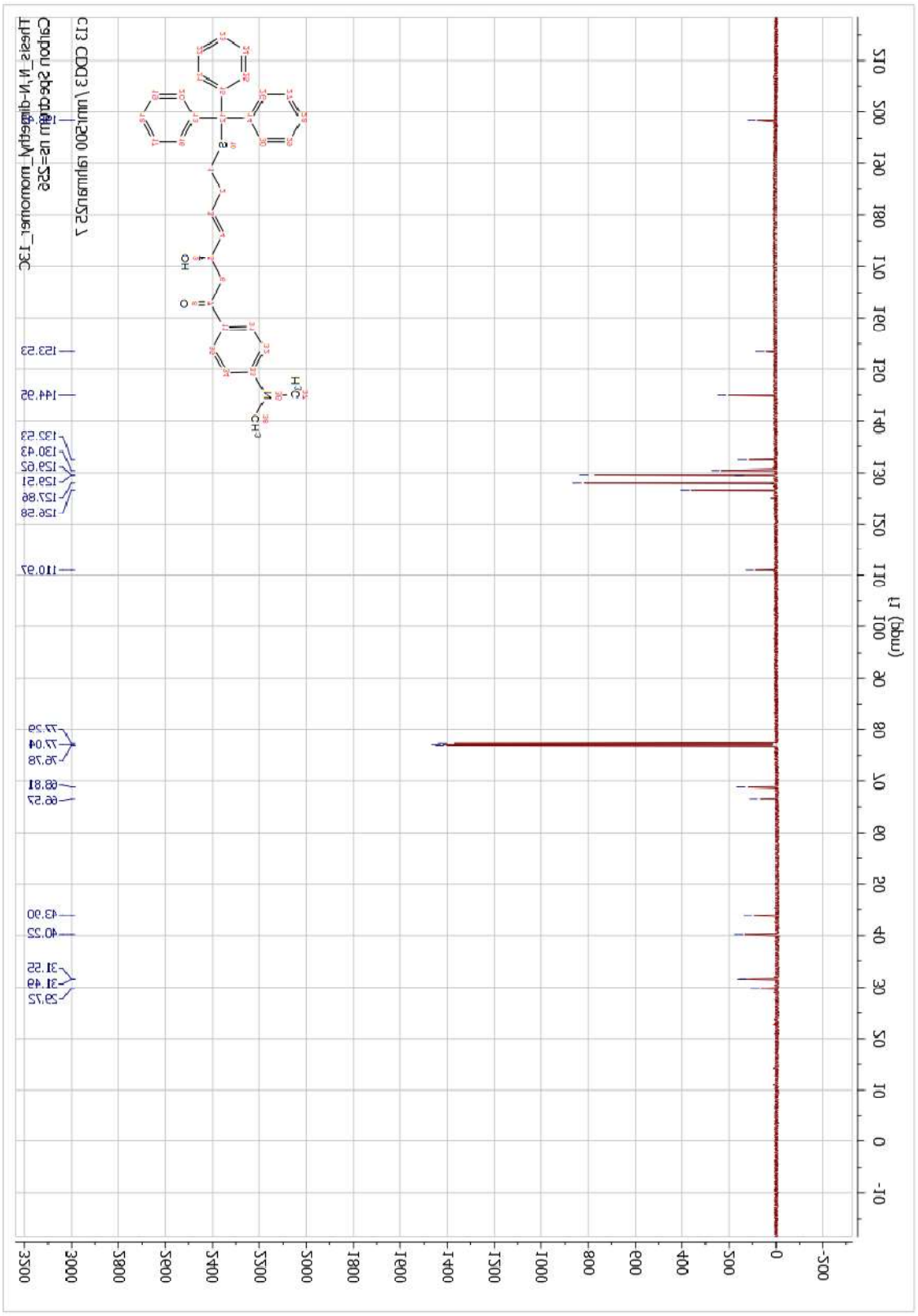
$^{13}C\{1H\}$ (proton-decoupled carbon) NMR Spectrum of (4E,4'E)-7,7'-disulfanediylbis(3-hydroxy-1-(4-(trifluoromethoxy)phenyl)hept-4-en-1-one), JRM-14



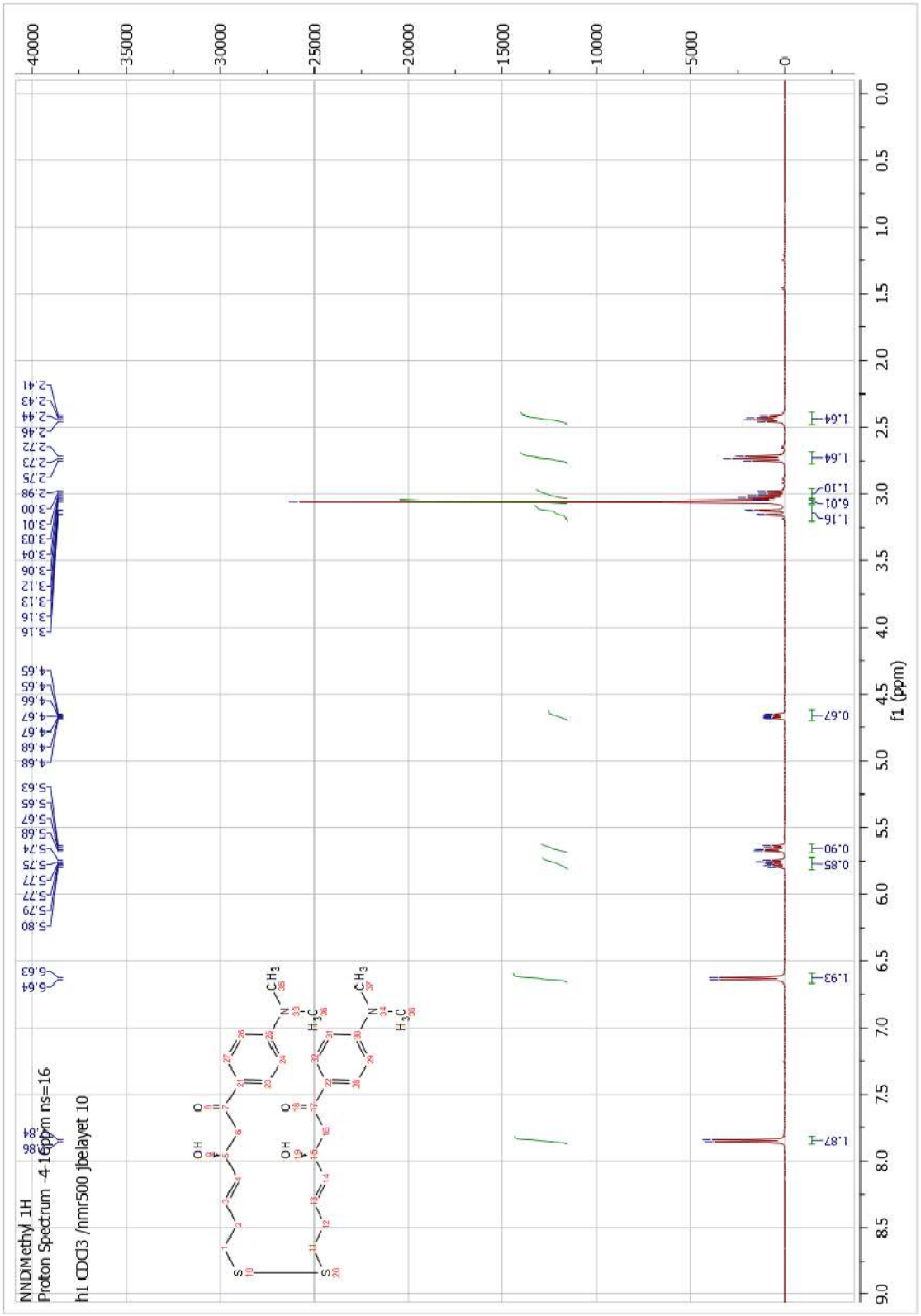
^{1}H NMR Spectrum of (E)-1-(4-(dimethylamino)phenyl)-3-hydroxy-7-(tritylthio)hept-4-en-1-one, 9f



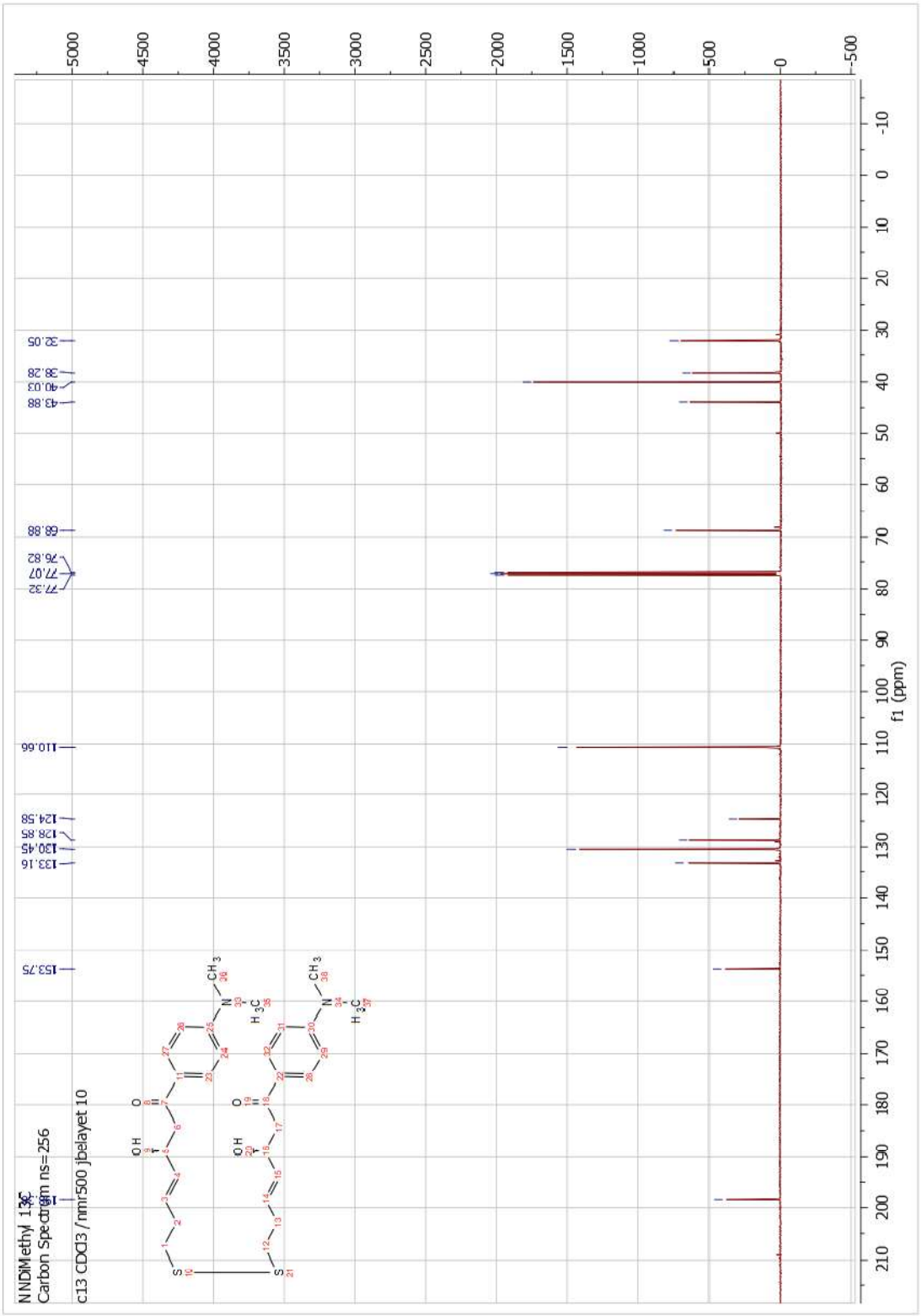
$^{13}C\{1H\}$ (proton-decoupled carbon) NMR Spectrum of (E)-1-(4-(dimethylamino)phenyl)-3-hydroxy-7-(tritylthio)hept-4-en-1-one, 9f



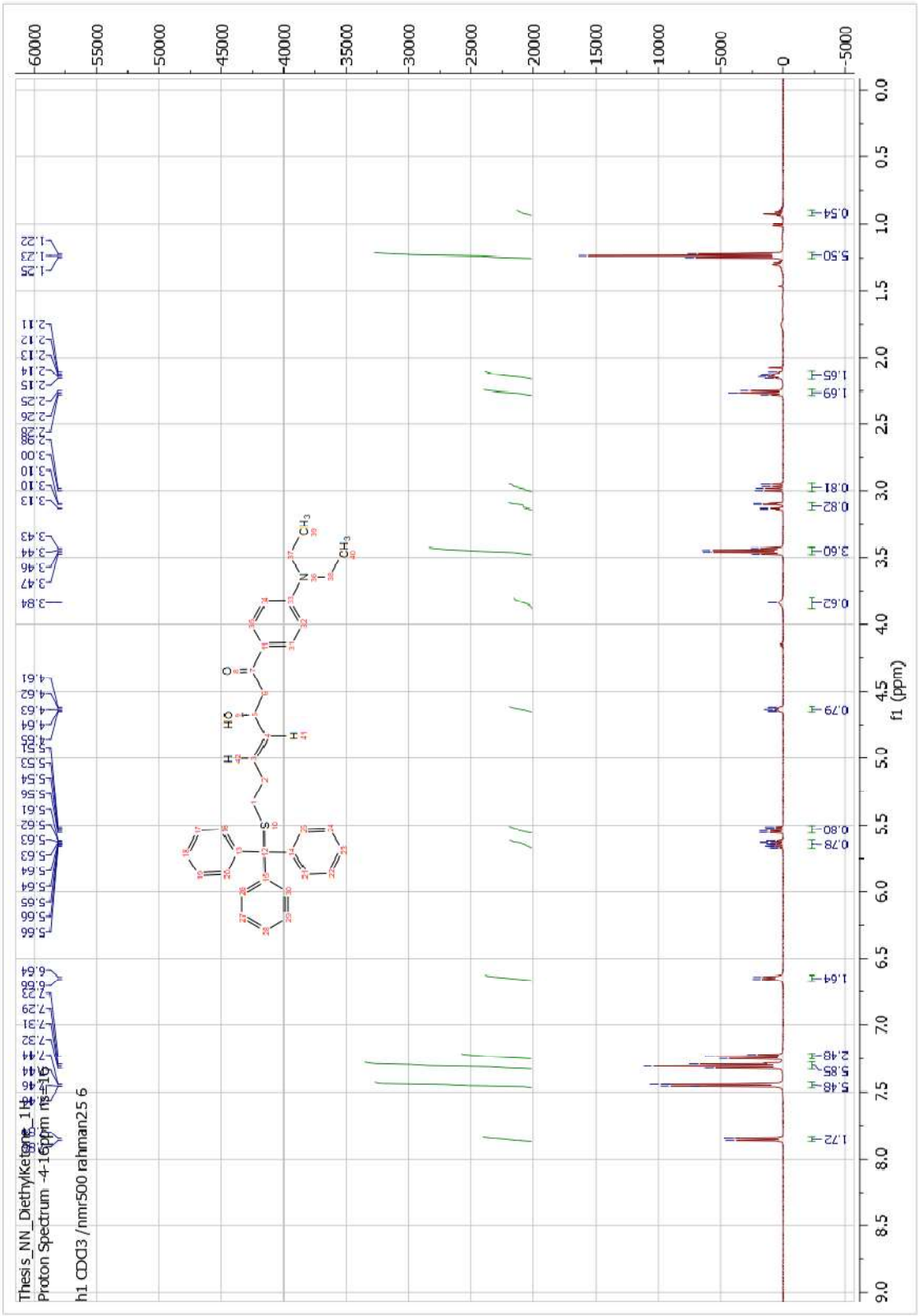
^{1}H NMR Spectrum of (4E,4'E)-7,7'-disulfanediylbis(1-(4-(dimethylamino)phenyl)-3-hydroxyhept-4-en-1-one), JRM-15



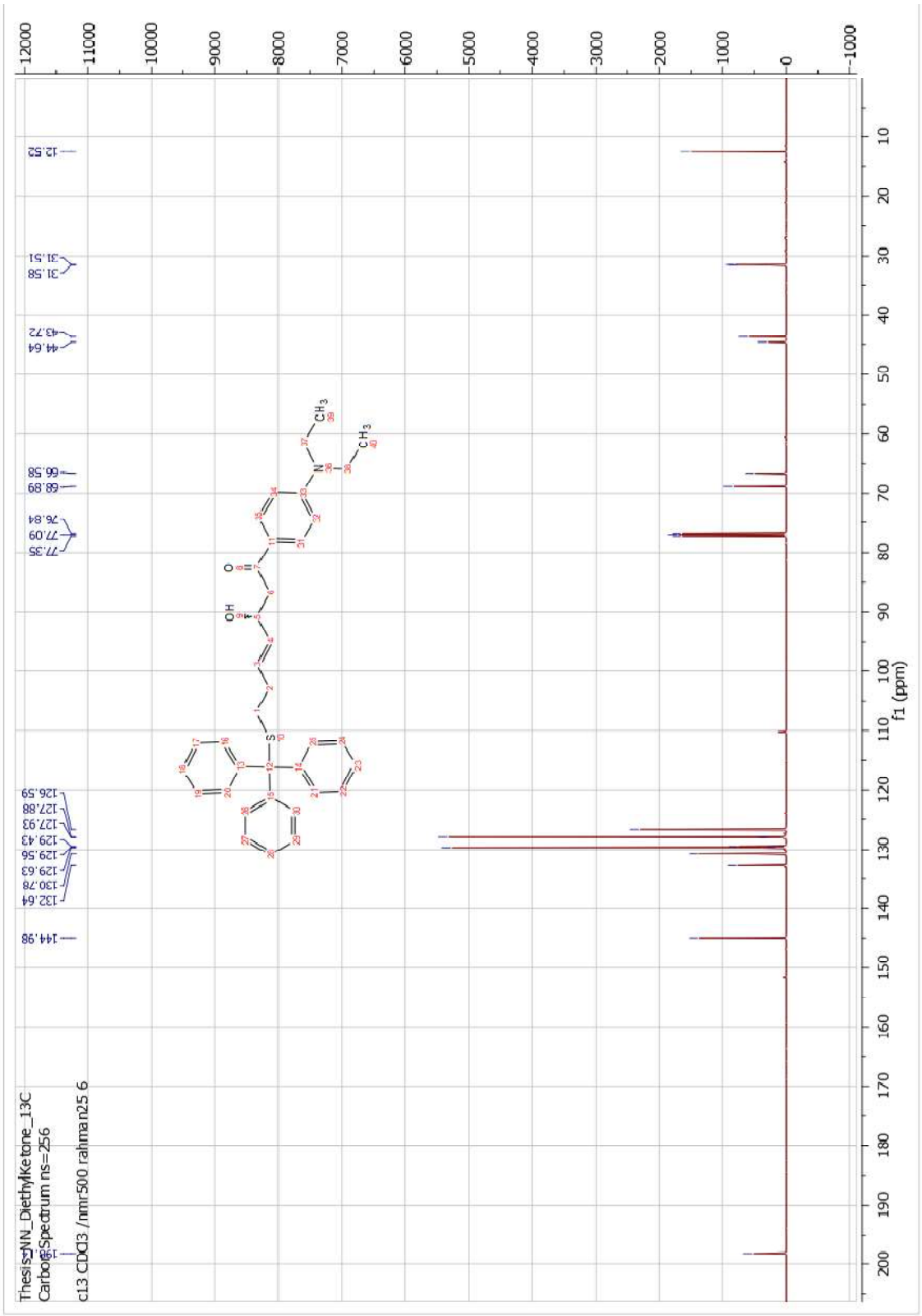
$^{13}C\{1H\}$ (proton-decoupled carbon) NMR Spectrum of (4E,4'E)-7,7'-disulfanediylbis(1-(4-(dimethylamino)phenyl)-3-hydroxyhept-4-en-1-one), JRM-15



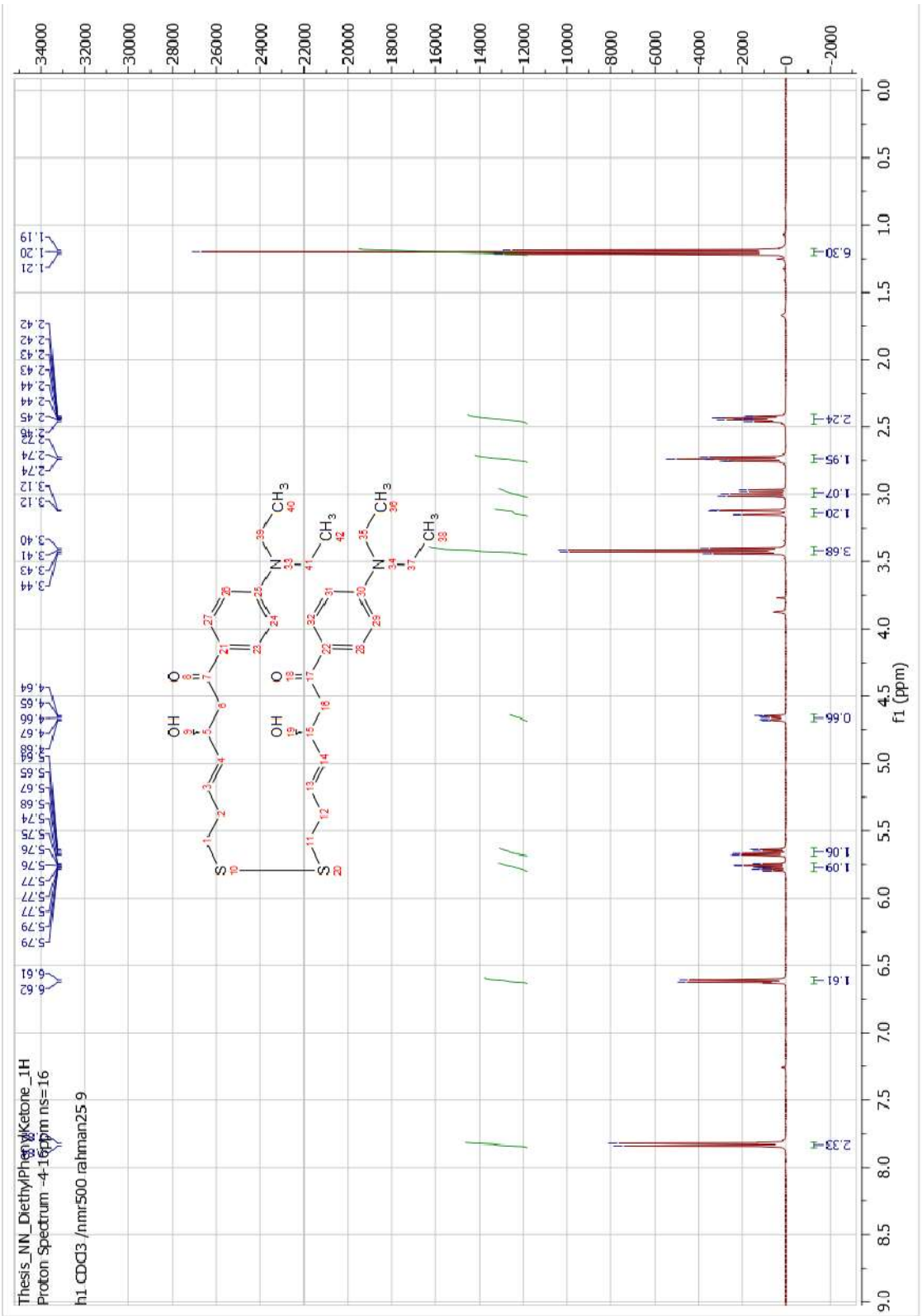
^{1}H NMR Spectrum of (E)-1-(4-(diethylamino)phenyl)-3-hydroxy-7-(tritylthio)hept-4-en-1-one, 9g



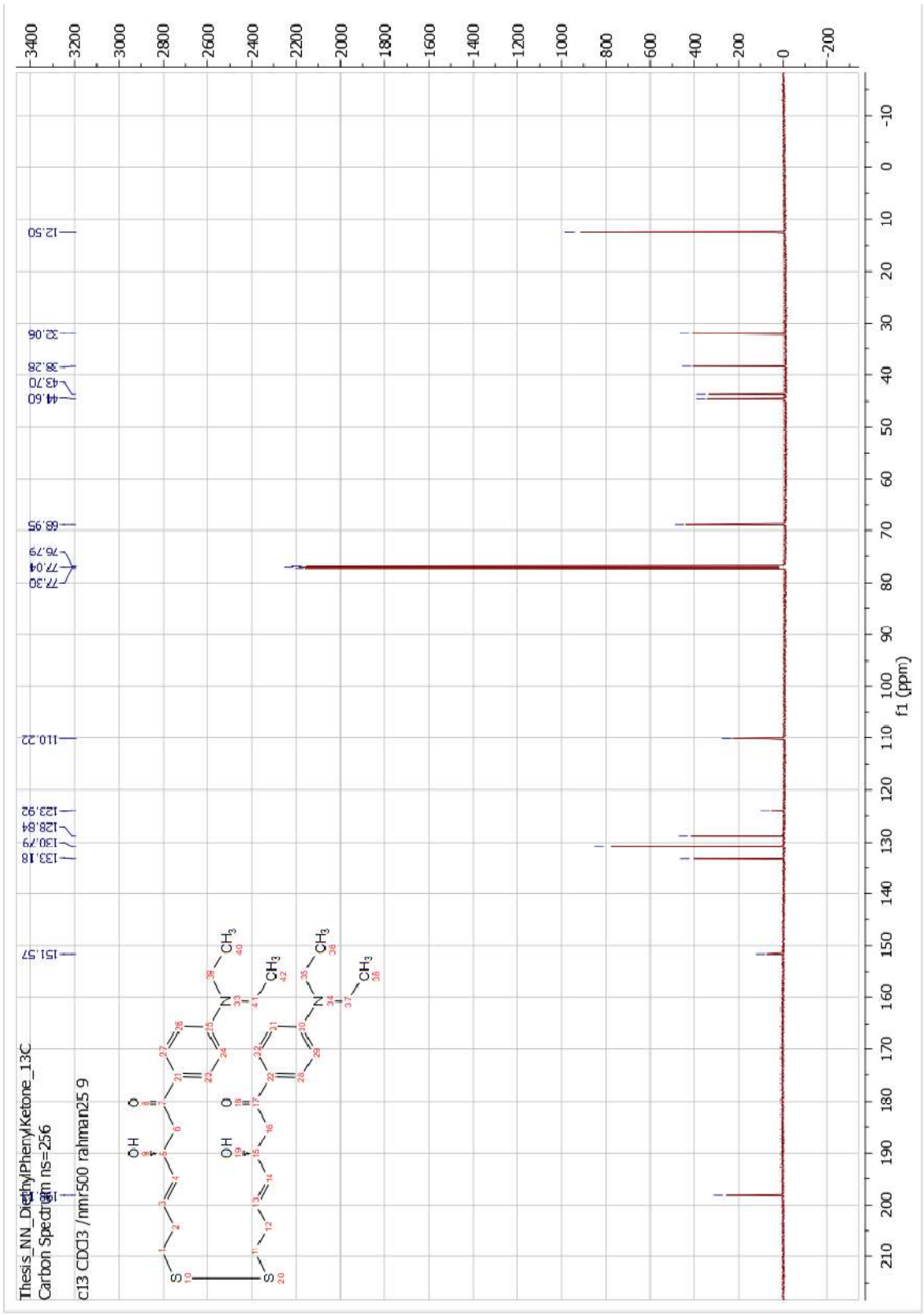
$^{13}C\{1H\}$ (proton-decoupled carbon) NMR Spectrum of (E)-1-(4-(diethylamino)phenyl)-3-hydroxy-7-(tritylthio)hept-4-en-1-one, 9g



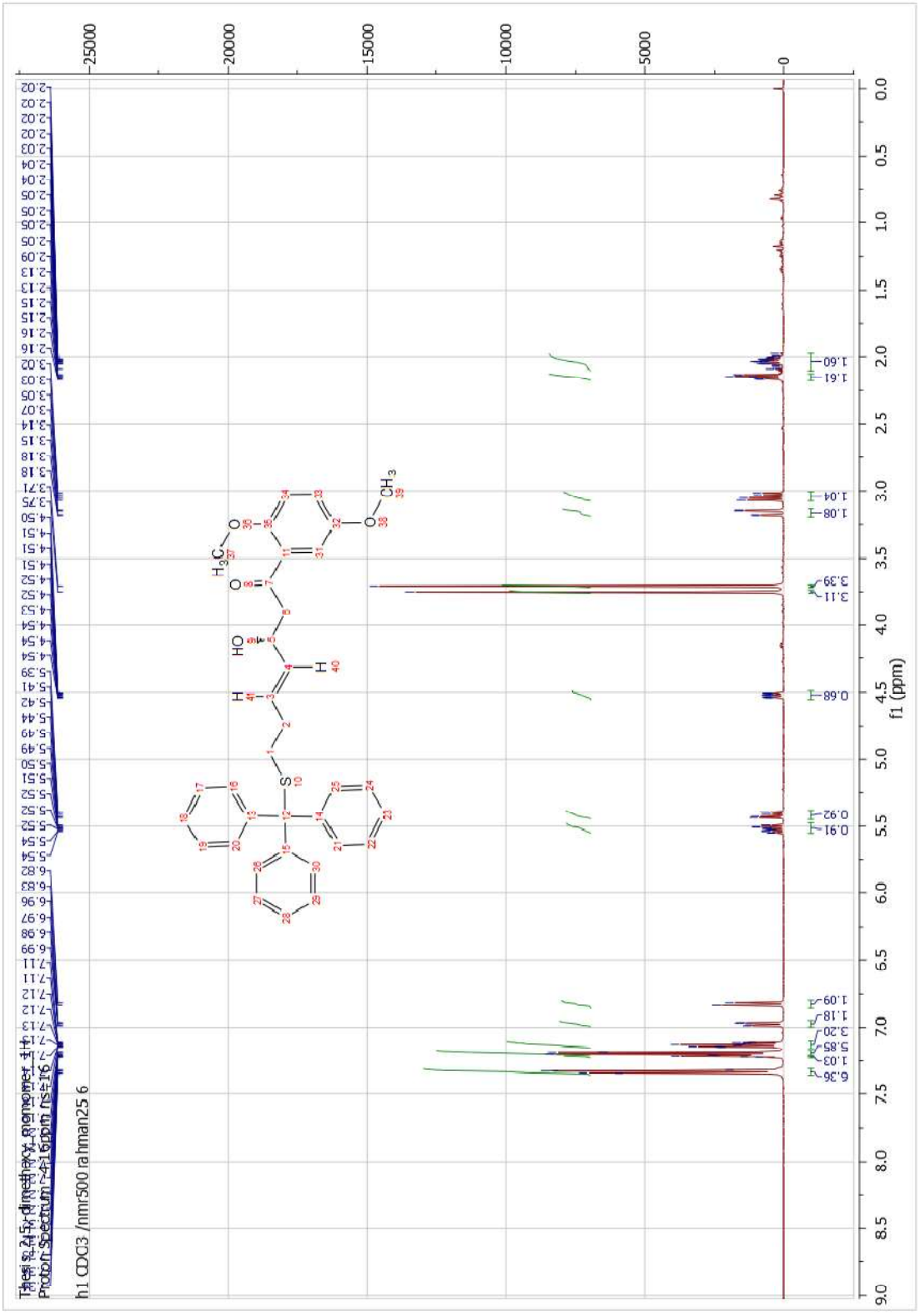
^{1}H NMR Spectrum of (4E,4'E)-7,7'-disulfanediylbis(1-(4-(diethylamino)phenyl)-3-hydroxyhept-4-en-1-one), jrm-16



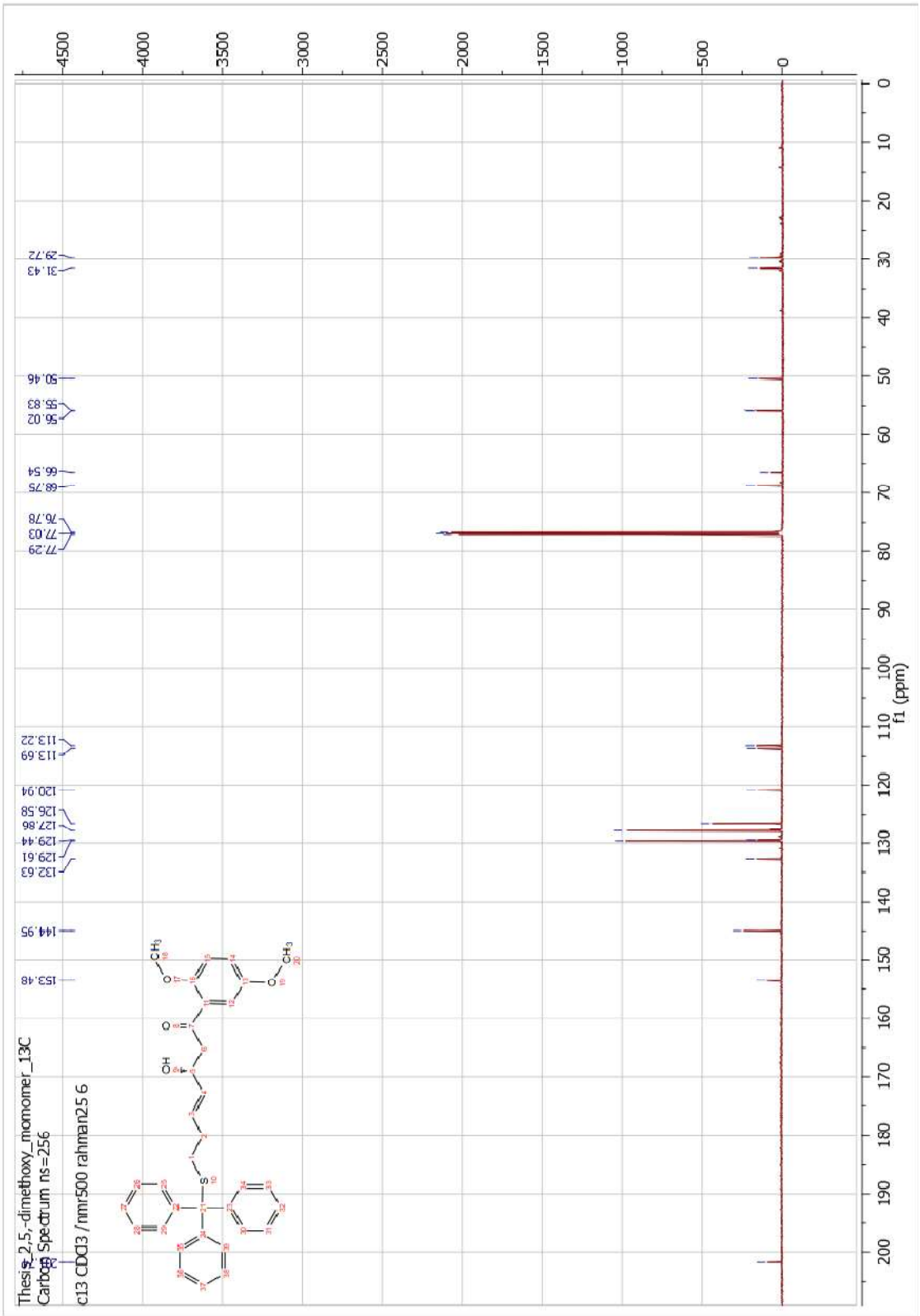
$^{13}C\{1H\}$ (proton-decoupled carbon) NMR Spectrum of (4E,4'E)-7,7'-disulfanediylbis(1-(4-(diethylamino)phenyl)-3-hydroxyhept-4-en-1-one), JRM-16



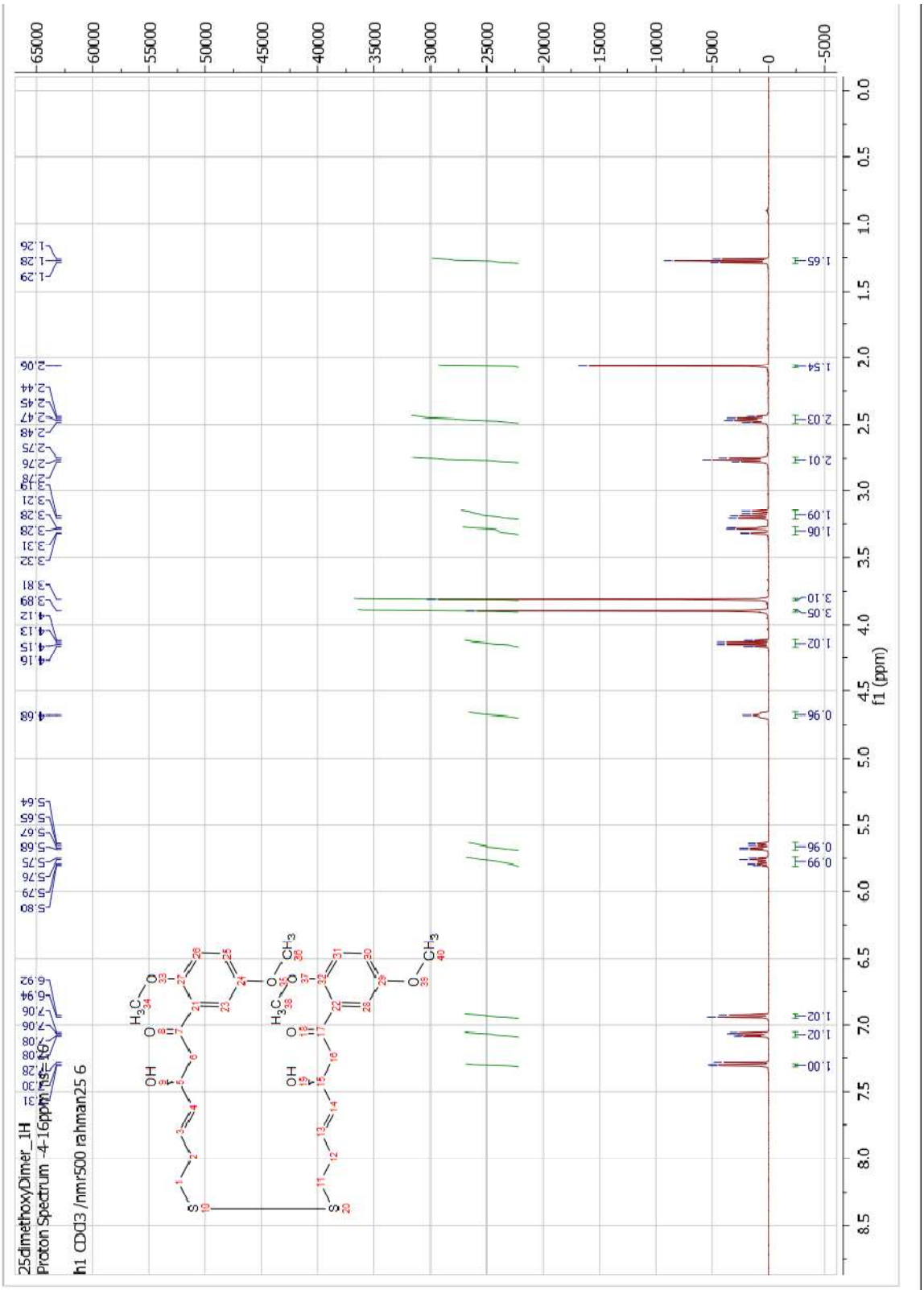
^{1}H NMR Spectrum of (E)-1-(2,5-dimethoxyphenyl)-3-hydroxy-7-(tritylthio)hept-4-en-1-one, 9h



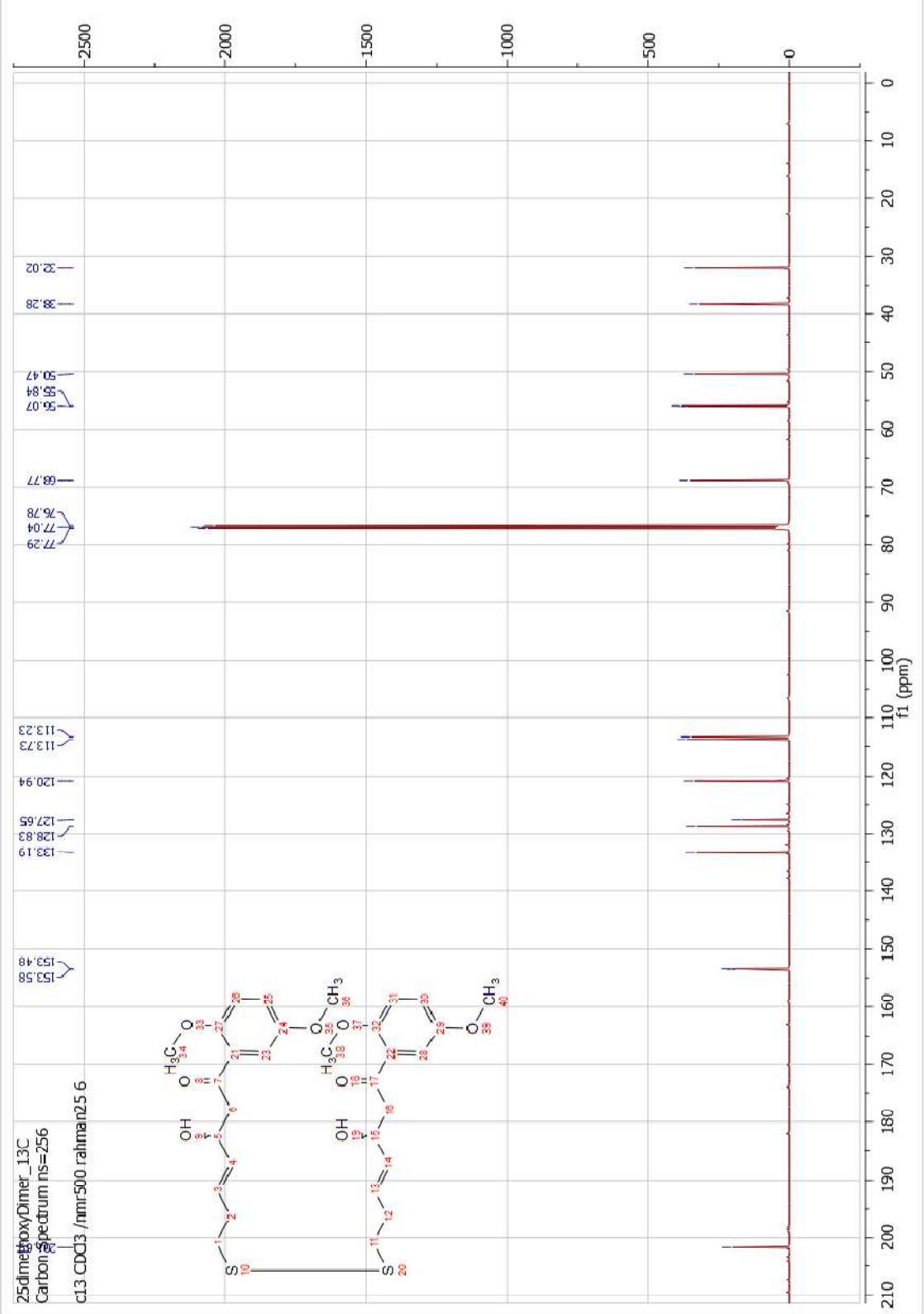
$^{13}C\{1H\}$ (proton-decoupled carbon) NMR Spectrum of (E)-1-(2,5-dimethoxyphenyl)-3-hydroxy-7-(tritylthio)hept-4-en-1-one, 9h



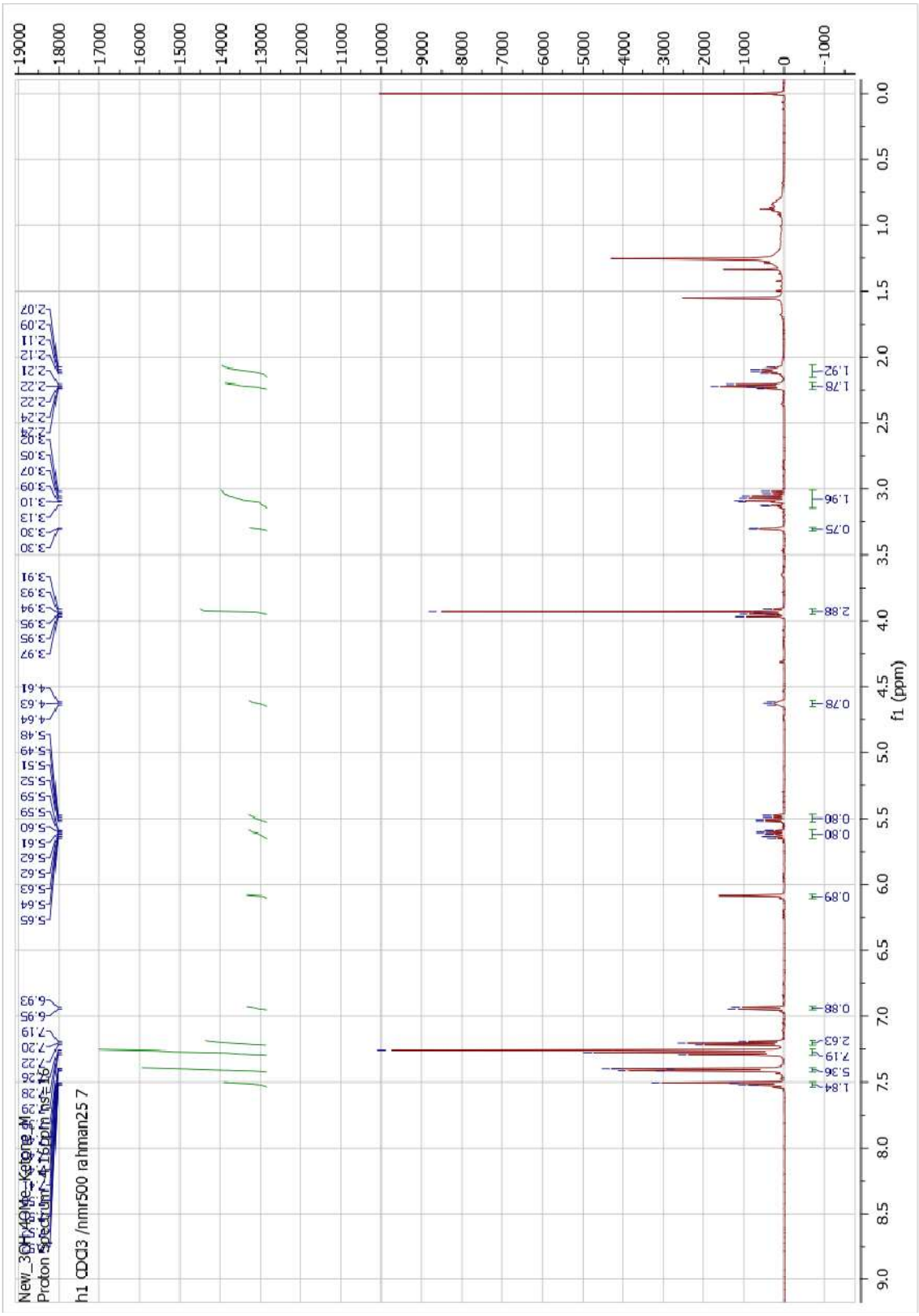
^{1}H NMR Spectrum of (4E,4'E)-7,7'-disulfanediylbis(1-(2,5-dimethoxyphenyl)-3-hydroxyhept-4-en-1-one), JRM-17



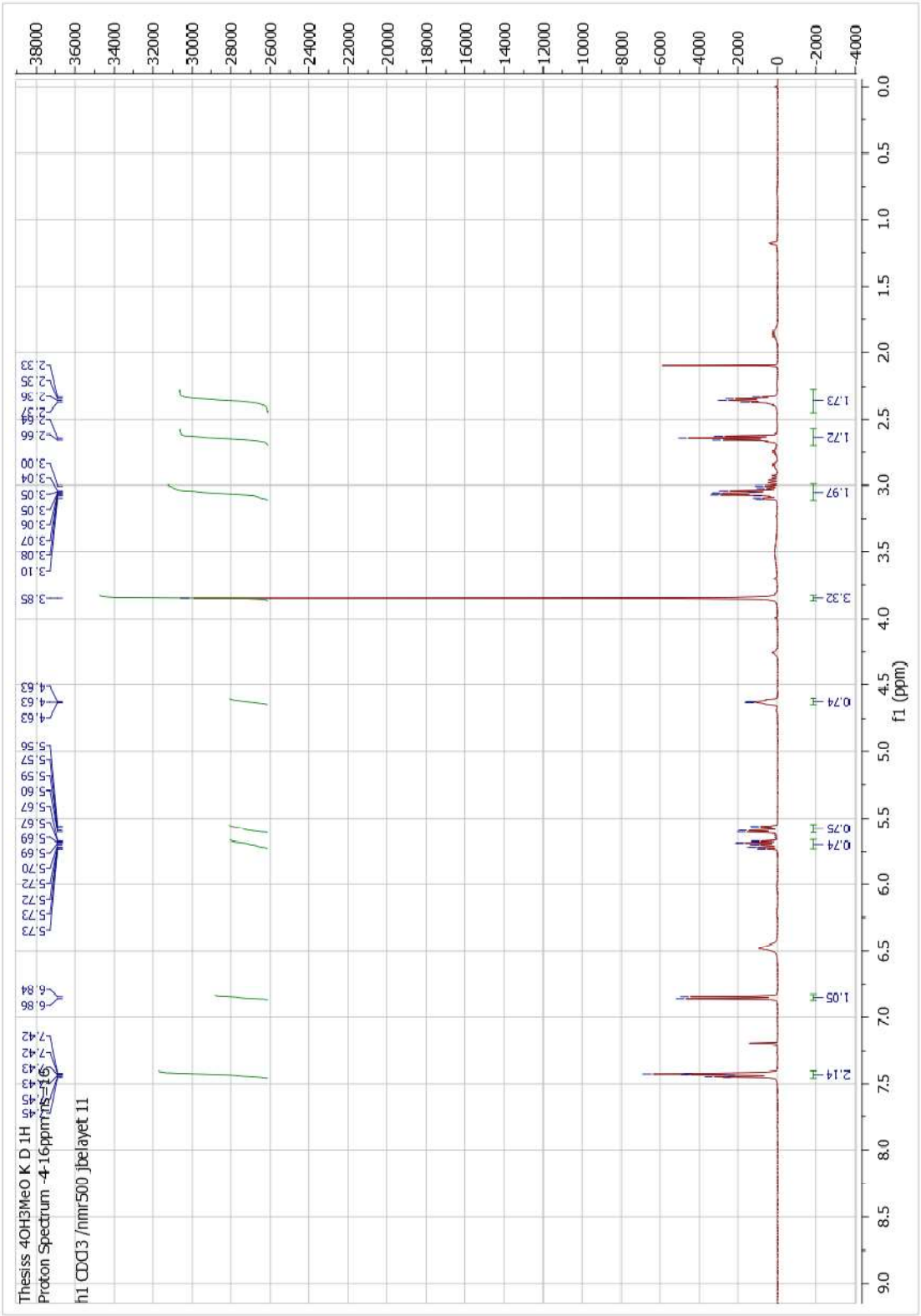
$^{13}C\{1H\}$ (proton-decoupled carbon) NMR Spectrum of (4E,4'E)-7,7'-disulfanediylbis(1-(2,5-dimethoxyphenyl)-3-hydroxyhept-4-en-1-one), JRM-17



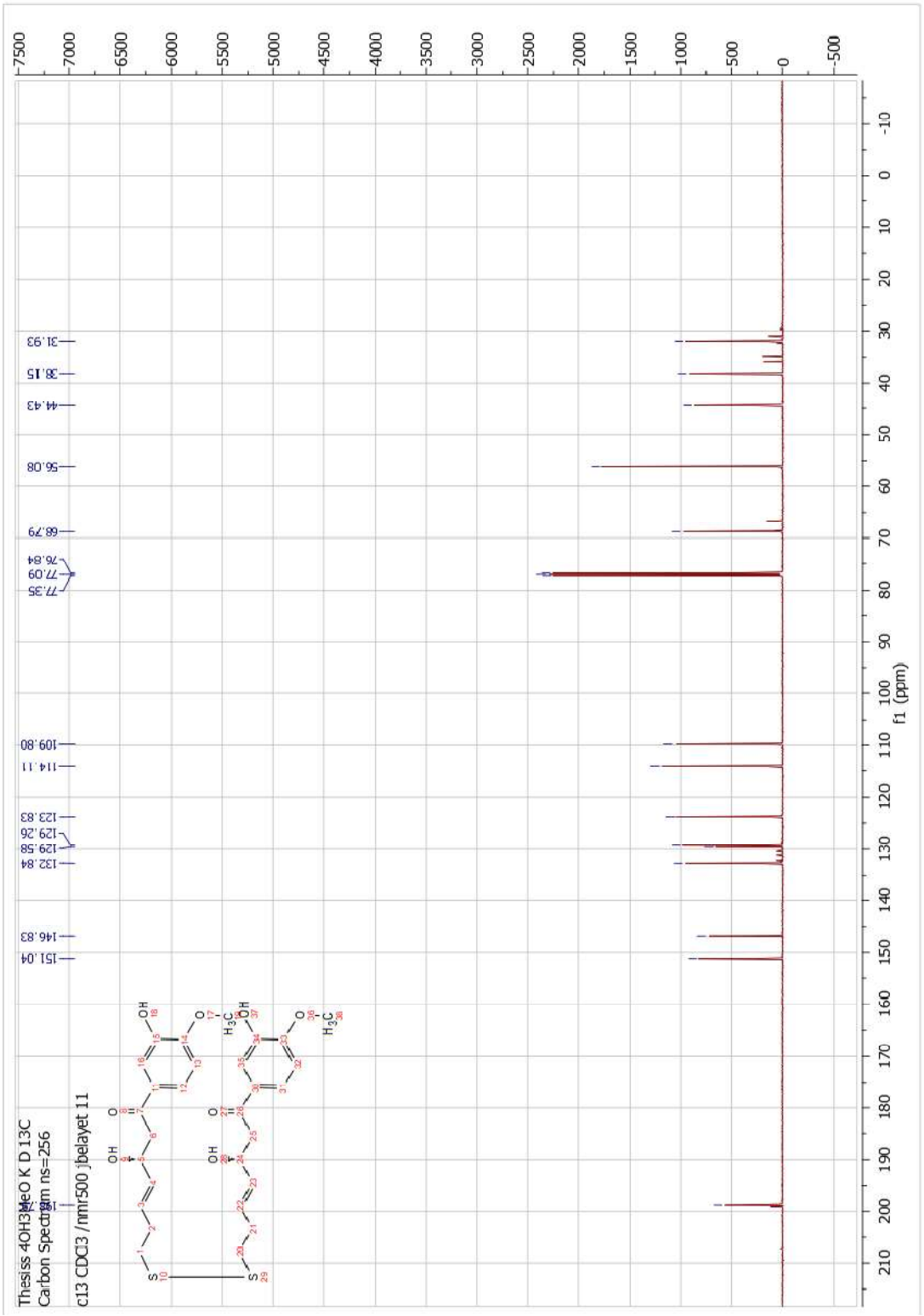
^{1}H NMR Spectrum of (E)-3-hydroxy-1-(3-hydroxy-4-methoxyphenyl)-7-(tritylthio)hept-4-en-1-one, 9i



^{1}H NMR Spectrum of (4E,4'E)-7,7'-disulfanediylbis(3-hydroxy-1-(3-hydroxy-4-methoxyphenyl)hept-4-en-1-one), JRM-18



$^{13}C\{1H\}$ (proton-decoupled carbon) NMR Spectrum of (4E,4'E)-7,7'-disulfanediylbis(3-hydroxy-1-(3-hydroxy-4-methoxyphenyl)hept-4-en-1-one), JRM-18

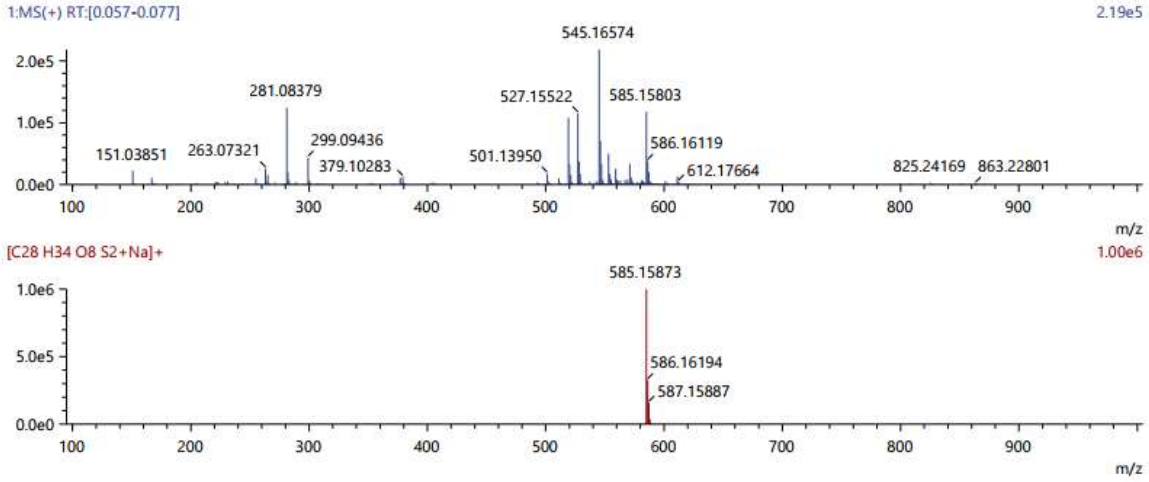


HRMS (4E,4'E)-7,7'-disulfanediylbis(3-hydroxy-1-(3-hydroxy-4-methoxyphenyl)hept-4-en-1-one), JRM-18

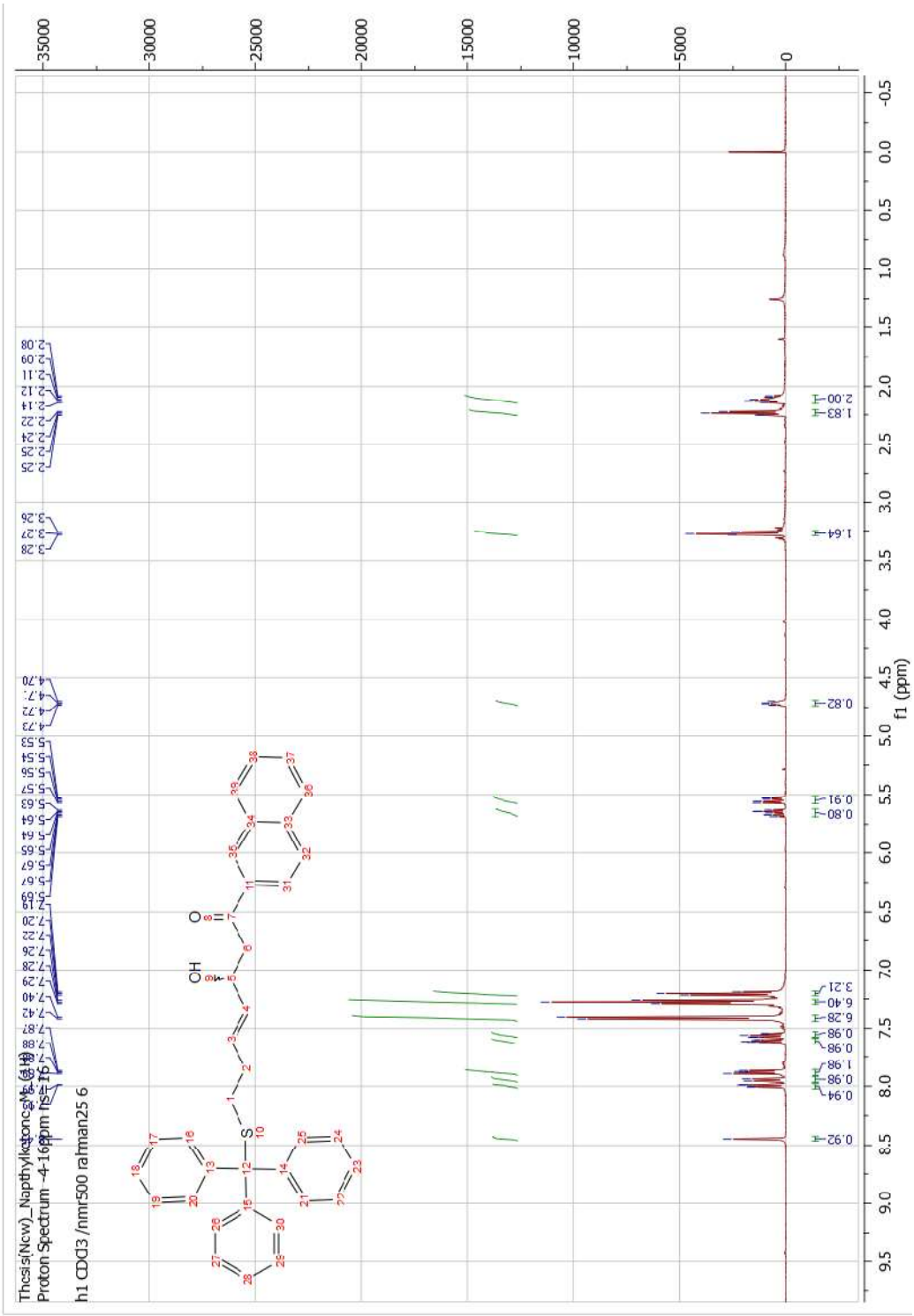
Jawad HRMS.lcb

Formula Predictor Result	**C28 H34 O8 S2**
Mass	585.15803
Error Margin	5 ppm
DBE Range	0 - 1000
Electron Ions	Both configurations
HC Ratio	Not Used
Nitrogen Rule	Used

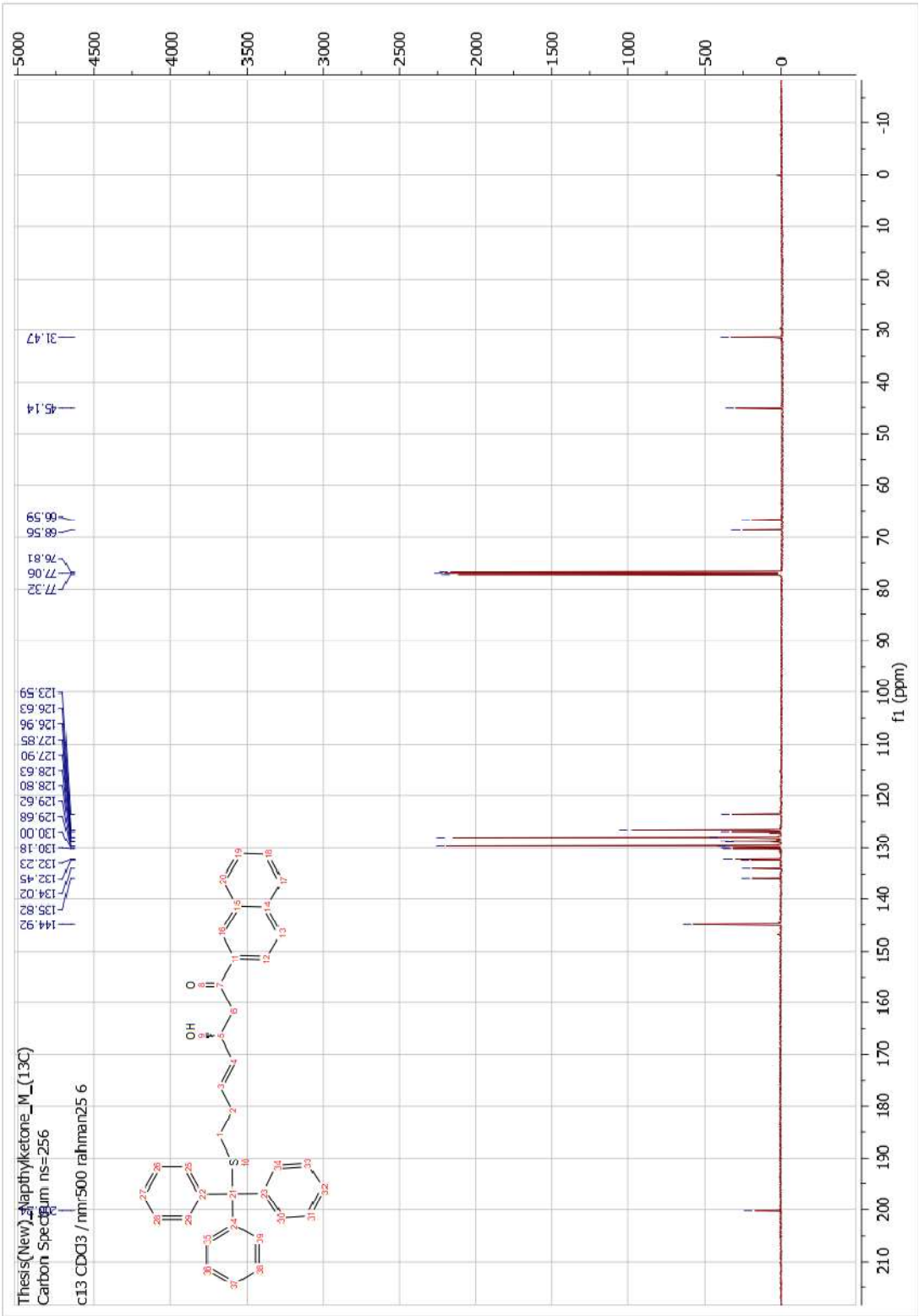
Score	Pred. (M)	Pred. m/z	Meas. m/z	Diff. (mDa)	Formulae (M)	Ion	Diff. (ppm)	Iso Score	DBE
94.56	562.16951	585.15873	585.15803	-0.70	C28 H34 O8 S2	[M+Na]+	-1.196	94.58	12.0



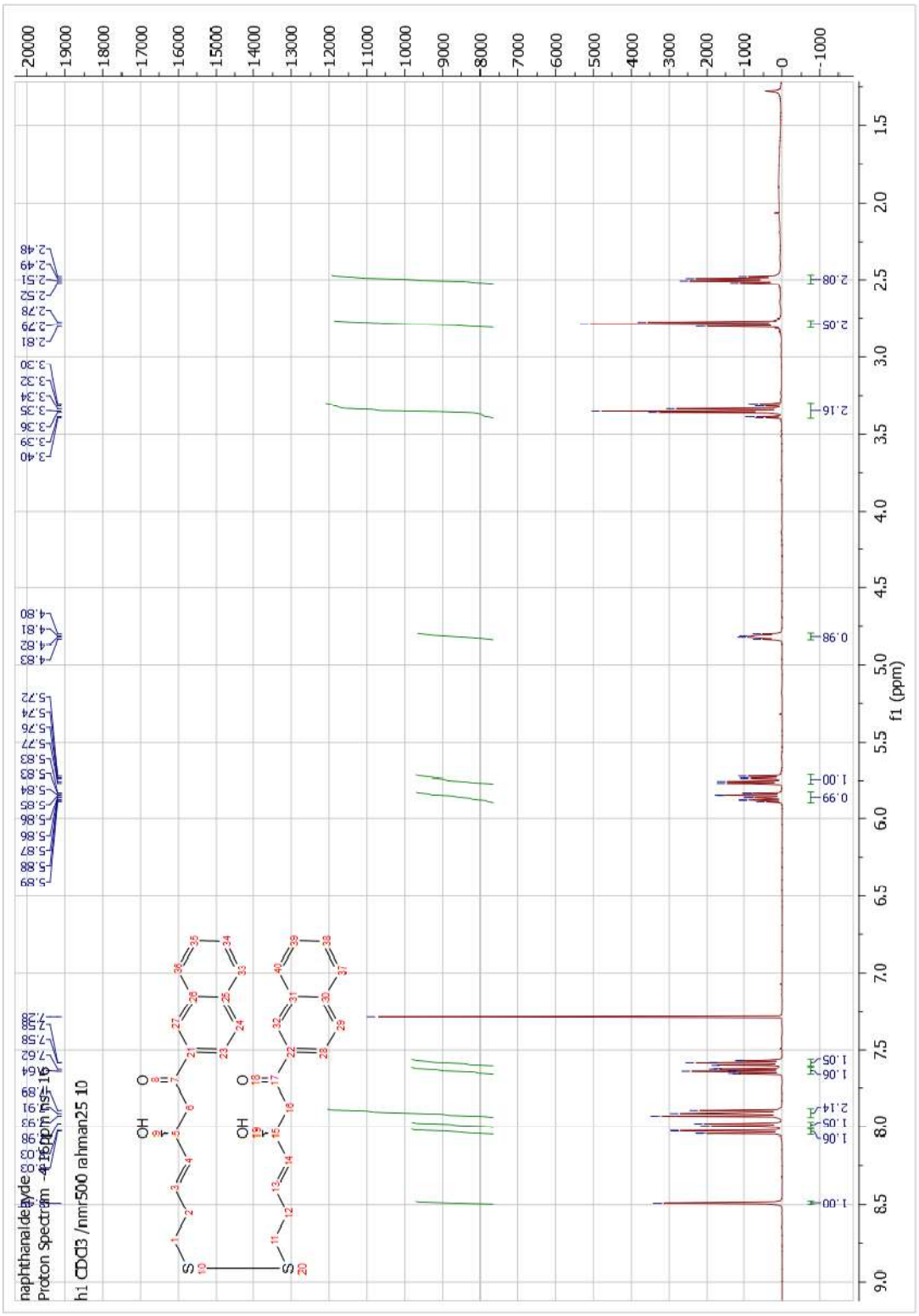
^{1}H NMR Spectrum of (E)-3-hydroxy-1-(naphthalen-2-yl)-7-(tritylthio)hept-4-en-1-one, 9j



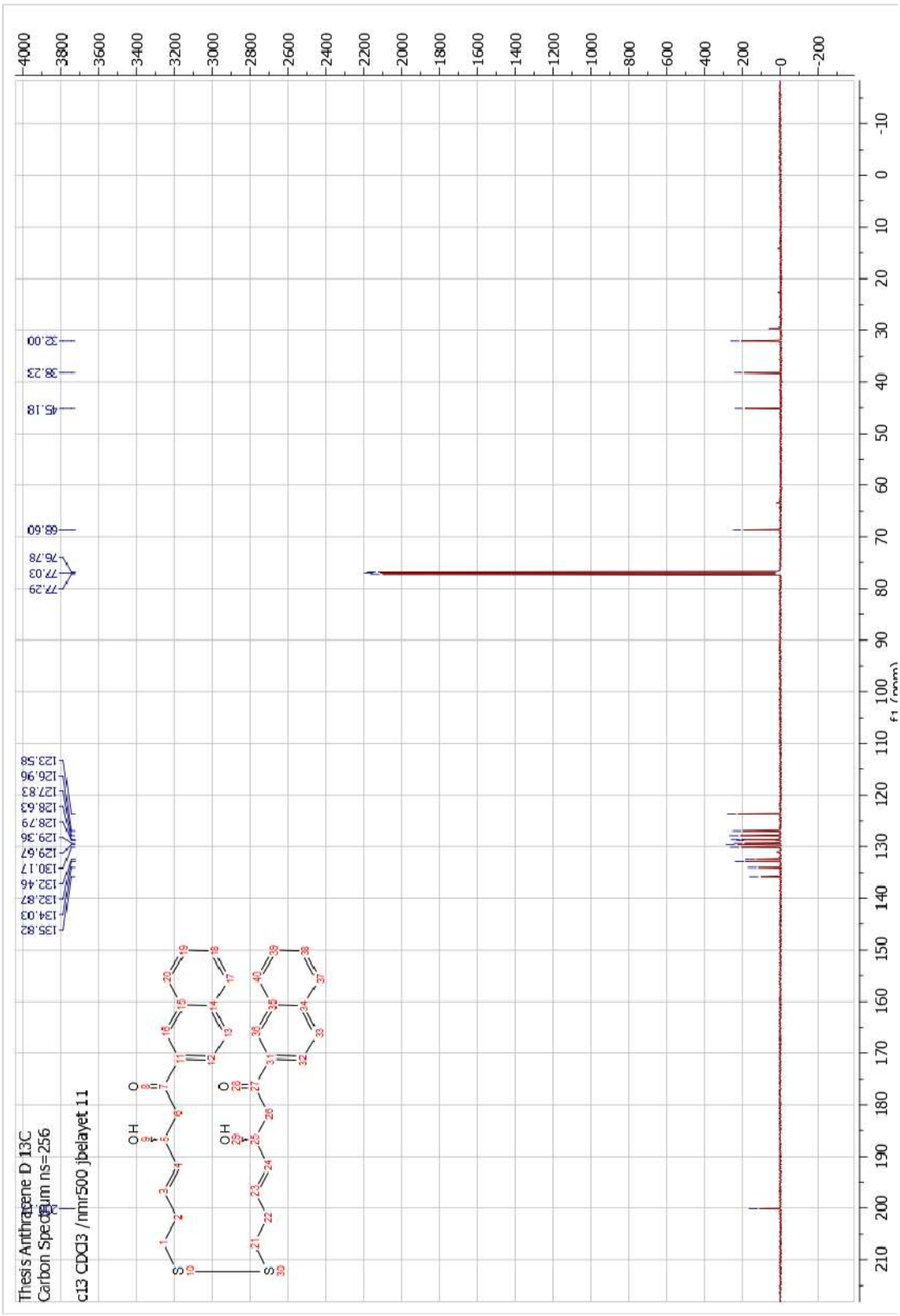
$^{13}C\{1H\}$ (proton-decoupled carbon) NMR Spectrum of (E)-3-hydroxy-1-(naphthalen-2-yl)-7-(tritylthio)hept-4-en-1-one, 9j



^{1}H NMR Spectrum of (4E,4'E)-7,7'-disulfanediylbis(3-hydroxy-1-(naphthalen-2-yl)hept-4-en-1-one), JRM-19



$^{13}C\{1H\}$ (proton-decoupled carbon) NMR Spectrum of (4E,4'E)-7,7'-disulfanediylbis(3-hydroxy-1-(naphthalen-2-yl)hept-4-en-1-one), JRM-19

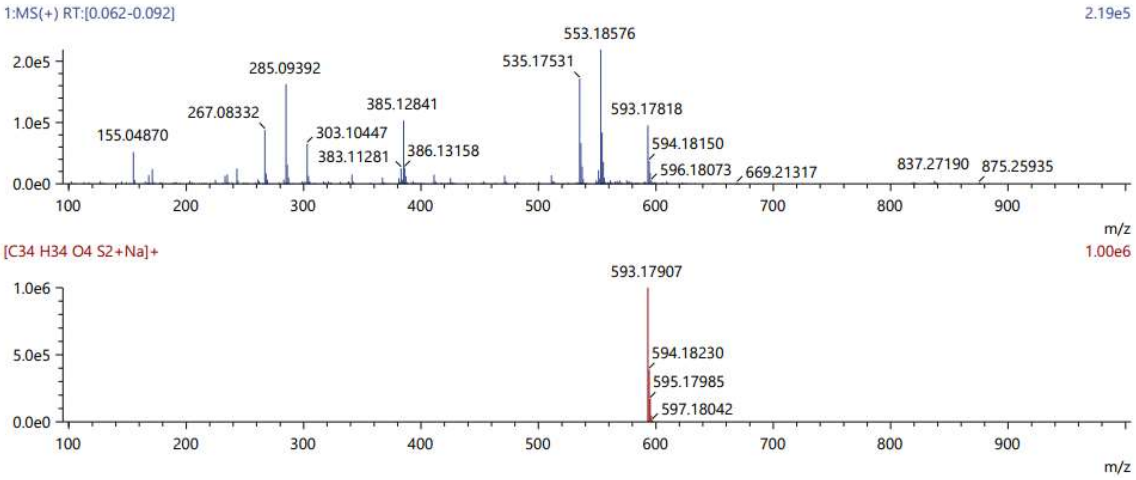


HRMS (4E,4'E)-7,7'-disulfanediylbis(3-hydroxy-1-(naphthalen-2-yl)hept-4-en-1-one), JRM-19

Jawad HRMS.lcb

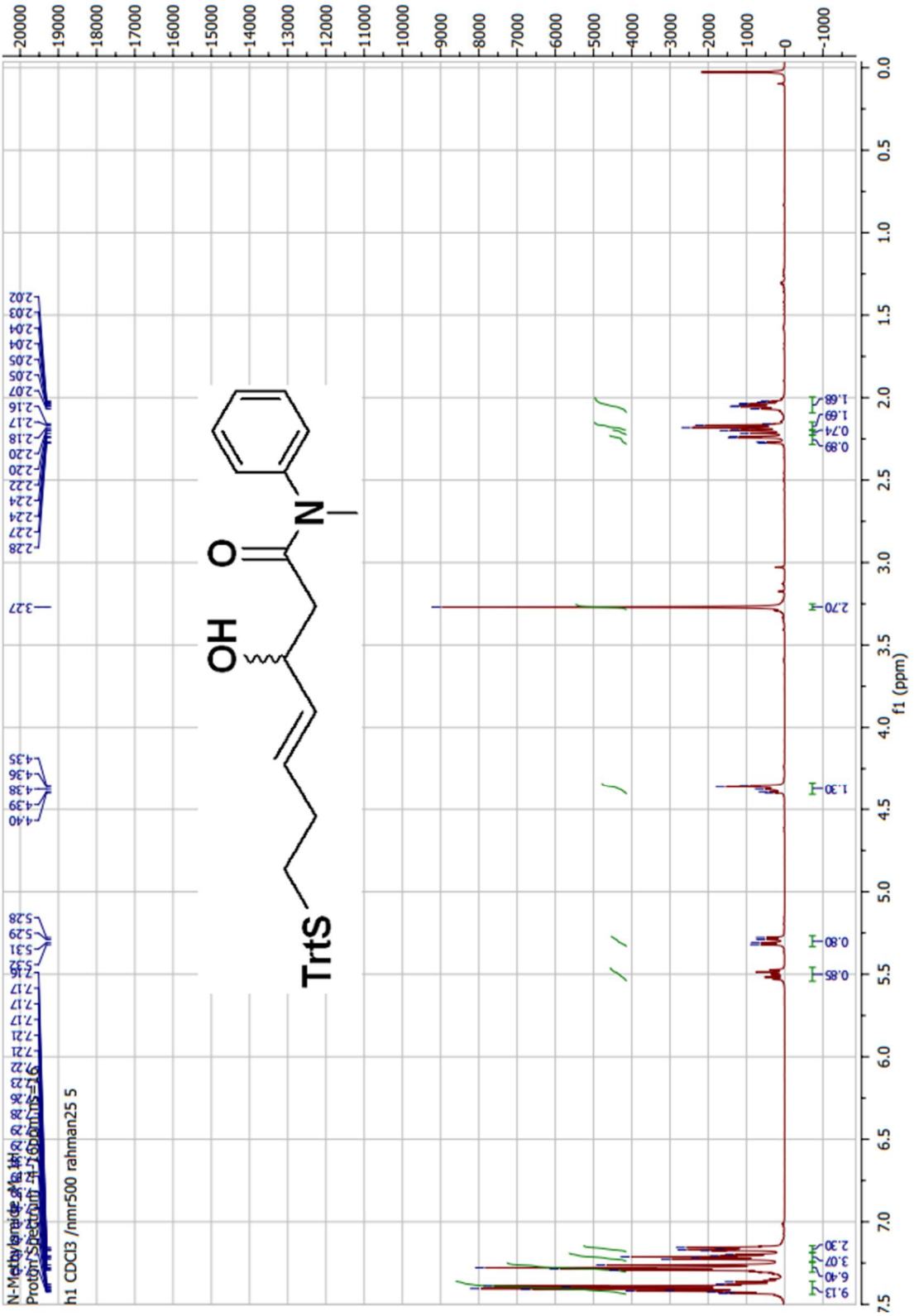
Formula Predictor Result	**C34 H34 O4 S2**
Mass	593.17818
Error Margin	5 ppm
DBE Range	0 - 1000
Electron Ions	Both configurations
HC Ratio	Not Used
Nitrogen Rule	Used

Score	Pred. (M)	Pred. m/z	Meas. m/z	Diff. (mDa)	Formulae (M)	Ion	Diff. (ppm)	Iso Score	DBE
94.31	570.18985	593.17907	593.17818	-0.89	C34 H34 O4 S2	[M+Na]+	-1.500	94.50	18.0

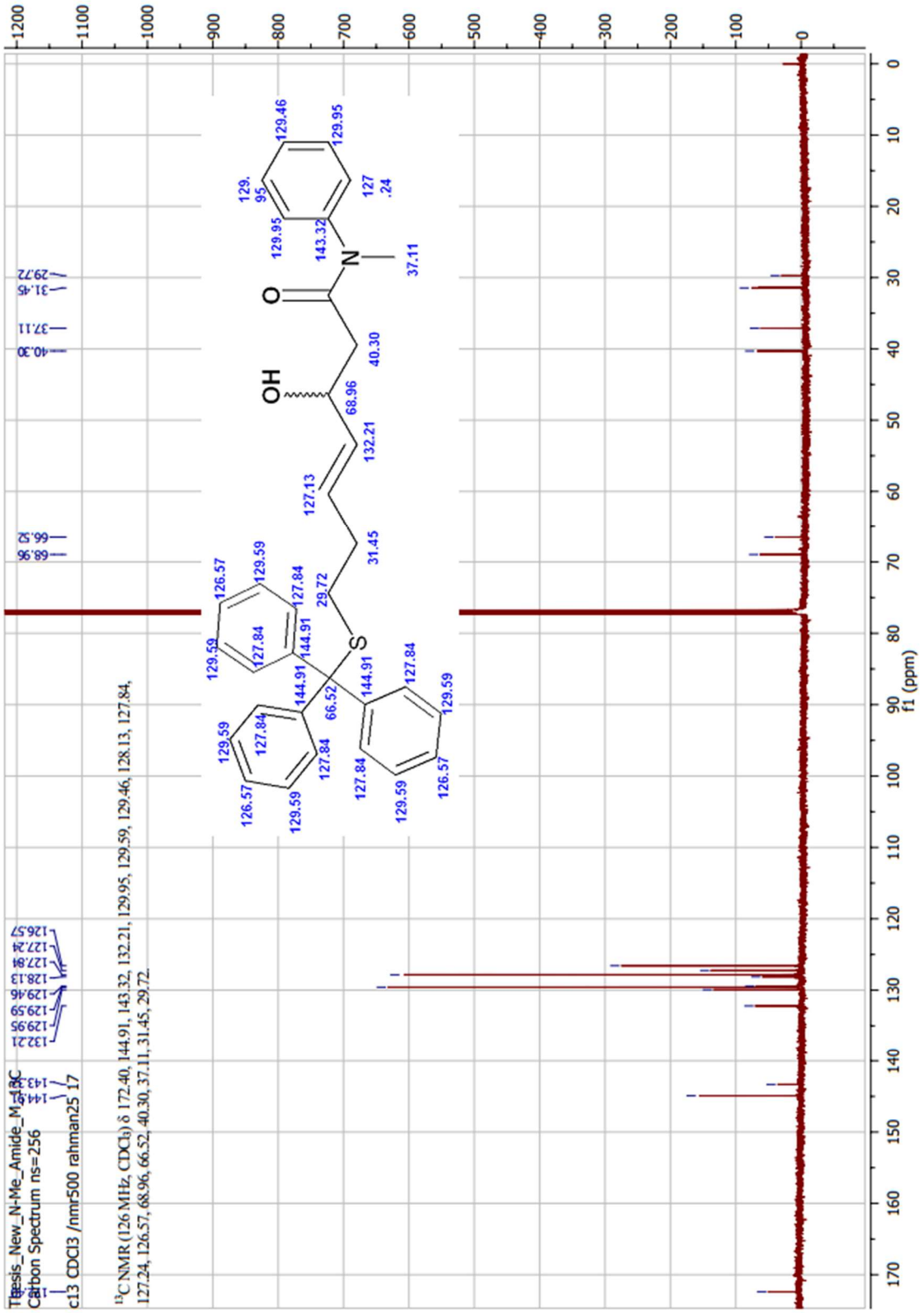


Series 3: Amide

^{1}H NMR Spectrum of (E)-3-hydroxy-N-methyl-N-phenyl-7-(tritylthio)hept-4-enamide, 7

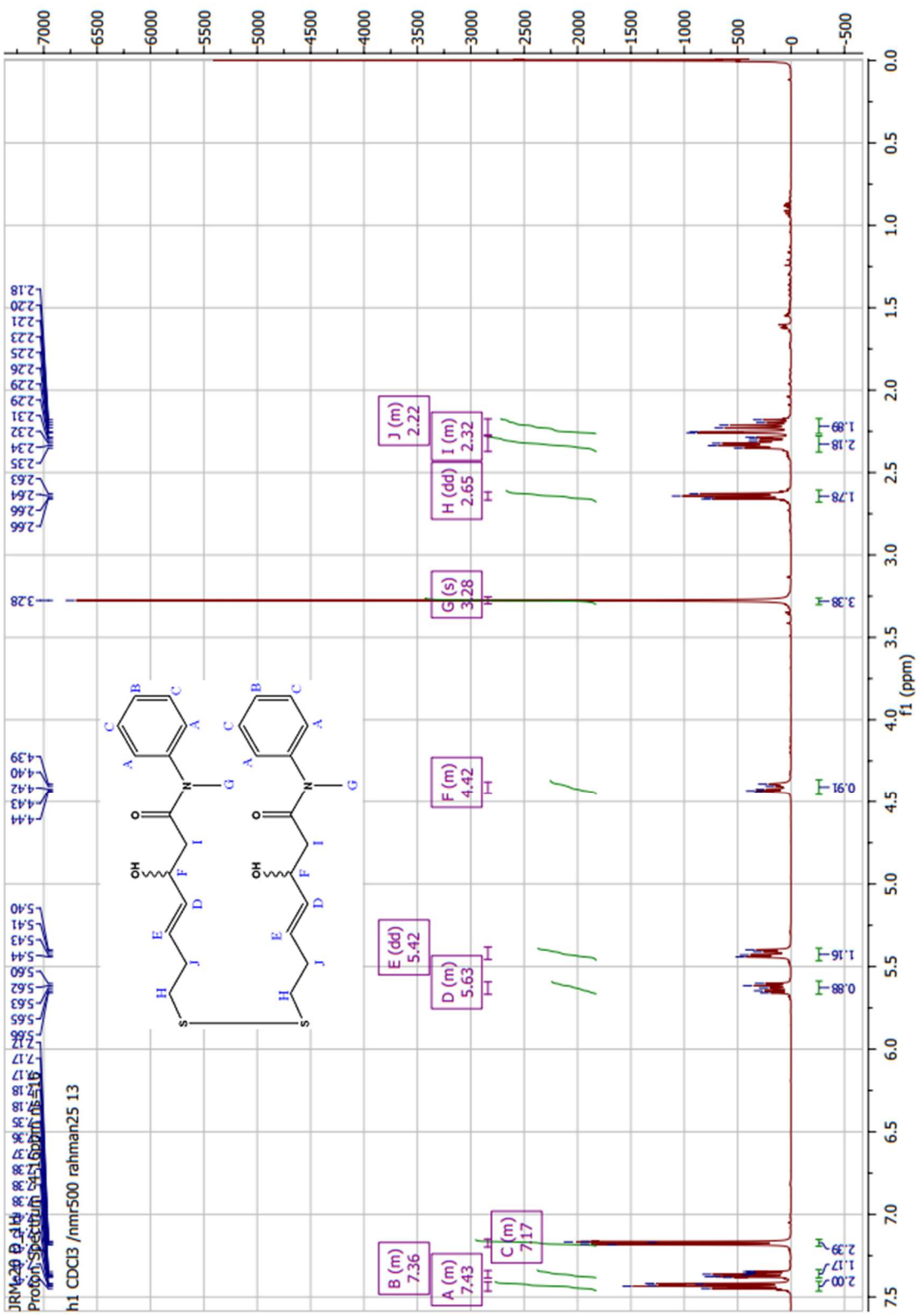


$^{13}C\{1H\}$ (proton-decoupled carbon) NMR Spectrum of (E)-3-hydroxy-N-methyl-N-phenyl-7-(tritylthio)hept-4-enamide, 7

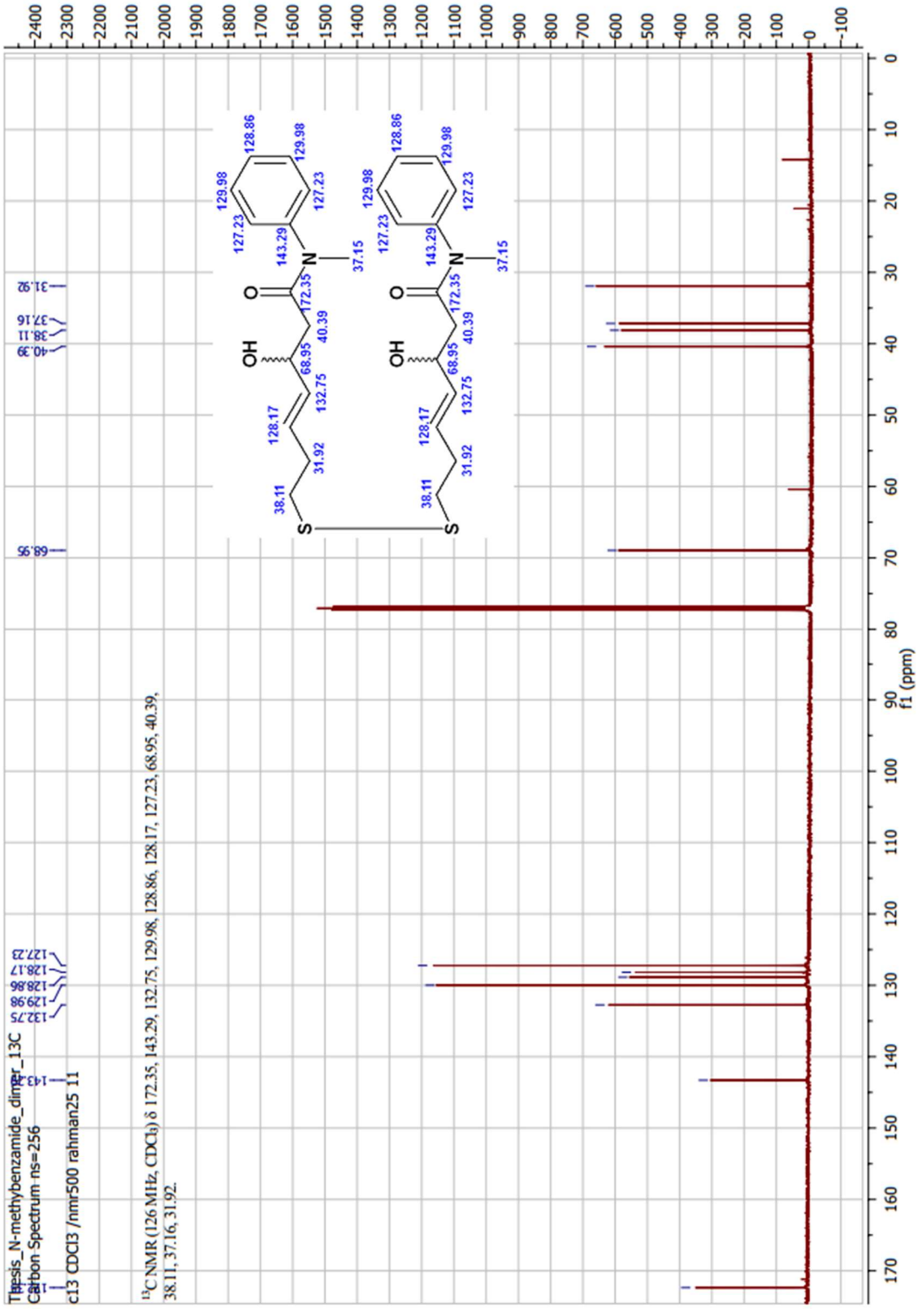


HRMS of (E)-3-hydroxy-N-methyl-N-phenyl-7-(tritylthio)hept-4-enamide, 7

^{1}H NMR Spectrum of (4E,4'E)-7,7'-disulfanediylbis(3-hydroxy-N-methyl-N-phenylhept-4-enamide), JRM-20



$^{13}C\{1H\}$ (proton-decoupled carbon) NMR Spectrum of (4E,4'E)-7,7'-disulfanediylbis(3-hydroxy-N-methyl-N-phenylhept-4-enamide), JRM-20



HRMS (4E,4'E)-7,7'-disulfanediylbis(3-hydroxy-N-methyl-N-phenylhept-4-enamide), JRM-20

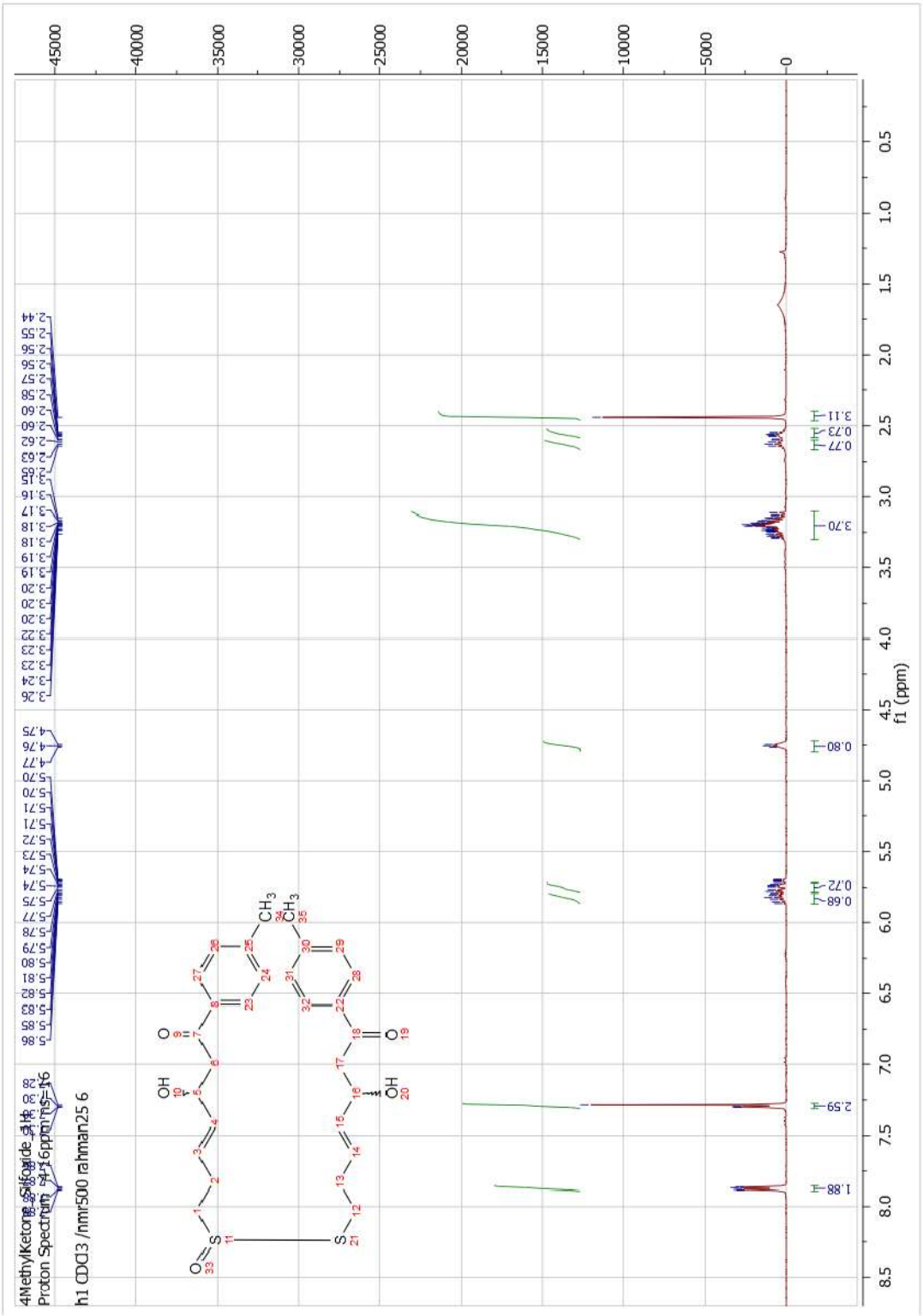
4-30-2024.lcb

Formula Predictor Result	C28 H36 N2 O4 S2
Mass	529.22028
Error Margin	100 ppm
DBE Range	0 - 1000
Electron Ions	Both configurations
HC Ratio	0 - 3
Nitrogen Rule	Not Used

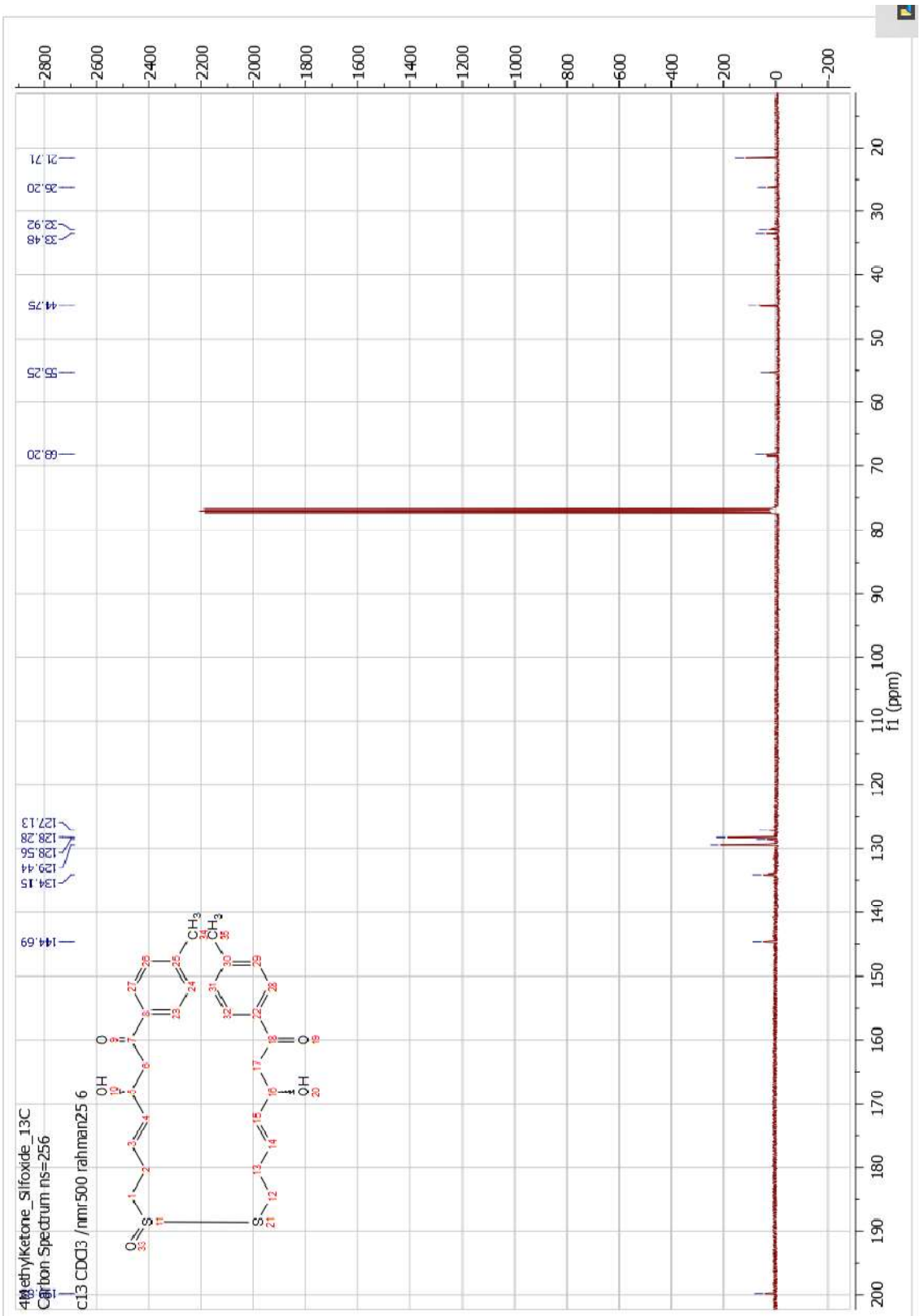
Score	Pred. (M)	Pred. m/z	Meas. m/z	Diff. (mDa)	Formulae (M)	Ion	Diff. (ppm)	Iso Score	DBE
51.77	528.21165	529.21893	529.22028	1.35	C28 H36 N2 O4 S2	[M+H]+	2.551	48.09	12.0

Series 4: Sulfoxide Analog

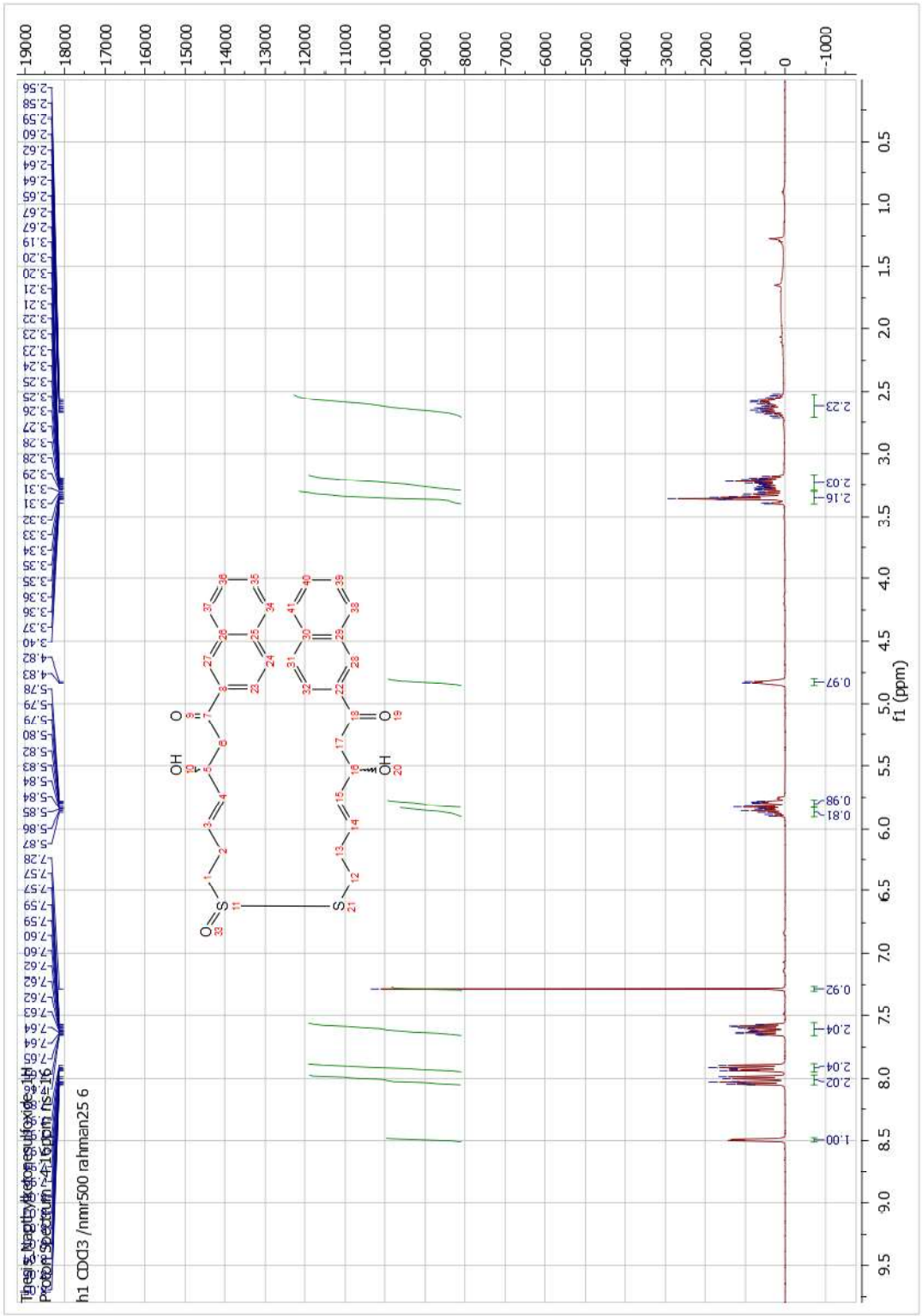
^{1}H NMR Spectrum of S-((E)-5-hydroxy-7-oxo-7-(p-tolyl)hept-3-en-1-yl) (E)-5-hydroxy-7-oxo-7-(p-tolyl)hept-3-ene-1-sulfinothioate, JRM-22



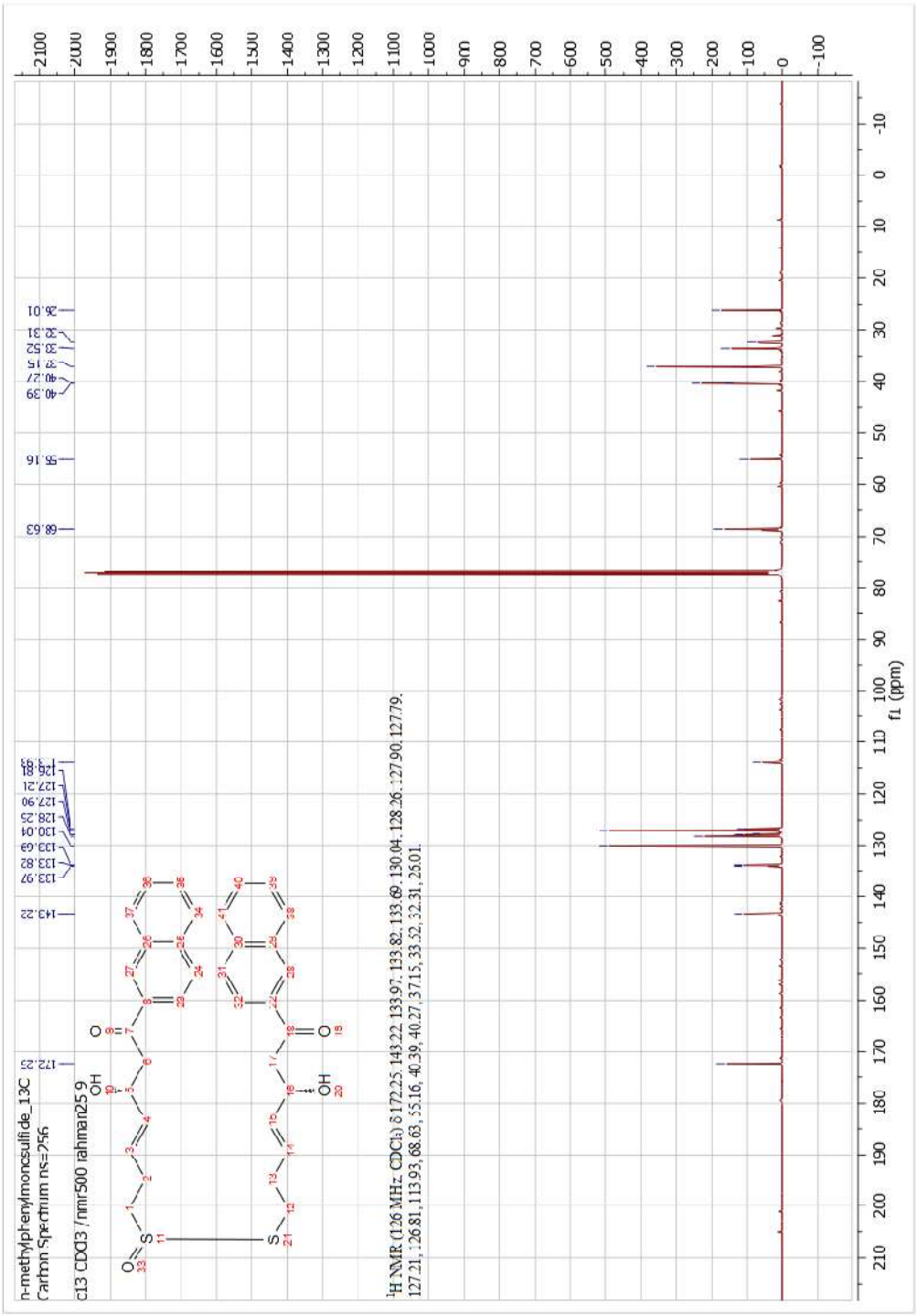
$^{13}C\{1H\}$ (proton-decoupled carbon) NMR Spectrum of S-((E)-5-hydroxy-7-oxo-7-(p-tolyl)hept-3-en-1-yl) (E)-5-hydroxy-7-oxo-7-(p-tolyl)hept-3-ene-1-sulfinothioate, JRM-22



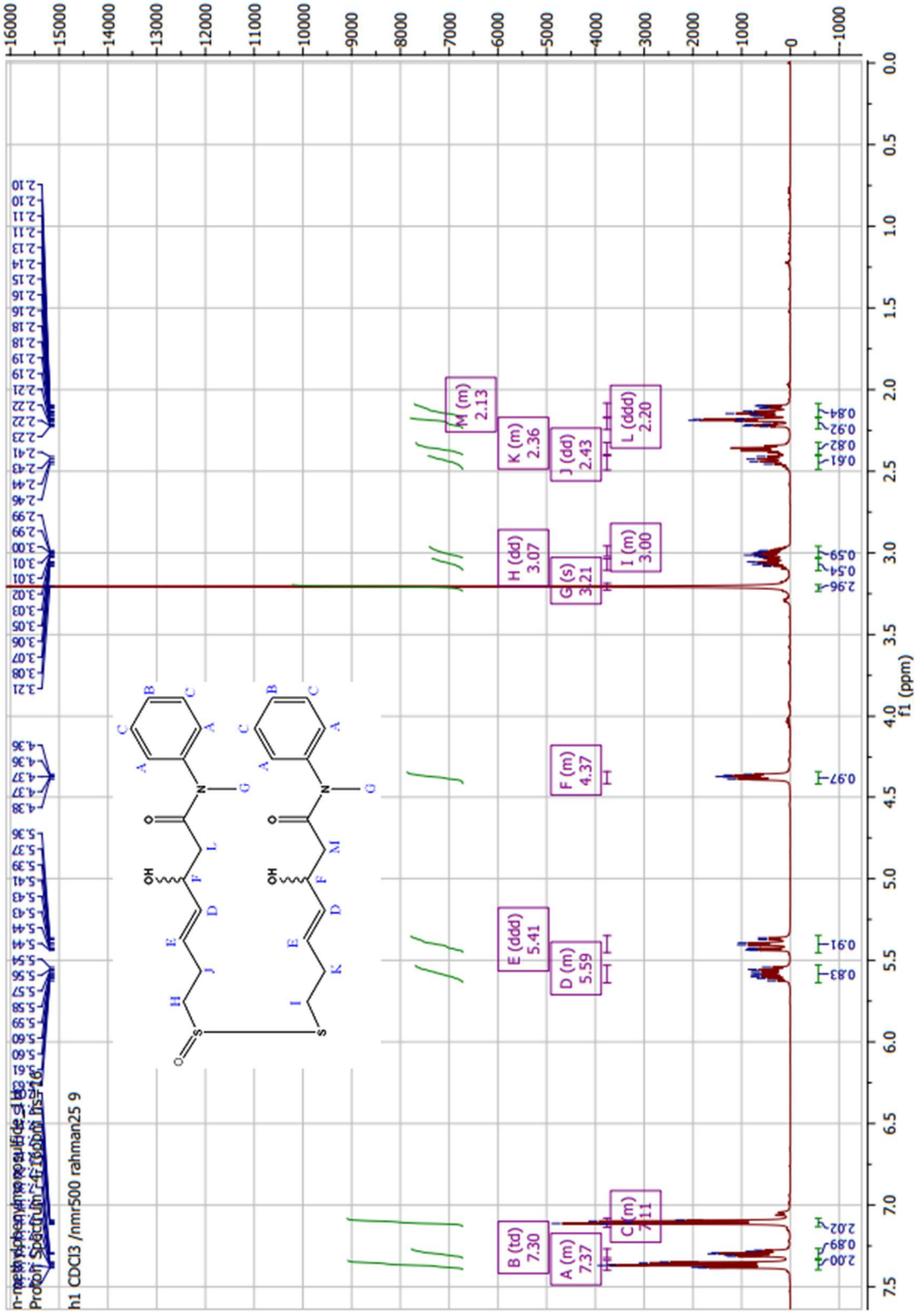
^{1}H NMR Spectrum of NMR S-((E)-5-hydroxy-7-(naphthalen-2-yl)-7-oxohept-3-en-1-yl)-(E)-5-hydroxy-7-(naphthalen-2-yl)-7-oxohept-3-ene-1-sulfinothioate, JRM-23



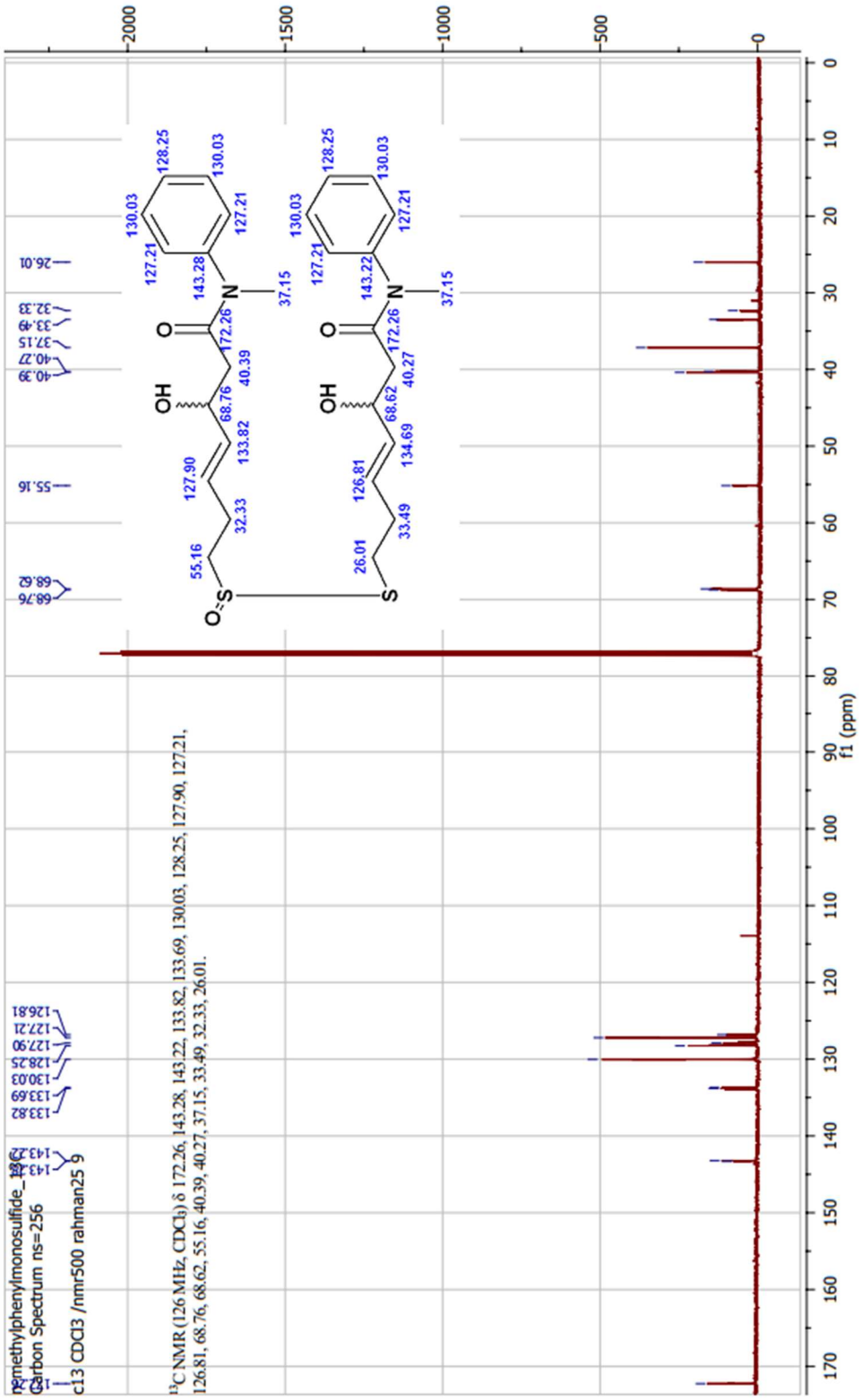
$^{13}C\{1H\}$ (proton-decoupled carbon) NMR Spectrum of S-((E)-5-hydroxy-7-(naphthalen-2-yl)-7-oxohept-3-en-1-yl)-(E)-5-hydroxy-7-(naphthalen-2-yl)-7-oxohept-3-ene-1-sulfinothioate, JRM-23



^{1}H NMR Spectrum of S-((E)-5-hydroxy-7-(methyl(phenyl)amino)-7-oxohept-3-en-1-yl)-(E)-5-hydroxy-7-(methyl(phenyl)amino)-7-oxohept-3-ene-1-sulfinothioate, JRM-24



$^{13}C\{1H\}$ (proton-decoupled carbon) NMR Spectrum of S-((E)-5-hydroxy-7-(methyl(phenyl)amino)-7-oxohept-3-en-1-yl)-(E)-5-hydroxy-7-(methyl(phenyl)amino)-7-oxohept-3-ene-1-sulfinothioate, JRM-24

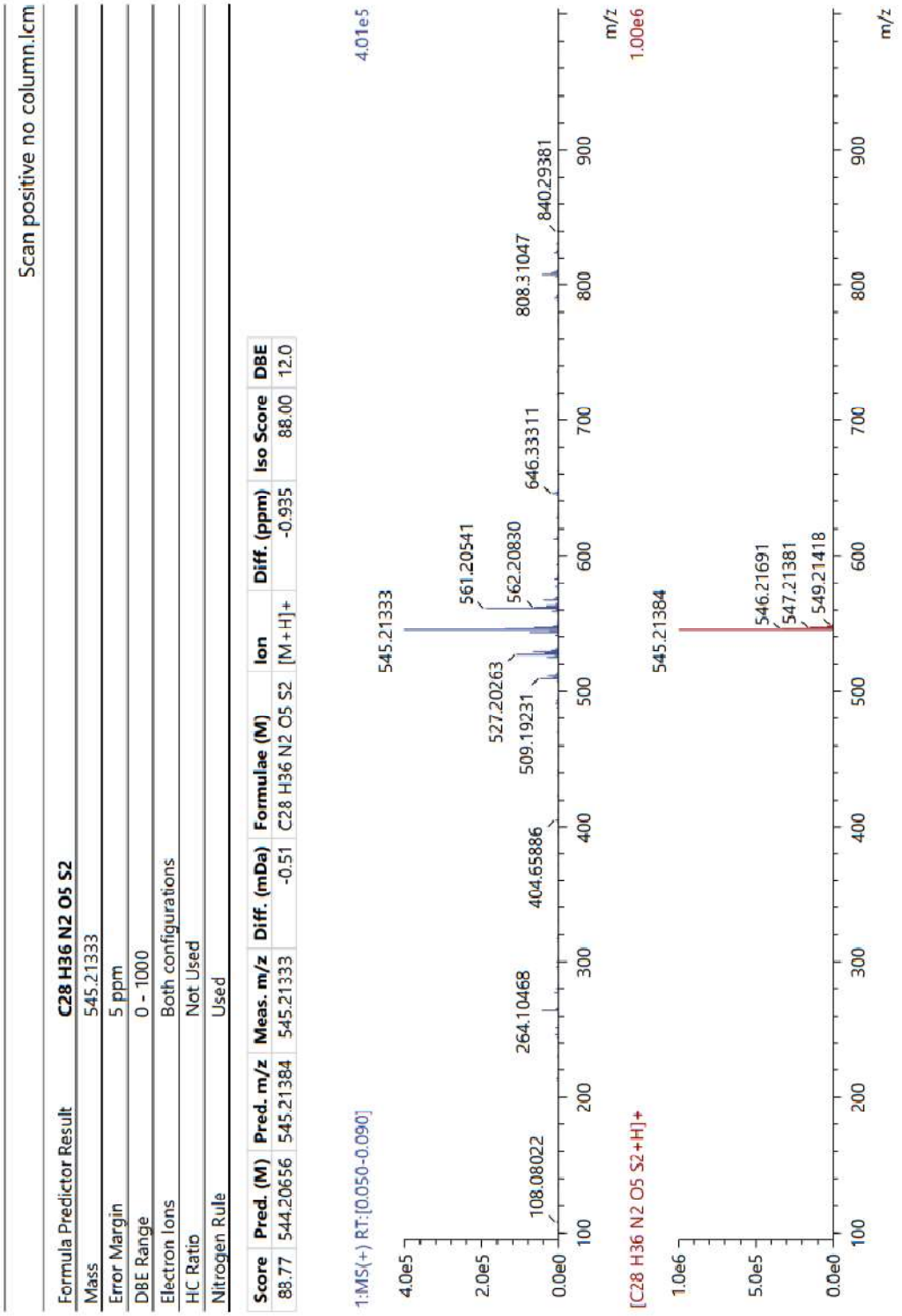


HRMS of S-((E)-5-hydroxy-7-(methyl(phenyl)amino)-7-oxohept-3-en-1-yl)-(E)-5-hydroxy-7-(methyl(phenyl)amino)-7-oxohept-3-ene-1-sulfinothioate, JRM-24

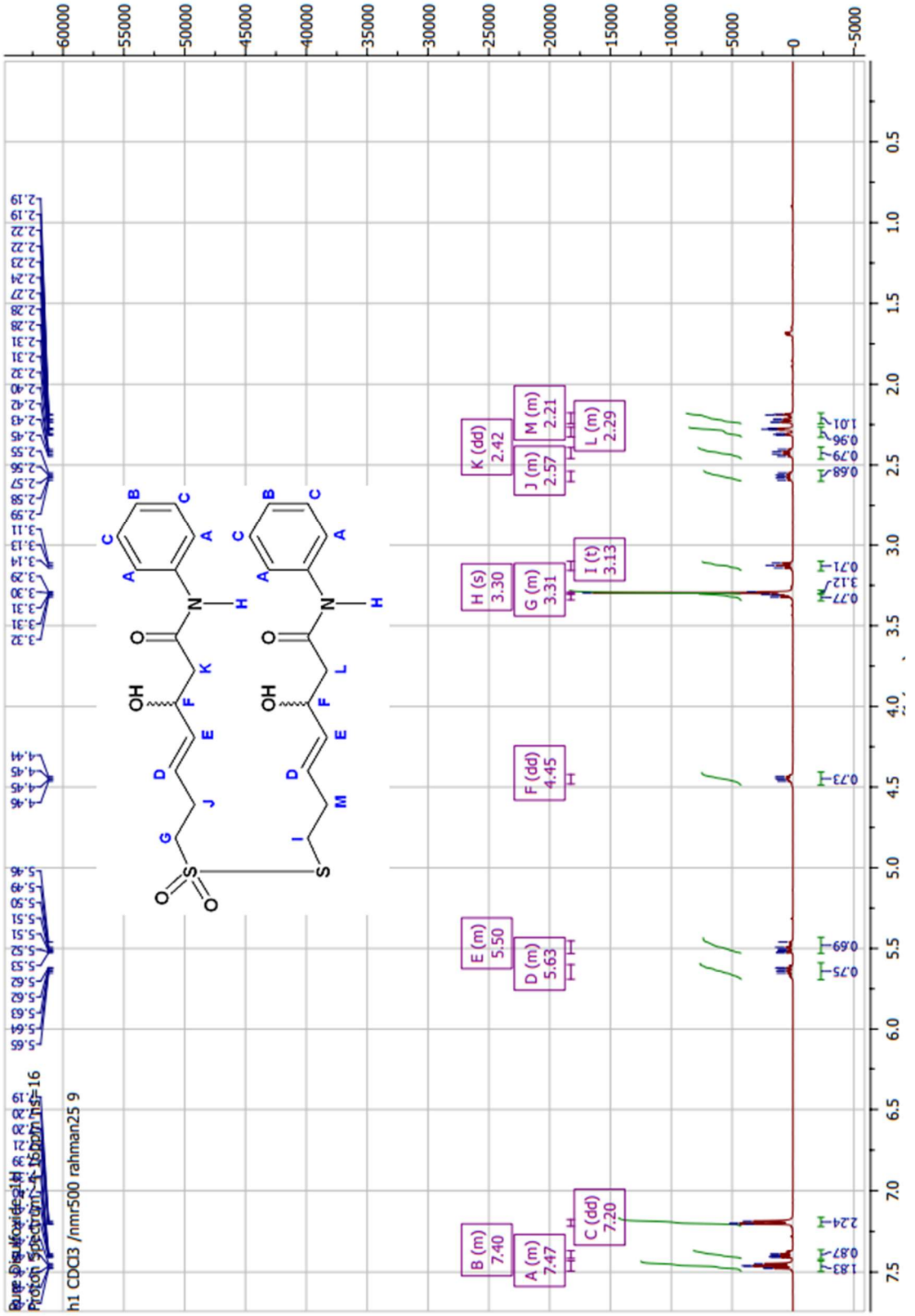
Scan positive no column.lcm

Formula Predictor Result	C28 H36 N2 O5 S2
Mass	545.21333
Error Margin	5 ppm
DBE Range	0 - 1000
Electron Ions	Both configurations
HC Ratio	Not Used
Nitrogen Rule	Used

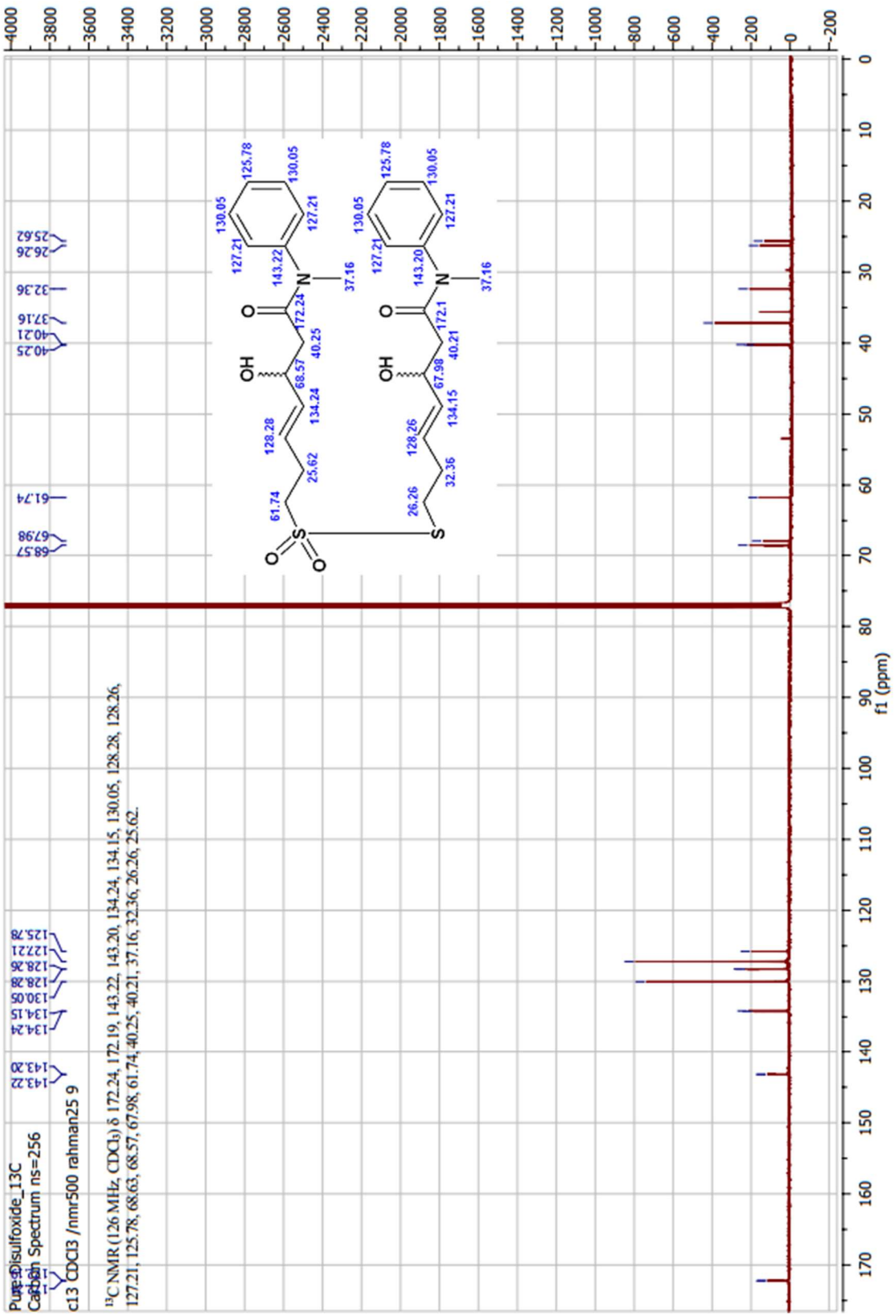
Score	Pred. (M)	Pred. m/z	Meas. m/z	Diff. (mDa)	Formulae (M)	Ion	Diff. (ppm)	Iso Score	DBE
88.77	544.20656	545.21384	545.21333	-0.51	C28 H36 N2 O5 S2	[M+H]+	-0.935	88.00	12.0



^{1}H NMR Spectrum of JRM-28



$^{13}C\{1H\}$ (proton-decoupled carbon) NMR Spectrum of JRM-28



4-8-2024.lcb

Formula Predictor Result	**C28 H36 N2 O6 S2**
Mass	561.20907
Error Margin	1000 ppm
DBE Range	0 - 1000
Electron Ions	Both configurations
HC Ratio	0 - 3
Nitrogen Rule	Not Used

Score	Pred. (M)	Pred. m/z	Meas. m/z	Diff. (mDa)	Formulae (M)	Ion	Diff. (ppm)	Iso Score	DBE
31.71	560.20148	561.20876	561.20907	0.31	C28 H36 N2 O6 S2	[M+H]+	0.552	24.38	12.0

